



**Hugo Miguel Bento Rebelo**

Master in Civil Engineering

## **Development and study of a high performance protective solution against blast loads**

Thesis submitted in partial fulfilment  
of the requirements for the degree of

Doctor of Philosophy in  
**Civil Engineering**

Adviser: Corneliu Cismaşiu, Associate Professor, Faculdade de Ciências e Tecnologia, Universidade NOVA de Lisboa

### Examination Committee

Chair: Professor Doutor Fernando Manuel dos Anjos Henriques  
Rapporteurs: Professor Doutor David Lecompte  
Professor Doutor Filipe Amarante dos Santos  
Members: Professor Doutor Luís Manuel Coelho Guerreiro  
Professor Doutor Corneliu Cismaşiu  
Professor Doutor Válder José da Guia Lúcio  
Doutor Jorge Filipe Marques Moniz Côrte-Real Andrade



## **Development and study of a high performance protective solution against blast loads**

Copyright © Hugo Miguel Bento Rebelo, NOVA School of Science and Technology, NOVA University Lisbon.

The NOVA School of Science and Technology and the NOVA University Lisbon have the right, perpetual and without geographical boundaries, to file and publish this dissertation through printed copies reproduced on paper or on digital form, or by any other means known or that may be invented, and to disseminate through scientific repositories and admit its copying and distribution for non-commercial, educational or research purposes, as long as credit is given to the author and editor.



# Acknowledgements

The present thesis would not have been accomplished without the guidance, support and assistance of several individuals and institutions to which I wish to express my sincere gratitude.

First and foremost, I would like to express my deepest and heartfelt recognition to my adviser, Professor Corneliu Cismaşiu, not only during the doctoral program, but since the beginning of our collaboration in 2015. I would like to express my gratitude towards him for his priceless scientific teachings, commitment and invaluable guidance in every stage of my research. It has been both a pleasure and a privilege.

The support provided by teaching staff at the Civil Engineering Department (NOVA School of Science and Technology) is also acknowledged, since they contributed to my growth as an engineer, researcher and human being.

I would like to express my gratitude towards my PhD colleagues from the Portuguese Army who introduced me into the challenging world of blast research. Their companionship and support helped me to overcome the initial hurdles related to these topics. Thanks Basto, Gomes, Marques, Matias and company.

I would like to thank Professor David Lecompte from the Royal Military Academy, Belgium, for the opportunity and conditions provided to me during my short stay there. Special thanks go to Jonet, Bachir and Bruno for their invaluable help and teachings regarding the conduction of experimental tests resorting to explosive charges. Thank you Rodrigo and Andreia for the friendship and the countless scientific chats in Portuguese even though in a foreign country.

The collaboration with Professor Pedro Rosa and Eng. Afonso Gregório from the Mechanical Engineering Department (Lisbon University) regarding the mechanical characterisation of 3D printed PLA is greatly acknowledged.

I am sincerely grateful to my friends and colleagues, specially David H., David M., Guilherme and Nuno, for their friendship, support, sharing their knowledge, mutual help and good humour over these years.

Lastly, I thank my family, specially my father, mother and sister for all their love, support and inspiration. I would like to thank Teresa and Paulo for our monthly game night and Simão for reminding us that we have not met in a while. *Obrigado pelos almoços semanais avô!*

I acknowledge the financial support of the Portuguese funding institution FCT - Fundação para a Ciência e Tecnologia, through contracts SFRH/BD/115599/2016 and PTDC/ECI-EST/31046/2017.



# Abstract

The increasing use of improvised explosive devices in terrorist attacks against civil targets has challenged the scientific community to find new strengthening or protective solutions able to mitigate the effects of the blast loads. As a response to this demand, the main purpose of the present thesis is the development and study of a high performance protective solution based on the concept of sacrificial claddings. Due to the high flexibility, precision and relatively low costs, additive manufacturing has been increasingly used in the search of new material disposition patterns that improve the mitigation capabilities of crushable cores.

The present work assesses the performance of a PLA crushable core manufactured through fused deposition modelling 3D printing. An experimental campaign is conducted to determine the mechanical behaviour of the PLA. These results allow the selection and calibration of an adequate numerical constitutive model, which considers the anisotropy and compressive/tensile asymmetry exhibited in additively manufactured materials.

Once the constitutive material calibrated, the results of a second experimental campaign resorting to an explosive driven shock tube are used to validate a numerical model that allows the deterministic design of a sacrificial cladding which successfully improves the blast resistant capabilities of a given structural element.

However, when verified taking into account the model's uncertainties and the probabilistic distribution of the structural element's properties, the cladding solution might, for certain blast scenarios, negatively impact the performance of the structural element it intends to protect.

Therefore, one may conclude that the use of a probabilistic approach in the design of such protective solutions is recommended, as the deterministic approach might yields results against safety.

**Keywords:** Blast loads; Sacrificial cladding; Additive manufacturing; Explosive driven shock tube; Robustness assessment.





# Resumo

O uso crescente de engenhos explosivos improvisados para a realização de ataques terroristas contra infraestruturas tem desafiado a comunidade científica a desenvolver novas soluções de reforço e proteção capazes de mitigar os efeitos de cargas explosivas. De forma a dar resposta a este problema, o objetivo principal da presente tese é o desenvolvimento e estudo de uma solução de proteção de alto desempenho baseada no conceito de revestimento sacrificial. Devido à sua elevada flexibilidade, precisão e custos relativamente baixos, a manufatura aditiva tem vindo a ser cada vez mais utilizada na procura de novas geometrias que melhorem as capacidades de mitigação de núcleos dissipativos.

O presente estudo avalia o desempenho de um núcleo dissipativo em PLA e produzido através de impressão 3D por extrusão. O comportamento mecânico do PLA é determinado através de uma campanha experimental, permitindo a seleção e calibração de um modelo constitutivo numérico adequado. Este modelo considera a anisotropia e a assimetria de compressão/tração exibidas por materiais fabricados recorrendo a manufatura aditiva.

Uma vez calibrado o modelo constitutivo, os resultados obtidos através de uma segunda campanha experimental, que recorre a um tubo de choque, são utilizados para validar um modelo numérico. Este permite o dimensionamento determinístico de um revestimento sacrificial, melhorando assim a resistência de um determinado elemento estrutural contra os efeitos de uma explosão.

Contudo, quando a verificação de segurança é realizada tendo em conta as incertezas do modelo e a distribuição probabilística das propriedades do elemento estrutural, o revestimento sacrificial pode, em certos cenários, piorar o desempenho do elemento estrutural que este pretende proteger.

Consequentemente, conclui-se que o uso de uma abordagem probabilística durante o dimensionamento deste género de soluções é recomendado pois a abordagem determinística poderá conduzir a resultados contra a segurança.

**Palavras-chave:** Efeito de explosivos; Revestimento sacrificial; Manufatura aditiva; Tubo de choque; Avaliação da robustez



# Contents

- List of figures** **xv**
- List of tables** **xxi**
- List of abbreviations, acronyms and symbols** **xxiii**
- 1 Introduction** **1**
  - 1.1 Background and motivation . . . . . 1
  - 1.2 Objectives and methodology . . . . . 4
  - 1.3 Thesis outline . . . . . 4
  - 1.4 Published work . . . . . 6
- 2 Explosive blast loading** **7**
  - 2.1 Introduction . . . . . 7
  - 2.2 Blast wave phenomena . . . . . 7
  - 2.3 Rankine-Hugoniot conditions . . . . . 8
  - 2.4 Blast wave reflection . . . . . 9
  - 2.5 Scaling laws . . . . . 10
  - 2.6 Blast wave characterisation . . . . . 12
    - 2.6.1 Blast wave parameters . . . . . 12
    - 2.6.2 Pressure-time history approximation . . . . . 13
    - 2.6.3 Experimental validation . . . . . 18
  - 2.7 Non-ideal reflective surface . . . . . 21
    - 2.7.1 Fluid-structure interaction . . . . . 21
    - 2.7.2 Pressure applied to a finite area . . . . . 23
  - 2.8 Blast load simulation in LS-DYNA . . . . . 26
  - 2.9 Structural response to blast loading . . . . . 27
    - 2.9.1 Material performance under high strain rate loading . . . . . 28
    - 2.9.2 Performance criteria . . . . . 30
    - 2.9.3 Structural analysis . . . . . 33
    - 2.9.4 Single-degree-of-freedom method . . . . . 35
    - 2.9.5 Pressure-impulse and charge weight-standoff diagrams . . . . . 40
  - 2.10 Conclusions . . . . . 43

---

<b>3</b>	<b>Protective solutions</b>	<b>45</b>
3.1	Introduction . . . . .	45
3.2	Reinforced concrete . . . . .	46
3.2.1	High strength concrete . . . . .	46
3.2.2	Fibre reinforced concrete . . . . .	47
3.2.3	Ultra-high performance concrete . . . . .	48
3.3	Externally bonded steel plates . . . . .	48
3.4	Composite materials . . . . .	49
3.5	Sacrificial cladding solution . . . . .	50
3.5.1	Energy absorption principles . . . . .	51
3.5.2	Cellular solids . . . . .	52
3.5.3	Simplified models . . . . .	78
3.6	Conclusions . . . . .	90
<b>4</b>	<b>Experimental testing</b>	<b>93</b>
4.1	Introduction . . . . .	93
4.2	Sample preparation . . . . .	94
4.3	Material characterisation . . . . .	95
4.3.1	Mechanical testing . . . . .	97
4.4	Blast testing . . . . .	100
4.4.1	Preliminary quasi-static tests . . . . .	101
4.4.2	Experimental set-up . . . . .	102
4.4.3	Instrumentation . . . . .	102
4.4.4	Blast load on rigid and fixed boundary . . . . .	105
4.4.5	Preliminary tests on the experimental set-up . . . . .	105
4.4.6	Sacrificial cladding . . . . .	108
4.5	Conclusions . . . . .	111
<b>5</b>	<b>Development, verification and validation of numerical models</b>	<b>113</b>
5.1	Introduction . . . . .	113
5.2	Material model calibration . . . . .	113
5.2.1	Laminated Composite Fabric material model . . . . .	114
5.2.2	Numerical model . . . . .	121
5.2.3	Results . . . . .	122
5.3	Blast testing . . . . .	126
5.3.1	FE numerical model . . . . .	126
5.3.2	Simplified model . . . . .	134
5.3.3	Results of FE numerical model . . . . .	136
5.3.4	Results of simplified model . . . . .	147
5.4	Conclusions . . . . .	153
<b>6</b>	<b>Design of a sacrificial cladding solution</b>	<b>157</b>

---

6.1	Introduction . . . . .	157
6.2	Simplified models . . . . .	157
6.2.1	Pressure-impulse diagram . . . . .	158
6.2.2	Structure . . . . .	159
6.2.3	Load-Cladding-Structure (LCS) model . . . . .	167
6.3	Case study . . . . .	174
6.3.1	Experimental campaign . . . . .	174
6.3.2	Simplified model . . . . .	176
6.3.3	Blast resistant capability . . . . .	177
6.3.4	Sacrificial cladding solution design . . . . .	179
6.3.5	Robustness assessment of the designed solution . . . . .	182
6.4	Conclusions . . . . .	192
<b>7</b>	<b>Conclusions and future research</b>	<b>197</b>
7.1	Summary and conclusions . . . . .	197
7.2	Innovative aspects . . . . .	201
7.3	Future research . . . . .	202
	<b>Bibliography</b>	<b>205</b>



# List of figures

- 1.1 Worldwide number of terrorist attacks that resorted to improvised explosive devices . . . . . 1
- 1.2 Aftermath of blast scenario on buildings . . . . . 2
- 2.1 Pressure-time profile of an incident blast wave . . . . . 8
- 2.2 Diagram of a shock front travelling with velocity  $U$  through undisturbed air 9
- 2.3 Pressure-time profile of a reflected blast wave . . . . . 10
- 2.4 Hopkinson-Cranz scaling law . . . . . 11
- 2.5 Positive phase blast wave parameters . . . . . 14
- 2.6 Negative phase blast wave parameters . . . . . 15
- 2.7 Comparison of Kingery & Bulmash semi-empirical method and experimental results obtained by Bogosian and team and Netherton & Stewart . . . . . 20
- 2.8 Ratio between Rankine-Hugoniot conditions and Kingery & Bulmash predictions for  $P_r$ ,  $\rho_s$  and  $U$  . . . . . 23
- 2.9 Rarefaction wave resulting from diffraction of blast wave around a free edge 24
- 2.10 Blast wave clearing correction . . . . . 25
- 2.11 Spatial and temporal distribution of the rarefaction wave . . . . . 27
- 2.12 Dynamic Increase Factors for concrete . . . . . 29
- 2.13 Dynamic Increase Factors for reinforcement steel bars . . . . . 30
- 2.14 Dynamic systems . . . . . 36
- 2.15 Maximum response of undamped elastoplastic single-degree-of-freedom system due to a triangular load pulse . . . . . 38
- 2.16 Fixed-end beam response modes and corresponding resistance-deflection function . . . . . 39
- 2.17 Typical pressure-impulse and charge weight-standoff diagrams . . . . . 41
- 2.18 Numerical approaches to compute PI curves . . . . . 43
- 3.1 Enhancement of blast resistance of RC column by means of steel jacketing . 49
- 3.2 Sacrificial cladding’s philosophy . . . . . 51
- 3.3 Cellular solid examples . . . . . 53
- 3.4 Compressive behaviour of cellular solids . . . . . 54
- 3.5 Full-scale tests using aluminium foam as the crushable core of a sacrificial cladding solution . . . . . 56

LIST OF FIGURES

---

3.6	Influence of PU thickness . . . . .	57
3.7	Simulation of continuous-density graded cellular materials . . . . .	59
3.8	Guruprasad and Mukherjee’s sacrificial cladding solution . . . . .	60
3.9	Four cable pendulum set-up . . . . .	60
3.10	Experimental study of impulse transferred by crushable tube cores . . . . .	61
3.11	Triple tube (TT) system for blast mitigation . . . . .	62
3.12	Schematic view and photograph of small-scale air blast test set-up . . . . .	62
3.13	Schematic representation of the experimental set-up for the sacrificial cladding	63
3.14	Deformation patterns of empty recyclable beverage cans . . . . .	64
3.15	Development of deformation patterns of a metal beverage can . . . . .	64
3.16	Sacrificial cladding with SDK crushable core . . . . .	65
3.17	Metallic lattice structure . . . . .	66
3.18	Blast-loaded specimens based on the $[0^\circ, \pm 45^\circ]$ pillar-octahedral unit cell . .	67
3.19	Development of hybrid lattice structure based on square honeycomb . . . . .	68
3.20	Normalised quasi-static compressive stress-strain response of hybrid lattice structure . . . . .	69
3.21	Straight strut structure based on an open-celled foam . . . . .	70
3.22	Relative densities of graded lattice structures . . . . .	71
3.23	Compressive stress–strain curves of the lattice structures . . . . .	71
3.24	Geometrical configuration of lattice cylindrical shells . . . . .	72
3.25	Typical deformation modes of lattice cylindrical shells . . . . .	73
3.26	Assembling of unit cell to form an honeycomb structure . . . . .	74
3.27	In-plane compressive response of TPU honeycomb structure . . . . .	75
3.28	Development of hierarchical honeycomb structure . . . . .	75
3.29	Quasi-static compressive response of regular and hierarchical honeycombs .	76
3.30	Negative stiffness honeycomb structure . . . . .	76
3.31	Sandwich panels with alternative cellular core architectures . . . . .	77
3.32	Experimental force-displacement curves of 3D printed with alternative cellu- lar core configurations, cell topologies and relative densities . . . . .	78
3.33	Infinitesimal element of a bar with uniform cross-section represented in ma- terial coordinates . . . . .	81
3.34	Infinitesimal controlled volume of a bar with uniform cross-section repre- sented in spatial coordinates . . . . .	82
3.35	Quasi-static stress-strain relation vs. the Rayleigh line . . . . .	85
3.36	Schematic representation of the blast-loaded aluminium foam bar’s simplified model . . . . .	86
3.37	Free body diagrams of aluminium foam bar at times $t$ and $t + dt$ . . . . .	86
3.38	Schematic representation of the Load-Cladding-Structure model . . . . .	87
3.39	Free body diagram of the Load-Cladding-Structure model . . . . .	88
3.40	Commonly used simplified constitutive relations for cellular materials . . .	90



4.1	Prusa Mk3 3D printer . . . . .	94
4.2	Schematic of a Fused Deposition Modelling 3D printer . . . . .	94
4.3	Angle between 3D printing orientation and loading direction . . . . .	96
4.4	True stress-true strain curves for specimens of different diameters . . . . .	96
4.5	Geometry of the tested specimens . . . . .	97
4.6	Mechanical characterisation of the commercial PLA . . . . .	97
4.7	Schematic representation and nomenclature of the specially designed split-Hopkinson bar apparatus . . . . .	98
4.8	Maximum stress of PLA as a function of the strain rate . . . . .	99
4.9	3D printed PLA stress response with respect to strain and strain rate . . . . .	100
4.10	Experimental sample of the 3D printed crushable core . . . . .	101
4.11	Specimens' cross section . . . . .	101
4.12	Quasi-static stress-strain curve dependence on the relative density . . . . .	102
4.13	Experimental set-up . . . . .	103
4.14	Two-dimensional projection of SC solution on HSC . . . . .	105
4.15	Average reflected overpressure-time history measured on rigid and fixed boundary . . . . .	106
4.16	Schematic representation of the remainder of the experimental set-up and corresponding force-time history . . . . .	107
4.17	Schematic representation of the PCB 203B load cell installation . . . . .	107
4.18	Force-time history on rigid and fixed boundary . . . . .	108
4.19	Photo of the specimens after being subjected to blast load . . . . .	109
4.20	Influence of layer height on nonlinear reponse of the proposed sacrificial cladding solution . . . . .	110
5.1	Failure planes of the lamina . . . . .	115
5.2	Multisurface $f$ , formed by $f_{\perp}$ and $f_{\parallel}$ in the effective stress space . . . . .	117
5.3	Damage evolution law . . . . .	119
5.4	Typical MAT058 stress-strain curve for longitudinal and transverse directions (compression/tension) . . . . .	120
5.5	Schematic of the single element compression/tension simulations . . . . .	122
5.6	Experimental and numerical stress-strain curves under compressive loading . . . . .	123
5.7	Experimental and numerical stress-strain curves under tensile loading . . . . .	124
5.8	Experimental and numerical stress-strain curves under high strain rate compressive loading . . . . .	125
5.9	FE model of the set-up . . . . .	126
5.10	FE model of the sacrificial cladding solution . . . . .	127
5.11	Dynamic relaxation verification . . . . .	132
5.12	Mesh sensitivity analysis . . . . .	133
5.13	One-dimensional simplified model . . . . .	134
5.14	Logical diagram of MATLAB implementation for the simplified model . . . . .	136

LIST OF FIGURES

---

5.15	Force-time history on rigid and fixed boundary . . . . .	137
5.16	Force-time history dependence on the relative density . . . . .	138
5.17	Displacement and velocity-time histories dependence on the relative density	139
5.18	Side view of the sacrificial cladding solutions under dynamic compression .	141
5.19	Stress-strain curve ( $\bar{\rho} = 5\%$ ) . . . . .	142
5.20	Evolution of the crushing mechanism in the PLA honeycomb ( $\bar{\rho} = 5\%$ ) . . . .	142
5.21	Stress-strain curve ( $\bar{\rho} = 7.5\%$ ) . . . . .	143
5.22	Evolution of the crushing mechanism in the PLA honeycomb ( $\bar{\rho} = 7.5\%$ ) . . .	143
5.23	Stress-strain curve ( $\bar{\rho} = 10\%$ ) . . . . .	144
5.24	Evolution of the crushing mechanism in the honeycomb ( $\bar{\rho} = 10\%$ ) . . . . .	144
5.25	Comparison of force-time histories obtained with full and “independent” model	147
5.26	Displacement and velocity-time histories obtained with the simplified model	148
5.27	Numerical contact stress between aluminium front plate and 3D printed solid plate . . . . .	149
5.28	Acceleration distribution over the specimen’s side and resultant acceleration- time histories of the front plate and the honeycomb structure . . . . .	151
5.29	Displacement and velocity-time histories obtained with the modified simpli- fied model . . . . .	152
6.1	Pivot search numerical method to compute pressure-impulse diagrams . . . .	158
6.2	Logical diagram of the pivot search numerical method to compute Pressure- Impulse diagrams . . . . .	159
6.3	Response of a reinforced concrete structural element . . . . .	160
6.4	Generic RC cross-section . . . . .	161
6.5	Bilinear hysteretic model . . . . .	165
6.6	Logical diagram of MATLAB implementation for bilinear SDOF system . . . .	166
6.7	Non-dimensional maximum response an undamped elasto-plastic SDOF due to a triangular load pulse . . . . .	167
6.8	Logical diagram of MATLAB implementation for LCS model . . . . .	170
6.9	Non-dimensional maximum displacement of a structure protected with a foam sacrificial cladding . . . . .	172
6.10	Non-dimensional pressure-impulse diagram of the structure . . . . .	172
6.11	Logical diagram of the determination of pressure-impulse diagram resorting to charge weight-standoff diagram . . . . .	174
6.12	Geometry and reinforcement details for one-way RC beams . . . . .	175
6.13	Experimental set-up of the RC beam and explosive charge within the shock tube . . . . .	176
6.14	Experimental and analytical resistance-displacement curves of a simply-supported RC beam . . . . .	177
6.15	Experimental and numerical displacement-time histories of RC beam sub- jected to a blast load . . . . .	178

---

6.16 Pressure-impulse diagram considering that a triangular pulse (solid line) or the modified Friedlander equation (dashed line) is applied to the structural element . . . . .	179
6.17 Density as a function of plateau stress of 3D printed honeycomb structure .	180
6.18 Scaled maximum displacement as a function of non-dimensional parameters $\kappa$ and $\tau$ when a 6000 kPa·ms impulse is imparted on the case study's structural element . . . . .	181
6.19 Pressure-impulse diagrams of bare RC beam and with 3D printed sacrificial cladding solution . . . . .	181
6.20 Probabilistic distribution of the chosen key parameters . . . . .	184
6.21 Evolution of the standard deviation and its relative error throughout the sample space . . . . .	185
6.22 Pressure-impulse diagrams of the bare RC beam considering probabilistic variability of key parameters . . . . .	186
6.23 Pressure-impulse diagrams of the RC beam with 3D printed sacrificial cladding solution considering probabilistic variability of key parameters . . . . .	188
6.24 Performance-based pressure-impulse diagrams . . . . .	189
6.25 Performance-based pressure-impulse diagrams of bare RC beam and with 3D printed sacrificial cladding solution (5% conditional probability) . . . . .	190
6.26 Fragility curves for the bare RC beam and with 3D printed sacrificial cladding solution . . . . .	191



# List of tables

- 2.1 Statistical values for experimental/K&B ratio ( $P_r$ ) . . . . . 19
- 2.2 Statistical values for experimental/K&B ratio ( $i_r$ ) . . . . . 19
- 2.3 Dynamic Increase Factors for the design of reinforced concrete elements . . 30
- 2.4 Building levels of protection . . . . . 31
- 2.5 Component damage depending on the level of protection of the building . . 31
- 2.6 Response limits for reinforced concrete elements . . . . . 34
- 2.7 Response limits for structural steel elements . . . . . 34
- 2.8 Transformation factors for beams . . . . . 38
  
- 3.1 Summary of the use of high strength concrete for blast resistant design . . . 47
- 3.2 Summary of the use of fibre reinforced concrete for blast resistant design . . 47
- 3.3 Summary of the use of composite materials for the strengthening of reinforced concrete components . . . . . 50
- 3.4 Summary of experimental set-up to evaluate the dynamic compressive behaviour of cellular solids . . . . . 55
  
- 4.1 Printing parameters . . . . . 95
- 4.2 Summary of the measured mechanical properties for all considered orientations 99
- 4.3 Properties of the regular hexagon honeycomb . . . . . 100
- 4.4 Summary of 3D printed honeycomb mechanical properties under quasi-static loading . . . . . 101
- 4.5 Specification of PCB 203B force load cell . . . . . 103
- 4.6 Specification of PCB 102B force load cell . . . . . 104
- 4.7 Summary of the experimental results . . . . . 109
  
- 5.1 Material model properties for PLA . . . . . 120
- 5.2 Nonphysical parameters for material model . . . . . 121
- 5.3 Material properties for aluminium and steel . . . . . 131
- 5.4 Mesh sensitivity analysis of the set-up . . . . . 133
- 5.5 Mesh sensitivity analysis of sacrificial cladding solution (5% relative density) 134
- 5.6 Summary of the experimental/numerical results . . . . . 145
- 5.7 Additional numerical estimates . . . . . 146
- 5.8 Summary of the experimental and simplified results (Diff. [%]) . . . . . 153

LIST OF TABLES

---

6.1	Event functions for the LCS model . . . . .	169
6.2	Blast wave parameters and experimental results obtained by Magnusson when specimen B100-D2(12) is subjected the effects of a 2.0 kg explosive charge .	176
6.3	SDOF's properties . . . . .	177
6.4	Response limits considered for the case study . . . . .	178
6.5	Probabilistic characterisation of key parameters . . . . .	183

# List of abbreviations, acronyms and symbols

## Abbreviations

K&B Kingery & Bulmash

TNT Trinitrotoluene

## Acronyms

ABS Acrylonitrile–butadiene–styrene

AM Additive manufacturing

ANFO Ammonium nitrate/fuel oil

DIF Dynamic Increase Factor

DTRA Defense Threat Reduction Agency

EDST Explosive driven shock tube

ETT Extended Taylor theory

FDM Fused deposition modelling

FSI Fluid-structure interaction

HSC High strength concrete

KNR Kambouchev, Noels and Radovitzky

LoP Level of protection

MM-ALE Multi-material Arbitrary Lagrangian-Eulerian

## SYMBOLS

---

NSC	Normal strength concrete
ODE	Ordinary differential equation
PI	Pressure-impulse
PLA	Polylactic acid
PU	Polyurethane
RC	Reinforced concrete
RPH	Rigid-plastic hardening
RPPL	Rigid-perfectly plastic-locking
SDK	Square dome-shape kirigami
SDOF	Single-degree-of-freedom
<i>SEA</i>	Specific energy absorption
SLM	Selective laser melting
SLS	Selective laser sintering
TPU	Thermoplastic polyurethane
UHPC	Ultra-high performance concrete

## Symbols

$\alpha$	“Stress limiting factor” (MAT058)
$\alpha_e$	Modular ratio
$\gamma$	Specific heat ratio
$\delta$	Hudson’s non-dimensional time
$\delta_m$	Maximum displacement of a structural component
$\varepsilon$	Nominal strain
$\varepsilon_d$	Densification initiation strain of a cellular solid
$\varepsilon_f$	Nominal failure strain (MAT058)
$\dot{\varepsilon}$	Strain rate
$\zeta$	Distribution coefficient



---

$\eta$	Energy efficiency parameter Hudson's non-dimensional length
$\theta$	Blast wave's angle of incidence Support's rotation
$\kappa$	Non-dimensional parameter that relates the resistance of the sacrificial cladding and the structural element (LCS Model)
$\mu$	Ductility ratio Mean Reduced bending moment
$\nu$	Poisson's ratio
$\rho$	Density of a material
$\rho^*$	Density of a cellular solid
$\rho_s$	Density of a cellular solid's constituent material
$\bar{\rho}$	Relative density of a cellular solid
$\sigma$	Nominal stress Standard deviation
$\sigma_{pl}$	Plateau stress of a cellular solid
$\hat{\sigma}$	Effective stress (MAT058)
$\tau$	Non-dimensional parameter that relates the impulse transmitted by sacrificial cladding and the one required to fully compress the crushable core (LCS Model) Shear stress
$\hat{\tau}$	Effective shear stress (MAT058)
$\psi$	Physical quantity (continuum mechanics model framework)
$\omega$	Angular frequency of a structural element Mechanical reinforcement ratio of a reinforced concrete section
$\omega$	Damage parameters (MAT058)

---

$a_0$	Speed of sound in undisturbed air
$A$	Longitudinal direction (MAT_058)
$AOPT$	Material axes option (MAT_058)
$b$	Decay parameter of shock wave's pressure-time history
$B$	Transverse direction (MAT_058)
$c$	Spatial wave velocity (continuum mechanics model framework)
$C$	Intrinsic wave velocity (continuum mechanics model framework)
$\mathbf{C}$	Constitutive tensor (MAT_058)
$C_r^-$	Negative reflection coefficient (Teich & Gebbeken)
$C_r$	Reflection coefficient
$D$	Shock wave's velocity (continuum mechanics model framework)
$e$	Specific energy Sacrificial cladding's efficiency
$E$	Young's modulus
$ERODS$	Maximum strain for layer failure (MAT_058)
$f_y$	Yield strength of steel
$f_u$	Ultimate strength of steel
$f_{\parallel}$ and $f_{\perp}$	Loading criteria defined in the effective stress space (MAT_058)
$G$	Shear modulus
$i_r$	Reflected specific impulse
$i_s$	Specific impulse
$k$	Structural element's stiffness
$K_e$	Equivalent stiffness of SDOF system
$K.E.$	Kinetic energy
$K_L$	Load factor
$K_{LM}$	Load-mass factor
$K_M$	Mass factor
$K_R$	Resistance factor
$m$	Mass per unit length of one-dimensional bar
$M_1$	Front plate's mass (sacrificial cladding solution)

---

$M_e$	Equivalent mass of SDOF system
$M_{pl}$	Moment capacity
$P_a$	Ambient air pressure
$P_r$	Peak reflected overpressure
$P_r^-$	Peak negative reflected overpressure
$P_{so}$	Peak incident overpressure
$P_{so}^-$	Peak negative incident overpressure
$P_{stag}$	Stagnation pressure
$r$	Damage threshold (MAT_058)
$\bar{R}$	Sach's scaled distance
$R_m$	Maximum resistance
$S_C$	Shear strength (MAT_058)
$S.E.$	Strain energy
$S_{LIM}$	Stress limit factor
$t_a$	Arrival time of a shock wave
$t_c$	Characteristic clearing time
$t_o^+$	Positive phase duration
$t_o^-$	Negative phase duration
$t_{o,lin}$	Positive phase duration of a triangular pulse
$t_{o,lin}^-$	Negative phase duration of the triangular approximation
$t_R$	Reduced time constant (KNR method)
$T SIZE$	Time step for automatic element deletion (MAT_058)
$TSSFAC$	Time step scale factor
$U$	Shock front's velocity (Blast wave framework)
$U_{pl}$	Absorbed/transmitted energy
$v$	Particle's velocity (Blast wave and continuum mechanics model framework)
$W_E$	Equivalent weight of TNT
$W.E.$	Work done by a load
$x$	Location in space (continuum mechanics model framework)
$x_I$ and $x_{II}$	Neutral axis positions of uncracked and cracked reinforced concrete cross-sections

---

$X$	Mass point (continuum mechanics model framework)
$X_C$ and $X_T$	Longitudinal compressive and tensile strength (MAT_058)
$Y_C$ and $Y_T$	Transverse compressive and tensile strength (MAT_058)
$Z$	Hopkinson-Cranz's scaled distance

# Chapter 1

## Introduction

### 1.1 Background and motivation

Since the dawn of time, there has been a constant drive to design structures which withstand the effects of gravity, wind, temperature changes and earthquake's actions. However, accidental explosions and the use of improvised explosive devices in terrorist attacks against civil engineering structures increased significantly during the last decades (see Figure 1.1) establish the need to consider blast loads in the design of important structures. One mention that an explosion within or surrounding a building may result in the failure of critical load bearing members, with subsequent social disruption and psychological impact on society, as well as high economic and environmental losses.

Throughout history, see Figure 1.2, society has been challenged with several blast events. For example, on April 19<sup>th</sup>, 1995, a truck containing approximately 2300 kg of equivalent trinitrotoluene (TNT), detonated close to the Alfred P. Murrah Federal Building in Oklahoma City, USA. As illustrated in Figure 1.2(a), a third of the building collapsed due to the destruction of the first floor columns, which supported a 12 m long transfer girder. Additionally, the blast destroyed or damaged 324 buildings in a 16 block

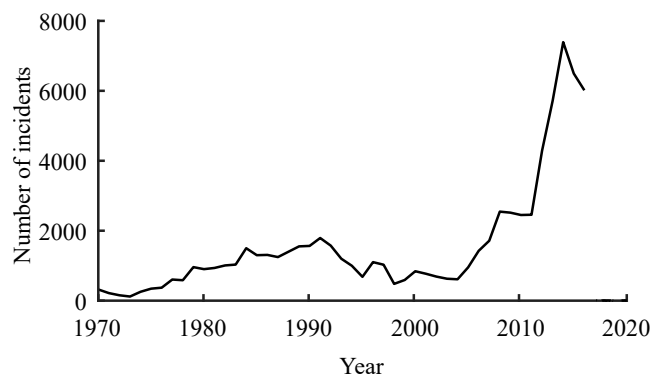


Figure 1.1: Worldwide number of terrorist attacks that resorted to improvised explosive devices (Data from [110])

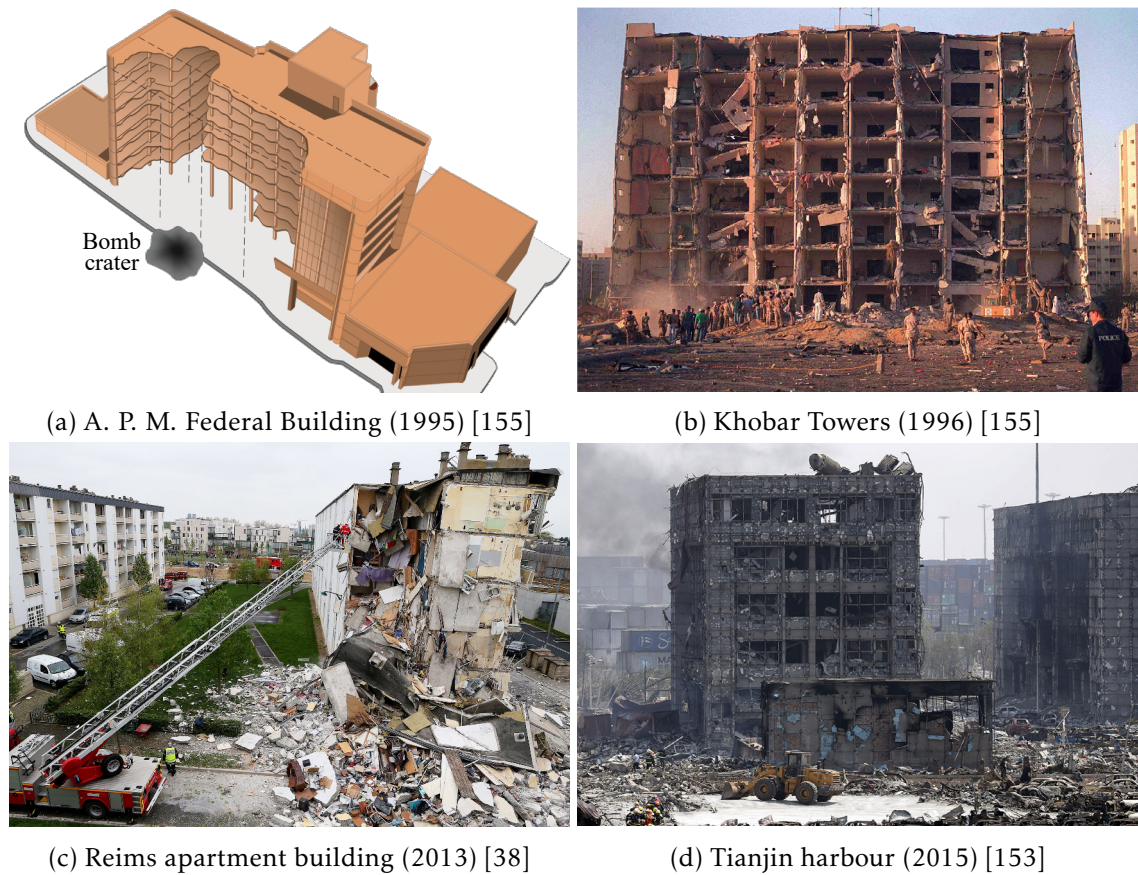


Figure 1.2: Aftermath of blast scenario on buildings

radius. In 1996, a large truck containing approximately the equivalent to 9000 kg of TNT attacked the Khobar Towers military housing in Saudi Arabia. Despite being a pre-cast concrete structure, the bolted connections of these towers were designed according to the British standards for blast-resistant structures. As a result, as depicted in Figure 1.2(b), the damage resulting from the detonation was less extensive than the damage of the Alfred P. Murrah Federal Building [155].

Additionally, civil society also faces the danger of explosions resulting from accidental explosions. As an example, in 2013, a gas explosion inside an apartment led to the partial collapse of the five storey building (see Figure 1.2(c)) [138]. In August 2015, a warehouse for hazardous materials at the port of Tianjin, China, suffered two explosions as a consequence of a fire of unknown origin, leading to a massive loss of lives and severe injuries and to significant material losses. It was estimated that the first explosion had an equivalent weight of 3000 kg of TNT, while the second one had an equivalent weight of 21,000 kg of TNT [21]. Figure 1.2(d) shows a building damaged by the explosions and the resulting debris.

The implementation of protective techniques is crucial to mitigate the effects of blast loads on structures and to ensure their survivability. According to Krauthammer [69] and Dusenberry [31], increasing the standoff distance is the most effective mitigation

approach when designing structural elements to resist blast loads. However, this approach requires the creation of a secured perimeter to guarantee the specified distances, which might not be available in an urban environment. Consequently, in such cases, the mitigation of damage is only possible using preventive techniques. According to Bangash [5], if a given structure is designed to withstand blast loads, reinforced concrete elements behave better than their steel counterparts, as a result of their increased mass, damping and energy absorbing capacity. Therefore, the traditional protective techniques are based on the use of a thicker reinforced concrete, ultra high-performance and fibre reinforced concrete structural elements [16, 171, 178]. Nonetheless, these techniques are time consuming and labour intensive, which leads to an increase in construction cost both during the strengthening process and due to retrofit if damaged, and are heavy and often difficult to install in existing facilities. The use of externally bonded steel plates and composite materials (usually fibre reinforced polymers) as a protective technique has been studied and reported in the literature [15, 103]. However, the use of externally bonded steel plates greatly increases the dead weight of the structure and leads to high costs. The use of composite materials result in high costs.

An alternative solution is the use of protection solutions with reduced mass and high energy absorption, which are considered to be advantageous when compared with the traditional strengthening methods used to improve the blast resistance capabilities of structural elements [188]. These solutions are commonly referred to as sacrificial claddings and are positioned on the outer surface of the structural elements in order to mitigate the blast load to a relatively lower level for a longer time span, absorbing most of the blast induced energy. They are usually composed by a crushable core, which undergoes a progressive deformation under a relatively low stress, and two skin plates (front and rear). The crushable core is usually materialised by a cellular material or structure, while the plates aim to evenly distribute the blast load to the crushable core and may be made metallic or composite.

Additive manufacturing (AM), also referred to as three-dimensional (3D) printing, has recently become a viable manufacturing process as a result of the numerous advantages over traditional subtractive manufacturing techniques when complex geometries are required. Despite covering a large range of techniques, the majority of the currently available AM processes build parts in a similar fashion: the base material is deposited, fused, or cured in successive two-dimensional layers that, ultimately, form a three-dimensional object [30]. Amongst the available technologies, fused deposition modelling (FDM), which is based on extrusion additive manufacturing, is the most common in consumer-level 3D printers working with polymer composites. As a result of the geometrical freedom, the use of 3D printing as a manufacturing technique for energy absorption structures has grown in interest in recent years, since it allows tailored properties.

Finite element (FE) modelling is considered to be a valuable tool to study additively manufactured protective solutions [19, 71, 145]. These protective solutions are commonly based on thin walled structures [19, 71]. Due to their dimensions, the layers of these walls

are usually manufactured in the same direction, resulting in an anisotropic mechanical behaviour of the constitutive materials. Nonetheless, most of the studies reported in the literature consider the 3D printed material as homogeneous and isotropic, which is a major drawback of these numerical models. Additionally, although the energy absorption capabilities of 3D printed components are proved to be strain rate dependent, most of the experimental compression tests are performed under quasi-static regime [1, 7, 20].

## 1.2 Objectives and methodology

The present thesis aimed to develop and study a high performance protective solution against blast loads. These solutions were based on the concept of sacrificial claddings with a crushable core manufactured using the FDM 3D printing technique.

The protective solutions were studied in terms of their energy absorption capabilities and efficiency, obtained by comparing the impulse resulting from a given blast load and the impulse transmitted to a given structural element. According to Zhou and co-workers [188], the crushable core must have sufficient thickness to avoid full crushing, since at this instant the transferred load might increase to values larger than those observed if no sacrificial cladding was used.

In order to overcome the limitations related to the mechanical behaviour of 3D printed components, an experimental campaign was conducted in order to calibrate their numerical constitutive model. Moreover, a suitable experimental set-up was required to correctly attain the nonlinear response of the additively manufactured crushable core when subjected to blast loads. Subsequently, the experimental results allowed the validation of a FE numerical model and a simplified model. Finally, resorting to the validated simplified model, the sacrificial cladding was designed to improve the blast resistant capabilities of a given structural element and a robustness assessment of the design was conducted while considering a probabilistic approach.

## 1.3 Thesis outline

The content of the thesis is organized into the following chapters:

### **Chapter 2** – Explosive blast loading

This chapter provides the basics related to shock wave phenomena and a review of the currently available semi-empirical and numerical methods commonly used to evaluate blast loads on infinite and rigid boundaries, as well as the effects resulting from blast wave clearing on a finite target and fluid-structure interaction due to the elasticity of the target. Finally, a review of the performance criteria of structural components subjected to blast loads is also given, together with the available methods for predicting their dynamic response.



**Chapter 3 – Protective solutions**

This chapter presents a brief state of the art on traditional strengthening techniques, followed by an extensive review on the concept of sacrificial claddings and their use as energy dissipation solutions, including a brief reference to protective solutions manufactured using 3D printing. The most common simplified numerical models used to simulate the nonlinear response of sacrificial claddings are also reviewed.

**Chapter 4 – Experimental testing**

This chapter details two experimental testing campaigns. The first one, conducted in the Mechanical Testing Laboratory of IDMEC aims, in a first stage, to attain the mechanical characterisation of unidirectional 3D printed samples with special focus on anisotropy and compression/tension asymmetry by means of quasi-static tests. In the second stage, a split-Hopkinson bar apparatus was used to carry out the compression tests under high strain rate conditions. The second campaign, conducted in the Laboratory for the Analysis of Explosive Effects at the Royal Military Academy in Brussels and resorted to an explosive driven shock tube, was used to characterise the energy absorption capabilities of the sacrificial cladding.

**Chapter 5 – Development, verification and validation of numerical models**

This chapter is dedicated to the development and validation of the numerical models used in the present study. The calibration of an anisotropic constitutive model available in LS-DYNA is conducted based on the experimental results reported in Chapter 4. Next, the results attained during the blast testing are used to validate the estimates of a FE and a simplified numerical model. Further insights on the crushing mechanisms observed in their interior are obtained resorting to the FE numerical model.

**Chapter 6 – Design of a sacrificial cladding solution**

This chapter reviews the design procedure of a sacrificial cladding solution for a given case study in order to increase the blast resistant capabilities of the considered structural element when subjected to a given blast load. A robustness assessment of the designed solution is performed resorting to a probabilistic approach in which several key parameters are varied according to a given probabilistic distribution.

**Chapter 7 – Conclusions and future research**

A summary of the current research, the conclusions and several suggestions for future research are presented in this chapter.

## 1.4 Published work

During the development of this work, the author published the following scientific works:

### Technical papers in international journals

- H. B. Rebelo, D. Lecompte, C. Cismaşiu, A. Jonet, B. Belkassem, and A. Maazoun. “Experimental and numerical investigation on 3D printed PLA sacrificial honeycomb cladding.” In: *International Journal of Impact Engineering* 131 (2019), pp. 162–173. DOI: 10.1016/j.ijimpeng.2019.05.013
- H. B. Rebelo, F. Amarante dos Santos, C. Cismaşiu, and D. Santos. “Exploratory study on geodesic domes under blast loads.” In: *International Journal of Protective Structures* 10.4 (2019), pp. 439–456. DOI: 10.1177/2041419618820540
- C. Cismaşiu, H. B. Rebelo, V. J. G. Lúcio, M. T. M. S. Gonçalves, G. J. Gomes, and J. P. F. Basto. “Numerical Simulation of Blast Effects on Fibre Grout Strengthened RC Panels.” In: *Key Engineering Materials*. Vol. 755. Trans Tech Publications Ltd. 2017, pp. 18–30. DOI: 10.4028/www.scientific.net/KEM.755.18

### Technical papers in national journals

- C. Cismaşiu, J. R. G. Ferreira, and H. B. Rebelo. “Modelação tridimensional de ondas de choque em LS-DYNA.” In: *Construção Magazine* 86 (2018), pp. 24–28

### International proceedings papers

- H. B. Rebelo, D. Lecompte, C. Cismaşiu, A. Jonet, B. Belkassem, and A. Maazoun. “3D printed PLA sacrificial honeycomb cladding blast mitigation.” In: *Proceedings of 18th International Symposium on Interaction of the Effects of Munitions with Structures, Panama City Beach, FL, USA*. 2019
- H. B. Rebelo and C. Cismaşiu. “A Comparison between three air blast simulation techniques in LS-DYNA.” In: *11th European LS-DYNA Conference, Salzburg, Austria*. 2017

### Presentation at international conferences

- H. B. Rebelo, A. Gregório, P. A. R. Rosa, D. Lecompte, and C. Cismaşiu. “Experimental characterization of 3D printed PLA under uniaxial high strain rate loading.” In: *AuxDefense 2018 – 1st World Conference on Advanced Materials for Defense, Lisbon*. 2018

## Chapter 2

# Explosive blast loading

### 2.1 Introduction

This chapter aims to introduce the blast loading and its associated effects on the target, taking into account the fluid-structure interaction and clearing. The review presents the currently available semi-empirical and numerical methods that can be used to evaluate blast loads on an infinite and rigid boundary, as well as the proposed modifications to the original blast load profile to include the previously referred effects. The performance criteria of structural components, as defined by several standards, and the available methods to estimate their response to blast loads are also reviewed.

### 2.2 Blast wave phenomena

According to the literature [68, 172], an explosion can be defined as a quasi-instantaneous release of energy that generates a rapidly expanding pressure disturbance, characterised by a finite length in space. This expansion propagates through the surrounding air at a rate faster than the speed of sound in the undisturbed air. Due to the compressible nature of air, the length of this disturbance's front will be reduced as it travels through the air until it forms a shock front, i.e. a nearly discontinuous increase in pressure, density and temperature propagating outwards from the detonation's centre.

Considering the detonation source as spherical and an homogeneous atmosphere, one may establish the parameters of the resultant blast wave as a function of the distance from the centre of its source, defined by  $R$ , and time  $t$ . At a given distance, the pressure-time profile yielded by an ideal blast wave is illustrated in Figure 2.1. This profile is characterised by an instantaneous pressure rise from ambient air pressure  $P_a$  to a peak incident overpressure  $P_{s0}$  at arrival time  $t_a$ , followed by an exponential decay back to ambient pressure, whose duration is commonly referred to as positive phase duration  $t_o^+$ . Note that the term overpressure does not refer to an absolute pressure value, but rather to a pressure increase above the ambient air pressure due to the blast wave. A negative phase, characterised by a reverse air flow, is verified after the positive phase as a result

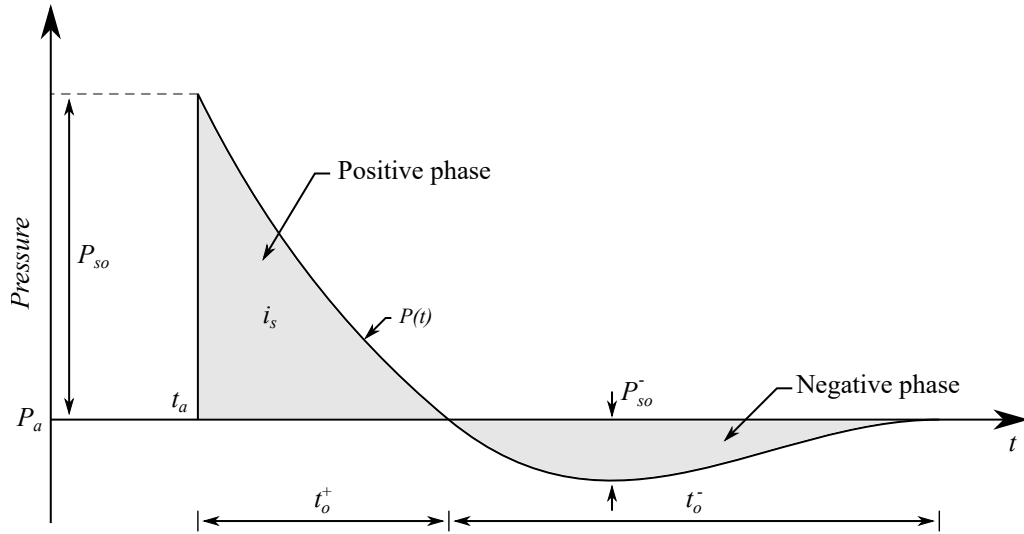


Figure 2.1: Pressure-time profile of an incident blast wave

of the over expansion of air following the shock front. A minimum pressure of  $P_{so}^-$  and a duration of  $t_o^-$  define the negative phase, after which the pressure is restored to the initial conditions. The impulse,  $i_s$  for the positive phase, is computed resorting to the integral of the pressure with respect to time, i.e. it is given by the area under the pressure-time profile.

### 2.3 Rankine-Hugoniot conditions

As previously referred, the propagation of a blast wave through undisturbed air is delimited by a shock front. Consequently, this process must be considered as nonlinear since the traditional fluid dynamic equations are not valid across the shock front. The conservation of mass, momentum and energy across a shock front, as the one depicted in Figure 2.2, is given by a set of equations commonly referred to as the Rankine-Hugoniot conditions [111, 172].

Figure 2.2 illustrates the diagram of a one-dimensional shock front travelling with velocity  $U$  through undisturbed air, which is instantaneously modified into shocked air due to the shock front. On the referred figure, one can also observe the pressure  $P$ , density  $\rho$ , particle velocity  $v$  and specific energy  $e$  of the undisturbed air, identified by subscript “0”, and the shocked air, depicted with subscript “s”. Equations (2.1), (2.2) and (2.3) respectively define the conservation of mass, momentum and energy across the shock front.

$$\rho_s (U - v_s) = \rho_0 U \quad (2.1)$$

$$P_s - P_0 = \rho_0 U v_s \quad (2.2)$$

$$\frac{1}{2} \rho_0 U v_s^2 + \rho_0 U (e_s - e_0) = P_s v_s \quad (2.3)$$

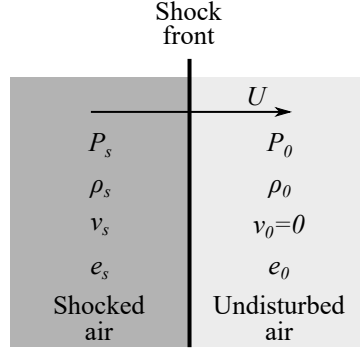


Figure 2.2: Diagram of a shock front travelling with velocity  $U$  through undisturbed air

Although only the one-dimensional case is presented here, it is important to refer that the Rankine-Hugoniot conditions are also valid in a multi-dimensional space.

## 2.4 Blast wave reflection

When the incident blast wave impacts on a structure or the ground, usually considered as rigid and infinite surfaces, it suffers a reflection and amplification of almost all its parameters, as illustrated in Figure 2.3. The overpressure of the resultant shock wave  $P_r$  has a higher value than its incident counterpart  $P_{s0}$ , leading to a larger specific impulse  $i_r$ . Nonetheless, it is important to refer that, as illustrated in Figure 2.3, the positive and negative phase durations remain unchanged.

According to the Rankine-Hugoniot conditions, namely the conservation of mass and energy across the shock front, one may compute the density  $\rho_s$  and particle velocity  $v_s$  behind the shock front as,

$$\rho_s = \rho_0 \frac{2\gamma P_a + (\gamma + 1) P_{s0}}{2\gamma P_a + (\gamma - 1) P_{s0}} \quad (2.4)$$

$$v_s = P_{s0} a_0 \sqrt{\frac{2}{\gamma \rho_0 [2\gamma P_a + (\gamma + 1) P_{s0}]}} \quad (2.5)$$

where  $\gamma$  is the specific heat ratio and  $a_0$  is the speed of sound in undisturbed air. A dynamic pressure, whose magnitude is defined in equation (2.6), arises from the air flow.

$$q_s = \frac{1}{2} \rho_s v_s^2 = \frac{P_{s0}^2}{2\gamma P_a + (\gamma - 1) P_{s0}} \quad (2.6)$$

When a normal reflection occurs, i.e. when the blast wave impinges normally upon a solid surface, the resulting reflected overpressure  $P_r$  may be computed as a function of the incident overpressure  $P_{s0}$  and the dynamic pressure  $q_s$ ,

$$P_r = 2P_{s0} + (\gamma + 1) q_s \quad (2.7)$$

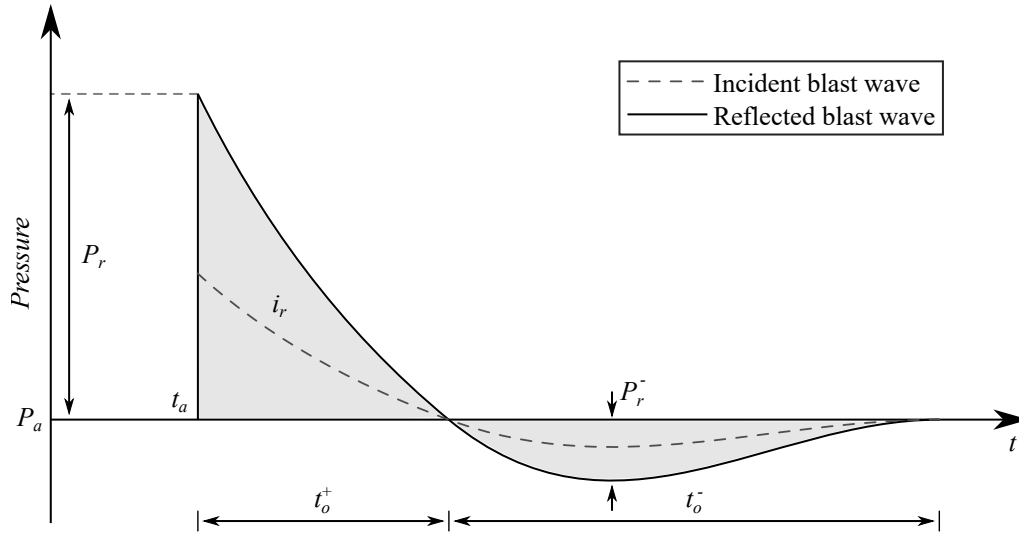


Figure 2.3: Pressure-time profile of a reflected blast wave

where the first term is the resulting reflection of the incident overpressure in the acoustic regime, and the second term is related to the increase in pressure due to bringing the compressed fluid to a stop at the reflecting surface.

Considering the air as an ideal gas with a constant specific heat ratio of 1.4 (which is considered as a good approximation up to an incident overpressure of 2 MPa [111]), the previously presented equation for the reflected overpressure is simplified as follows:

$$P_r = 2P_{so} + \frac{7P_a + 4P_{so}}{7P_a + P_{so}} \quad (2.8)$$

The reflection coefficient  $C_r$ , defined as the ratio between the reflected and incident overpressures  $C_r = P_r/P_{so}$ , has an upper limit of 8 if the air is considered as an ideal gas at extremely high pressures and temperatures. Nonetheless, when real gas effects are considered, e.g. dissociation and ionisation of air molecules, the reflection coefficient has been reported to be as high as 20 [172].

## 2.5 Scaling laws

Due to the high costs of parametric experimental blast campaigns, in combination with the burdensome characterisation of the blast waves and correlation between different tests, several researchers have attempted to define scaling laws that would increase the applicability of experimental studies [172].

The most commonly used scaling law was independently formulated by Hopkinson [56] and Cranz [25] and is referred to as the “cube root” or Hopkinson-Cranz scaling law. This law states that similarity between the blast waves formed at the same scaled distances is attained when two explosive charges of similar geometry and composition but different size are detonated in the same atmosphere. This similarity is clearly illustrated

in Figure 2.4, where it is visible that the blast profile at a distance  $R$  from an explosive charge with mass  $W$  will be similar to the one resulting from the detonation of  $k^3W$  at  $kR$ .

The Hopkinson-Cranz scaling law, which is founded on dimensionless modelling and is based on atmospheric conditions at sea level, defines the scaled distance  $Z$  as,

$$Z = \frac{R}{W_E^{1/3}} \quad \text{or} \quad Z = \frac{R}{E^{1/3}} \quad (2.9)$$

where  $R$  is the distance from the centre of the explosive charge to the point of interest and  $W_E$  and  $E$  are the equivalent weight of TNT and energy of the explosive charge, respectively. According to [172], the use of the energy is preferred over the equivalent weight because the important parameters for the generation of a blast wave are the total energy and energy density of the explosive. Nonetheless, the equivalent weight  $W_E$  is commonly used and is computed through the following expression,

$$W_E = \frac{e_{Exp}}{e_{TNT}} W_{Exp} \quad (2.10)$$

where  $e_{Exp}$  and  $W_{Exp}$  are the specific energy and the weight of the explosive in question and  $e_{TNT}$  is the specific energy of the TNT. Additionally, the previously reviewed scaling law denotes that all parameters with dimension of pressure and velocity are unchanged in the scaling process, while time and impulse are scaled by the cubic root of the equivalent weight of TNT or the energy of the explosive charge.

Nonetheless, the Hopkinson-Cranz scaling law does not consider the effects of eventual changes in ambient pressure and/or temperature. Consequently, Sachs [144] derived a more general blast scaling law that takes into consideration the referred effects. The author states that the scaled distance  $\bar{R}$  depicted in equation (2.11) depends not only on

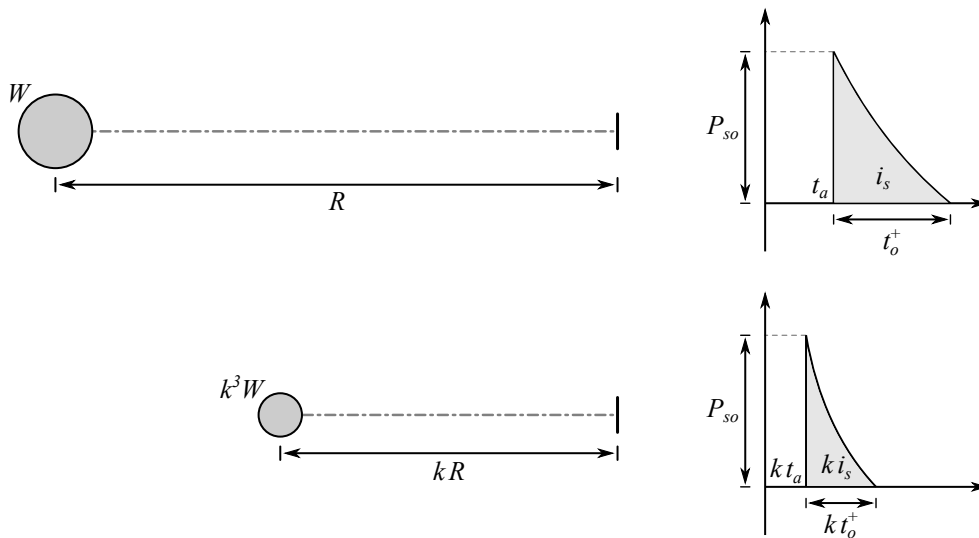


Figure 2.4: Hopkinson-Cranz scaling law [172]

the distance between the centre of the explosive and the point of interest and the energy of the explosive charge, but also on the ambient atmospheric pressure,  $P_a$ .

$$\bar{R} = \frac{R P_a^{1/3}}{E^{1/3}} \quad (2.11)$$

## 2.6 Blast wave characterisation

The structural response assessment under explosive loads requires the accurate definition of several key parameters that characterise the positive and negative phases of a given blast scenario. As previously reviewed, the former is characterised by its peak overpressure ( $P_{s0}$  or  $P_r$ ), specific impulse ( $i_s$  or  $i_r$ ) and duration  $t_0^+$ . Similarly, the parameters that allow the definition of the latter are the negative counterparts of the presented parameters ( $P_{s0}^-$  or  $P_r^-$ ,  $i_s^-$  or  $i_r^-$  and  $t_0^-$ ). These parameters and the commonly used approximations for the blast wave's pressure-time history are briefly presented in what follows.

### 2.6.1 Blast wave parameters

Some of the earliest analytical predictions for blast parameters considered the blast as a point source with an instantaneous release of energy and assume that the atmospheric pressure is negligible when compared to peak overpressure [14, 166]. However, these predictions can not be applied directly to compute the structural response to blast waves since they only establish the parameters of incident blast waves.

Nowadays, the most commonly used method to obtain the parameters that characterise a given blast scenario is the semi-empirical method proposed by Kingery & Bulmash [67] due to its simplicity. This method is materialised by a curve fit to both experimental (medium to large-scale) and numerical data of the required blast parameters for  $0.067 \leq Z \leq 39.67 \text{ m/kg}^{1/3}$ .

The Kingery & Bulmash method characterises the blast parameters for two main types of blast scenarios: a spherical free-air burst (blast wave suffers no amplification or reflection from its source to the point of interest); and a hemispherical surface burst (ground surface is considered as flat and rigid). The previously referred fit is achieved through high-order polynomial curves which are not usually presented in the literature due to their burdensome use. Nonetheless, the Kingery & Bulmash polynomial curves are used by the UFC 3-340-02 [173] and the computer code ConWep [58] to determine the blast wave parameters that are used for the design of structures against blast loads.

Due to the onerous use of the Kingery & Bulmash polynomial curves, Swisdak [161] proposed a set of simplified polynomials to determine the blast parameters resulting from a surface burst, whose values lie within a 1% accuracy. Additionally, several authors, more prominently Baker [172] and Kinney & Graham [68], provide simple relationships to compute blast wave parameters (see [66] for a detailed review). On the other hand, both Bogosian and colleagues [12] and Rigby and team [142] performed a comparison of



the blast parameters obtained through the Kingery & Bulmash method and by means of an experimental campaign, concluding that the semi-empirical method predicts the positive phase parameters with a high level of agreement.

Figure 2.5 illustrates the positive phase blast wave parameters proposed by Kingery & Bulmash for spherical free-air and surface bursts.

As previously reviewed, the positive phase is followed by a negative phase, whose parameters are also presented in the UFC 3-340-02 [173]. Nonetheless, due to the fact that some experimental data records did not possess sufficient duration and/or quality to extract accurate negative phase parameters, both in terms of peak pressure and impulse, Bogosian and co-workers [12] state that there is some uncertainty about the precise origin of the UFC 3-340-02 curves. On the other hand, Rigby [140] refers that the original source of these negative phase parameters might be the analytical work performed by Granström [43]. Figure 2.6 depicts the negative phase parameters, as shown in the UFC 3-340-02 for spherical free-air and hemispherical surface bursts.

### 2.6.2 Pressure-time history approximation

The earliest and simplest form of approximation for the form of a blast wave as a function of time is the triangular pulse [37], where the positive phase is given by the following expression,

$$P(t) = P \left( 1 - \frac{t}{t_{o,lin}} \right) \quad (2.12)$$

where the linear positive phase duration  $t_{o,lin}$  may be defined in order to preserve duration, i.e.  $t_{o,lin} = t_o^+$ , or to maintain impulse ( $t_{o,lin} = 2i/P$ ).

Alternatively, the commonly known as Taylor form [167] proposes, for the positive phase of the blast wave, the exponential decay function defined by equation (2.13), which is controlled by parameter  $t_i$ . A better fit to experimental results is attained when using this approximation, since one is able to match both the peak overpressure  $P$  and either the initial decay rate or the positive phase impulse. It is important to refer that, although the referred expression does not return to ambient atmospheric pressure, it yields a finite impulse.

$$P(t) = P e^{-\frac{t}{t_i}} \quad (2.13)$$

Nonetheless, the positive phase is usually described by an improved expression, known as the modified Friedlander equation,

$$P(t) = P \left( 1 - \frac{t}{t_o^+} \right) e^{-b \frac{t}{t_o^+}} \quad (2.14)$$

where the waveform parameter  $b$  controls the decay of the pressure-time history [172]. This description of the blast wave is able to match three out of four blast parameters ( $P$ ,  $t_o^+$ ,  $i$  and the initial decay rate). Several authors have defined the values of  $b$  as a function of scaled distance  $Z$ . However, according to Hyde [58], the most realistic approach is to

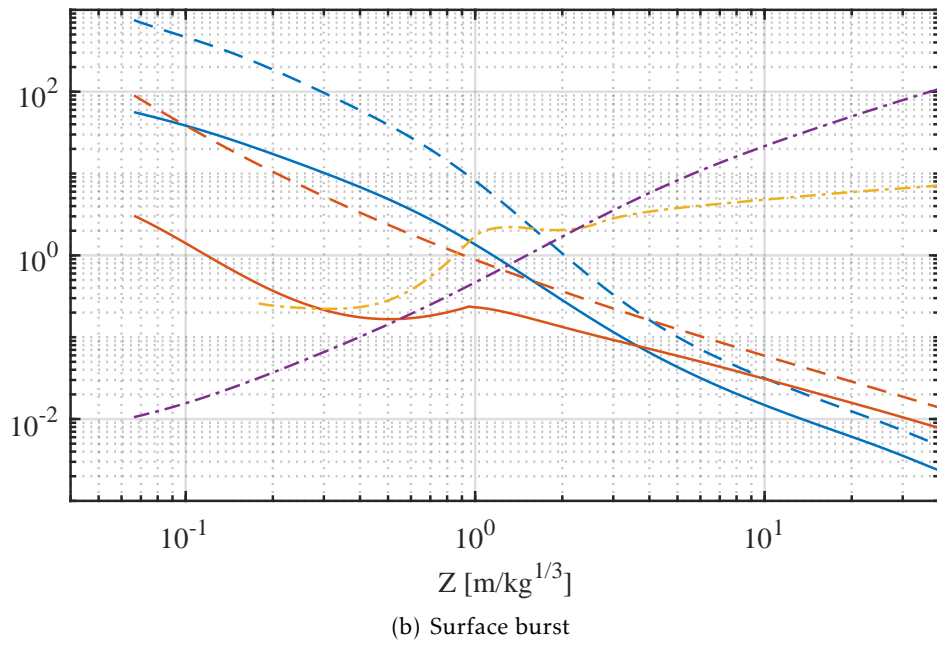
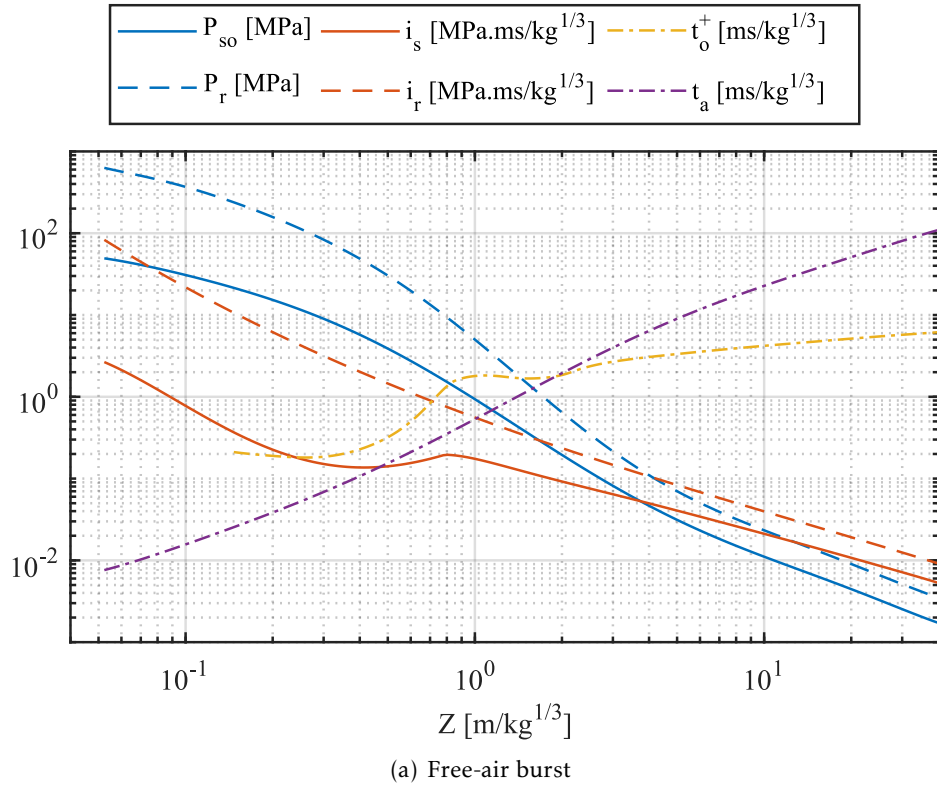
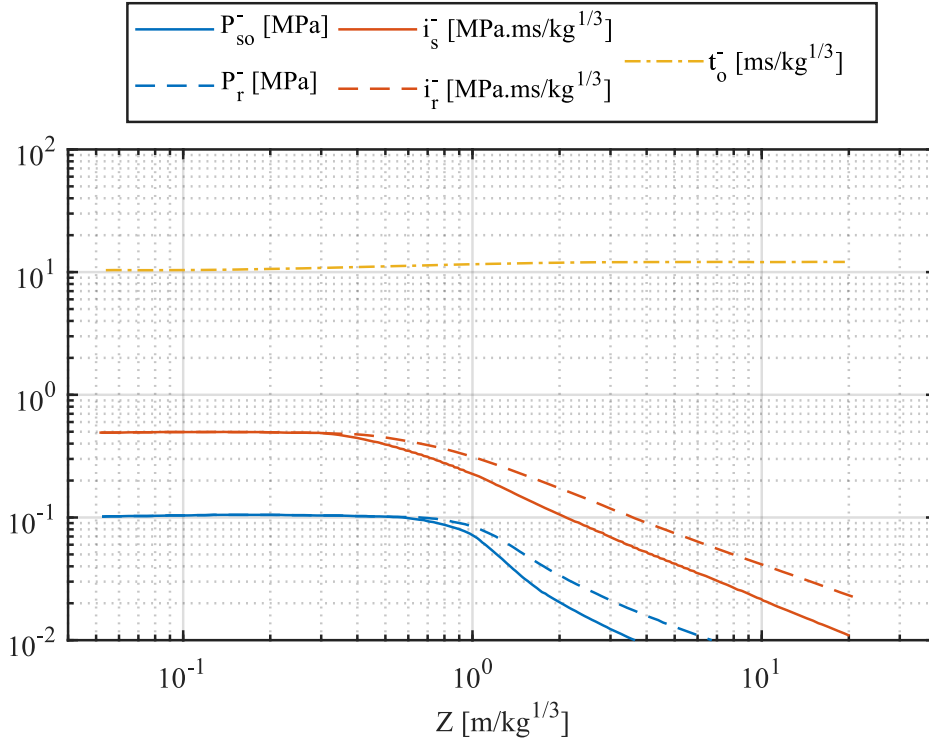
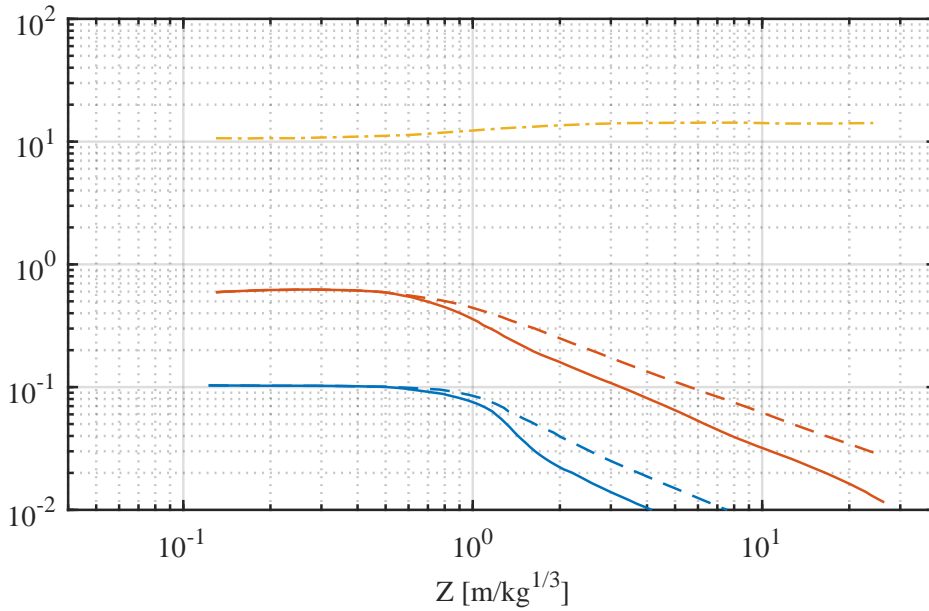


Figure 2.5: Positive phase blast wave parameters [173]



(a) Free-air burst



(b) Surface burst

Figure 2.6: Negative phase blast wave parameters [173]

determine the waveform parameter  $b$  through an iterative process using blast wave parameters  $P$ ,  $t_o^+$  and  $i$ . Integrating the positive phase of the modified Friedlander equation (equation (2.14)) with respect to time, one obtains the left hand side of equation (2.15). An iterative process, in which the waveform parameter  $b$  is varied, is then performed until the equality given in equation (2.15) is within the required level of accuracy.

$$\frac{P t_o^+}{b^2} (b - 1 + e^{-b}) = i \quad (2.15)$$

Note that the three forms, given by equations (2.12), (2.13) and (2.14), are valid for both the incident and normally reflected blast wave, with the peak overpressure taking values of  $P_{so}$  and  $P_r$ , respectively, while the specific impulse is respectively depicted by  $i_s$  and  $i_r$ . In the event of a non-normal blast wave reflection on the target, or if the shock front may not be considered as planar across the whole target's surface, the angle of incidence of the blast wave must be taken into consideration. Both the computer code ConWep [58] and the FE software LS-DYNA [130] consider that the overpressure acting at any point of a given target is a function of the incident and normally reflected overpressure-time histories at the referred point and the angle of incidence of the blast wave  $\theta$ , according to the following expression:

$$P(t, \theta) = P_r(t) \cos^2 \theta + P_{so}(t) (1 + \cos^2 \theta - 2 \cos \theta) \quad (2.16)$$

Although the common procedure in blast design is to disregard the negative phase of a blast wave, since its overpressure and impulse are relatively small when compared to their positive counterparts for smaller scaled distances, Needham [111] states that this phase might yield significant effects on buildings. Despite the fact that the negative phase is generally weaker than the positive phase, as the scaled distance increases its duration becomes larger and, consequently, the negative phase impulse constantly increases until, for  $Z > 8 \text{ m/kg}^{1/3}$ , surpasses its positive phase counterpart.

Similarly to the positive phase of the blast wave, a linear equation was firstly used to approximate the negative phase time history. This approximation consists on the piecewise, bilinear expression given by equation (2.17), where the rise time has a duration of 1/4 of the total negative phase duration, while the remainder of the time history is characterised by a linear decay back to ambient pressure. The negative phase duration  $t_{o,lin}^-$  may be determined to preserve the impulse  $t_{o,lin}^- = 2i^-/P^-$ . Note that, if the linear approximation is used for the positive phase of the blast load, the beginning of the negative phase remains unchanged at  $t_o$ , resulting in a period of null overpressure between the two phases. The UFC 3-340-02 [173] recommends a linear approximation for both the positive and negative phase.

$$P(t) = \begin{cases} -P^- \left( \frac{t - t_o}{0.25 t_{o,lin}^-} \right) & t_o < t \leq t_o + 0.25 t_{o,lin}^- \\ -P^- \left[ 1 - \frac{t - (t_o + 0.25 t_{o,lin}^-)}{0.75 t_{o,lin}^-} \right] & t_o + 0.25 t_{o,lin}^- < t \leq t_o + t_{o,lin}^- \end{cases} \quad (2.17)$$

Alternatively, one could simply extend the modified Friedlander equation (2.14) to  $t \rightarrow \infty$  in order to simulate the negative phase. This approximation has been used by several authors [40, 169, 177] and is the procedure implemented in LS-DYNA [130] (keyword `LOAD_BLAST_ENHANCED`).

As previously referred, according to Hyde [58], the most realistic method to compute the waveform parameter  $b$  is to match the specific impulse given by the blast wave parameters to the definite integral of the modified Friedlander equation (2.15) over the duration of the positive phase through an iterative process. However, since the negative phase is approximated as an extension of the modified Friedlander equation calibrated to correctly model the positive phase of the blast load, one could readily conclude that this negative phase approximation only depends on the blast parameters defined for the positive phase. Consequently, no variables are available to properly calibrate this approximation to the negative phase's peak pressure and impulse given by the semi-empirical predictions (Figure 2.6). Equation (2.18) depicts the negative phase's specific impulse obtained by integrating the negative phase of the modified Friedlander equation.

$$i^- = - \int_{t_o}^{\infty} P \left( 1 - \frac{t}{t_o} e^{-bt/t_o} \right) dt = \frac{P t_o}{b^2} e^{-b} \quad (2.18)$$

In order to overcome the referred limitation, Teich & Gebbeken [169] proposed the inclusion of a negative reflection coefficient  $C_r^-$  given by the following expression,

$$C_r^- = \frac{1.9Z - 0.45}{Z}, \quad \text{with } Z > 0.5 \quad (2.19)$$

which should be used with the waveform parameter defined as:

$$b = 1.5 Z^{-0.38}, \quad \text{for } 0.5 < Z < 30 \quad (2.20)$$

Using the negative reflection coefficient, it is now possible to match the peak negative phase reflected overpressure given by  $C_r^- P_{so}$ , to the one defined by the semi-empirical predictions illustrated in Figure 2.6. However, the given waveform parameter is again calibrated to correctly model the positive phase impulse with the modified Friedlander equation. Therefore, the negative phase impulse cannot be controlled on the presented approximation. Furthermore, it is possible to verify that the extended Friedlander approximation yields a finite pressure value regardless of  $t$  and, consequently, the duration of the negative phase is relatively difficult to be estimated [141].

Alternatively, both the NavFac Design Manual 2.08 [24] and the US Army Blast Effects Design Spreadsheet, SBEDS [100] recommend the cubic expression proposed by Granström [43], shown in equation (2.21). This approximation allows one to calibrate the negative phase time history through the correction of the negative phase duration to  $t_o^- = 16 i^- / 9 P^-$ , which guarantees that both the peak negative phase overpressure and impulse are equal to the blast parameters proposed by the semi-empirical predictions.

$$P(t) = -P^- \left( \frac{6.75 (t - t_o)}{t_o^-} \right) \left( 1 - \frac{t - t_o}{t_o^-} \right)^2 \quad (2.21)$$

It should be noted that the previously presented approximations, given in equations (2.17), (2.14) and (2.21), are usually applied to the reflected blast load imparted on a target. Therefore, the reflected negative phase parameters ( $P_r^-$ ,  $i_r^-$  and  $t_o^-$ ) should be used. As a result of the uncertainty regarding the approximation of the negative phase, the SBEDS [100] proposes that the semi-empirical reflected blast wave parameters defined for the negative phase should be used when the angle of incidence of the blast wave is lower than  $45^\circ$ , otherwise, the incident blast wave parameters are of interest.

### 2.6.3 Experimental validation

The present subsection presents a comparison between the Kingery & Bulmash semi-empirical blast predictions and a range of available experimental data from the literature [12, 113, 142].

The first data set is the one reported by Bogosian and colleagues [12], which comprised a total of almost 300 individual measurements captured at low heights above the ground, a few on small cubicles and others on larger buildings with a scaled distance ranging between approximately 1 and  $40 \text{ m/kg}^{1/3}$ . According to the authors, this range dilutes possible variations between the compared tests due to details of the experimental arrangement.

The second data set considered here yielded from the work of Netherton and Stewart [113] who carried out over 90 detonations of PE4 charges, resulting in more than 425 individual data records [114, 115]. The tests were conducted in a field laboratory with scaled distances ranging from 0.65 to  $3.2 \text{ m/kg}^{1/3}$ . The main focus of the experimental campaign was the appropriate capture of the pressure-time history and to estimate the incident blast wave's variability. Although in the referred experimental campaign, only the pressure of the incident wave was registered, the authors suggest the existence of a strong positive correlation between the variability of the incident and reflected blast waves.

The third data set considered in the present analysis was published by Rigby and team [142] and represents the result of 82 pressure-time histories recorded during a set of hemispherical surface bursts of PE4 charges. The mass of the charges was varied between 180 and 350 g, while the pressure sensors were placed between 2 and 6 m, yielding scaled distances ranging from 5.39 to  $10.02 \text{ m/kg}^{1/3}$ . Contrary to the tests performed by Netherton and colleagues, this experimental campaign was designed to adequately obtain the reflected blast wave parameters.

In what follows, the uncertainty of the Kingery & Bulmash semi-empirical predictions is expressed through the ratio between the experimental values ( $v$ ) and the K&B estimates ( $v_{K\&B}$ ), followed by the computation of the mean  $\mu$  and standard deviation  $\sigma$  of these ratios. These statistical measurements allow the verification of the existence of a bias. Additionally, assuming that the spread of the observed values follows a normal distribution, lower ( $v_l$ ) and upper ( $v_u$ ) bounds containing approximately 95% of the

considered values ( $v$ ) may be defined as well:

$$v_{u,l} = v_{K\&B}(\mu \pm 2\sigma) \quad (2.22)$$

Tables 2.1 and 2.2 present a summary of the mean and standard deviation values computed for the three data sets, while Figure 2.7 shows the Kingery & Bulmarsh's semi-empirical predictions for the peak overpressure and impulse of a normally reflected blast wave, resulting from a hemispherical surface burst. The figure also illustrates the mean (plain coloured line) and the lower and upper bounds (dashed coloured lines) obtained using the data sets reported by Bogosian and team [12] and Netherton and Stewart [113], respectively. It should be noted that the data set variability obtain by Rigby and team [142] is not depicted in the referred figure since the mean value attained by the authors is close to unity and the standard deviation is almost null. Consequently, the graphical representation of the mean and the lower and upper bounds would not be clearly visible.

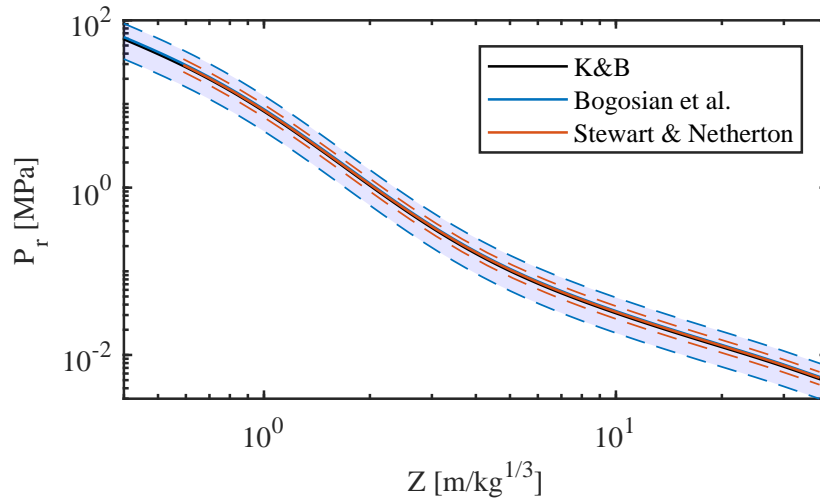
Through the analysis of the referred tables and figure, one can verify that the semi-empirical curves defined by Kingery & Bulmarsh are in good agreement with the illustrated experimental data. However, a larger dispersion is observed for the values attained by Bogosian and team [12]. According to Netherton and Stewart [112], the statistical measurements obtained by Bogosian and co-workers most likely represent an upper bound of the blast wave parameters' variability, since a large array of experimental tests, in terms of set-up, together with nonrepeated tests, were used by the authors to verify the uncertainty of blast wave parameters. Despite the smaller range of scaled distances, the experimental results obtained by Rigby and co-workers and by Netherton and Stewart suggest that the proposed semi-empirical approximation is accurate and may be used with confidence to compute blast loads resulting from blast scenarios with simple geometries.

Table 2.1: Reflected pressure: ratio between experimental values and K&B estimates

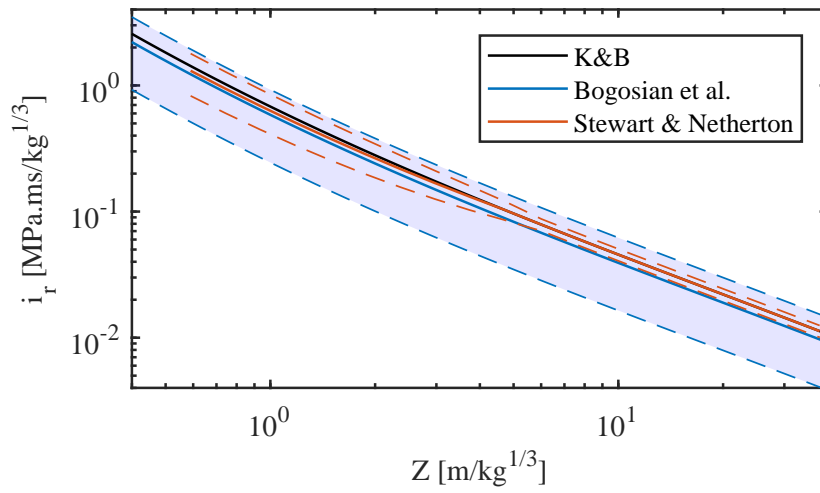
	Bogosian et al.	Stewart & Netherton	Rigby et al.
$\mu$	1.06	1.03 + 0.001 $Z$ ( $0.59 \leq Z \leq 6.0$ ) 1.04 ( $6.0 < Z \leq 40.0$ )	1.00
$\sigma$	0.24	0.09 ( $0.59 \leq Z \leq 40.0$ )	0.04

Table 2.2: Reflected impulse: ratio between experimental values and K&B estimates

	Bogosian et al.	Stewart & Netherton	Rigby et al.
$\mu$	0.86	0.91 + 0.02 $Z$ ( $0.59 \leq Z \leq 4.7$ ) 1.00 ( $4.7 < Z \leq 40.0$ )	1.01
$\sigma$	0.25	0.18 - 0.02 $Z$ ( $0.59 \leq Z \leq 4.7$ ) 0.20 - 0.02 $Z$ ( $4.7 \leq Z \leq 6.0$ ) 0.05 ( $6.0 < Z \leq 40.0$ )	0.03



(a) Peak reflected overpressure



(b) Reflected impulse

Figure 2.7: Comparison of Kingery & Bulmash semi-empirical method and experimental results obtained by Bogosian and team and Netherton & Stewart [12, 67, 113]



## 2.7 Non-ideal reflective surface

As previously referred, the surface upon which the blast loads are impinged is commonly considered as rigid and infinite. However, if the reflecting surface may not be considered as rigid, the fluid-structure interaction must be considered in order to correctly determine the acting blast loads. On the other hand, in the case of finite targets, when the disturbances caused by the free edges cannot be ignored, blast wave clearing must taken into consideration.

### 2.7.1 Fluid-structure interaction

The structures subjected to blast loads, depending on their properties, might be assumed to be flexible. Consequently, the movement of the structure will influence the transmitted pressure-time history, namely reducing the reflected impulse. Two scenarios bound the fluid-structure interaction (FSI) effects: as the mass/stiffness of the structure approaches an infinite value, no pressure attenuation is verified due to FSI and the fully reflected blast load is impinged on the structure; on the other hand, if the mass/stiffness of the structure is assumed to be negligible, it will move with exactly the same speed as the shock front and, therefore, only the incident impulse is imparted on the structure.

This effect was firstly studied by Taylor [167] for an underwater blast scenario, in the acoustic range. Despite being admissible for conventional underwater explosions, the acoustic assumption may not be used for air blast scenarios, due to the significance of nonlinear compressibility effects in air. Consequently, Kambouchev and co-workers [61, 62] extended Taylor's theory to take into consideration such effects in the pressure attenuation resulting from FSI. The commonly referred to as KNR method, which was derived for free standing plates (back face subjected to constant atmospheric pressure) and resorts to the Taylor form of the pressure-time history given in equation (2.13), states that the FSI effects result in a reduced time constant  $t_R$ , i.e. a faster exponential decay when compared with the fully reflected blast wave. To determine the reduced time constant  $t_R$ , parameter  $f_R$ , related to the properties of air (considered as an ideal gas) and the intensity of the blast load is introduced:

$$f_R = \left( \frac{6P_{so}}{P_a} + 7 \right) \sqrt{\frac{(6 + C_r)(P_{so}/P_a) + 7}{[(P_{so}/P_a) + 7][(1 + 6C_r)(P_{so}/P_a) + 7][C_r(P_{so}/P_a) + 7]}} \quad (2.23)$$

Subsequently, the relative transmitted impulse, defined as the ratio between the transmitted and applied impulses, considering an infinitely heavy plate is denoted as  $\gamma_R$  and computed using the following expression:

$$\gamma_R = 8 - 42 \frac{P_{so}}{P_a} \ln \left( 1 + \frac{P_{so}}{7P_a} \right) \quad (2.24)$$

The shock front velocity is presented in equation (2.25), while peak air density may

be computed with equation (2.4).

$$U = a_0 \sqrt{\frac{6P_{so}}{7P_a} + 1} \quad (2.25)$$

Assuming that the plate upon which the impulse is transmitted has a density of  $\rho_p$  and a thickness of  $h_p$ , a specific time  $t_s^*$ , given as the ratio between the mass of the plate and across the shock front, is defined by Kambouchev and co-workers as:

$$t_s^* = \frac{\rho_p h_p}{\rho_s U} \quad (2.26)$$

Lastly, defining  $\beta_s$  as the ratio between the original time constant  $t_i$  and the specific time  $t_s^*$ , the reduced time constant  $t_R$  is defined as follows:

$$t_R = t_i f_R^{\beta_s/(1+\beta_s)} \beta_s^{\beta_s/(1-\beta_s)} \left( \frac{\gamma_R}{C_r} \right)^{1+\beta_s} \quad (2.27)$$

As previously referred, the KNR method assumes that the plate's back face is subjected to a constant atmospheric pressure. However, if this condition is not verified, e.g. when modelling plates with a backing material, the impulse transmitted to the plate will be larger than the one predicted by the KNR method [127]. Therefore, this method may be considered as non-conservative and a lower bound of the transmitted impulse. Similarly, it is important to refer that, when a rigid and infinite wall is considered to compute the reflected impulse, it materialises the upper bound of the real transmitted impulse.

Similarly to Kambouchev, Aleyaasin and colleagues [2] also uses the work done by Taylor [167] to predict the fluid-structure interaction effects on a target. The authors developed the extended Taylor theory (ETT) which considers the reflected overpressure as a function of both the incident blast wave and the velocity of the target  $v$ , according to equation (2.28). Rankine-Hugoniot jump conditions are used to determine the reflected overpressure  $P_r$ , the air density  $\rho_s$  and the velocity of the shock front  $U$  as given by equations (2.8), (2.4) and (2.25), respectively<sup>1</sup>.

$$P(t) = (P_r - \rho_s U v(t)) e^{-t/t_i} \quad (2.28)$$

Figure 2.8 depicts a comparison between the values of reflected overpressure, air density behind the shock front and its velocity computed using the Rankine-Hugoniot conditions and the semi-empirical values predicted by Kingery & Bulmash's method as a function of the peak incident overpressure. While the reflected overpressure computed using the Rankine-Hugoniot jump conditions has a limit value of 8 (because the air is considered as an ideal gas at extremely high pressures and temperatures), the K&B semi-empirical predictions do not have this limit (as they are obtained from experimental

---

<sup>1</sup>Although Aleyaasin and team state that equation (2.25) yields the sound velocity in disturbed air, literature review indicates that the referred equation defines the velocity of the shock front [68, 111]. Consequently, it is possible to conclude that the extended Taylor theory resorts to the mass across the shock front to approximate FSI effects.

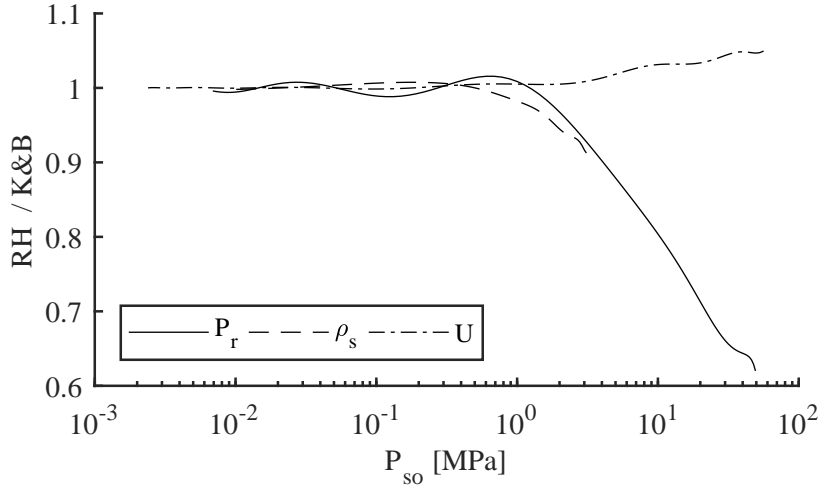


Figure 2.8: Ratio between Rankine-Hugoniot conditions and Kingery & Bulmash predictions for  $P_r$ ,  $\rho_s$  and  $U$  [67]

tests). Consequently, for larger peak incident overpressures, the reflected overpressure ratio diverges from unity, with a maximum difference of almost 40%. Alternatively, the velocity of the shock wave is proved to be similar between the two methods, with a maximum difference of 5%. This small difference was expected since the K&B peak overpressures were also determined using the Rankine-Hugoniot conditions [67]. Lastly, as referred by Needham [111], the consideration of the air as an ideal gas, with  $\gamma = 1.4$ , yields a very good accuracy for the density of air below peak incident overpressures of approximately 2 MPa.

Consequently, due to the limitations of the Rankine-Hugoniot conditions when computing  $P_r$ , this blast wave parameter is estimated resorting to the K&B method. Alternatively, since no significant differences were found for the velocity of the shock front and density of air, the Rankine-Hugoniot jump conditions are used to compute these parameters. Additionally, the exponential decay defined by the modified Friedlander equation (2.14) is used to simulate the pressure-time history as follows:

$$P(t) = (P_r - \rho_s U v(t)) \left(1 - \frac{t}{t_0}\right) e^{-b \frac{t}{t_0}} \quad (2.29)$$

### 2.7.2 Pressure applied to a finite area

A reflected blast wave is formed when the incident shock front impacts a surface. The K&B semi-empirical predictions consider this surface as infinite and perfectly rigid. Nonetheless, if the target is finite, i.e. it has free edges, blast wave clearing will take place.

This effect starts when the incident blast wave arrives at the free edge of a finite target surface. At this location, the reflected blast wave begins to reflect away from the surface, whilst the incident shock front surpasses the free edge unobstructed, resulting

in a diffraction region around the edge. Simultaneously, a pressure inequality between the reflected and incident pressure regions generates a flow between the higher and lower pressure regions as a consequence of the pressure equalisation process. Additionally, a rarefaction wave characterised by a lower pressure is generated in the diffraction region and moves into the target surface due to the previously referred flow conditions. This wave begins its movement at the free edges and propagates inward into the centre of the target, reducing the loading pressure and, consequently the positive phase impulse applied to the target [140]. This process is illustrated in Figure 2.9.

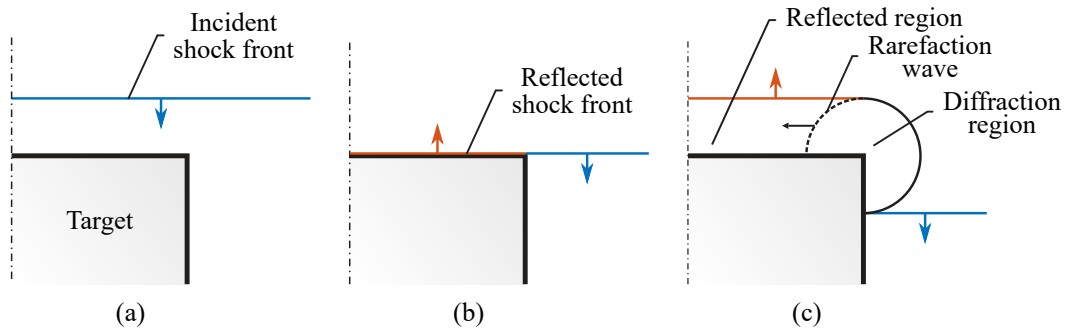


Figure 2.9: Rarefaction wave resulting from diffraction of blast wave around a free edge (Adapted from [140])

The first predictions of this effect were based on experimental data, both from nuclear [104, 106] and small-scale (shock tube) tests [168], and aimed to adjust the impulse applied to the whole surface of the target, disregarding the temporal and spatial distribution of cleared pressures. It is important to refer that this is a result of experimental observations where the blast wave's length was considerably larger when compared to the size of the target, i.e. the time required to propagate the rarefaction wave across the target's surface and, consequently, decay to stagnation pressure value, was very small when compared with the positive phase of the blast waves.

The proposed empirical methods consider that the reduction of pressure due to clearing effects is uniform over the whole surface of the target and immediately begins at the arrival time of the blast wave. Consequently, the pressure-time history, instead of following the fully reflected pressure curve, has a linear decay from the peak reflected overpressure to the stagnation pressure  $P_{stag}$  defined by equation (2.30), over a characteristic clearing time  $t_c$ , as illustrated in Figure 2.10.

$$P_{stag}(t) = P_{so}(t) + C_D q_s(t) \quad (2.30)$$

Observing equation (2.30), it is possible to verify that the stagnation pressure  $P_{stag}$  is defined as the sum of the incident  $P_{so}$  and drag  $C_D q_s$  pressures, where  $C_D$  is the drag coefficient which, according to the UFC 3-340-02 [173], takes a unitary value for front wall loading, and  $q_s$  which is the dynamic pressure given in equation (2.6).

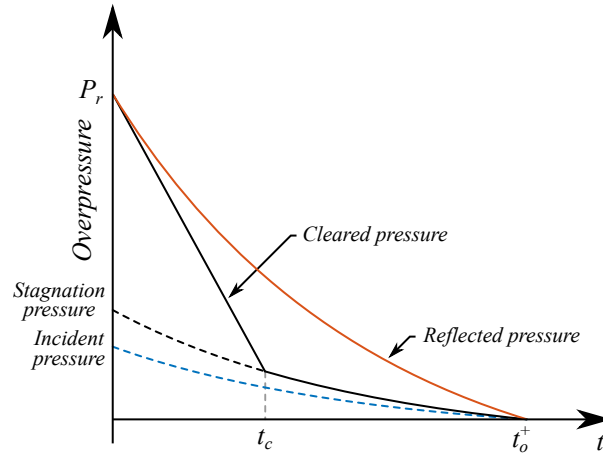


Figure 2.10: Blast wave clearing correction [68, 173]

Several definitions for the characteristic time may be found in the literature. According to Kinney & Graham [68], this parameter is defined as,

$$t_c = \frac{3S}{a} \quad (2.31)$$

where  $S$  is the height or half of the target's width, whichever is smaller, and  $a$  is the sound velocity inside the reflected region.

Alternatively, the characteristic clearing time proposed by the UFC 3-340-02 depends on both of the target's dimensions, as illustrated in equation (2.32), where  $R$  represents the  $S/G$  ratio and  $G$  depicts the height or half the structure's width, whichever is larger.

$$t_c = \frac{4S}{(1+R)a} \quad (2.32)$$

One might consider that the expression proposed by Kinney & Graham represents a two-dimensional case, since it only considers clearing effects due to the closest free edge, while the expression defined by the UFC 3-340-02 might be classified as a three-dimensional case because it takes into account clearing propagating along the height and width of the target.

The presented empirical predictions, despite yielding different clearing times, assume that the cleared blast pressure is constant throughout the entire surface of the target and reaches the stagnation pressure after a given number of rarefaction wave crossings. If one considers a target with infinite height and a width of  $2S$ , the time required for a rarefaction wave to propagate to the centre of the target would be  $S/a$ . For the specified target, the 2D case considers that the stagnation pressure is reached at  $3S/a$ , during which the rarefaction wave has interacted at the target's centre, edge and centre again (3 rarefaction wave crossings). Alternatively, the expression proposed by the UFC 3-340-02 predicts that the clearing time will occur after 4 wave interactions.

For the majority of blast scenarios, the length of the incident blast wave is more comparable to the size of the target and, consequently, the early empirical clearing predictions

might not be applicable. In this scenarios, the characteristic clearing time might be comparable to or larger than the duration of the positive phase or, for targets with large dimensions, the rarefaction wave might not propagate across its entire surface during the positive phase. If the previously described cases are verified, according to [140], it is assumed that clearing will not occur, which is not accurate. Additionally, the assumption that the clearing process begins at the arrival time of the shock front, despite being considered as valid for the net effect of the blast load, it is not accurate for a point placed far away from a free edge because of the time needed to propagate the rarefaction wave.

Due to these limitations, Hudson [57] defined both the spatial and temporal distribution of a rarefaction wave resulting from the impact of a planar blast wave on a rigid finite target. The proposed method assumes that the shock is weak, i.e. the rarefaction wave propagates through the shocked air at the ambient sound velocity  $a_0$ , that the incident blast wave is planar and that the target's depth is large enough such that no clearing waves propagating from the back face arrive during the loading's duration. Considering that the referred assumptions are valid, this method may be used to compute the pressure loading in any point of the target face, yielding the complete spatial and temporal distribution of the cleared blast pressure.

The author states that the relief pressure  $P$ , normalised against peak incident overpressure, is a function of both the non-dimensional length  $\eta$  and time  $\delta$  parameters, as depicted in Figure 2.11. The non-dimensional length parameter  $\eta$  proposed by Hudson is defined as,

$$\eta = \frac{x}{a_0 t_o} \quad (2.33)$$

where  $x$  depicts the distance between the point of interest and the considered free edge, while equation (2.34) presents the Hudson's times scale  $\delta$ .

$$\delta = \frac{t}{t_o} - \eta \quad (2.34)$$

## 2.8 Blast load simulation in LS-DYNA

Explicit finite element code LS-DYNA [83] may be used to simulate the effects of blast loading on structures. The most commonly used approaches are the Lagrangian method, in which the semi-empirical predictions of Kingery & Bulmash, or a pressure-time curve defined by the user, are directly applied to a Lagrangian mesh, and the multi-material Arbitrary Lagrangian-Eulerian (MM-ALE) method, which explicitly models the explosive detonation and the resulting shock wave propagation through the surrounding medium. Additionally, a coupling method that enables the application of the semi-empirical blast pressures on an air domain simulated with the MM-ALE method is also available in LS-DYNA.

The application of a semi-empirical blast load, either to a Lagrangian mesh of elements or to a layer of MM-ALE elements (coupled method), is available in LS-DYNA through

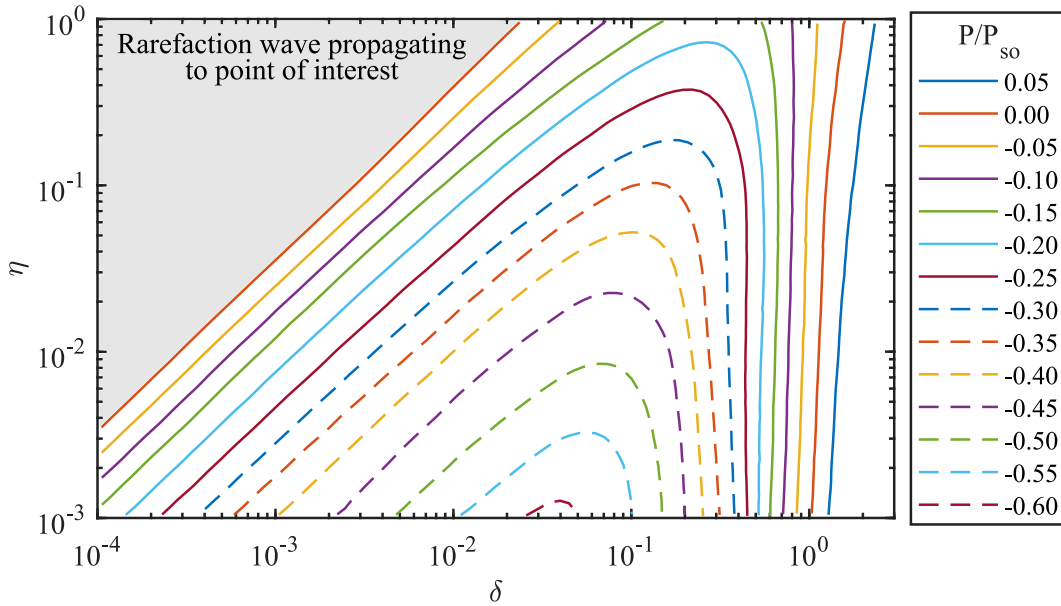


Figure 2.11: Spatial and temporal distribution of the rarefaction wave [57]

the `LOAD_BLAST_ENHANCED` keyword. This method is based on the implementation of the Kingery & Bulmash fit to experimental and numerical TNT data [67] conducted by Randers-Pehrson & Bannister [130]. This approach does not require the explicit simulation of the air between the explosive charge and the structure and, consequently, a significant reduction in computational effort is attained. However, it does not consider shadowing and focusing of blast waves due to the presence of obstacles during the propagation of the blast wave.

The method requires the definition of the location of the explosive and the target surfaces to which the blast loading will be applied, via the `SET_SEGMENT` keyword. Resorting to this information, the blast wave parameters are computed according to the semi-empirical curves presented in Figure 2.5, except the peak reflected overpressure, which is determined resorting to equation (2.16). The pressure-time profile used for the positive and negative phase, although the user is allowed to ignore the latter, is the modified Friedlander equation (2.14).

Alternatively, the user may apply an arbitrary pressure-time curve to a Lagrangian mesh. Similarly, the surfaces to which this curve is applied are defined through the `SET_SEGMENT` keyword.

## 2.9 Structural response to blast loading

The present section reviews the areas of research relevant to the topic of structural response to blast loads. Initially, the behaviour of common building materials such as concrete and steel, subjected to high strain rate loadings will be reviewed.

When designing a structural component to resist blast loads, it is common practice to resort to performance criteria, which defines the limits on its response. Therefore, a revision of the performance criteria for blast design defined in several standards is performed in the present section. Subsequently, a brief introduction of the available methods for structural analysis is presented. From the available methods, a more detailed explanation is given for the single-degree-of-freedom (SDOF) and pressure-impulse (PI) diagrams.

### 2.9.1 Material performance under high strain rate loading

The structural response under blast loading may vary significantly when compared with that under static and quasi-static loading. When subjected to any dynamic load, inertial effects arise due to the rapid acceleration of mass, leading to a resistance to abrupt velocity changes that need to be taken into account in dynamic analysis. Additionally, due to the rapid deformation of the structural component, high deformation rates will be attained and the mechanical properties of its constituent materials will change due to the commonly referred to as strain rate effects. Specifically, an increase in the material's strength is usually observed as a result of these effects [90]. The static properties of the materials are usually converted to their corresponding dynamic properties resorting to Dynamic Increase Factors (DIFs).

#### 2.9.1.1 Concrete

Several studies have experimentally defined the compressive and tensile strength of concrete at different strain rates [10, 39, 92, 94]. The authors verified the existence of two distinct intervals with different strain rate dependencies and a relatively sharp transition zone between them. The first interval is characterised by a more moderate dependency which, for compression loads, results from the build-up of internal pressure due to water movement inside the concrete, delaying crack initiation. A similar effect is attained when the specimens are subjected to tensile loads, due to the resisting force of the water inside the concrete's micro-pores. After the transition zone, the strain rate dependency can be attributed to lateral confinement and inertia effects, e.g. if a compressive load is rapidly applied in the axial direction, inertial restrains will prevent the specimen of instantaneously expand in the radial direction. This creates a finite lateral confinement, resulting in an increase in the compressive strength of the material [90].

A model for the concrete's strain rate dependence, valid for strain rates up to  $300 \text{ s}^{-1}$ , is presented in the CEB-FIP Model Code 1990 [17]. Figure 2.12(a) illustrates the CEB-FIP model for a 30 MPa compressive strength concrete. Figure 2.12(b) depicts the Malvar & Crawford's [92] model for concrete under tensile loading, which considers that the transition zone occurs at  $1 \text{ s}^{-1}$  instead of  $30 \text{ s}^{-1}$ , as defined by the CEB-FIP model, fits the experimental tests' data better. The Young's modulus of concrete is also affected by the strain rate. According to Bischoff and Perry [10], the increase of the Young's modulus for



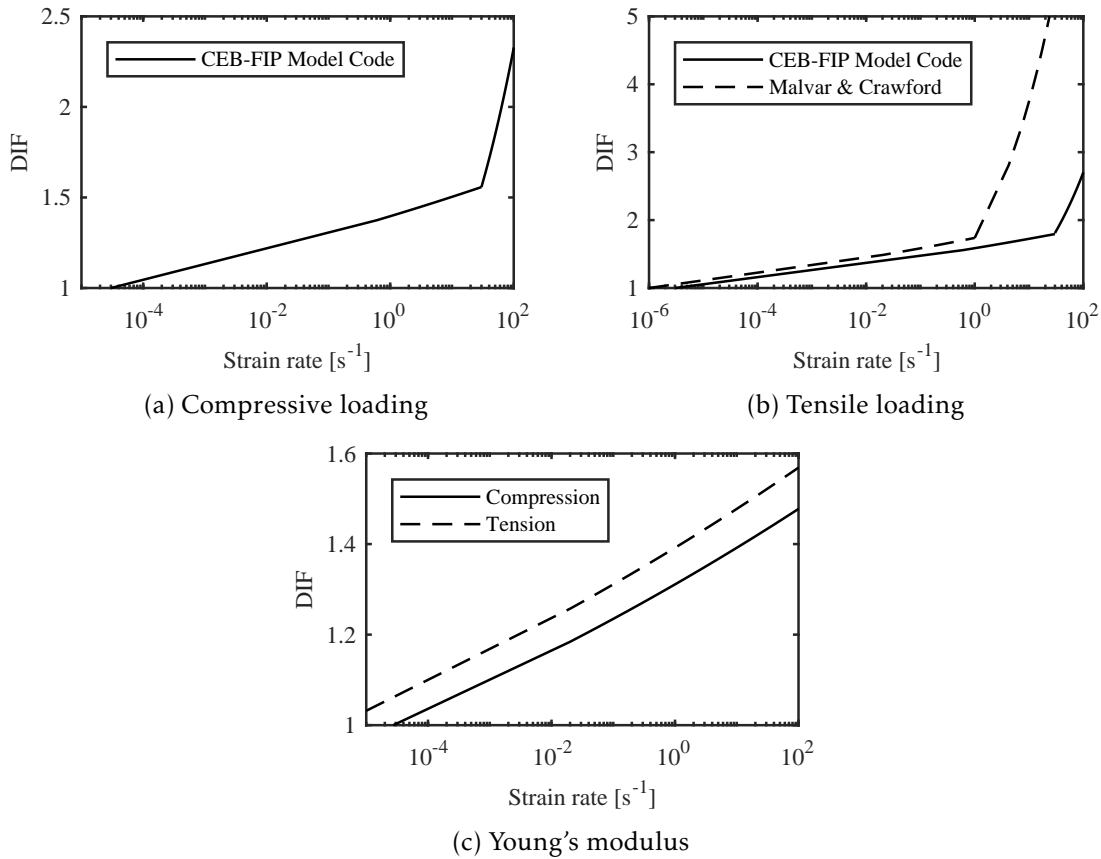


Figure 2.12: Dynamic Increase Factors for concrete [17, 92]

dynamic loadings might be due to the decrease in the internal micro-cracking, for a given stress level, as the strain rate increases. The CEB-FIP Model Code 1990 [17] proposes the strain rate dependency illustrated in Figure 2.12(c).

### 2.9.1.2 Reinforcement steel bars

The steel used in reinforcement bars is also affected by the strain rate effects, which enhances both the yield and ultimate strengths. Nonetheless, according to Malvar and Crawford [93], the Young's modulus remains constant regardless of the strain rate. The authors proposed a formulation that only depends on the yield strength of the steel  $f_y$  and is valid for steel bars with yield stresses between 290 and 710 MPa. According to this formulation, the yield stress's dependence on strain rate is higher than that of the ultimate stress, as depicted in Figure 2.13.

### 2.9.1.3 Structural component

The UFC-3-340-02 [173] proposes a set of Dynamic Increase Factors to be used whilst designing structural components subjected to blast loads in the far and close-in design ranges. These design values are shown in Table 2.3 for reinforced concrete elements

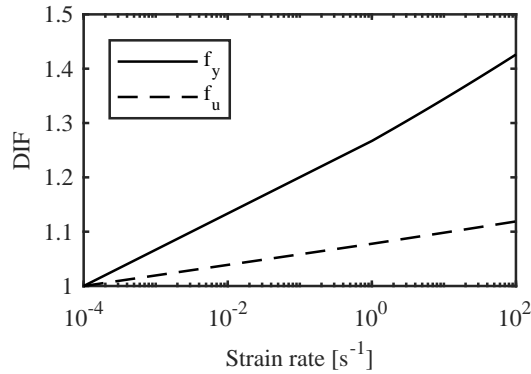


Figure 2.13: Dynamic Increase Factors for reinforcement steel bars [93]

Table 2.3: Dynamic Increase Factors for the design of reinforced concrete elements [173]

Stress type	Far design range			Close-in design range		
	Reinforcement bars		Concrete	Reinforcement bars		Concrete
	$f_{dy}/f_y$	$f_{du}/f_u$	$f_{dc}/f_c$	$f_{dy}/f_y$	$f_{du}/f_u$	$f_{dc}/f_c$
Bending	1.17	1.05	1.19	1.23	1.05	1.25
Diagonal tension	1.00	-	1.00	1.10	1.00	1.00
Direct shear	1.20	1.00	1.10	1.10	1.00	1.10
Compression	1.10	-	1.12	1.13	-	1.16

according to the material and the stress state (bending, diagonal tension, direct shear and compression). As expected, since the magnitude of close-in detonations is higher than that of an explosion located far from the structural element, the strain rate is larger for the former and consequently, the design values of DIF follow the same trend.

## 2.9.2 Performance criteria

The design of buildings against blast loads is commonly based on performance criteria that defines the quantitative limits on the response of its structural elements. Therefore, the structural elements are usually designed by means of a dynamic analysis that computes their maximum dynamic response when subjected to the design blast scenario. This maximum response is subsequently compared with the quantitative limit, defined for a certain overall building design objective, to verify its compliance [31].

Several standards, such as the ASCE/SEI 59-11 [158], the UFC 4-010-01 [174] and the PDC TR-06-08 [154], are based on the previously referred design philosophy to establish the requirements for blast design. Therefore, blast design of buildings is mainly performed at a structural element level, where each component is individually analysed. However, performance goals are commonly set in terms of life safety, functionality and reusability for the entire building. The PDC TR-06-08 [154] proposes a methodology in which a building level of protection (LoP) must be selected in order to attain the desired

performance goal (see Table 2.4). Additionally, the expected overall building damage corresponding to each performance goal is also shown in the referred table.

According to [154], the structural elements may be classified as:

- Primary structural: elements whose collapse would affect a significant number of other elements (supported by this member) and disturb the overall stability of the building;
- Secondary structural: members supported by a primary structural elements;
- Nonstructural: elements which are not necessary for the overall stability of the building and, consequently, whose loss would have little effect on it.

Table 2.5 shows the allowable damage for each element category (primary, secondary and nonstructural) in order to achieve the required building LoP. The damage levels shown in the referred table may be described as follows:

- Blowout: structural member is completely overpowered by blast load, leading to debris with significant velocities;
- Hazardous failure: collapse of the structural member with velocities of debris ranging from insignificant to very significant;
- Heavy damage: structural member does not fail, however, the resultant significant permanent deflections deem it unrepairable;
- Moderate damage: permanent deflection of the structural member. Although member is repairable, replacement might be more economical and aesthetic;
- Superficial damage: no permanent damage is visible on the component.

Table 2.4: Building levels of protection [154]

Level of protection	Overall building damage	Performance goal
Below Standard	Severe	N/A
Very Low (I)	Heavy	Collapse prevention
Low (II)	Moderate	Life safety
Medium (III)	Minor	Property preservation
High (IV)	Superficial	Continuous occupancy

Table 2.5: Component damage depending on the level of protection of the building [154]

Level of protection	Component damage		
	Primary	Secondary	Nonstructural
Below Standard	Hazardous	Blowout	Blowout
Very Low (I)	Heavy	Hazardous	Hazardous
Low (II)	Moderate	Heavy	Heavy
Medium (III)	Superficial	Moderate	Moderate
High (IV)	Superficial	Superficial	Superficial

It is important to refer that “Below Standard” does not constitute a level of protection and, consequently, it is never considered as a design goal. Its associated overall building damage is classified as severe, in which component damage is expected to be in the Hazardous/Blowout range (larger than the one accepted by the “Very Low” LoP), resulting in a very likely progressive collapse of the building. The “Very Low” level of protection expects damage levels up to the onset of structural collapse but progressive collapse is unlikely. Additionally, the moderate and minor overall building damage may be differentiated through the economic feasibility of the structure’s repair. Lastly, when a “High” level of protection is required, only superficial damage is acceptable, i.e. permanent deformations must not be present on the building.

### 2.9.2.1 Response parameters

The traditional performance criteria for static loading, such as the one foreseen in Eurocode 0 [34], is based on two types of limit states, the ultimate and serviceability limit states. The former aims to avoid the collapse of the structure and, as an example, its performance criteria may be based on the limitation of stress levels on structural components in order to avoid their failure. Alternatively, the latter concerns the correct functioning of the structure under normal use, namely the avoidance of excessive deformations that could impair the serviceability of the structure. However, these methodologies are not easily applicable to blast design due the dynamic effects and large construction costs, since permanent deflections are expected for the majority of levels of protection. Therefore, the response parameters used in blast design are established on the maximum dynamic deflection of the structural element, which is relatively easy to attain resorting to experimental blast tests or numerical methods. Additionally, this maximum deflection allows for an approximate methodology for the level of acceptable damage or plastic deformation [31]. When subjected to blast loads, two dimensionless parameters, the ductility ratio  $\mu$  and the support rotation  $\theta$ , are commonly used to define the maximum dynamic deflection of structural components, such as beams, walls, columns and slabs. The ductility ratio, defined in equation (2.35), is computed as a function of the maximum  $\delta_m$  and yield  $\delta_y$  displacements, while the support rotation is shown in equation (2.36), where  $l_{min}$  is the shortest distance from the point of maximum displacement, determined resorting to the Theory of Plasticity, to a support.

$$\mu = \frac{\delta_m}{\delta_y} \quad (2.35)$$

$$\theta = \arctan\left(\frac{\delta_m}{l_{min}}\right) \quad (2.36)$$

According to Dusenberry [31], damage starts to occur at some location of a given structural component when the observed plastic strains approach the material failure strain. Therefore, if one assumes that the section remains plane and that the curvature

in the regions of maximum moment increases proportionally with deflection after yield, the ductility ratio may be thought as an approximate measure of plastic strain. Nonetheless, this approximation is only valid when the strains that lead to the collapse of the structural element occur at the damage initiation's location, e.g. the extreme fibre of a steel beam. Distinctively, the collapse of reinforced concrete components may be caused by compressive strain, while initial damage results from concrete cracking under tensile stresses and yielding of steel reinforcement. Consequently, the ductility ratio may not provide an accurate approximation of the flexural damage verified on reinforced concrete elements. Additionally, when subjected to blast loads, very ductile structural members, materialised with steel, develop a tension membrane response at high ductility ratios, which causes high strains and failure at the connections, as opposed to mid-span (initial yielding). Therefore, for such cases, it is considered that the support rotation yields a better approximation of damage, when compared with the ductility ratio.

Tables 2.6 and 2.7 present the response parameters defined by both the American Society of Civil Engineers [158] and the Protective Design Center of the U.S. Army Corps of Engineers [154] for several types of structural elements subjected to blast loads. Analysing the referred tables, it is possible to verify that the superficial damage always corresponds to an unitary ductility ratio, i.e. no permanent deflection is allowed on the structural element. As reviewed, the limits established for the reinforced concrete components, when permanent damage is admissible, are mainly defined in terms of support rotation. On the other hand, both ductility ratio and support rotation are used to define the allowable damage on structural steel elements. Dusenberry [31] states that the reviewed response parameters were mainly based on empirical correlations between the damage levels observed during experimental blast tests and the corresponding response parameters (support rotation and ductility ratio) determined with the measured maximum dynamic deflection of the structural element.

### 2.9.3 Structural analysis

To attain the previously presented performance criteria, several methods are available to analyse the response of structural elements subjected to blast loading. According to ASCE/SEI 59-11 [158], four methods may be used: Single element response analysis; Structural system multi-degree-of-freedom finite element response analysis; Explicit linear or nonlinear finite element analysis; Pressure-impulse diagrams [158].

The first available method considers that the analysis of structural components may be performed independently for each component resorting to either a single-degree-of-freedom (SDOF) or a multi-degree-of-freedom (MDOF) nonlinear model. Specifically, the SDOF model only requires a numerical integration method with respect to time, in combination with the structural properties (mass, stiffness, yield strength) and the blast scenario (peak overpressure and impulse) to compute the maximum response of a given structural element. Despite their simplicity, the accuracy of SDOF models rely mainly on

Table 2.6: Response limits for reinforced concrete elements (Adapted from [154, 158])

Element type	Superficial		Moderate		Heavy		Hazardous	
	$\mu_{max}$	$\theta_{max}$	$\mu_{max}$	$\theta_{max}$	$\mu_{max}$	$\theta_{max}$	$\mu_{max}$	$\theta_{max}$
Flexural elements								
Single-reinforced slab or beam	1	-	-	2°	-	5°	-	10°
Double-reinforced slab or beam without shear reinforcement	1	-	-	2°	-	5°	-	10°
Double-reinforced slab or beam with shear reinforcement	1	-	-	4°	-	6°	-	10°
Combined flexure and compression								
Single-reinforced beam-column	1	-	-	2°	-	2°	-	2°
Double-reinforced beam-column without shear reinforcement	1	-	-	2°	-	2°	-	2°
Double-reinforced beam-column with shear reinforcement	1	-	-	4°	-	4°	-	4°
Compression elements ( $\mu = \Delta L_m / \Delta L_y$ )								
Wall or seismic column	0.9	-	1	-	2	-	3	-
Non-seismic column	0.7	-	0.8	-	0.9	-	1	-

Table 2.7: Response limits for structural steel elements (Adapted from [154, 158])

Element type	Superficial		Moderate		Heavy		Hazardous	
	$\mu_{max}$	$\theta_{max}$	$\mu_{max}$	$\theta_{max}$	$\mu_{max}$	$\theta_{max}$	$\mu_{max}$	$\theta_{max}$
Flexural elements								
Beam (compact section)	1	-	3	3°	12	10°	25	20°
Beam (non-compact section)	0.7	-	0.85	3°	1	-	1.2	-
Plate bent about weak axis	4	1°	8	2°	20	6°	40	12°
Combined flexure and compression								
Beam-column (compact section)	1	-	3	3°	3	3°	3	3°
Beam-column (noncompact section)	0.7	-	0.85	3°	0.85	3°	0.85	3°
Compression elements ( $\mu = \Delta L_m / \Delta L_y$ )								
Column (axial failure)	0.9	-	1.3	-	2	-	3	-

the approximations that are used to characterize the dynamic response of the structural element.

The structural system MDOF finite element response analysis takes into account the interaction between the response of linked structural components. Therefore, this method, although it simulates the structural system with simplified MDOF finite element models, is able to compute the phasing between the response of interconnected components and the flexibility of the boundary conditions.

However, when the previously referred models are not able to properly attain the response of the structure, e.g. when the spatial or temporal distribution of the loading and spatial variation on mass or structural properties cannot be represented by simplified models, an explicit linear or nonlinear finite element analysis shall be used [158].

Alternately, pressure-impulse (PI) diagrams summarize the performance of a structural element subjected to a wide range of blast scenarios. These diagrams might be determined from an analytical database of performance, through a fit to available test data or by means of numerical analysis resorting to the reviewed methods.

#### 2.9.4 Single-degree-of-freedom method

The single-degree-of-freedom (SDOF) method, proposed by Biggs [9], provides a computationally inexpensive approach which allows rapid analysis of complex structures. Several design guidance manuals, such as SBEDS [100], UFC-3-340-02 [173] and ASCE/SEI 59-11 [158], recommend this method for the blast design of structural elements. Resorting to physically valid approximations, the method may be used to compute, within a reasonable accuracy, the typical response of structural elements and provide an initial estimate of the likely damage that the target will sustain when subjected to a given blast load.

The dynamic equation of motion of a structural element, such as the one illustrated in Figure 2.14(a), is commonly written as follows:

$$m \frac{d^2 y}{dt^2} + c \frac{dy}{dt} + k y = F(t) \quad (2.37)$$

where  $m$ ,  $c$  and  $k$  are the distributed mass, damping and stiffness of the system, respectively,  $d^2 y/dt^2$ ,  $dy/dt$  and  $y$  are the acceleration, velocity and displacement and  $F(t)$  is the externally applied force. According to Biggs [9], more often than not, the distributed system may be reduced into an equivalent SDOF system, by evaluating its parameters so that the deflection of the SDOF system is the same as that of the significant point of the structure, e.g. the mid-span of the beam depicted in Figure 2.14(a). The equation of motion of the equivalent system is:

$$M_e \frac{d^2 y}{dt^2} + K_e y = F_e(t) \quad (2.38)$$

where  $M_e$ ,  $K_e$  and  $F_e(t)$  are the equivalent mass, stiffness and force, respectively. It should be noted that, as reported by the UFC-3-340-02 [173], damping is scarcely considered in

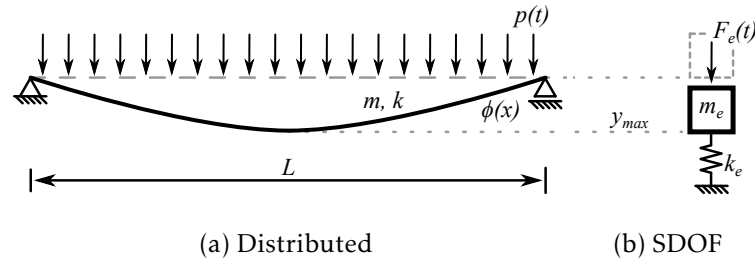


Figure 2.14: Dynamic systems

blast design due to its very little influence on the first peak response, which usually is the only cycle of response that is of interest. The equivalent parameters must guarantee that, at each response time, the equivalent mass possesses equal kinetic energy, the equivalent resistance has the same internal strain energy and the equivalent loading yields equal work to that of the distributed system [100]. Assuming that the structural element responds in a given assumed shape, which can be taken to be the same as that resulting from the static application of the dynamic loads, it is possible to correctly perform the conversion resorting to the concept of transformation factors. It is important to refer that, although the dynamic response of the systems is equal, the stresses and forces observed in the idealized system are not directly correlated to the same quantities in the real structure. However, using the deflection, the forces and stresses of the distributed system may be computed [9].

#### 2.9.4.1 Transformation factors

Transformation factors are required to determine the mass, stiffness and load of the equivalent SDOF system, based on the corresponding properties of the structural element. The assumed deflection shape function is normalised by the deflection at the point of interest, usually the point of maximum deflection,  $\phi(x) = y(x)/y_{max}$ .

The ratio of the equivalent mass to the total mass of the distributed system, commonly referred to as mass factor  $K_M$ , is computed by equating the kinetic energy of both systems, yielding the following expression,

$$K_M = \frac{M_e}{M_t} = \frac{\int_0^L m \phi(x)^2 dx}{\int_0^L m dx} \quad (2.39)$$

where  $L$  is the entire span of the structural element. The external work energy done on the equivalent SDOF system by the equivalent load  $F_e(t)$  must be equal to that of the total



load  $F_t(t)$ . Therefore, the load factor  $K_L$  is given by:

$$K_L = \frac{F_e(t)}{F_t(t)} = \frac{\int_0^L p(t)\phi(x)dx}{\int_0^L p(t)dx} \quad (2.40)$$

The resistance factor  $K_R$  is determined by equating the strain energy, defined as the internal work energy produced by the resisting force of the structural component, on both systems. Assuming that the resisting force has the same spatial distribution as the applied load and that the structural element has the same deflected shape as the shape used to define the load factor  $K_L$ , it is possible to conclude that the resulting resistance factor has the same value as the load factor ( $K_R = K_L$ ). Therefore, the dynamic equation of motion of the equivalent system now becomes:

$$K_M M_t \frac{d^2 y}{dt^2} + K_L k y = K_L F_t(t) \quad (2.41)$$

For convenience, equation (2.41) may be written in terms of a load-mass factor, which is defined as  $K_{LM} = K_M/K_L$ . Table 2.8 shows the transformation factors based on static deformation shapes for beams under different support conditions. The maximum resistance  $R_m$  is determined resorting to the moment capacity at mid-span  $M_{pl}^m$  and at the supports  $M_{pl}^s$ . The stiffness of the structural element  $k$  is computed as a function of its bending stiffness  $EI$ . Resorting to the equivalent mass and stiffness, the natural period of the SDOF under free vibrations is computed as follows,

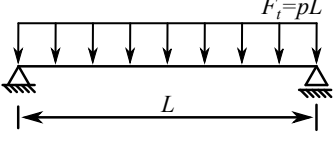
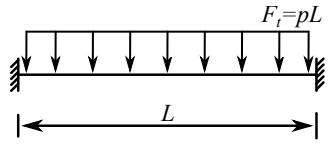
$$T = \frac{2\pi}{\omega} = 2\pi \sqrt{\frac{M_e}{K_e}} \quad (2.42)$$

where  $\omega$  is the angular frequency of the SDOF system. Given the properties of the equivalent system and the blast scenario, the charts formulated by Biggs [9] may be used to determine the peak dynamic displacement. These charts were obtained by means of solving the equivalent SDOF equation of motion under a number of load shapes and different target properties. Figure 2.15 presents such a chart, where the peak dynamic displacement was obtained when an undamped elastoplastic SDOF system is subjected to a triangular pulse.

#### 2.9.4.2 Resistance function

It is assumed that the majority of blast-loaded components will suffer some kind of permanent damage. Consequently, the term related to their structural stiffness  $K_L k y$  on the dynamic equation of motion of the SDOF system becomes invalid and it might be advantageous to define it according to a resistance function, which is based on the ductile flexural response of the blast-loaded component. Considering the case of a fixed-end beam in ductile, flexural response, subjected to a uniform load, one can observe its response modes in Figures 2.16(a) to 2.16(c). Initially, as represented in Figure 2.16(a), the

Table 2.8: Transformation factors for beams [9]

Loading diagram	Strain range	$K_L$	$K_M$	$R_m$	$k$
	Elastic	0.64	0.50	$\frac{8M_{pl}^m}{L}$	$\frac{384EI}{5L^3}$
	Plastic	0.50	0.33	$\frac{8M_{pl}^m}{L}$	0
	Elastic	0.53	0.41	$\frac{12M_{pl}^s}{L}$	$\frac{384EI}{L^3}$
	Elastoplastic	0.64	0.50	$\frac{8}{L}(M_{pl}^s + M_{pl}^m)$	$\frac{384EI}{5L^3}$
	Plastic	0.50	0.33	$\frac{8}{L}(M_{pl}^s + M_{pl}^m)$	0

applied load results in a elastic deformation until the beam yields simultaneously at both supports. Subsequently, the beam deforms in an elastoplastic mode (Figure 2.16(b)), with stiffness  $k_{ep}$ , as the load increases until the ultimate resistance  $R_m$  (yielding at mid-span resulting in the mechanism illustrated in Figure 2.16(c)). Lastly, the displacement increases, while the resistance remains constant, until the failure deflection is reached. The

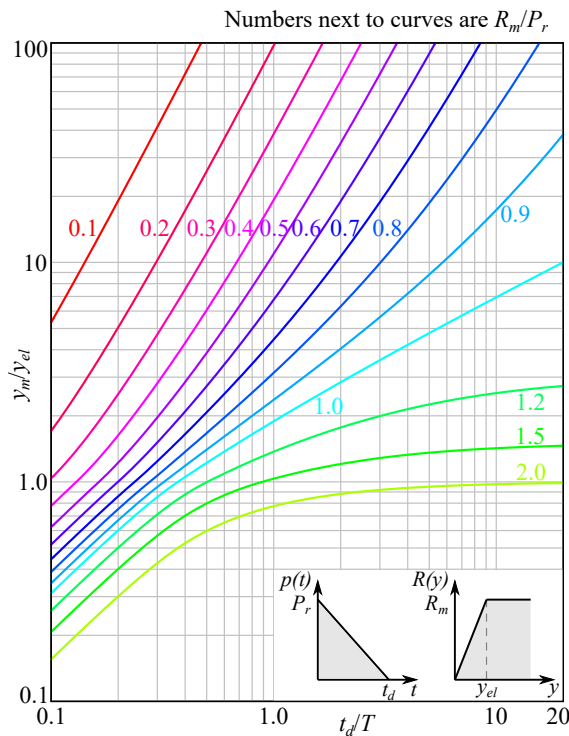


Figure 2.15: Maximum response of undamped elastoplastic single-degree-of-freedom system due to a triangular load pulse [9, 173]

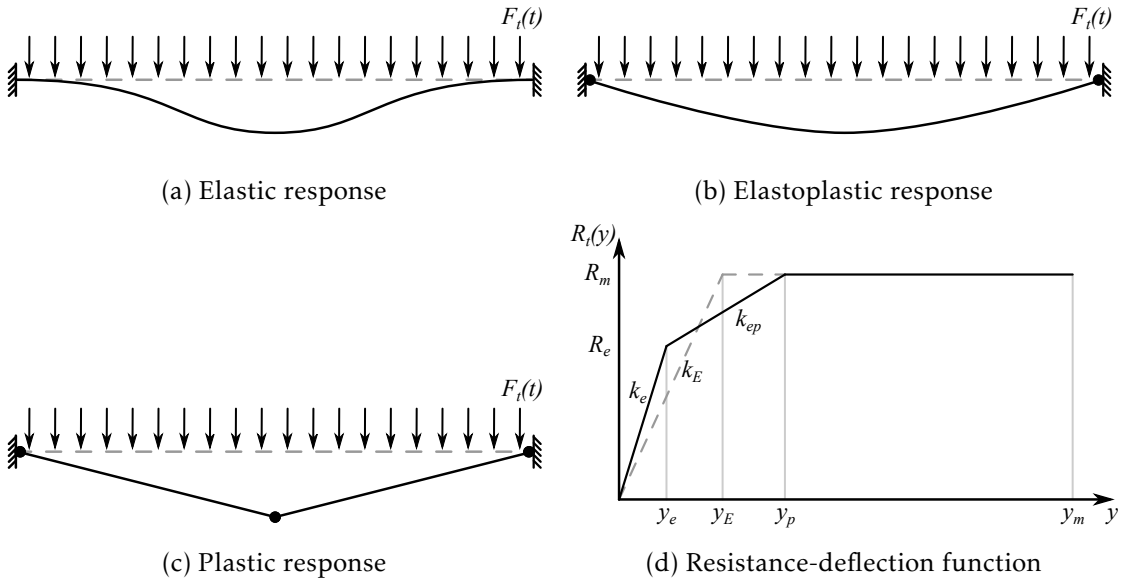


Figure 2.16: Fixed-end beam response modes and corresponding resistance-deflection function

resulting resistance-deflection curve for this example may be observed in Figure 2.16(d). An equivalent elastic region, with stiffness  $k_E$ , may be considered for design. This equivalent parameter is computed as presented in equation (2.43), so that the strain energies under both resistance-deflection relationships are equal [100].

$$k_E = \frac{R_m}{y_E}, \quad \text{with } y_E = y_e + y_p \left(1 - \frac{R_e}{R_m}\right) \quad (2.43)$$

### 2.9.4.3 Limitations

The equivalent SDOF method is recommended to be used in modelling the blast response of structural elements on nearly rigid supports when subjected to relatively uniform blast loads (or a concentrated load near the centre) and when the deflection during the elastic, elastoplastic, and plastic response is dominated by the fundamental mode shape, which is similar to the one resulting from the static application of the load. Moreover, it is considered to be a better assumption when the structural component presents a large plastic deformation due to the domination of the response by the fundamental mode, rather than components with a large elastic deformation, which are more likely to be influenced by higher mode shapes. Therefore, the SDOF method is a computationally inexpensive approach which allows the computation, within a reasonable accuracy, of the nonlinear response of structural elements presenting large plastic deflections when subjected to blast loads. Nonetheless, according to SBEDS [100], there are some limitations to this method, which will be succinctly described in this section.

As reviewed, the main response mode used in SDOF analysis is the flexural response. However, one has the possibility to include the influence of multiple response modes

that contribute to the resistance-deflection relationship, such as compression and tension membrane. Hence, the accuracy of the method is highly dependent on one's knowledge and experience of when and how to include the applicable response modes.

In a SDOF analysis, the structural element is decoupled from the building, since the analysis is performed with an independent SDOF model with rigid boundaries. Therefore, interactions between components are not directly accounted for (such as a supported structural element, directly loaded by the blast, and the supporting component, which is loaded by the dynamic reactions forces from the supported element). The inertial force of the supporting component receives a contribution from a portion of mass from the supported component, while the deflection of the supporting element influences the response of the supported component. It is usually conservative to ignore the effects on the supported component and to include the influence of the supported component on the supporting component by including approximately 20% of the supported component's mass on the dynamic reaction force [100].

Lastly, for close-in and confined explosions, the spatial distribution of the loads is very difficult to approximate with a simple SDOF analysis. Hence, pressure-time histories resulting from these blast scenarios have to be converted into an equivalent blast load that is spatially uniform over the whole area of the component, as this analysis usually considers a spatially uniform load. Additionally, these non-uniform spatial distributions may excite higher mode shapes, which are not included in the SDOF analysis.

### 2.9.5 Pressure-impulse and charge weight-standoff diagrams

The design of a structural component subjected to a blast load is simply conducted in terms of the maximum dynamic peak deflection, instead of a detailed computation of the complete displacement-time history. The charts formulated by Biggs [9] constitute a useful tool for the design of blast-loaded structural components. Nonetheless, the response spectra, i.e. the peak dynamic displacement as function of the structural properties and blast scenario, may be presented in different ways. A pressure-impulse (PI) diagram, usually used to assess the damage of a structural component, is such an alternative [70].

Figure 2.17(a) shows a typical non-dimensional PI diagram for an undamped, perfectly elastic SDOF system under suddenly applied loads. The ratio of the load duration to the natural period of the structure ( $t_d/T$ ) may be categorized in three different regimes: impulsive, dynamic and quasi-static. The impulsive and quasi-static regimes are easily distinguished by means of the vertical and horizontal asymptotes depicted in the referred figure. It should be noted that, since all the points on a PI curve represent combinations of load, or pressure, and impulse that will cause a certain deflection on the considered structural element, the design combinations of pressure and impulse that will induce, or not, a specified damage level are readily obtained through the use of a PI diagram. As illustrated in Figure 2.17(a), combinations to the left and below the curve will not cause the damage level, i.e. the structural element is "safe", while those to the right and above

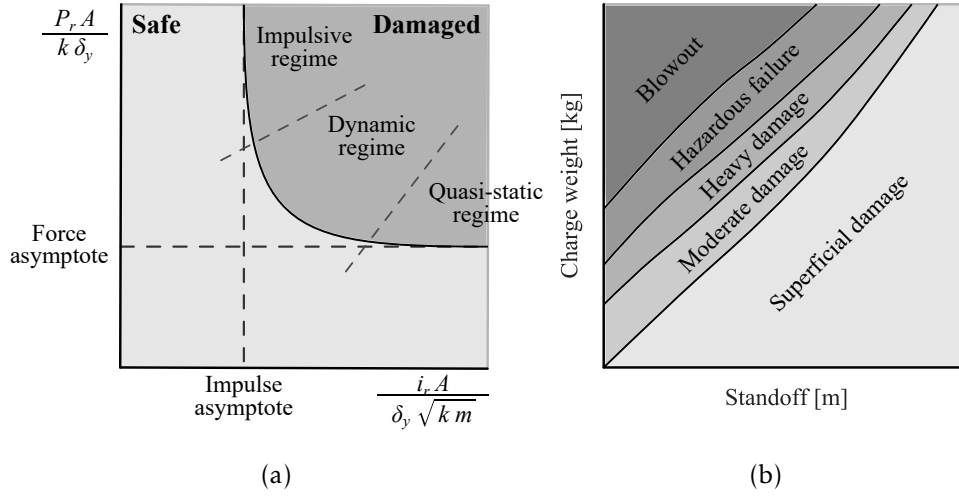


Figure 2.17: Typical (a) pressure-impulse and (b) charge weight-standoff diagrams

will exceed the limit, e.g. the maximum displacement [70].

Non-dimensional pressure  $p$  and impulse  $i$  may be defined as a function of the properties of the SDOF system as:

$$p = \frac{P_r A}{k \delta_y} \quad (2.44)$$

$$i = \frac{i_r A}{\delta_y \sqrt{k m}} \quad (2.45)$$

Alternatively, a typical charge weight-standoff diagram, from which one can readily observe the resulting structural component's damage for a given blast scenario, is illustrated in Figure 2.17(b). Charge weight-standoff diagrams may be used to compute PI diagrams when the pressure-time profile can not be directly obtained from a given pressure-impulse combination (when the modified Friedlander equation is used to approximate the pressure-time profile, two blast wave parameters ( $t_o$  and  $b$ ) influence the resulting impulse). The PI combinations corresponding to each charge weight-standoff may be determined resorting to the Kingery & Bulmash's semi-empirical predictions for the blast wave parameters (see Section 2.6.1).

### 2.9.5.1 Analytical solutions (PI diagrams)

The impulsive and quasi-static asymptotes are usually determined by guaranteeing the conservation of mechanical energy,

$$K.E. = S.E. \quad \rightarrow \quad \text{impulsive asymptote} \quad (2.46)$$

$$W.E. = S.E. \quad \rightarrow \quad \text{quasi-static asymptote} \quad (2.47)$$

where  $K.E.$  is the kinetic energy resulting from a very short pulse,  $W.E.$  is the work done by the load that deforms the system from rest to the maximum displacement, and

$S.E.$  is the strain energy of the system at maximum displacement. For the case of a perfectly elastic, undamped system, whose PI diagram is illustrated in Figure 2.17(a), the presented energy expressions result in the dimensionless impulsive and quasi-static asymptotes at 1 and 0.5, respectively [70]. However, the energy balance method is only applicable to the impulsive and quasi-static regimes. Although the dynamic regime may be approximated resorting to analytical expressions, their application is limited to simple structural systems, resistance models, and load functions. Therefore, the use of numerical approaches to compute PI diagrams for more complex problems is reviewed in the following section.

### 2.9.5.2 Numerical approaches (PI diagrams)

Numerical approaches may be used to generate a sufficient number of points, each from a single dynamic analysis, to allow for curve fitting. However, determining all possible pressure and impulse combinations that yield a specific structural maximum deflection is computationally expensive. Hence, the use of a search algorithm to compute the necessary points is considered advantageous. The numerical approach allows for complex nonlinear resistance-deflection relationships, complex loading functions, and can describe the behaviour of the PI curve in the dynamic response regime as well.

Rhijnburger and team [139] proposed an approach to determine PI diagrams using a combination of analytical and numerical techniques. Initially, the energy balance method is used to estimate both asymptotes, while a numerical approach generates the dynamic regime resorting to a branch-tracing technique (see Figure 2.18(a)). The method resorts to the slope of the two previously known points to compute a prediction point. Subsequently, if the obtained displacement does not agree with the design requirement, correction steps are performed until the result gets within a certain tolerance. However, according to Soh and Krauthammer [156] (as cited in [70]), the reviewed method may become unstable, since it assumes that the PI curves are smooth and continuous. The discrete nature of numerical integration may violate this assumption and lead to sudden slope changes.

In order to solve the stability problems of the above mentioned method, Soh and Krauthammer developed a stable numerical approach, which also resorts to the energy balance method to estimate the location of the asymptotes, but evaluates a large number of dynamic analyses within specified limits of the asymptotes, as illustrated in Figure 2.18(b). Subsequently, the limits are tightened until the PI curve is obtained. Alternatively, Ng and Krauthammer [116] (as cited in [70]) derived a numerical procedure that does not require the determination of the asymptotes and is based on the concept of a threshold curve. While keeping a constant pressure, threshold points are found through the variation of impulse and verification if a certain PI combination is either “safe” or “damaged”. If a certain point is “safe”/“damaged”, the impulse is increased/reduced until the point returns the opposite state. There, between the “safe” and “damage” points, a threshold point is found, as shown in Figure 2.18(c).

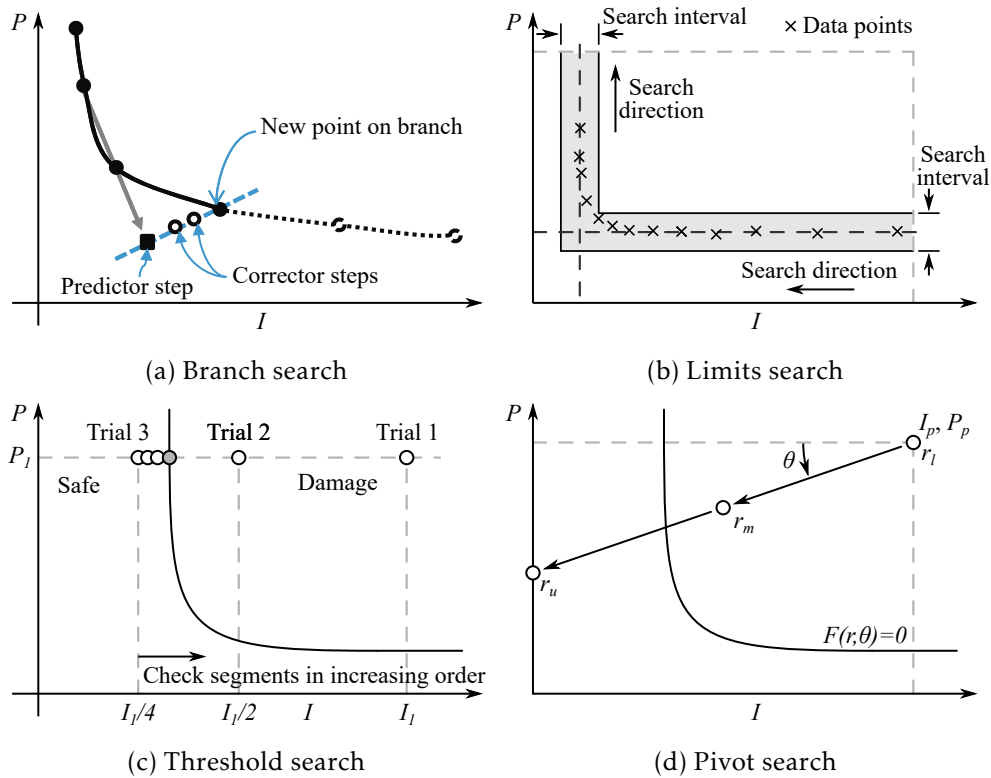


Figure 2.18: Numerical approaches to compute PI curves (Adapted from [70])

Despite yielding PI diagrams with reasonable accuracy, the previously presented numerical approaches are computationally expensive and require a large amount of unnecessary data. To take advantage of multi-processor and multi-core computing capabilities, Blasko et al. [11] (as cited in [70]), used a polar coordinate system and the bisection method to determine PI diagrams, as shown in Figure 2.18(d). A pivot point  $(I_p, P_p)$ , located in the “damaged” region, is defined as the origin of the polar coordinate system. Subsequently, the bisection method is used to compute the radius  $r_i$  to the threshold point for each angle  $\theta$ . Similarly to the threshold search method, this procedure does not require the determination of the asymptotes. Nonetheless, the authors state that the line that passes through both the origin and the asymptotes’ intersection is ideal for positioning the pivot point, since the points on this line are equally distant from both asymptotes. The pivot point approach may be used to determine the PI diagram of any structural system for which a resistance function can be defined [70].

## 2.10 Conclusions

The present chapter summarised the current state of the art regarding the formation of shock waves and their interaction with targets, including the effects of fluid-structure interaction, i.e. when the reflecting surface may not be considered as rigid, and blast wave clearing due to a finite area. The semi-empirical methods for predicting the positive

and negative phase parameters of an ideal blast wave, as well as the pressure-time curve approximations, were presented. The semi-empirical predictions of the positive phase parameters of a reflected blast wave, while considering the reflective surface as rigid and infinite, were compared to experimental measurements available on the literature in order to verify their applicability. A good agreement was found between the Kingery & Bulmash's semi-empirical predictions, which were mainly based on large-scale tests and the experimental results when controlled small-scale laboratory tests are used to obtain the blast wave positive phase parameters. The effects of both fluid-structure interaction and blast wave clearing on the original blast load profile were also examined and the available methods currently employed to consider these phenomena reviewed.

The analysis of structures subjected to blast loads was reviewed, namely in terms of materials performance under high strain rate, performance criteria and methods of structural analysis. The performance criteria of structural components (reinforced concrete and steel) subjected to blast loads, was presented as defined by two American standards. A summary of the available methods to analyse the response of blast-loaded structural elements was presented, with special focus on the single-degree-of-freedom method and pressure-impulse and charge weight-standoff diagrams.

According to the information presented on this chapter, it is considered as best practice the use of the Kingery & Bulmash's semi-empirical predictions as a base for the definition of blast wave parameters. The positive phase blast wave profile is achieved resorting to the modified Friedlander equation, while the negative phase, when considered, is approximated by the cubic expression proposed by Granström. Subsequently, to take into account the effects of blast wave clearing and fluid-structure interactions on the original blast wave profile, the method proposed by Hudson and the extended Taylor theory will be cumulatively used on the remainder of the present work.

The SDOF method will be used to compute the peak dynamic deflection of the considered structural elements, in combination with the assumed blast wave profile and the consideration of a non-ideal reflective surface.



## Chapter 3

# Protective solutions

### 3.1 Introduction

A historical survey of important structures on which blast loads were directly imparted revealed that, if blast scenarios are considered during their design, reinforced concrete elements behave better than their steel counterparts, as a result of their increased mass, damping and energy absorbing capacity [5]. Consequently, the traditional structural blast protection methods are based on strengthening with thicker reinforced concrete, ultra high-performance and fibre reinforced concrete structural elements [3, 16, 78, 171, 178]. However, these techniques are time consuming and labour intensive, which leads to an increase in construction cost both during the strengthening process and due to retrofit if damaged, and are heavy and often difficult to install in existing facilities. The influence of externally bonded steel plates and composite materials, namely fibre reinforced polymers (FRP) by means of externally bonded and near surface mounted (NSM) systems, on the blast resistance of reinforced concrete structural elements has also been studied and reported in the literature [15, 103].

Alternatively, the use of protection solutions with reduced mass and high energy absorption is considered to be advantageous when compared with traditional strengthening methods [188]. These solutions, commonly referred to as sacrificial claddings, are commonly positioned on the outer surface of the already existent structural elements in order to mitigate the blast load to a relatively lower level for a longer time span, absorbing most of the blast induced energy. They are usually composed by a crushable core, which undergoes a progressive deformation under a relatively low stress, and two skin plates (front and rear). The core is commonly materialised by a cellular material or structure, while the plates aim to evenly distribute the blast load to the crushable core and may be made of a thin metallic or composite plate.

The current chapter aims to introduce a brief state of the art on traditional strengthening techniques and, since the main objective of the present work is the development and study of a sacrificial cladding (3D printed crushable core), an extensive review on the concept of sacrificial cladding solutions. Firstly, the fundamental energy absorption

principles are presented, followed by the definition of cellular solids and the analysis of their experimental behaviour, namely their typical compressive stress-strain curve and the subsequent determination of their energy absorption capabilities. Secondly, the state of the art on additively manufactured solutions for energy absorption is reported. The chapter ends with a revision of the relevant simplified numerical models readily available in the literature to simulate the nonlinear behaviour of sacrificial claddings.

## 3.2 Reinforced concrete

Over the past decades, several research works have examined the blast response of structural elements materialized with high strength concrete [78, 91, 171] and fibre reinforced [16] concrete independently. More recently, ultra-high performance concrete members have been subjected to several blast scenarios in order to evaluate their response [3, 32, 178, 181].

### 3.2.1 High strength concrete

The designation of high strength concrete commonly refers to concrete whose compressive strength surpasses 80 MPa. Magnusson and Hallgren [91] and Li and co-workers [181] resorted to a shock tube to examine the response of simply-supported high strength concrete beams subjected to shock wave loading. Also applying blast loads using a shock tube, Thiagarajan and team [171] evaluated the nonlinear response of simply-supported one-way slabs materialised with high strength concrete. It should be noted that all the referred studies simultaneously tested normal strength concrete structural elements to establish a baseline response and that the geometrical reinforcement ratio was maintained constant in all the reported studies.

Table 3.1 shows a summary of the results obtained by the referred authors, in terms of maximum deflection at mid-span, for both normal (NSC) and high (HSC) strength concrete. Analysing the table, it is possible to verify that, contrarily to the expected, the maximum displacement recorded by Magnusson and Hallgren [91] increased with the use of high strength concrete. Nonetheless, the high strength concrete beam was able to recover most of the displacement and present a small residual deformation. Unfortunately, due to a sensor malfunction, the residual deformation of the normal strength concrete beam was not recorded. On the other hand, Li and team [181] state that, when subjected to blast loading, the effect of concrete seems to be insignificant in terms of maximum displacement. However, the use of high strength concrete yields a significant reduction of residual displacements when failure is verified. A reduction of approximately 60% was reported by Thiagarajan and co-workers [171]. Nonetheless, the authors reported a 13% increase on the reflected impulse applied to the slab. Therefore, taking into account the results reported in the literature, it is not evident the advantage of using high over normal strength concrete for blast protection.

Table 3.1: Summary of the use of high strength concrete for blast resistant design

	$f_c$ [MPa]		$\delta_m$ [mm]	
	NSC	HSC	NSC	HSC
Magnusson & Hallgren [91]	53.8	124.4	12.0	18.6
Li et al. [181]	58.0	108.0	48.0	44.5
Thiagarajan et al. [171]	27.6	107.0	221.0	140.0

### 3.2.2 Fibre reinforced concrete

The addition of fibres to concrete increases its post-cracking resistance which, ultimately, enhances strain capacity, toughness and damage tolerance [77]. Therefore, fibre reinforced concrete is expected to be a good material for blast resistant design of structural members. To understand the blast performance enhancements provided by the addition of steel fibres to concrete, Burrell and team [16] subjected a series of half-scale simply-supported columns to a simulated blast load, which resorts to a shock tube facility, while several combinations of transverse reinforcement detailing as well as steel fibre content were investigated. A transverse reinforcement spacing of 38 and 75 mm, which correspond to a seismic and nonseismic detailing, respectively, in combination with plain concrete and a steel fibre content of 0.5% were considered in the referred study. A summary of the relevant results is presented in Table 3.2. When seismic detailed is considered during the design of columns, the addition of steel fibres seems to have little influence on the maximum displacement at mid-span (8%), while presenting a 20% reduction for the residual displacement. Alternatively, when seismic loads are not taken into account for the detailing of the column (75 mm spacing), a greater reduction on both the maximum and residual displacement is verified between the 0 and 0.5% steel fibre content. The authors concluded that the observed reduction in terms of maximum deflection of fibre reinforced concrete columns with the increase of fibre content may be a result of their increased stiffness, when compared with reinforced concrete columns with no fibre content. Likewise, the tensile capacity and development of post-cracking strength of the fibre reinforced concrete enhances the flexural capacity of columns subjected to combined axial loads and lateral blast loads. Additionally, they observed that the inclusion of fibres yields a superior damage tolerance, namely a reduction of the concrete's fragmentation and the elimination of spalling.

Table 3.2: Summary of the use of fibre reinforced concrete for blast resistant design [16]

Reinforcement spacing	38		75	
	0.0	0.5	0.0	0.5
Steel fibre content [%]				
$d_{max}$ [mm]	92.0	99.7	126.2	93.8
$d_{res}$ [mm]	56.8	69.2	108.6	60.6

### 3.2.3 Ultra-high performance concrete

Recently, advances in concrete technology allowed the development of ultra-high performance concrete (UHPC), characterized by its composition (fine-grained sand, silica fume, steel fibres and high-strength Portland cement) and by compressive strengths larger than 150 MPa. Due to the addition of steel fibres, UHPC may be considered as ductile and that it is able to withstand tensile loads, since it possesses a direct tensile strength over 15 MPa and a flexural strength in excess of 50 MPa [178]. Several studies reported in the literature focus on the blast response of UHPC structural elements.

Ellis and co-workers [32] subjected four simply-supported one-way UHPC panels without steel reinforcement bars to reflected impulses, which varied between 0.77 and 2.05 MPa·ms, by means of a shock tube. The experimental campaign allowed the authors to verify that the one-way panels failed when subjected to reflected impulses in between 0.97 and 1.47 MPa·ms. Subsequently, resorting to the experimental results, a hierarchical multi-scale model was developed and used to conduct a parametric study, which demonstrated that the parameters that increase the quasi-static tensile strength (fibre geometry, packing and volume fraction), increase energy dissipation and, consequently, enhance the blast resistance of unreinforced UHPC panels.

Alternatively, free-air explosive tests were conducted and reported in the literature by Yi and team [181]. The blast loads, resulting from the detonation of 4-6 kg of ammonium nitrate/fuel oil (ANFO) at a distance of 1.5 m, were imparted on three two-way panels (clamped on all four sides), which were materialised by normal strength, high strength and a proprietary ultra-high performance concrete. When compared to the normal strength and high strength panels, the UHPC panel showed an improved blast response, evidenced by their reduced maximum and residual deflections and controlled cracking, which led to reduced spalling.

UHPC columns under combined axial and simulated blast loads were tested by Aoude and co-workers [3]. Nine full-scale columns were subjected to several pressure-impulse combinations through the use of a shock tube. The authors found that, despite the important role of the fibre and steel reinforcement, the UHPC significantly enhances the blast resistance and damage tolerance of columns.

Analysing the results reported by the referred experimental blast tests, UHPC structural elements with steel fibres exhibit, under blast loads, high ductility, limited residual deflection and considerable energy absorption capabilities, with limited fragmentation.

## 3.3 Externally bonded steel plates

Strengthening of existing reinforced concrete structures has been attempted by externally bonded steel plates, which enhances the flexural strength of beams, walls and slabs. RC columns are strengthened through a lateral confinement of concrete, improving both the axial compressive strength and ductility. However, the use of this protective solution

is hindered by large installation times and is prone to corrosion, resulting in increased maintenance costs [15].

An experimental campaign, composed by three blast tests, was conducted by the Defense Threat Reduction Agency (DTRA) to evaluate the enhancements in blast resistance of RC columns when a steel jacketing was used. A full-scale four-story RC building was built to this purpose and the columns located on the ground floor were subjected to similar blast loads. Figure 3.1 illustrates the RC columns with and without steel jacketing after the blast test. Analysing the conventional RC column, a diagonal shear failure, which resulted from the large transverse reinforcement spacing, may be observed. Nonetheless, comparing the performance of this column with the one strengthened with externally bonded steel, one can conclude that the latter has a significantly improved performance, since it was able to withstand the same blast load with little to none damage [103].



Figure 3.1: Enhancement of blast resistance of RC column by means of steel jacketing (Adapted from [103])

### 3.4 Composite materials

According to Buchan and Chen [15], the increase in the use of composite materials over steel for the enhancement of blast resistance in structural elements may be a result of their higher strength, corrosion resistance and greater ease of transportation and handling. Moreover, composite materials may be easily adapted to a specific application with optimised performance when compared with other materials. Research has shown that the use of composite materials improves the blast resistance capabilities of a structure,

since it augments the structural strength and ductility of its components and, simultaneously, reduces fragmentation. Several materials have been studied by the scientific community for the enhancement of the blast resistance of RC components, from which the most commonly used are: carbon (CFRP) and glass fibre reinforced polymeric (GFRP) composites. A summary of the experimental and numerical studies conducted to evaluate the behaviour of RC components strengthened with fibre reinforced polymeric composites under blast loads is depicted in Table 3.3.

Table 3.3: Summary of the use of composite materials for the strengthening of reinforced concrete components

Structural component	Composite material	
	CFRP	GFRP
Beam	[143]	[82]
Column	[103, 107, 108]	[59]
Slab	[75, 89, 105, 143]	[46, 75, 109]
Panel	[49]	[131]

It is widely accepted by the scientific community that FRP retrofitting significantly improves the blast resistance of RC structures, through the increase of its strength and ductility, allied with a fragmentation reduction. The available studies usually evaluate the blast resistance of the structural components in terms of composite delamination, cracking/failure patterns, amount of debris and corresponding speed, flexural strength and ductility enhancement and energy absorption capabilities. Therefore, according to Buchan and Chen [15], the majority of the conducted research may be considered as qualitative in character and that the fundamental behaviour of FRP retrofitted structures, when subjected to blast loads, is still not fully understood. Consequently, the technology has only been used in simple structural systems and large scale applications have not been widespread, which may be a result of the lack of confidence, the complexity of the problem and the sheer number of variables on the experimental campaigns. Moreover, the evaluation of the considered materials' performance and their subsequent comparison has been hindered by the large range of blast scenarios used in the literature.

### 3.5 Sacrificial cladding solution

A sacrificial cladding may be characterised as a protective layer with reduced mass which is fixed on the exterior of structural components, as depicted in Figure 3.2. A given blast scenario will apply a pressure-time history  $p(t)$  on the sacrificial cladding's front plate. This plate must guarantee a uniform distribution of the blast load and compacts the crushable core, which suffers a large deformation under a relatively constant nominal stress. Consequently, the applied high pressure short pulse is transmitted to the structural element with a lower level for a longer time span, as a result of momentum conservation (see Figure 3.2).

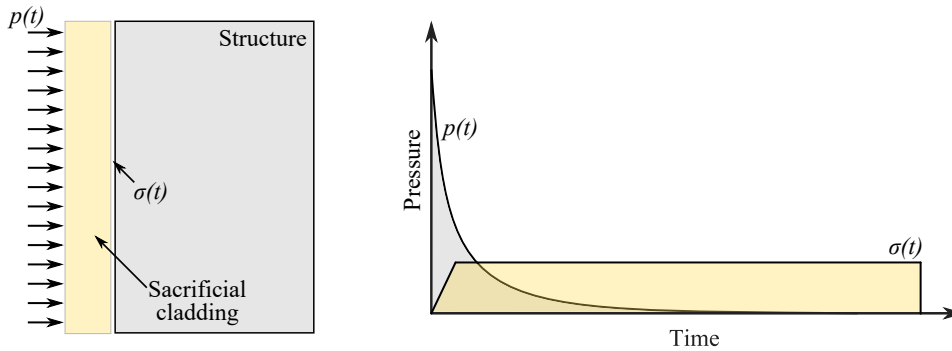


Figure 3.2: Sacrificial cladding's philosophy

According to Guruprasad and Mukherjee [47], the sacrificial cladding must deform with a certain level of predictability and efficiency for a broad spectrum of blast scenarios. The authors also state that the most important characteristics of structures undergoing large plastic deformations are their mode of deformation, on which all the other parameters depend, the impulse transfer, the amount of energy absorbed during the deformation process and their collapse space efficiency. One of the major challenges when designing a sacrificial cladding solution is the possible change in deformation mode with the variation of load intensity and, subsequently, front plate velocity, since this change will affect the predictability of the performance under different blast scenarios. Therefore, the use of crushable cores with a consistent deformation mode for the expected range of blast loads is considered as paramount. Additionally, Guruprasad and Mukherjee [47] considered that the protection solution should transfer as little impulse as possible to the structural element. Similarly, Zhou and co-workers [188] state that even though the sacrificial cladding might have the ability to absorb a large amount of energy, it does not necessarily imply that will be an effective protection solution against blast loads. Consequently, when designing this kind of solutions, the authors consider that the impulse applied to the cladding and, subsequently, transmitted to the structural element should be analysed, rather than energy absorption. It should be noted that, as a result of the referred load transformation, the crushable core must have sufficient thickness to avoid full crushing, since at this instant the transferred load will increase to values larger than those observed if no sacrificial cladding was used.

### 3.5.1 Energy absorption principles

The design and selection of energy absorbing structures/materials depends on the requirements of the specific purpose/circumstances in which they will be employed. However, a common goal is to dissipate the kinetic energy attained by the front plate in a controlled manner or at a pre-established rate [86]. Therefore, the following fundamental principles are considered to be valid in a wide range of applications and may be considered as guidelines for the design and selection of energy absorbing structures/materials:

- Irreversible energy conversion: the structure/material should convert the majority of the kinetic energy into strain energy that mainly yields plastic deformation, in order to avoid its release (if only elastic deformation occurs);
- Restricted and constant transmitted force: the peak reaction force should be kept under a given threshold to avoid the occurrence of damage in the protected structure, and, preferably, constant throughout the entire deformation process;
- Large deformation capacity: since the ideal transmitted force is constant, the deformation capacity of the structure/material greatly influences its energy absorption capacity;
- Stable and repeatable deformation mode: in the order to ensure that the energy absorbing structure/material is predictable under service, stable and repeatable deformation mode and energy absorption capacity are paramount;
- Light weight and high specific energy absorption capacity: the crushable core should be as light as possible and, simultaneously, exhibit large specific absorption capacity, i.e. energy absorption capacity per unit mass;
- Low cost and easy installation: the selected structure/material must be easily available and its installation should be efficient. This principle is fundamental for sacrificial cladding solutions, due to their single use and subsequent replacement after being subjected to a blast load.

### 3.5.2 Cellular solids

In the last decades, several materials have been considered as candidates for crushable cores of sacrificial cladding solutions. Amongst them, cellular solids have been of particular interest as a result of their reduced mass and energy absorption capabilities.

Cellular solids are defined as an assembly of cells, i.e. an enclosed space containing air, packed together so that they occupy a given space. Therefore, one might consider a cellular solid as being composed by an interconnected assembly of solid struts or plates which constitute the edges and faces of the cells, respectively. The former is usually classified as open-celled, since the cells are connected through open faces, while the latter, in which the cells are sealed off from its adjacent cells, is commonly referred to as a closed-celled cellular solid. It should be noted that they might also be classified as partly open or partly closed [41]. Alternatively, cellular solids may be categorised as a cellular structure, e.g. honeycombs and tubular cores, or a cellular material, such as cork, foams, expanded polystyrene.

Due to their large porosity, cellular solids, when compared to a solid bulk materialised by their base material, are lightweight, while their stiffness, strength or other mechanical properties may have a per unit weight of material advantage [86]. Similarly, Gibson and Ashby [41] refer that the decrease in a given mechanical property is commonly smaller



than the reduction in weight. Consequently, the most relevant property for a cellular solid is its relative density  $\bar{\rho}$ , defined as the ratio between the density of the cellular solid  $\rho^*$ , and the density of its constituent material  $\rho_s$ . Additionally, according to Gibson and Ashby [41], the mechanical properties of the cellular material greatly depend on the cell shape. If the cells are equal in all three-dimensional axis, the properties of the cellular solid will be isotropic. However, when cells are elongated or flattened, even if just slightly, the mechanical properties will vary with the direction, often strongly. Lastly, it is possible to distinguish cellular solids based on their topology. A common unit cell may be repeated to generate the walls of two-dimensional cells, such as in a honeycomb. Contrarily, the walls on a cellular solids with three-dimensional cells have random orientations in space, e.g. a foam. Figure 3.3 illustrates several examples of cellular solids.

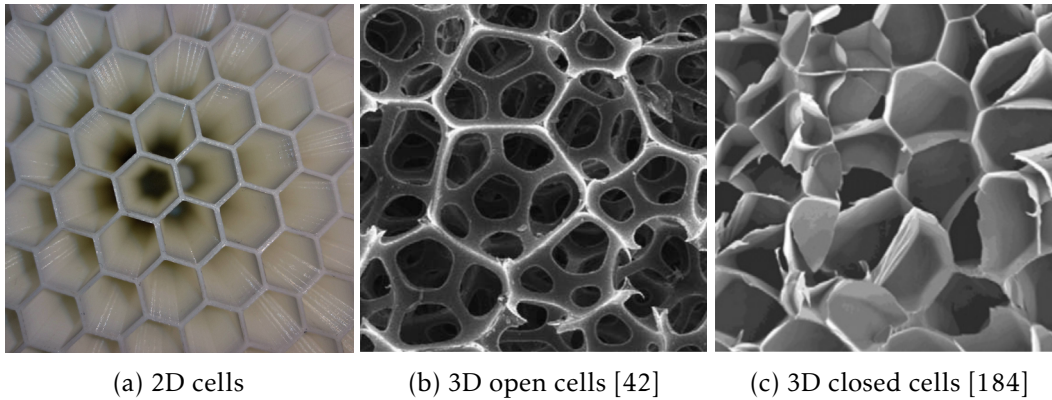


Figure 3.3: Cellular solid examples

### 3.5.2.1 Compressive behaviour

The typical compressive stress-strain curve for cellular solids, both cellular structures and materials, is illustrated in Figure 3.4(a). Analysing the depicted curve, one may observe an initial elastic phase, followed by a plateau regime with almost constant stress, which ends with a densification phase [41]. Taking into account the presented behaviour, it is readily visible that cellular materials and structures have the ability to absorb a large amount of energy at a relatively low stress, when compared to its base material, as a result of the wide stress plateau under compression with a strain usually larger than 0.8 [4, 41, 86]. The plateau stress  $\sigma_{pl}$ , along with the densification initiation strain  $\varepsilon_d$ , are the most important characteristics of a sacrificial cladding solution, as they control its energy absorption capabilities. Consequently, their correct determination is crucial. Tan and team [162] proposed a method for the determination of the densification initiation strain through an energy efficiency parameter  $\eta$ , defined in equation (3.1) as function of the nominal stress  $\sigma$  and strain  $\varepsilon$ . The authors state that the densification initiation strain corresponds to the point where the efficiency is a global maximum, as presented in Figure 3.4(b).

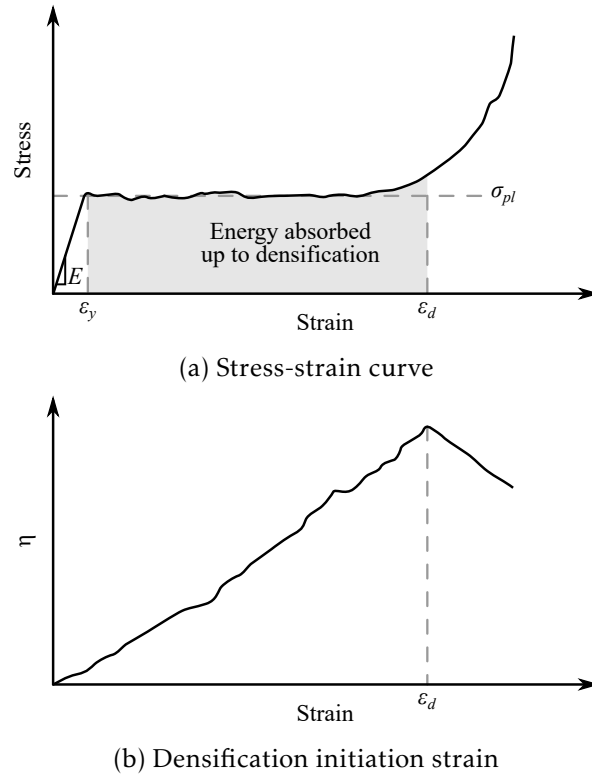


Figure 3.4: Compressive behaviour of cellular solids

$$\eta(\varepsilon) = \frac{1}{\sigma(\varepsilon)} \int_0^\varepsilon \sigma(\varepsilon) d\varepsilon \quad (3.1)$$

Following the determination of the referred strain, the plateau stress can be computed through the energy equivalence on the plateau regime. In the resulting equation (3.2),  $\varepsilon_y$  stands for the plastic phase initiation strain.

$$\sigma_{pl} = \frac{1}{(\varepsilon_d - \varepsilon_y)} \int_{\varepsilon_y}^{\varepsilon_d} \sigma(\varepsilon) d\varepsilon \quad (3.2)$$

Subsequently, the estimation of the energy absorption capability of a cellular material may be obtained through equation (3.3), which commonly ignores the elastic energy, as well as the energy of the pre-collapse and densification stages [159]. Scaling the absorbed energy with the mass of the crushed cellular solid, one obtains the corresponding specific energy absorption, *SEA*.

$$U_{pl} = \int_{\varepsilon_y}^{\varepsilon_d} \sigma(\varepsilon) d\varepsilon \approx \sigma_{pl} (\varepsilon_d - \varepsilon_y) \quad (3.3)$$

Lastly, the efficiency of the sacrificial solution  $e$ , is a function of the ratio between the transmitted and applied impulses,  $i_s^t$  and  $i_r$ , respectively:

$$e = 1 - \frac{i_s^t}{i_r} \quad (3.4)$$

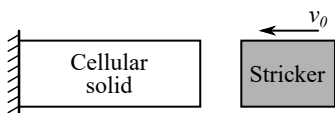
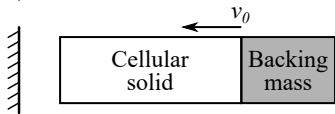
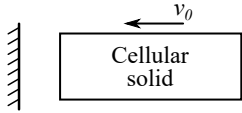
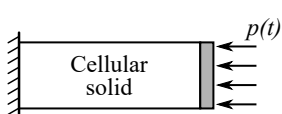
Several experimental set-ups have been used by the scientific community to determine the dynamic compressive behaviour of cellular solids. Table 3.4 depicts the experimental set-ups used to study the compressive behaviour of cellular solids, which may be divided into two categories: impact and blast load set-ups. The former is characterised by the use of a pressure bar, depicted as rigid in the referred table, on which a strain gage is placed. Furthermore, as shown in Table 3.4, stationary, reverse or modified Taylor impacts may be distinguished according to the initial conditions of the test. On the stationary, or forward impact, the sample is supported by the pressure bar, while a striker impacts the sample with an initial velocity (controlled by the test apparatus). Alternatively, on the reverse, or direct impact, both the sample and the backing mass are imparted into the pressure bar with an initial velocity. The modified Taylor impact does not resort to a backing mass. The blast load set-ups are commonly used to test sacrificial cladding solutions and use an explosive charge to impart an impulse to the front plate, which will compress the crushable core.

### 3.5.2.2 Cellular materials

Aluminium foam has been one of the first cellular materials to be considered for blast mitigation. This material is lightweight, with excellent energy absorbing characteristics resulting from its almost perfectly plastic compressive behaviour.

Hanssen and team [51] performed a set of full-scale tests using aluminium foam as the crushable core of a sacrificial cladding solution to evaluate its blast mitigation capabilities. Since the behaviour of both the aluminium foam claddings and the resulting structural response was of interest, the pendulum test set-up illustrated in Figure 3.5(a) was chosen. The effect of fitting aluminium foams with various densities, in combination

Table 3.4: Summary of experimental set-up to evaluate the dynamic compressive behaviour of cellular solids

Schematic representation of experimental set-up	Description	Application examples
	Stationary impact	[6, 33, 52, 53, 63, 65, 76, 99, 148, 179, 185, 187]
	Reverse impact	[6, 33, 52, 65, 76, 99, 137, 149, 163–165, 185, 187]
	Modified Taylor impact	[63, 84, 99, 129, 186]
	Blast load	[2, 29, 51, 53, 64, 73, 74, 79, 87, 88, 99, 120, 122, 170, 175, 180, 183, 189]

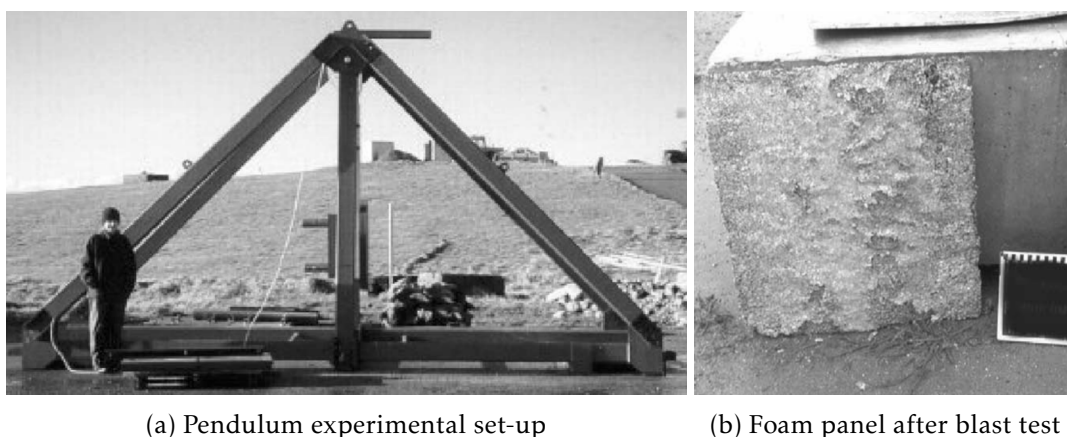


Figure 3.5: Full-scale tests using aluminium foam as the crushable core of a sacrificial cladding solution [51]

with the use of a front panel, was assessed by recording and comparing the maximum swing attained by the pendulum during each blast test. These values are directly related to the corresponding transferred energy and impulse, which can be, therefore, indirectly obtained. PE4 charges of 1 and 2.5 kg were detonated at a distance of 0.5 m, maintained constant throughout the reported experimental campaign. The foam panels had an area of approximately  $0.7 \times 0.7 \text{ m}^2$ , whereas their thickness was 60 and 70 mm with and without a front panel, respectively. Additionally, two different foam densities, approximately  $0.15$  and  $0.35 \text{ kg/m}^3$ , were considered. Figure 3.5(b) shows an aluminium foam panel after the blast test. As a result of the addition of the front plate, no severe fragmentation can be observed.

Analysing the obtained results, the authors verified an increase in the amount of energy and impulse transferred to the pendulum when the aluminium foam was used. This result was not expected by the authors, since it was assumed that the use of sacrificial cladding would lower the energy transferred to the pendulum as a result of the aluminium foam's plastic deformation. Additionally, Hassen and co-workers [51] concluded, from numerical simulation, that the contact stress at the distal end of the aluminium foam is lower than the one observed when no protection solution is used. Nonetheless, as a result of momentum conservation, the duration of the transferred load is proportionally increased to the reduction in contact stress. Therefore, taking into account that the global response of the pendulum does not vary with the shape of the transferred impulse, the authors state that the global response of an impulsively loaded structure may not be reduced through the use of a sacrificial cladding solution. Alternatively, Langdon and team [74] refer that a large crushable core thickness is required to absorb the energy resulting from high pressure pulses, since the magnitude of the transmitted stresses due to the densification of the foam (insufficient thickness) may be larger than the magnitude of the blast load.

The use of open and closed cell polyurethane (PU) foam as the crushable core of a

sacrificial cladding was evaluated by Ousji and team [120, 121]. An explosive driven shock tube was used by the authors to generate a planar blast load at its end. Two different experimental campaigns were performed and reported in the literature. Firstly, the blast load was imparted on the sacrificial cladding fixed to a rigid structure, in order to examine the stress transmitted by the crushable core [120]. Secondly, the effectiveness of the proposed sacrificial cladding, when applied to a small-scale simply supported steel beam, was verified [121]. Both the effects of the PU properties (plateau stress and thickness) and the front plate's mass were investigated in terms of the transmitted stress and the structural deflection. The authors used PU densities of 30, 35, 50 kg/m<sup>3</sup>, while considering front plate masses between 86 and 497 g.

Analysing the results depicted in Figure 3.6, one may conclude that the thickness of the low density foam greatly influences the profile of the transmitted pressure and the maximum and residual displacements of the simply supported steel beam. The transmitted pressure-time histories shown in Figure 3.6(a) reveal that, if the thickness of the foam is not sufficient to guarantee that no densification will take place, a sudden increase of stress occurs (that may exceed the reflected overpressure of the applied blast load). On the contrary, if it surpasses the minimum requirement, an almost constant plateau stress was observed [120]. This conclusions are further evidenced when the beam's mid-span deflection without a sacrificial cladding is compared with the ones obtained while using a crushable core of various thickness, as illustrated in Figure 3.6(b). When a PU (30 kg/m<sup>3</sup> density) foam with a thickness of 50 mm is used as the crushable core, it becomes fully compressed and the maximum deflection of the beam is only reduced by 6% (inside the experimental standard deviation). Contrarily, when the foam does not reach the densification strain (150 mm thickness) a 32.5% reduction of the maximum displacement was reported by the authors.

Ousji and co-workers [121] state that, in order to achieve a meaningful protection, the properties of both the crushable core and the front plate should be adapted to that

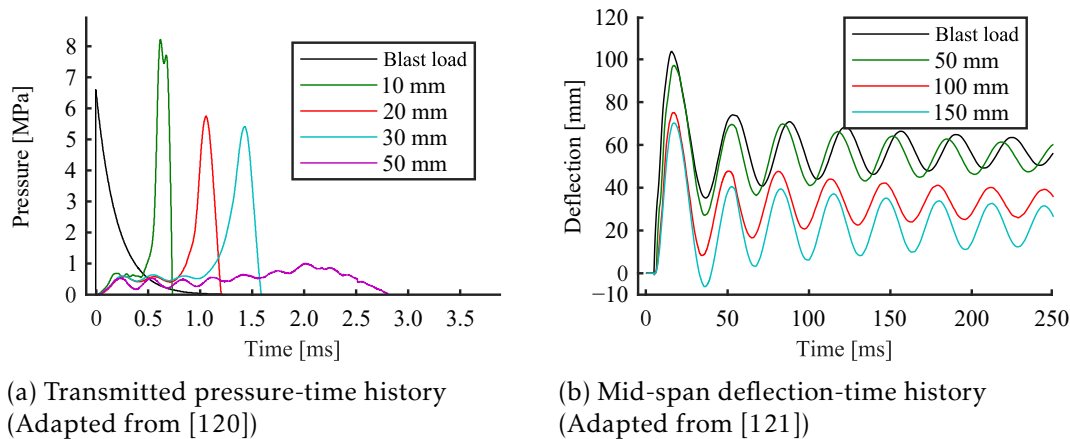


Figure 3.6: Influence of PU thickness (Adapted from [120, 121])

of the main structure. Firstly, the plateau stress of the crushable core should be comparable to the maximum resistance of the structure. Secondly, the front plate's material should be both rigid and lightweight. Thirdly, the minimum foam thickness must be computed according to the previously computed properties of the foam, front plate and the considered blast scenario.

As reviewed, the blast response of cellular materials with uniform density is considered to be well understood by the scientific community and provide a useful protective measure against blast loading [29, 51, 53, 87, 159, 180, 185, 187]. Nonetheless, the concept of graded cellular materials, both in a layer-by-layer and a continuous configuration, has lately been of increasing interest. The most commonly researched arrangements of density may be classified as positive and negative, in which the density increases as we approach the distal and proximal end of the cellular material, respectively. Shen and team [148] and Karagiozova and Alves [63] focused on the relative density's influence on the impact response of a layer-by-layer graded cellular material by means of analytical and numerical analyses. It should be noted that both studies resorted to solid elements, in combination with the "crushable foam" material model available in ABAQUS/EXPLICIT, to verify the proposed analytical models and obtain further insights on the behaviour of the graded cellular material. The authors verified that placing the cellular solid with the lowest relative density near to the stationary end leads to lower transmitted stresses, as long as the kinetic energy is fully absorbed within the primary compaction wave and no reflection wave, resulting from the rigid boundary, is formed [63]. Similarly, Shen and co-authors [148] verified that if the transmission of stress to the protected structure is of concern, the strongest material should be placed at the impinged end. Additionally, the authors state that this solution will result in a small sacrifice in terms of energy absorption.

More recently, the one-dimensional blast response of continuous-density graded cellular materials has been examined, theoretically and numerically [73, 80]. The two-dimensional (Liang et al. [80]) and three-dimensional (Lan et al. [73]) Voronoi technique, see Figure 3.7(a), was used by the authors to simulate the cellular material with uniform and graded density. It should be noted that both studies achieved the variation of relative density by means of cell size.

Lan and team [73] verified that a cellular material with positive density gradient, on which the relative density increases as one approaches the front plate, yields the highest transferred impulse and energy absorption, while the opposite occurs for a negative density gradient, as illustrated in Figure 3.7(b). Similar findings were reported by Liang and co-workers [80].

Therefore, one might conclude that, when the protection of structural elements is the main interest, the ideal sacrificial cladding solution presents a high energy absorption and a low transmitted impulse. However, according to the previously presented results related to blast mitigation, attaining a large energy absorption and a low transmitted impulse simultaneously is not possible when resorting to cellular materials.

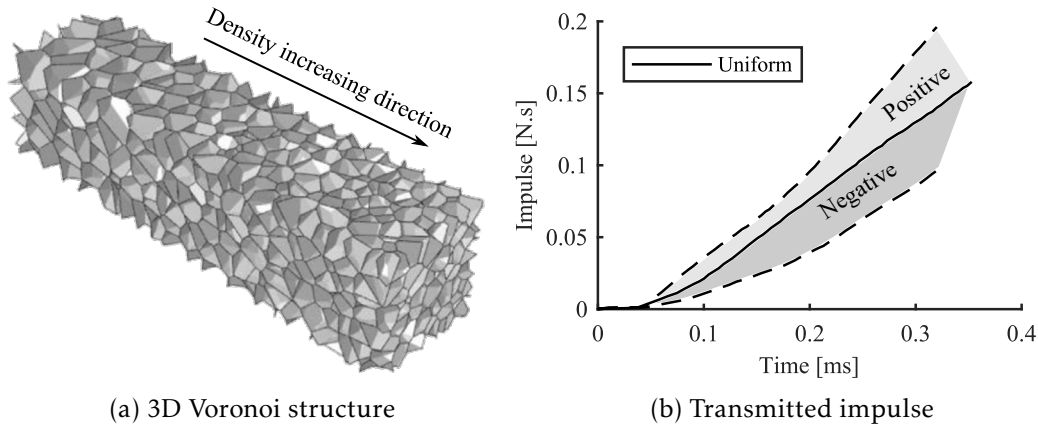


Figure 3.7: Simulation of continuous-density graded cellular materials (Adapted from [73])

### 3.5.2.3 Cellular structures

Cellular structures have also been considered as viable crushable core. Traditionally, these solutions are composed by tubular cells, which are stacked either axially or laterally between two face plates, and provide a reasonably constant crushing force and large energy absorption capabilities [86, 170].

A sacrificial cladding solution composed by layered thin mild steel plates was proposed by Guruprasad and Mukherjee [47, 48]. The cellular structure is constituted by three sacrificial layers, each with a given number of identical cells (see Figure 3.8), and was carefully designed to ensure the sequential progressive collapse of each layer. Firstly, the blast load impinges an initial velocity to the cover plate, which leads to the crushing of the outermost layer. Subsequently, when the first layer attains a “rigid” behaviour compared to the undeformed layers, compression of the second layer will take place until it also becomes “rigid”. Lastly, the third layer has a similar behaviour. It should be noted that if the last layer does not become “fully collapsed” the used of this sacrificial cladding successfully reduces the force transferred to the protected structure.

The referred authors verified the nonlinear behaviour of the proposed solutions when subjected to a blast load, by means of an experimental campaign, in combination with analytical and finite element models. A very good agreement was found between the used methods, whose results imply that the sacrificial layer effectively “isolates” the protected structure and, when not fully crushed, transfers a nearly constant force.

The blast mitigation capabilities of thin-walled tube structures, compressed both axially and laterally, has also been investigated. The tubes are commonly materialised with steel, aluminium or composite materials [170, 175, 182, 183, 189].

Theobald and Nurick [170] resorted to the four cable pendulum illustrated in Figure 3.9 to investigate the impulse transferred by crushable cores with five and nine tubes (see Figure 3.10(a)). This experimental set-up allows the computation of the transferred

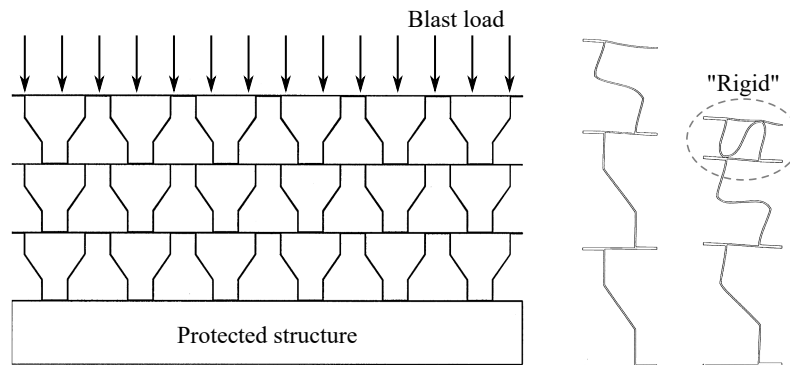


Figure 3.8: Guruprasad and Mukherjee's [47, 48] sacrificial cladding solution

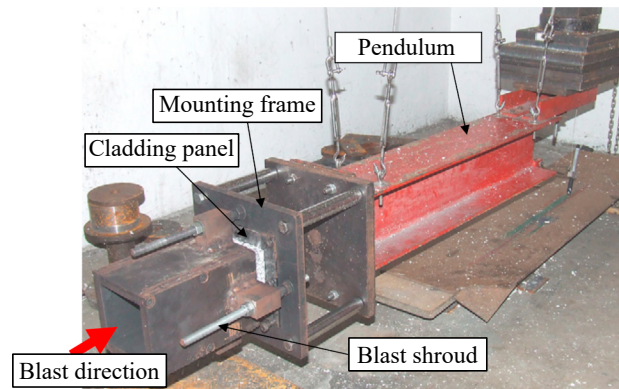


Figure 3.9: Four cable pendulum set-up [74, 170, 183]

impulse by means of the horizontal displacement of the pendulum. The authors considered both annealed mild steel tubes and aluminium alloy extrusions in order to verify the influence of the material's fracture strain on the resulting impulse, since both materials possess a similar yield stress but a significantly different fracture strain. Figure 3.10(b) shows an aluminium sacrificial cladding which was subjected to a blast load. According to the authors, despite the use of a hemispherical trigger indentation, buckling was not initiated in all the tubes and irregular buckling modes were observed in all the experimental tests where the maximum compression is well below the height of the tubes. Therefore, an optimization of the trigger is paramount to obtain localised buckling modes, resulting crush repeatability and increased impulse capacity. As illustrated in Figure 3.10(b), when the tubes are close to or become fully compressed, symmetric buckling modes are observed in nearly all tubes. Consequently, the authors state that, although buckling is initiated at different tube locations, progressive, symmetric collapse of the core may occur. An additional parametric study, performed by means of numerical analysis, allowed Theobald and Nurick to conclude that tubes which suffer compaction instead of buckling transmit forces significantly larger than the peak force observed when buckling is initiated.



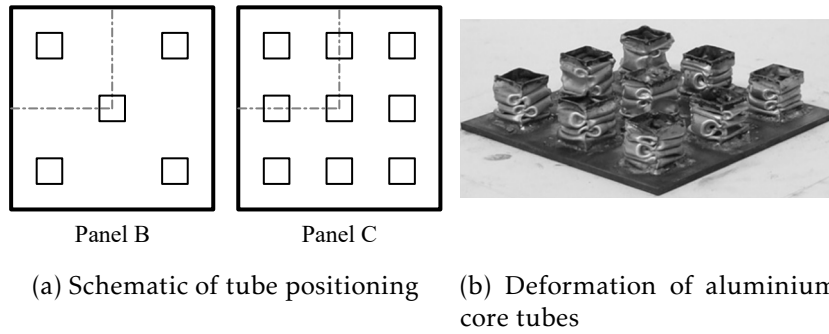


Figure 3.10: Experimental study of impulse transferred by crushable tube cores (Adapted from [170])

Alternatively, Yuen and co-workers [183] used the previously referred four cable pendulum to evaluate the impulse transferred by laterally crushed empty or foam-filled thin-walled circular tubes. Similarly to Theobald and Nurick [170], both aluminium and mild steel tubes were subjected to a blast load, which resulted from explosive charges ranging from 6 to 50 g at a distance of 200 mm propagated throughout a square tube, while the tubes were filled with several cellular foams (self-raising polyurethane, expanded polystyrene and cross-linked polyethylene). The obtained results shown that, when the distance between the circular tubes is smaller than a quarter of their diameter, a higher force is required to overcome the interaction between them and, consequently, a larger absorption capacity and transferred impulse was obtained. The inclusion of foam in the interior of the tubes did not seem to affect their deformation mode and, depending on the plateau stress of the foam, increased the absorption capacity of the sacrificial cladding layer.

A nested tube system, consisting of three circular tubes, was proposed by Yu and team [182] (see Figure 3.11(a)). A quasi-static experimental campaign was performed in order to compare its performance with that of a single tube system and to validate the developed numerical models. As illustrated in Figure 3.11(b), the triple tube (TT) system successfully transforms the applied blast load (a reduction of approximately 40% for the peak force was attained).

The dynamic behaviour of composite tubes has also been evaluated and presented to the scientific community [175, 189]. Van Paepegem and co-workers [175] studied a sacrificial cladding structure, composed of glass/polyester tubes, under blast loads. Firstly, the compaction of a single tube was obtained through a small-scale air blast test set-up (see Figure 3.12), which uses a spherical explosive charge (20–50 g C4) fixed above the skin plate that transmits the blast load to a single composite tube. It should be noted that a circular side cover, whose diameter was significantly larger than that of the composite tube, was used to prevent the blast wave from acting sideways on the composite tube during the deformation process. The small-scale air blast tests, in combination with quasi-static and impact tests, allowed the referred authors to conclude that, when

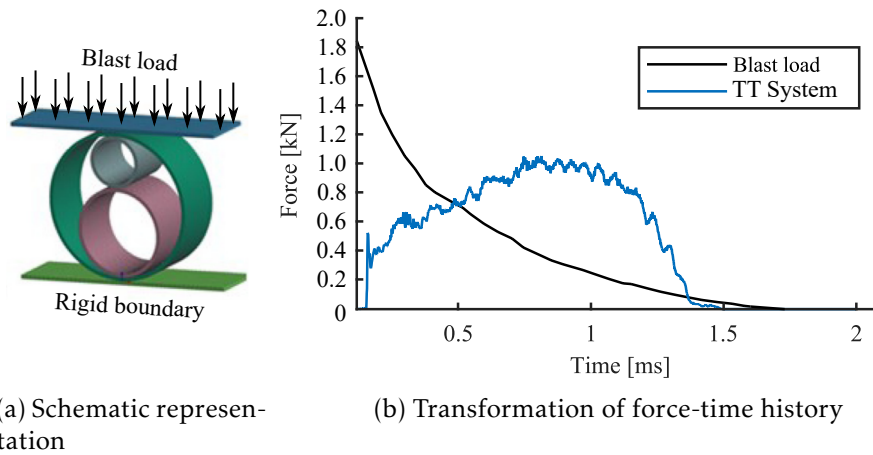


Figure 3.11: Triple tube (TT) system for blast mitigation (Adapted from [182])

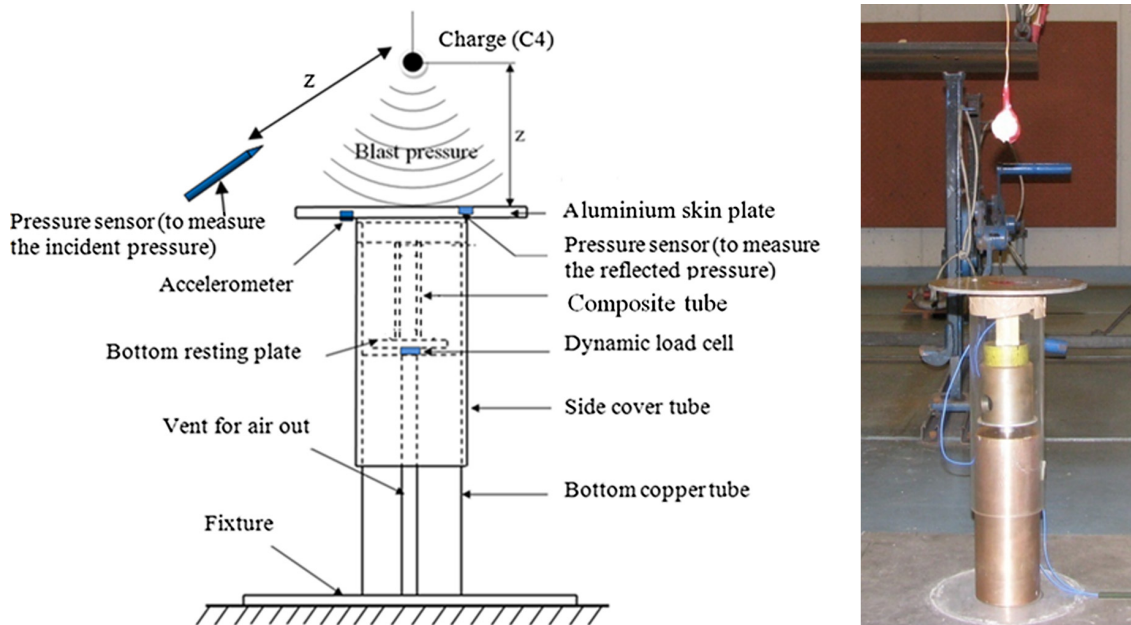


Figure 3.12: Schematic view and photograph of small-scale air blast test set-up [175]

catastrophic failure modes are avoided through the use of low density polyurethane foam, the deformation patterns of the considered composite tubes remained the same, namely the commonly observed brittle failure modes, such as delamination, axial cracks, lamina bending and fibre fracturing. Additionally, no strain rate sensitivity was reported by the authors in the full range of loading, which may result from the unidirectional fibre reinforcement of the composite tube.

Subsequently, a blast test was conducted by Van Paepegem and team [175] to examine the blast mitigation capabilities of an array of composite tubes, in combination with a sandwich composite front plate. The reported blast tests resorted to two segments of concrete sewage pipes in order to attain a planar blast load at the opposite end, as

depicted in Figure 3.13. Two different configurations were considered by the authors, which used 25 and 37 composite tubes. An average peak crush load of 86.5 and 103.1 kN, respectively, was reported by the authors. These transferred loads are lower than the ones observed for the reference case (no composite tubes) and result from the progressive crushing of the composite tubes. However, the authors state that local and global bending of the front and back plates, respectively, was noticed. The latter leads to a reduction of the registered transferred impulse and, consequently, a difference between the applied and transferred impulse. In order to avoid this problem, the authors refer that a plate with higher stiffness, while maintaining a low mass, should be used.

Palanivelu and co-workers [122] examined the dynamic crushing behaviour of a single recyclable metal beverage can using the small-scale air blast test set-up shown in Figure 3.12. However, according to the authors, repeatability seems to have not been attained during the experimental campaign, possibly due to initial geometry imperfections and insufficient applied impulse, which results from clearing problems around the top plate. Figure 3.14 clearly illustrates the influence of clearing and ground reflection on the obtained results.

To overcome the above limitations, Ousji [118] resorted to an explosive driven shock tube (EDST) to dynamically crush a single recyclable metal beverage can (MBC) fixed to a rigid and a flexible structure. The blast load, characterised by a 13 MPa and a 1487 Pa·s reflected peak overpressure and impulse, respectively, results from the detonation of 10 g of C4 at a distance of 30 mm from the entrance of the EDST. The initial velocity of the front plate is controlled by its mass, whose value was set by the author at 147, 339 and 497 g. The author verified the development of a nonsymmetric deformation pattern (diamond mode) on the cylindrical portion of the metal beverage can, as a result of its geometry. This deformation of the cylindrical body was found to be preceded by the collapse of the can's top part into the cylindrical body until the contact between the front plate and the upper circumference was attained, as depicted in Figure 3.15. Contrarily to Palanivelu

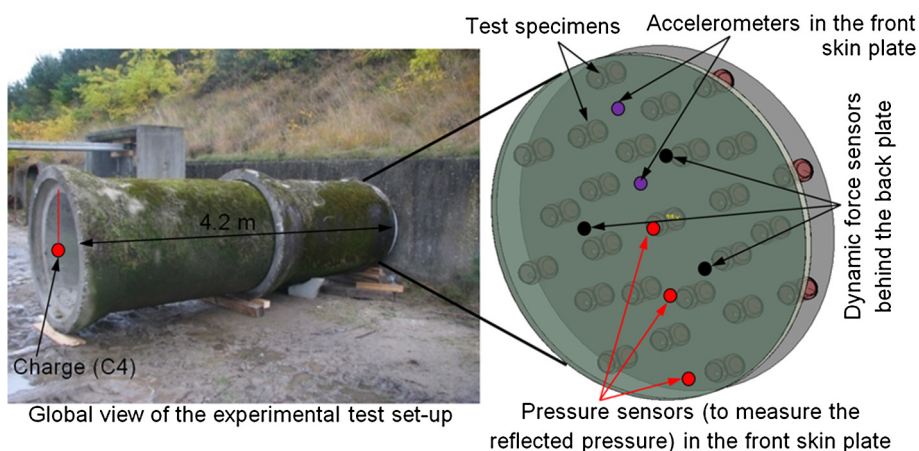


Figure 3.13: Schematic representation of the experimental set-up for the sacrificial cladding [175]

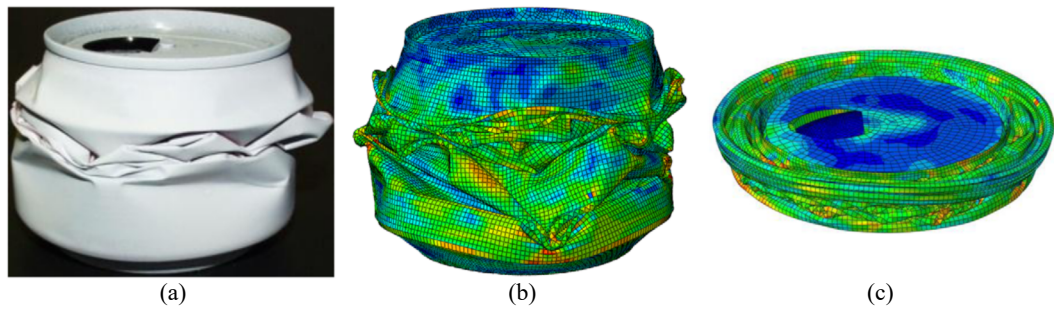


Figure 3.14: Deformation patterns of empty recyclable beverage cans: (a) Experimental; (b) Numerical (with clearing and ground reflection); (c) Numerical (without clearing and ground reflection) (Adapted from [122])

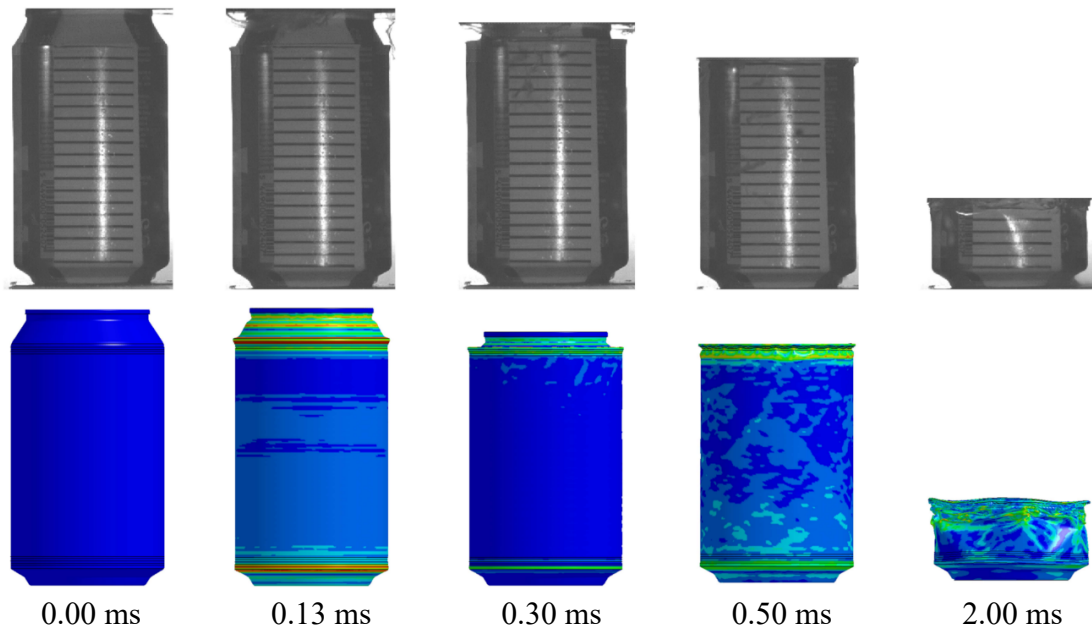


Figure 3.15: Development of deformation patterns of a metal beverage can (Adapted from [118])

et al. [122], Ousji [118] was able to observe a controlled, progressive and repeatable deformation pattern. Nonetheless, the mean transmitted load is clearly influenced by the loading rate, which, according to the author, arises from the strain hardening effects of the MBC's materials and the air resistance inside it.

As previously reviewed, Ousji [118] evaluated the effectiveness of sacrificial claddings that use an MBC as their crushable core by means of an experimental campaign which resorts to a simply-supported flexible steel beam. The applied blast load is similar to that used when a rigid structure was considered by the author and, when no sacrificial cladding is used, a maximum displacement of approximately 44 mm was recorded. Once again, three different front plate masses (147, 339 and 497 g) were considered, yielding maximum displacements of approximately 43, 28 and 27 mm, respectively. The use of the lightest front plate results in a faster crushing of the MBC, which leads to its

complete compaction and subsequent impact of the front plate on the flexible structure. Consequently, no significant reduction of maximum displacement was observed by the author. On the other hand, when one resorts to a heavier front plate (339 and 497 g), only partial MBC compaction was observed and a significant reduction in maximum displacement is attained. It should be noted that the authors state that a partial and nonsymmetric collapse is observed when the 497 g front plate is used. This undesirable phenomenon, which results from the low compaction velocity, may affect the efficiency of the crushable material and reduce the expected absorption capacity.

Recently, Li and team [79] investigated the performance of sacrificial claddings with square dome-shape kirigami (SDK) structures as the crushable core. The authors manufactured a sample of SDK core folded from a pre-cut aluminium sheet, see Figure 3.16, and subjected it to a quasi-static compression test. The unit cell of the SDK structure is depicted in Figure 3.16(a), while the original aluminium sheet is presented in Figure 3.16(b) with the corresponding crease pattern. Analysing the crease pattern, one may verify that the inclined sidewalls are connected on both sides by means of triangular connections that are folded inwards, leaving a 0.5 mm gap near the corners of resulting unit cell, clearly visible in Figure 3.16(a). Due to the hand folding of the specimens, the authors state that fabrication inaccuracies are inevitable and, as presented in Figure 3.16(c), the sidewalls of the specimen are slightly bent and a minor gap may be observed near the bottom edges. Nonetheless, they refer that machine stamping may be developed for this specific application, which would eliminate the inaccuracy and reduce the production time.

A numerical model of the SDK sample is developed and validated under quasi-static compression. Subsequently, the authors used this validated numerical model to simulate the proposed sacrificial cladding response under several blast scenarios. Comparing the obtained results with those of aluminium foams, Li and co-workers [79] concluded that, for the same relative density, a higher plateau stress is recorded when SDK structures are used. Additionally, comparing the applied blast load with the transmitted load, a reduction larger than 70% for the peak load and a relatively uniform crushing resistance were verified. Lastly, the authors refer that the collapse of the SDK structure may be

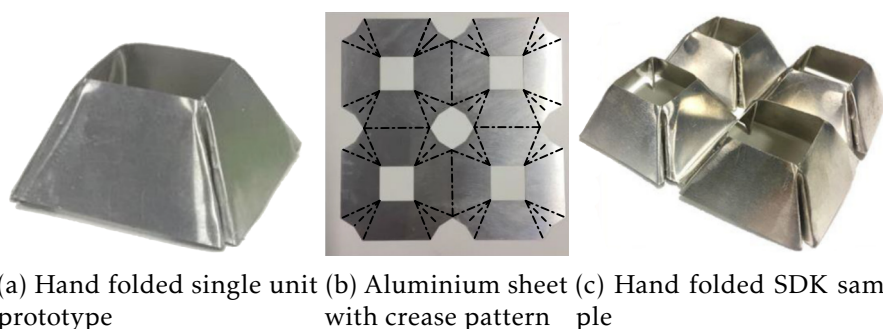


Figure 3.16: Sacrificial cladding with SDK crushable core (Adapted from [79])

classified as uniform and that it is similar to the one exhibited by the aluminium foam.

### 3.5.2.4 Additively manufactured solutions

Additive manufacturing (AM), also referred to as three-dimensional (3D) printing, is recently becoming a viable manufacturing process as a result of the numerous advantages over traditional subtractive manufacturing techniques when complex geometries are required. Despite covering a large range of techniques, the currently available AM processes build parts in a similar fashion: the base material is deposited, fused, or cured in successive two-dimensional layers that, ultimately, form a three-dimensional object. Amongst the available technologies, fused deposition modelling (FDM), which is based on extrusion additive manufacturing, is usually used in consumer-level 3D printers working with polymer composites [30]. As a result of the geometrical freedom, the use of 3D printing as a manufacturing technique for energy absorption structures has grown in interest in recent years, since it allows tailored properties.

One example of such novel application is the manufacturing of lattice structures, whose properties may be tailored to a specific application. These structures may be defined as the tessellation of a unit cell, usually composed by struts, as illustrated Figure 3.17.

McKown and team [98] resorted to the selective laser melting (SLM) technique to manufacture a range of metallic lattice structures, based on  $[\pm 45^\circ]$  and  $[0^\circ, \pm 45^\circ]$  unit cell topologies (see Figures 3.17(a) and 3.17(b)). Six lattice structures, materialised with stainless steel 316L, were investigated by the authors under quasi-static and blast loading conditions. The outer boundary of the tested samples was a cube with an edge of 20 mm. According to the authors, as a result of the vertical pillars, the  $[0^\circ, \pm 45^\circ]$  unit cell possesses a higher density when compared with its  $[\pm 45^\circ]$  counterpart. The influence of the lattice density on the mechanical properties was evaluated through the variation of the edge length of the unit cell, i.e edge lengths of 2.5 and 1.5 mm were used for the low and high density structures, respectively. Consequently, lattice structures with a relative density between 4.6 and 11.6% were investigated by the authors.

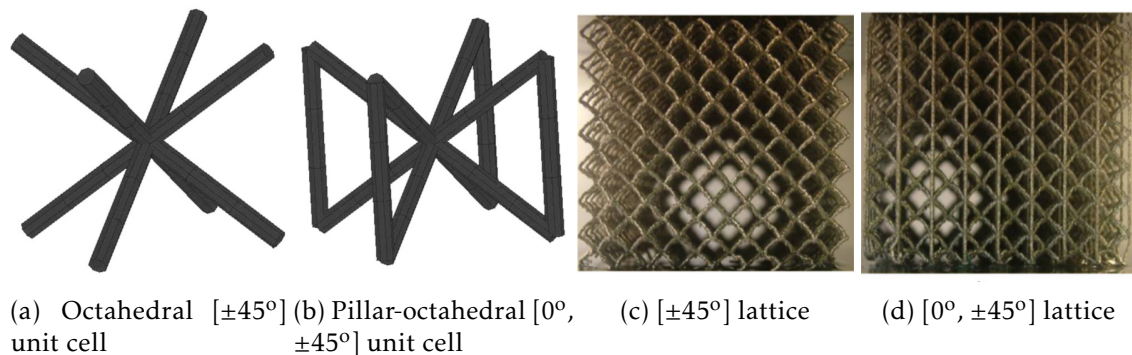


Figure 3.17: Metallic lattice structure (Adapted from [98])

The experimental blast campaign was achieved by means of a ballistic pendulum (see Figure 3.9). This experimental campaign was divided into two sets, on which the mass of the cylindrical front plate was maintained constant with values of 86.2 and 82.6 g. A PE4 20 mm disc, whose thickness was varied to apply different impulses, was used to accelerate the front plate uniformly and, subsequently, crush the lattice structure. A total of 25 blast tests were performed by the authors on the considered lattice structures.

Figure 3.18 presents photographs of specimens based on  $0^\circ$  and  $\pm 45^\circ$  pillar-octahedral unit cell after being subjected to a blast load. It should be noted that the asymmetry verified on some of the depicted samples was a result of the inherent difficulty in imparting a perfect incident blast wave on the specimen. Nonetheless, the authors refer that discernible crush behaviour and failure modes are still verified on the four considered lattices. The crush percentage shown in the referred figure was computed as the average of the four edge lengths after testing. Observing Figure 3.18, it is possible to verify that the high density lattice failure resulted from the propagation of a shear band at an angle of approximately  $45^\circ$  with respect to the loading condition. These bands initiated due to the buckling of the vertical pillars at the top edge of the samples. Despite the high crush percentage and resulting visualisation difficulties, the low density lattice structure also presented evidence of buckling on the vertical pillars. Alternatively, the octahedral

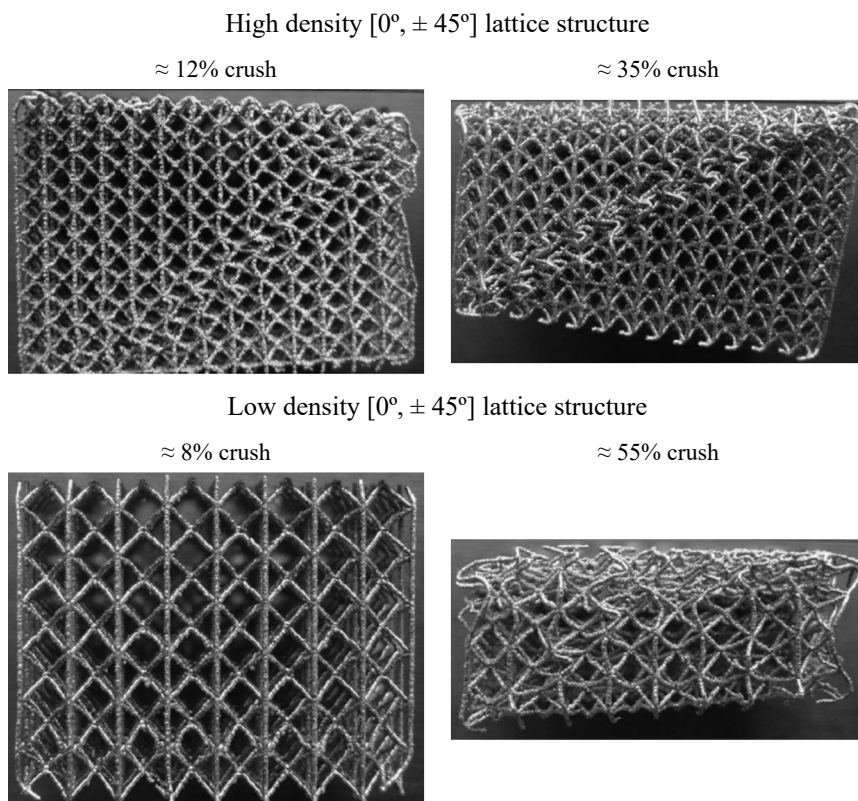


Figure 3.18: Blast-loaded specimens based on the [ $0^\circ, \pm 45^\circ$ ] pillar-octahedral unit cell (Adapted from [98])

lattices, not reported in this study (see Figure 13 in McKown et al. [98]), presented a global, stable and progressive crushing behaviour with no shear band formation. When comparing both structures, one may conclude that the presence of the vertical pillars allows, for a given crush percentage, the application of a higher impulse to the lattice structure. McKown and co-workers [98] verified that the failure modes observed during the experimental campaign are consistent with those verified by means of quasi-static compression. Lastly, due to the high strain rates involved in blast testing, the response of the lattice structures, namely the yield strength, doubled in value as a result of strain rate sensitivity of the base material.

The impact resistance of additively manufactured metallic hybrid lattice materials was investigated by Harris and team [54]. The same manufacturing technique was used by the authors. Nonetheless, the philosophy behind the proposed lattice structure differs from that presented by McKown and team [98]. The hybrid lattice structure considered by Harris and co-workers is based on a square honeycomb. Subsequently, as depicted in Figure 3.19, the solid walls of the square honeycomb are replaced with a planar lattice truss, whose struts possess a circular cross section. The diameter of this struts was chosen to obtain a relative density equal to that of the square honeycomb (approximately 20%). The specimens fit inside a cylinder with a diameter and height of 20 and 10 mm, respectively. The cell size of both the square honeycomb (SHC) and the lattice-walled square honeycomb (LW-SHC) was 2 mm, while the fine lattice-walled square honeycomb (FLW-SHC) cell size and strut diameter were reduced by a factor of two, resulting in a cell size of 1 mm.

Harris and team [54] subjected a single specimen of each topology to out-of-plane quasi-static compression with a strain rate of  $10^{-3} \text{ s}^{-1}$ . A normalised stress  $\bar{\sigma}$ , defined as ratio between the recorded stress  $\sigma$  and  $\bar{\rho}\sigma_y$ , where  $\sigma_y$  is the yield stress of the cell wall's base material, was used by the authors to analyse the quasi-static compressive behaviour of the cellular structures. Figure 3.20 depicts the recorded normalised stress as a function of strain for all the considered structures. Observing the referred figure, one might verify that the SHC exhibits a nearly constant plateau stress, whose value is close to unity, which

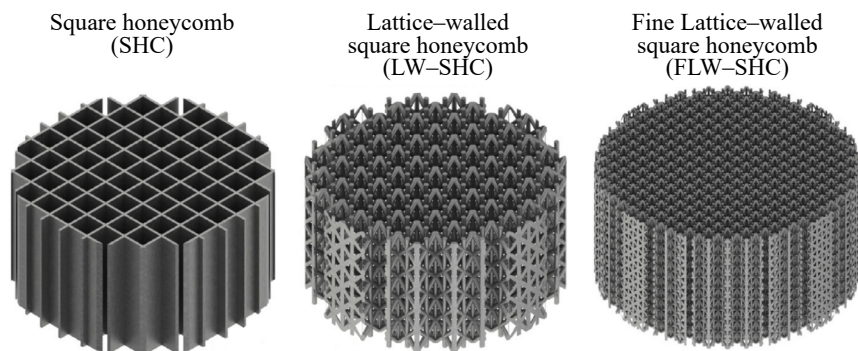


Figure 3.19: Development of hybrid lattice structure based on square honeycomb (Adapted from [54])



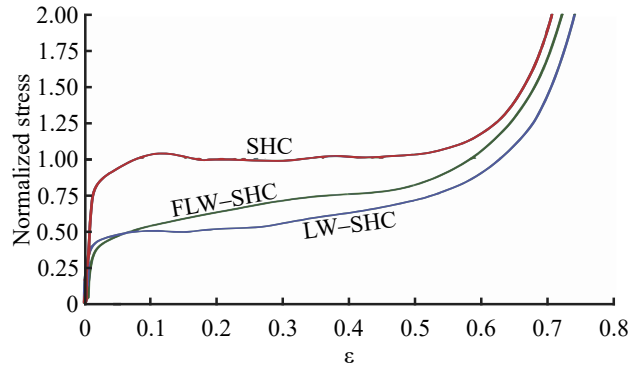


Figure 3.20: Normalised quasi-static compressive stress-strain response of hybrid lattice structure (Adapted from [54])

corresponds to  $\bar{\rho}\sigma_y$ . The authors consider that the negligible softening of the honeycomb compressive response may be a consequence of the considered relative density and cell aspect ratio, which leads to limited buckling of the walls. Similar normalised strengths were obtained for both lattice structures. Nonetheless, the FLW-SHC yields a higher degree of strengthening, when compared with the LW-SHC, which, according to [54], may be attributed to the lower porosity of the cell walls resulting from poor geometry resolution during the manufacturing process.

Additionally, the authors subjected the cellular specimens to both stationary and reverse impacts by means of a Hopkinson bar apparatus. Impact velocities of 50, 100 and 150 m/s, which correspond to strain rates of  $5 \times 10^3$ ,  $10 \times 10^3$  and  $15 \times 10^3$  s<sup>-1</sup>, respectively, were considered to verify the influence of strain rate on both the peak and plateau stress of the dynamic stress-strain response. Analysing the obtained results, the authors concluded that, when compared with both lattice-walled square honeycombs, the SHC exhibits the larger energy absorption up to the densification strain. Nonetheless, the peak response of this solution is more sensitive to the impact velocity than the lattice-walled square honeycombs, as a result of the stabilising effect of lateral inertia during the initial stages of compression, which leads to an increase of stress, namely at the impacted face. Considering the ratio between the energy absorption (up to densification) and the maximum stress as a metric of efficiency, the authors found that, although the SHC presents the highest peak stresses when subjected to impacts of 50 and 150 m/s, it yields a greater efficiency when compared with the other considered solutions. However, for the middle impact velocity (100 m/s), in which dynamic buckling effects are present but the effects of wave propagation are not significant, the LW-SHC has a greater efficiency when compared with the other considered solutions. Lastly, the authors concluded that the FLW-SHC, when compared with the other two structures, under-performed as a result of poor rendition of the geometry and excessive material deposition, which increases the relative density but it does not improve the mechanical properties.

The quasi-static compressive response of lattice structures, manufactured through

selective laser sintering (SLS), was investigated and reported in several studies [13, 95]. Taking into account that the smallest feasible strut diameter, imposed by technique limitations, is 0.4 mm, the minimum cell sizes must be an order of magnitude higher than the diameter of the strut (5 to 10 mm). Additionally, since the unsintered powder must be removed after the manufacturing process, only open-celled foams may be replicated resorting to SLS [13].

Brennan-Craddock [13] manufactured five samples in a mixture of 50% virgin/50% recycled PA 2200 material (nylon-12) on a laser sintering machine. The proposed lattice structure, depicted in Figure 3.21(a), is characterised by a straight strut, triangular cross section and fillets between the nodes, which aims to replicate the natural structure of a foam. The quasi-static compressive stress-strain curves are illustrated in Figure 3.21(b) and exhibited the three stage compressive response commonly obtained with foams, i.e. the initial elastic behaviour (A), followed by a plateau region (B), which is limited by an increase in stress due to densification (C).

Maskery and team [95] studied the crushing behaviour of octahedral and pillar-octahedral lattice structures (see Figures 3.17(a) and 3.17(b)), while resorting to the same manufacturing technique and material as the previously referred research team. A uniform 19% relative density was considered by the authors to compute the radius of the cylindrical struts, while different relative densities were assigned to six layers, corresponding to a linear decrease between 26% at the base to 12% at the top of the specimen (19% average relative density), to attain the graded lattice structures illustrated in Figure 3.22. The uniform density specimens were subjected to quasi-static crushing, both in the direction and perpendicular to the pillars, in order to verify the existence of mechanical anisotropic. Alternatively, the graded specimens were only compressed in the direction of the pillars, which allows the comparison between the performance of the uniform and graded structures.

The compressive stress-strain curves obtained by Maskery and co-workers [95] during

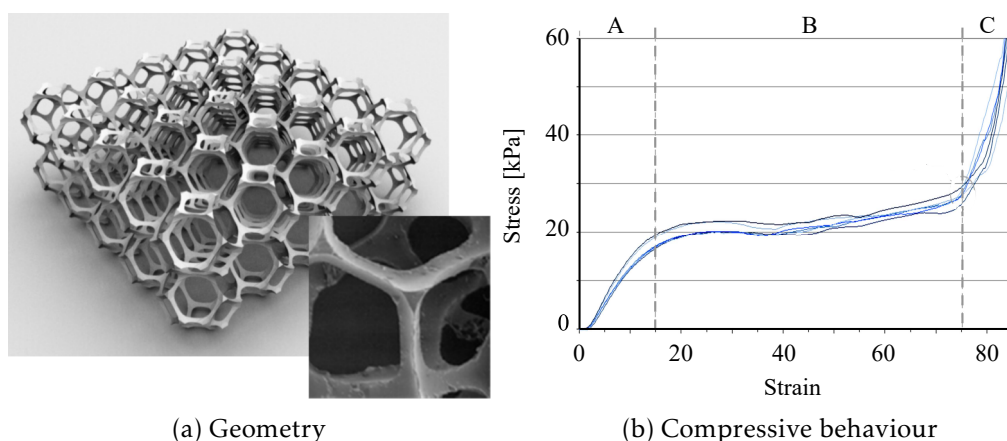


Figure 3.21: Straight strut structure based on an open-celled foam (Adapted from [13])

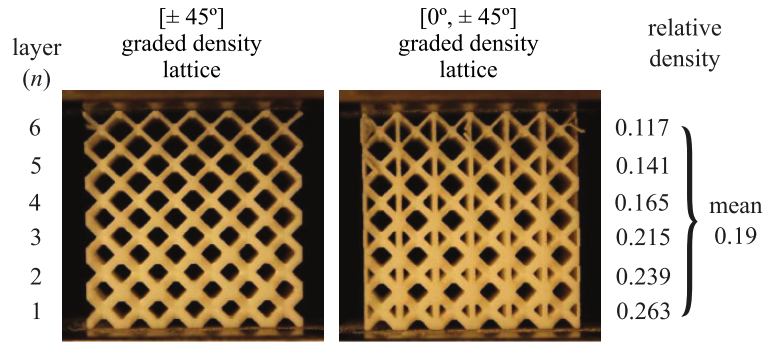


Figure 3.22: Relative densities of graded lattice structures (Adapted from [95])

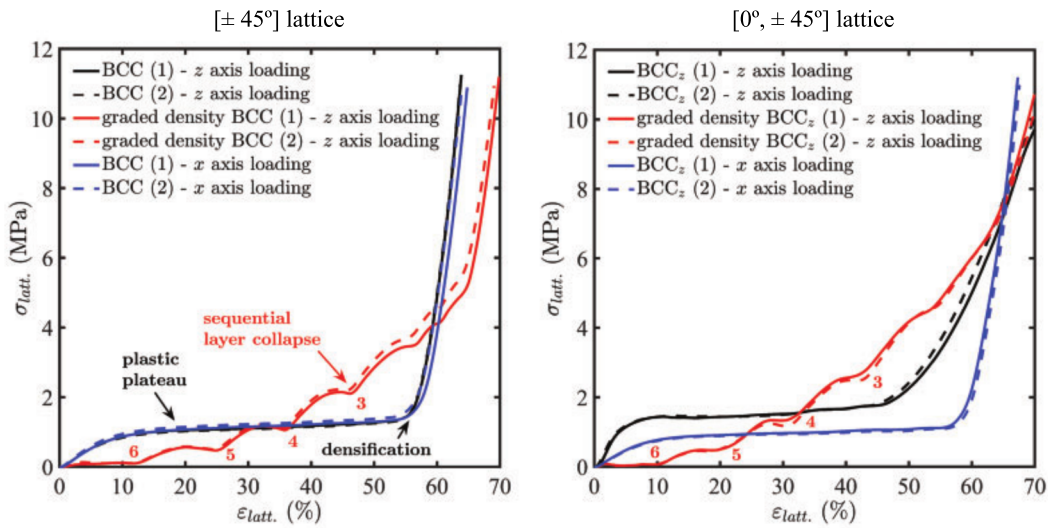


Figure 3.23: Compressive stress–strain curves of the lattice structures (Adapted from [95])

their experimental campaign are given in Figure 3.23. A typical behaviour may be observed on the referred figure for the specimens with a uniform relative density, regardless of the presence of reinforcement pillars. When verifying the influence of these pillars on the mechanical properties of the lattice structure, the authors observed that their presence yields a higher Young’s modulus and plastic collapse stress when compared with the octahedral lattice structure. However, when the compressive load is perpendicular to the reinforcing struts, a significant reduction in both the Young’s modulus and yield strength was obtained. Contrarily, as expected due to its planar symmetry, the direction of the load seems to have little influence on the nonlinear response of the octahedral lattice structure. Additionally, the sequential collapse of the graded density lattice structures’ layers is initiated at the layer with the lowest density, which possesses its own elastic and rather short plastic region, followed by the sequential collapse of the remaining layers with similar behaviour. This sequential process is clearly seen in Figure 3.23, in which the collapse of the layers is identified.

Comparing the quasi-static results obtained by McKown and Maskery, namely the collapsed stress of the octahedral lattice structures with relative densities of 16 and 19%, respectively. One verifies that, as expected, the yield stress of the base material (580 and 55 MPa) has a great influence on the collapse stress of the considered lattice structure, since values of 15 and 0.95 MPa were obtained by the referred authors, respectively.

The dynamic crushing behaviour of a graded lattice cylindrical structure composed by triangular and hexagonal unit cells, when subjected to axial impact loads, was theoretically and numerically studied by Chen and co-workers [19]. Figure 3.24 illustrates the geometrical configurations of the lattice cylindrical shells, when a uniform relative density is considered. Additionally, lattice sandwich cylindrical shells were obtained by means of the inclusion of inner and outer skin plates with constant thickness to the lattice structure. According to the authors, when a triangular configuration is used, the crushing mechanism of the structure is dominated by membrane response, while the hexagonal configuration leads to a response dominated by bending. The uniform relative density specimens were manufactured resorting to a fused deposition modelling (FDM) 3D printer and to acrylonitrile-butadiene-styrene (ABS). Quasi-static compressive tests were used by the authors to validate a numerical model, which was subsequently used to obtain the dynamic crushing behaviour, since a constant crushing velocity is difficult to maintain throughout an entire experimental crushing process [19].

Analysing the numerical results, Chen and team [19] found that the used normalised plastic energy dissipation (see [19] for more details) is directly proportional to the relative density of the triangular lattice cylindrical shell, regardless of the impact velocity. When the hexagonal lattice cylindrical shell is subjected to low velocity crushing, the normalised plastic energy dissipation increased for larger relative densities. However, for high velocity compression, the inverse is true up to a relative density of 6%, after which the relative density seemed to have little influence on the normalised plastic energy dissipation. Figure 3.25 shows the typical deformation modes of the triangular and hexagonal lattice cylindrical shells under low and high velocity crushing. Under low velocity crushing, most of the triangular cells in the same layer did not collapse simultaneously, which

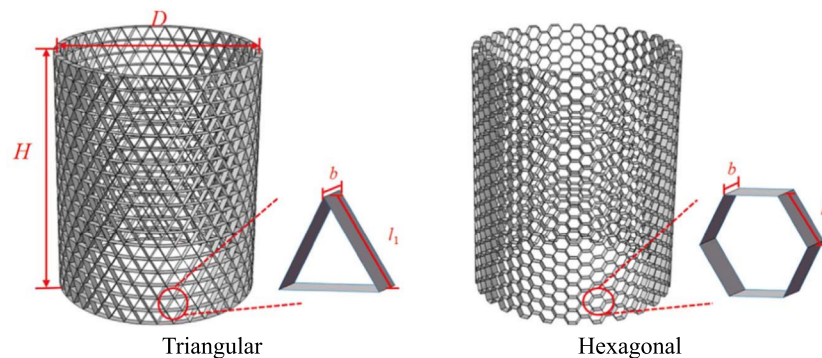


Figure 3.24: Geometrical configuration of lattice cylindrical shells (Adapted from [19])

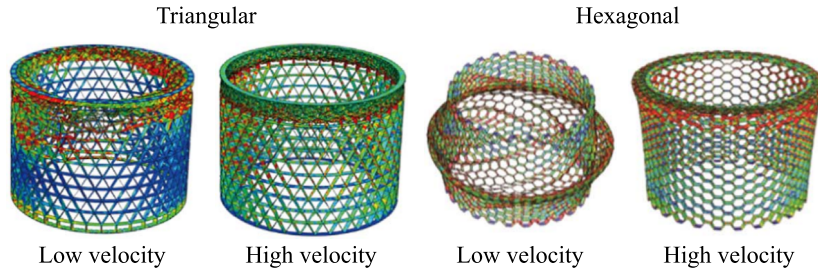


Figure 3.25: Typical deformation modes of lattice cylindrical shells (Adapted from [19])

leads to the appearance of shear bands and overall inward depression. Similarly, a “V” shape shear band appeared in the middle of the hexagonal lattice cylindrical shell and, with the increase of compressive strain, this band becomes a localised deformation region. The crushing of triangular lattice cylindrical shells under high velocity is initiated at the crushing side and, as a result of stress wave’s reflection, the layers close to the clamped side present a localised deformation band. In the case of the hexagonal lattice, the authors state that the deformation mode took the shape of an “I” and the middle of the structure would exhibit a global buckling mode.

The authors concluded that, under low velocity crushing, the energy absorption capabilities of density gradient lattice cylindrical shells surpassed that of lattice cylindrical shells with an uniform relative density when subjected to strains above 60%. Additionally, in high velocity crushing of both triangular and hexagonal lattice cylindrical shells, the energy absorption was enhanced or decreased if the density gradient was negative or positive, respectively. Lastly, Chen and co-workers [19] state that the main advantage of the negative density gradient is the significant reduction in peak crushing force, namely for triangular lattice sandwich cylindrical shells under low velocity crushing, while the hexagonal lattice structure’s peak crushing force is reduced in low and high impact velocities.

The in-plane response of 3D printed honeycomb structures, based on a single hexagonal cell, was examined by Bates and team [7] and Chen and co-workers [20]. The former resorted to the fused deposition modelling technique, in combination with two grades of Thermoplastic Polyurethane (TPU) filament which varied in stiffness, while the latter used a PolyJet 3D printer to manufacture the specimens from VeroWhite resin. Quasi-static compressive tests were used in both studies to evaluate the energy absorption capabilities of the 3D printed structures.

Bates and team [7] aimed to verify the durability of recoverable energy absorbing structures, namely testing their ability to withstand multiple compressions up to densification ( $\epsilon_{max} = 0.7$ ). Therefore, the authors subjected each unconstrained sample to 5 loading and unloading cycles at constant strain rates of 0.03, 0.095 and  $0.3 \text{ s}^{-1}$ . As depicted in Figure 3.26, the hexagonal unit cell was assembled into arrays, whose unit cells are  $90^\circ$  out of phase. Taking into account the nomenclature of traditional honeycomb

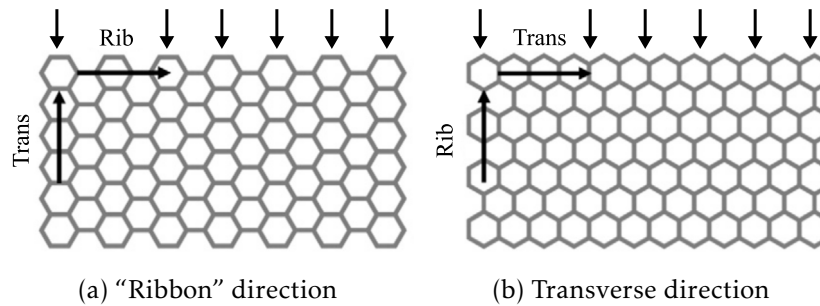


Figure 3.26: Assembling of unit cell to form a honeycomb structure (Adapted from [7])

structures, the “ribbon” and transverse directions were identified in the referred figure. It should be noted that the authors evaluated the compressive behaviour of 3D printed honeycomb structures when they are compressed in the “ribbon” (Figure 3.26(a)) and the transverse (Figure 3.26(b)) directions.

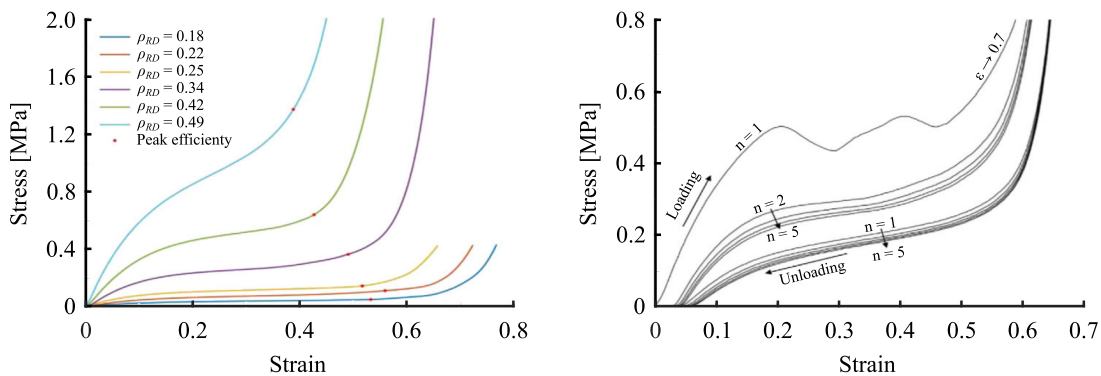
The influence of relative density on the stress-strain curve of a 3D printed TPU honeycomb structure compressed in the ribbon direction is presented in Figure 3.27(a), from which one can observe that the increase in relative density leads to an increase in plateau stress and a decrease in plateau “length” and densification strain. It should be noted that, although only the depicted plot is presented herein, Bates and team [7] illustrate the influence of relative density for both materials and loading directions (see Figure 8 in [7]). Analysing the results, the authors concluded that, when the structure is subjected to compression in the transverse direction, a larger increase of stress during the plateau region is obtained even for low relative densities. Additionally, the resulting buckling yields a more abrupt transition between the elastic and plateau regions when the quasi-static compression tests were performed in the “ribbon” direction. As depicted in Figure 3.27(b), a significant softening behaviour occurred, up to a reduction of 25% in energy absorption between the first and second cycle, when the samples are subjected to cyclic loading. According to the authors, this behaviour was expected since the base material (TPU) presents a similar behaviour under cyclic loading.

Chen and co-workers [20] evaluated the enhancement on the in-plane compressive performance of hierarchical honeycomb structures when compared with a regular honeycomb. These hierarchical structures were obtained through the replacement of cell walls in regular honeycombs with a triangular lattice structure (see Figure 3.28). Similarly to the previously reviewed study, the authors subjected the regular and hierarchical honeycomb structures to a quasi-static compressive test up to failure and a quasi-static cyclic loading test (maximum strains of 0.2, 0.4 and 0.6). To accelerate the experimental procedure and take full advantage of the shape memory effect of the VeroWhite, after a loading-unloading cycle, the samples were heated up to a temperature of 75°C for 10 min and, subsequently, cooled to room temperature before being subjected to another cycle.

Comparing the normalised stress-strain curves obtained when the regular and hierarchical honeycomb structures are compressed up to failure (see Figure 3.29(a)), Chen

and co-workers [20] verified that the introduction of a structural hierarchy into regular honeycombs improves its energy absorption, as consequence of local buckling, fracture of the cell walls and plastic deformation within the hierarchical structure. The brittle failure of the regular honeycomb may also be attributed to the small number of cells contained in the experimental specimen, as depicted in Figure 3.28. Similar findings were attained under cyclic loading conditions, in which the hierarchical honeycombs exhibit enhanced energy absorption and recoverability. Consequently, the authors concluded that slender cell walls may be used in an efficient manner to adapt the energy absorption and allow higher levels of recoverability.

A novel type of structure that arose with the advent of additive manufacturing is the negative stiffness honeycomb [28]. Similarly to conventional regular honeycombs, this structure exhibits a positive stiffness region, followed by a plateau region under compression. However, unlike their traditional counterparts, negative stiffness honeycombs are able to buckle elastically when the compressive loading surpasses the design threshold



(a) Relative density influence on stress-strain curve (b) Compressive cyclic loading under constant strain rate

Figure 3.27: In-plane compressive response of TPU honeycomb structure (Adapted from [7])

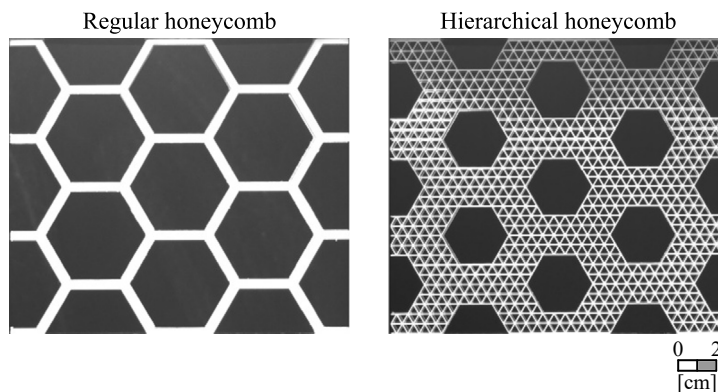


Figure 3.28: Development of hierarchical honeycomb structure (Adapted from [20])

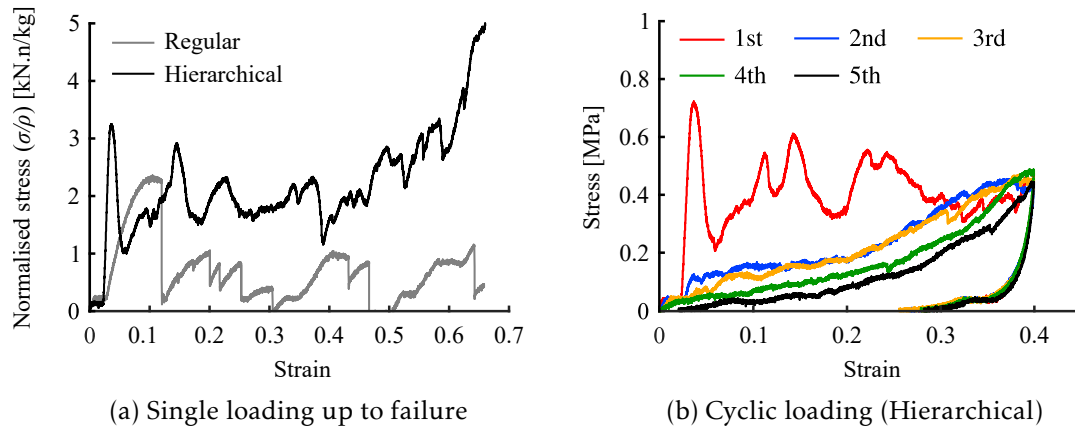


Figure 3.29: Quasi-static compressive response of regular and hierarchical honeycombs (Adapted from [20])

and, consequently, the resulting deformation is recoverable. The specimens used by Debeau and team [28] were manufactured by means of selective laser sintering (SLS) and resorting to nylon-11 due to its relatively large failure strain (approximately 15%). They were oriented in the build chamber so that the resulting layers were aligned with the desired cross section. Figure 3.30(a) illustrates an additively manufactured specimen.

A 5 kg block was dropped from an height of 12.7 cm and impacted on a 4×2 nylon negative stiffness honeycomb specimen. During the impact process, the accelerations present on the impactor were recorded by means of an accelerometer. Comparing the performance of a compressed (“rigid” configuration) and an uncompressed honeycomb, namely the acceleration-time history, the authors verified that the peak impact acceleration was approximately reduced from 40 to 5 g. As expected, due to momentum conservation, this reduction was associated with an increase of the impact’s duration. Figure 3.30(b) illustrates four consecutive experimental tests, on which the 5.0 kg block was dropped from an height of 12.7 cm and impacted the same negative stiffness honeycomb.

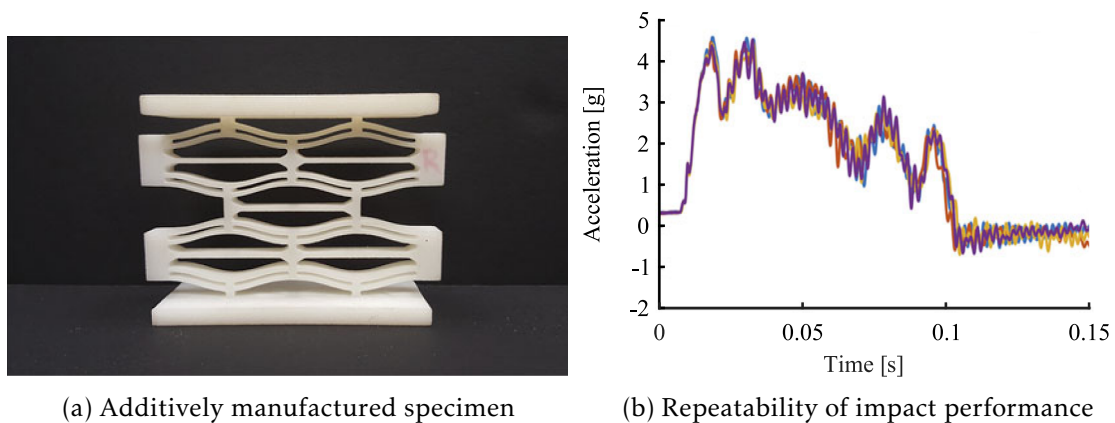


Figure 3.30: Negative stiffness honeycomb structure (Adapted from [28])



Consistent time histories may be observed in the referred figure. Therefore, the authors concluded that, as long as the kinetic energy of the impactor can be entirely absorbed by the elastic buckling of the structure, the force transmitted through the honeycomb is consistent. In the event that the structure becomes fully compressed, a sharp rise in acceleration and, consequently, transmitted force would be visible on the resultant time history [28].

Sarvestani and co-workers [145] studied the performance of 3D printed lightweight sandwich panels by means of experimental impact tests and numerical models. More specifically, the authors evaluated the energy absorption capability of six-sided cell topologies through the change of the geometrical parameters of the cells to obtain hexagonal ( $\theta = 120^\circ$ ) and auxetic ( $\theta = 70^\circ$ ) topologies. Auxetic topologies result in a structure with a negative Poisson's ratio. A FDM 3D printer was used by the authors to manufacture the experimental specimens with polylactic acid (PLA) filament. Taking into account that the nonlinear response and energy absorption capabilities of 3D printed structures depends on several parameters, namely their geometry, relative density, mechanical properties of the base material and the core cell topology, the authors took great care to maintain all these properties constant, while changing the topology of the core cell. Figure 3.31 illustrates the experimental specimens according to the considered core cell topology and the direction of the cells. Unless otherwise referred, the experimental specimens were subjected to a 3 J low velocity impact.

Figure 3.32 shows the resulting experimental contact force-displacement curves (at the impactor). In order to allow a straightforward comparison, this figure presents the results for alternative configurations of the core (in-plane and out-of-plane), cell topologies (hexagonal and auxetic) and relative densities (20 and 30%). Analysing the curves, the authors concluded that the topology of the cellular core has a great influence on the recorded force-displacement curve and, subsequently, on the resultant energy absorption

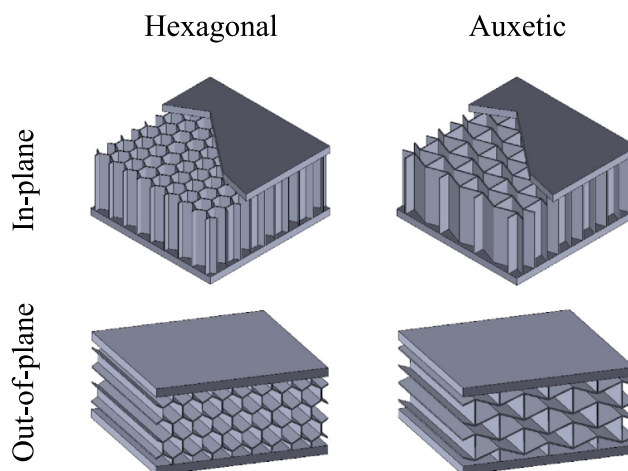


Figure 3.31: Sandwich panels with alternative cellular core architectures (Adapted from [145])

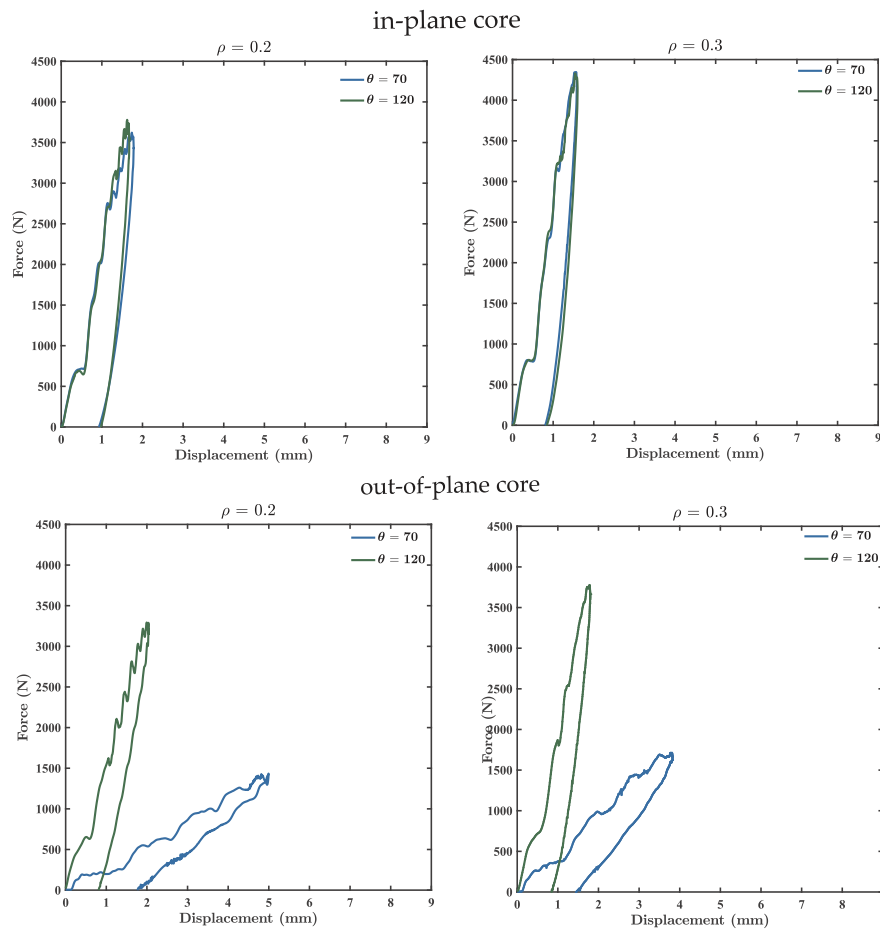


Figure 3.32: Experimental force-displacement curves of 3D printed with alternative cellular core configurations, cell topologies and relative densities (Adapted from [145])

capability. Additionally, the results showed that, for the in-plane configuration, the contact forces are very similar, regardless of the used topology, while the relative density seems to have a significant effect on the results. On the other hand, when the cellular core is perpendicular to the direction of impact (out-of-plane configuration), the auxetic cores have the lowest maximum contact force and yield a lower level of force at the same deformation level.

Due to the reviewed results, Sarvestani and co-workers [145] considered that the auxetic sandwich panel is a potential candidate for energy absorption applications, since they presented a large energy absorption capability while maintaining the response forces to a minimum.

### 3.5.3 Simplified models

The effects of using sacrificial claddings for blast mitigation are still not fully understood. Analytical, experimental and numerical methodologies have been developed and reported in the literature to study the absorption mechanisms, the main design parameters and

to predict the behaviour of such solutions under blast loads. Nonetheless, experimental research on the blast response of structural elements, with and without sacrificial claddings, requires a safe environment, which results in high costs and may become impractical. Consequently, numerical simulations represent an attractive alternative.

According to Sun and Li [159], the numerical models that are used to study the dynamic response of cellular materials may be categorised into either meso-scale or continuum mechanics models. The former are able to implicitly or explicitly take into account the influence of the cell's structures, while the latter treats the deformation, motion and force experienced by the cells in a continuum sense. More specifically, mass-spring models, which assume that a cellular material is represented by a series of lump masses and nonlinear springs, and models that are based on cells, such as the ones shown in Figures 3.7(a) and 3.24, may be considered as subdivisions of meso-scale models. Alternatively, when the framework of continuum mechanics is used to model the dynamic response of a cellular material, each of its cells may be represented by a material point from a macroscopic point of view. Taking into account that continuum mechanics models are generally more efficient and versatile when compared to cell-based models, the present section focus on the development of a one-dimensional continuum based model that simulates the dynamic response of sacrificial cladding solutions.

### 3.5.3.1 Continuum mechanics models

The response of a material can be modelled resorting to continuum mechanics models, on which the structure of the material is not taken into account, but rather idealised as continuously distributed mass points, denoted as  $X$ , defined by their unique location in space  $x$  at a given time  $t$  [176].

According to Wang [176], two coordinate systems may be used to study the movement of the medium in continuum mechanics, the material coordinate system (Lagrange method) and the spatial coordinate system (Euler method). On the former, the coordinate system follows the reference mass point and both the variation of physical quantities with time, for a fixed mass point, and the variation of these quantities within the mass points are examined. Therefore, a physical quantity  $\psi$  is defined as a function of the mass point  $X$  and time  $t$ ,  $\psi = F(X, t)$ , where the independent variable  $X$  is usually called Lagrange coordinate, or material coordinate. On the other hand, the Euler method considers a spatial point as the reference for the coordinate system in order to examine the motion of material. Consequently, a physical quantity  $\psi$  is defined as a function of spatial location  $x$  and time  $t$ ,  $\psi = f(x, t)$ , where the independent variable  $x$  is denoted as the spatial coordinate.

Accordingly, the material derivative, i.e. the time derivative of quantity  $\psi$  observed by following a fixed particle  $X$ , and the spatial derivative, i.e. the time derivative of quantity  $\psi$  at a fixed spatial location  $x$ , are defined in equations (3.5) and (3.6).

$$\frac{d\psi}{dt} = \left. \frac{\partial F(X, t)}{\partial t} \right|_X \quad (3.5)$$

$$\frac{\partial \psi}{\partial t} = \left. \frac{\partial f(x, t)}{\partial t} \right|_x \quad (3.6)$$

Considering the function  $F(X, t)$  as compound function of variables  $f[x(X, t), t]$ , the material derivative becomes,

$$\frac{d\psi}{dt} = \left. \frac{\partial f(x, t)}{\partial t} \right|_x + \left. \frac{\partial f(x, t)}{\partial x} \right|_t \left. \frac{\partial x}{\partial t} \right|_X \quad (3.7)$$

where  $\partial x/\partial t|_X$  is the material derivative of the spatial location  $x$  of particle  $X$ , i.e. the velocity of particle  $X$ , expressed by  $v$ . Disregarding the subscripts, one obtains the material derivative expressed in the spatial coordinate system:

$$\frac{d\psi}{dt} = \frac{\partial \psi}{\partial t} + v \frac{\partial \psi}{\partial x} \quad (3.8)$$

It is important to refer that the velocity of the wave depends on the considered coordinate system. Equations (3.9) and (3.10) define the intrinsic wave velocity  $\dot{\phi}(t)$ , defined in a material coordinate system, and the spatial wave velocity  $\dot{\phi}(t)$ , respectively. Although the presented expressions characterise the propagation behaviour of the same wave front, due to the variation in the coordinate system, generally they yield different values. Nonetheless, if the medium into which the wave front propagates is stationary and undeformed prior to its arrival, the intrinsic wave velocity is identical to the spatial wave velocity.

$$C = \left. \frac{dX}{dt} \right|_W = \dot{\phi}(t) \quad (3.9)$$

$$c = \left. \frac{dx}{dt} \right|_w = \dot{\phi}(t) \quad (3.10)$$

Lastly, a third derivative, commonly used in stress wave study, is defined. This derivative, commonly known as wave derivative, represents the total derivative of a physical quantity  $\psi$  with regard to time following the wave and can be expressed by the following expressions when a material or spatial coordinate system is used, respectively:

$$\left. \frac{d\psi}{dt} \right|_W = \left. \frac{\partial \psi}{\partial t} \right|_X + C \left. \frac{\partial \psi}{\partial X} \right|_t \quad (3.11)$$

$$\left. \frac{d\psi}{dt} \right|_w = \left. \frac{\partial \psi}{\partial t} \right|_x + c \left. \frac{\partial \psi}{\partial x} \right|_t \quad (3.12)$$

Considering the physical quantity as the spatial location of a mass point  $x(X, t)$ , and that, for a one-dimensional material motion,  $(\partial x/\partial X)_t = (1 + \varepsilon)$  is a valid definition, one can define the relationship between the previously defined wave velocities as:

$$c = v + C(1 + \varepsilon) \quad (3.13)$$

### Governing equations of one-dimensional longitudinal waves (material coordinates)

Consider the bar represented in Figure 3.33 with initial cross sectional area  $A_0$  and density  $\rho_0$ . It is assumed that, during the deformation process, the cross section of the bar remains planar and the axial stress distribution is uniform. According to Wang [176],

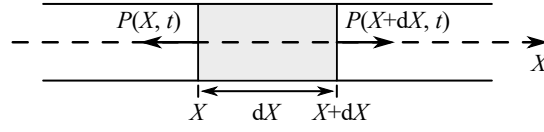


Figure 3.33: Infinitesimal element of a bar with uniform cross-section represented in material coordinates (Adapted from [176])

the governing equations for the present problem are obtained through both the mass and momentum conservation equations, in combination with the constitutive relation of the material.

The material coordinates are defined as the spatial coordinates before deformation ( $t = 0$ ). Considering an infinitesimal segment of the bar  $dX$ , it is possible to compute the force on the right section of the wave front as:

$$P(X + dX, t) = P(X, t) + \frac{\partial P(X, t)}{\partial X} dX \quad (3.14)$$

From Newton's second law:

$$\rho_0 A_0 dX \frac{\partial v}{\partial t} = P(X + dX, t) - P(X, t) = \frac{\partial P(X, t)}{\partial X} dX \quad (3.15)$$

Replacing in the engineering stress  $\sigma = P/A_0$ , the motion equation of the infinitesimal segment expressed in material coordinates is:

$$\rho_0 \frac{\partial v}{\partial t} = \frac{\partial \sigma(X, t)}{\partial X} \quad (3.16)$$

Additionally, the stress is assumed to be a rate-independent function of strain (equation (3.17)) and, due to the high wave velocity, the heat exchange of the segment with the neighbouring segments is considered to be very small and the deformation process is considered to be adiabatic. Therefore, there is no need to introduce other physical quantities on the energy conservative equations.

$$\sigma = \sigma(\varepsilon) \quad (3.17)$$

Taking into account that the function  $\sigma(\varepsilon)$  is continuously differentiable, introducing,

$$C^2 = \frac{1}{\rho_0} \frac{d\sigma}{d\varepsilon} \quad (3.18)$$

and expressing  $\varepsilon$  and  $v$  in terms of displacement  $u$ , one obtains the wave equation eliminating  $\sigma$  between equations (3.16) and (3.17):

$$\frac{\partial^2 u}{\partial t^2} - C^2 \frac{\partial^2 u}{\partial X^2} = 0 \quad (3.19)$$

### Governing equations of one-dimensional longitudinal waves (spatial coordinates)

A specified region in the space, denoted as the controlled volume, is considered to study the propagation of one-dimensional longitudinal waves with a spatial coordinate system. The conservation laws of mass, momentum and energy are usually applied to a fixed mass of the material. Consequently, in order to apply these laws to a controlled volume, both the variation of physical quantities within the volume and the flow of quantities across its surfaces must be contemplated [176].

A controlled volume of a bar between  $x$  and  $x + dx$  is considered in the present study (see Figure 3.34). The mass occupied by the spatial segment  $dx$  is:

$$M = \rho A dx = \rho_0 A_0 dX \quad (3.20)$$

where  $\rho$  and  $A$  depict the actual density and cross-section area of the bar, while  $\rho_0$  and  $A_0$  represent the initial density and cross-section area of the bar prior to deformation. It should be noted that  $dX$  is the infinitesimal length of the bar segment  $dx$  before it was deformed. Therefore, it is possible to verify that the presented equation illustrates the conservation of mass during the deformation process. Taking into account the definition of strain  $dx = (1 + \varepsilon)dX$ , one can define the mass per length of unit of the bar  $m$  as:

$$m = \rho A = \frac{\rho_0 A_0}{1 + \varepsilon} \quad (3.21)$$

Convenient mathematical manipulation of the mass and momentum conservation on the controlled volume, allow the definition of the continuous (3.22) and dynamic (3.23) equations expressed in spatial coordinates.

$$\frac{\partial \varepsilon}{\partial t} + v \frac{\partial \varepsilon}{\partial x} - (1 + \varepsilon) \frac{\partial v}{\partial x} = 0 \quad (3.22)$$

$$\frac{\rho_0}{1 + \varepsilon} \left( \frac{\partial v}{\partial t} + v \frac{\partial v}{\partial x} \right) = \frac{\partial \sigma}{\partial x} \quad (3.23)$$

Assuming that the stress is a function of strain and that  $C^2$  is defined by equation (3.18), the dynamic equation can be rewritten as:

$$(1 + \varepsilon) C^2 \frac{\partial \varepsilon}{\partial x} - \frac{\partial v}{\partial t} - v \frac{\partial v}{\partial x} = 0 \quad (3.24)$$

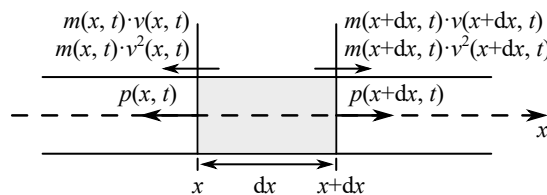


Figure 3.34: Infinitesimal controlled volume of a bar with uniform cross-section represented in spatial coordinates (Adapted from [176])

### Conservation conditions across wave front

Although the particle displacement  $u$  is usually continuous across a wave front, its derivatives may present a discontinuity, which is commonly referred to as a singular interface. If the particle velocity  $v$  and the strain  $\varepsilon$ , which are a first-order derivative of  $u$ , present a jump across the wave front, the singular interface is commonly referred to as a strong discontinuity. Consequently, the previously defined differential equations are not valid and several compatibility equations must be satisfied across the singularity, commonly known as Rankine-Hugoniot relations [176]. It should be noted that, although the Rankine-Hugoniot jump conditions have been presented in Section 2.3 for a shock wave propagating through undisturbed air, it is considered as important to review the compatibility equations under the scope of continuum mechanics.

Considering a planar wave front propagating along the  $X$  axis with material velocity  $D = dX/dt$  and a Lagrangian coordinate system, the wave derivative from equation (3.11) becomes:

$$\frac{d\psi}{dt} = \frac{\partial\psi}{\partial t} + D \frac{\partial\psi}{\partial X} \quad (3.25)$$

Depicting the values of  $\psi$  just before and after the discontinuity by  $\psi^b$  and  $\psi^a$ , in which superscripts “ $b$ ” and “ $a$ ” respectively identify the values just before and after the discontinuity, the difference between the wave derivative before and after discontinuity is:

$$\frac{d}{dt}(\psi^a - \psi^b) = \left( \frac{\partial\psi}{\partial t} \Big|_a - \frac{\partial\psi}{\partial t} \Big|_b \right) + D \left( \frac{\partial\psi}{\partial X} \Big|_a - \frac{\partial\psi}{\partial X} \Big|_b \right) \quad (3.26)$$

Considering that the wave front is a first-order singular surface, i.e.  $\psi$  is continuous across the wave front while its first-order derivatives are not, the equation above yields:

$$\left( \frac{\partial\psi}{\partial t} \Big|_a - \frac{\partial\psi}{\partial t} \Big|_b \right) = -D \left( \frac{\partial\psi}{\partial X} \Big|_a - \frac{\partial\psi}{\partial X} \Big|_b \right) \quad (3.27)$$

The kinematic compatibility condition on the wave front presented in equation (3.27), which physically represents the condition of mass conservation, may be defined in terms of the particle displacement  $u$ , resulting on the following expression:

$$v^a - v^b = -D(\varepsilon^a - \varepsilon^b) \quad (3.28)$$

The distance  $dX$  that the shock front covers in  $dt$  is a function of the wave velocity  $D$ :  $dX = Ddt$ . Applying the momentum conservation of the covered distance  $dX$ , one obtains,

$$(\sigma^b - \sigma^a)A_0dt = \rho_0A_0dX(v^a - v^b) \quad (3.29)$$

which can be simplified as:

$$(\sigma^a - \sigma^b) = -\rho_0D(v^a - v^b) \quad (3.30)$$

Combining equations (3.28) and (3.30), it is possible to express the variation of stress across the shock front as a function of the variation of strain,

$$(\sigma^a - \sigma^b) = \rho_0D^2(\varepsilon^a - \varepsilon^b) \quad (3.31)$$

enabling the computation of the shock wave velocity as follows:

$$D = \sqrt{\frac{1}{\rho_0} \frac{(\sigma^a - \sigma^b)}{(\varepsilon^a - \varepsilon^b)}} \quad (3.32)$$

It is important to refer that all the compatibility equations were established without the material properties and are valid for any continuum. Nonetheless, the wave speed determination requires the constitutive relation of the material. Assuming that the behaviour of the material does not depend on strain rate and has an unique stress-strain relationship, the following expression is attained,

$$\left( \frac{\partial \sigma}{\partial X} \Big|_a - \frac{\partial \sigma}{\partial X} \Big|_b \right) = \frac{d\sigma}{d\varepsilon} \left( \frac{\partial \varepsilon}{\partial X} \Big|_a - \frac{\partial \varepsilon}{\partial X} \Big|_b \right) \quad (3.33)$$

which reduces equation (3.32) into equation (3.18). Additionally, the velocity of the shock front may be computed with the secant slope of the  $\sigma(\varepsilon)$ , usually referred to as Rayleigh line (see Figure 3.35).

Lastly, referring to the material's internal energy in a unit mass as  $e$ , the conservation of energy of the bar segment  $dX$  is,

$$(\sigma^a v^a - \sigma^b v^b) = -\rho_0 D (e^a - e^b) - \frac{1}{2} \rho_0 D [(v^a)^2 - (v^b)^2] \quad (3.34)$$

which also can be expressed by:

$$\rho_0 (e^a - e^b) = \frac{1}{2} (\sigma^a + \sigma^b) (\varepsilon^a - \varepsilon^b) \quad (3.35)$$

As previously referred, equations (3.28), (3.30) and (3.35) comprise the mass, momentum and energy conservation conditions across a first-order singularity, or shock front, usually labelled as the Rankine-Hugoniot relationship. If the initial conditions of the material are known, namely  $\sigma^b$ ,  $\varepsilon^b$ ,  $v^b$  and  $e^b$ , this relationship, in combination with the material constitutive relationship, yield four equations (shock adiabatic lines) that connect any two of the five undetermined physical quantity  $\sigma^a$ ,  $\varepsilon^a$ ,  $v^a$ ,  $e^a$  and  $D$ . However, the shock adiabatic  $\sigma(\varepsilon)$  curve is not the constitutive  $\sigma(\varepsilon)$  curve of the material in adiabatic conditions. Assuming a unique  $\sigma(\varepsilon)$  relationship and, thus, neglecting the difference between these curves, it is possible to bypass the energy conservation equation and, through the remaining equations, compute  $\sigma^a$ ,  $\varepsilon^a$ ,  $v^a$  and  $D$  with the initial conditions.

It should be noted that the reviewed derivations remain valid for any continuum solid and do not comprise any constitutive constants. Sun and team [159] state that, when a shock wave propagates through a solid, the change of internal energy is computed as the area under the Rayleigh line which, as depicted in Figure 3.35 is usually larger than the strain energy determined by integrating the dynamic stress-strain curve. Similarly, Harrigan and co-workers [53] concluded that in order to attain the correct solution to a shock problem, the conservation equations for mass and momentum will suffice, while



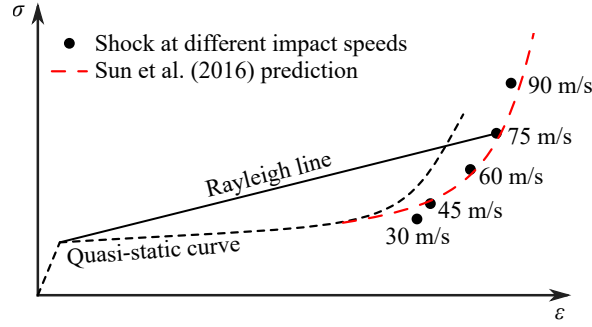


Figure 3.35: Quasi-static stress-strain relation vs. the Rayleigh line (Adapted from [160])

the “energy balance” method is not adequate since it does not consider the extra energy dissipated during shock propagation.

Sun and team [160] investigated if a critical condition is required for the occurrence of a shock front in a cellular solid subjected to compressive loads. The authors concluded that the formation of a shock front inside a cellular solid only occurs if a critical impact speed, which may be predicted by Hugoniot relations (see equation (15) in [160]), is surpassed.

### 3.5.3.2 Development of simplified model proposed by Hanssen et al. (2002)

Hanssen and team [51] established a simplified model to study the one-dimensional compaction of an aluminium foam bar subjected to a linearly decaying blast load. As illustrated in Figure 3.36, the foam bar is covered by a front plate, with mass  $M_1$  and cross-sectional area  $A$ , and the structural element is considered as rigid. The properties of the foam bar are its length  $l$ , cross-sectional area  $A$  and total mass  $\rho Al$ . When fully compressed, the density of the foam changes from  $\rho$  to  $\rho_d$ . The front plate is considered as rigid, while the constitutive behaviour of the foam is idealised with the rigid-perfectly plastic-locking (RPPL) material model. This model is characterised by a plateau stress of  $\sigma_{pl}$  and a densification strain of  $\varepsilon_d$ . Since the structural element is assumed to be rigid, the displacements at the right end of the foam bar are restrained and both the movement of the front plate and deformation of the bar are expressed by  $u(t)$ .

Conservation of mass of the entire foam bar at  $t$  (see Figure 3.37) yields the displacement of the front plate  $u$  as a function of the extent of the compacted zone  $x$ :

$$u = \frac{\varepsilon_d}{1 - \varepsilon_d} x \quad (3.36)$$

Considering the compacted segment with a length of  $dx$  depicted in Figure 3.37, equation (3.20) states that the mass of that controlled volume should remain constant, thus:

$$\rho A dx = \rho_d A dx \quad (3.37)$$

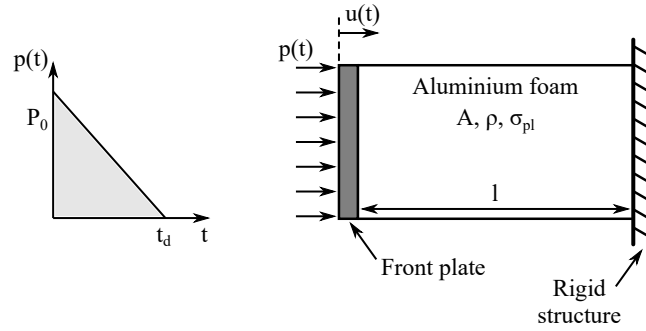


Figure 3.36: Schematic representation of the blast-loaded aluminium foam bar's simplified model (Adapted from [51])

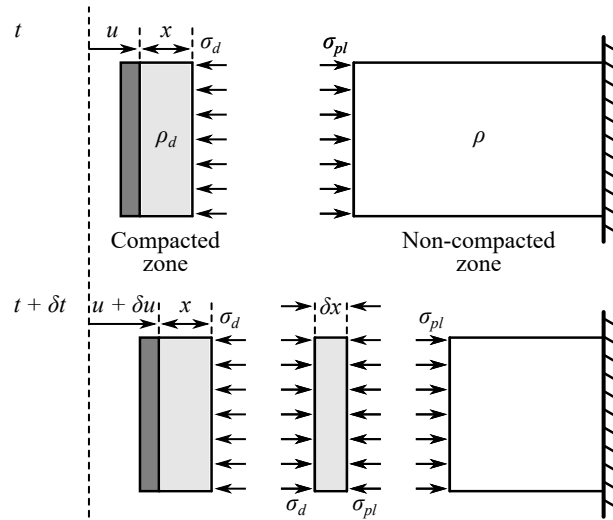


Figure 3.37: Free body diagrams of aluminium foam bar at times  $t$  and  $t + dt$  (Adapted from [51])

Assuming that the cross-sectional area of the bar, which is denoted by  $A$ , does not vary with compression and that  $dX = (1 - \varepsilon_d)dx$ , one obtains:

$$\rho_d = \frac{\rho}{1 - \varepsilon_d} \quad (3.38)$$

Applying both the mass and momentum conservation equations across the shock front, previously defined in equations (3.28) and (3.30), respectively, one obtains the stress of the densified foam  $\sigma_d$  as a function of the plateau stress  $\sigma_{pl}$ , the initial density  $\rho$ , the densification strain  $\varepsilon_d$  and the velocity of the front plate  $du/dt$  as follows:

$$\sigma_d = \sigma_{pl} + \frac{\rho}{\varepsilon_d} \left( \frac{du}{dt} \right)^2 \quad (3.39)$$

Alternatively, conservation of momentum of the rigid body consisting of the front

plate and densified foam region, whose length is defined by  $x$ , yields:

$$\left( M_1 + \frac{\rho_d A}{1 - \varepsilon_d} x \right) \frac{d^2 u}{dt^2} + [\sigma_d - p(t)] A = 0 \quad (3.40)$$

Combining equations (3.36), (3.38), (3.39) and (3.40), one obtains the differential equation that describes the problem:

$$\left( M_1 + \frac{\rho A}{\varepsilon_d} u \right) \frac{d^2 u}{dt^2} + \frac{\rho}{\varepsilon_d} \left( \frac{du}{dt} \right)^2 + [\sigma_{pl} - p(t)] A = 0 \quad (3.41)$$

### 3.5.3.3 Development of simplified model proposed by Ma and Ye (2007)

The previously presented model only considers the nonlinear behaviour of the sacrificial cladding solution and the influence of the protected structural element has been ignored, which may be considered as a limit situation. However, Ye and Ma [180] state that, in order to fully understand the design of sacrificial cladding solutions, the behaviour of both the cladding and structure must be taken into consideration.

The simplified model developed by Ma and Ye [87], commonly referred to as Load-Cladding-Structure (LCS) model, is similar to that of Hanssen and co-workers [51]. The LCS model also considers that the front plate, and consequently the cellular material are subjected to a triangular impulse. Nonetheless, the former considers the influence of the structure's movement  $y(t)$ , whose equivalent mass and stiffness are determined by means of the Bigg's method [9] and denoted by  $M_e$  and  $K_e$ , respectively, on the one-dimensional deformation behaviour of the cellular material. As illustrated in Figure 3.38, the initial properties of the cellular material are its length  $l$ , cross sectional area  $A$  and density  $\rho$ . As considered by Hanssen and team [51], Ma and Ye [87] models the behaviour of the cellular material with the RPPL approximation with a plateau stress  $\sigma_{pl}$  and a densification strain  $\varepsilon_d$ , at which the stress rises to  $\sigma_d$ .

Conservation of mass of the cellular material must be guaranteed throughout its deformation. Therefore, observing Figure 3.39, and considering that  $\rho_d = \rho/(1 - \varepsilon_d)$ , it is

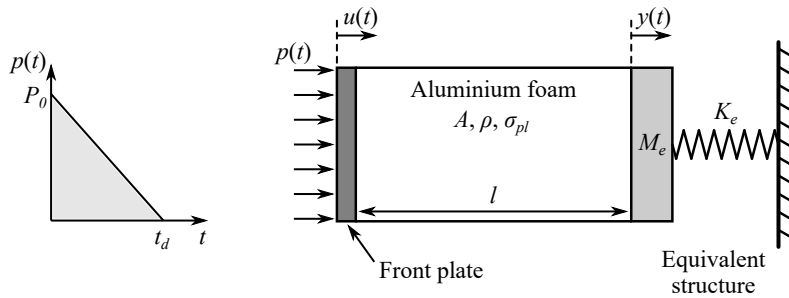


Figure 3.38: Schematic representation of the Load-Cladding-Structure model (Adapted from [87])

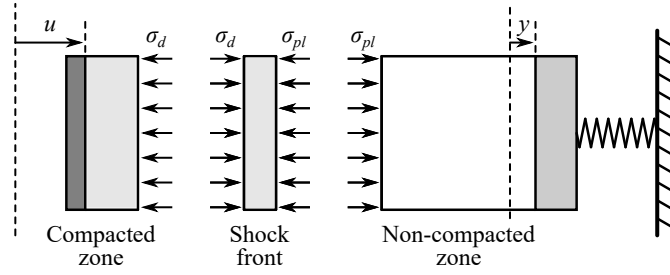


Figure 3.39: Free body diagram of the Load-Cladding-Structure model (Adapted from [87])

possible to obtain the variation of the length of the densified part of the material as a function of the difference between the movement of the front plate and the structure as follows:

$$x = \frac{1 - \varepsilon_d}{\varepsilon_d} (u - y) \quad (3.42)$$

Consequently, the mass of the densified length  $x$  is computed by:

$$m_d = \rho_d A x = \frac{\rho A}{\varepsilon_d} (u - y) \quad (3.43)$$

While the compressed length of the cellular material is moving at the same speed as the front plate, the undeformed part moves together with the structural element. Consequently, there is a velocity jump across the shock front ( $du/dt - dy/dt$ ) and the application of the momentum conservation equation across the shock front (see equation (3.30)) yields:

$$(\sigma_d - \sigma_{pl}) = \rho_d D \left( \frac{du}{dt} - \frac{dy}{dt} \right) \Leftrightarrow \sigma_d = \sigma_{pl} + \frac{\rho}{\varepsilon_d} \left( \frac{du}{dt} - \frac{dy}{dt} \right)^2 \quad (3.44)$$

Taking into account Newton's second law of motion, the equation of motion of the rigid body composed by the front plate and compacted foam may be written as,

$$(M_1 + m_d) \frac{d^2 u}{dt^2} = [p(t) - \sigma_d] A \quad (3.45)$$

which can be expressed as,

$$\left[ M_1 + \frac{\rho A}{\varepsilon_d} (u - y) \right] \frac{d^2 u}{dt^2} + \frac{\rho A}{\varepsilon_d} \left( \frac{du}{dt} - \frac{dy}{dt} \right)^2 + [\sigma_{pl} - p(t)] A = 0 \quad (3.46)$$

if combined with equations (3.43) and (3.44).

The general motion equation of an equivalent single-degree-of-freedom model subjected to a blast load is presented in equation (3.47). However, for the present problem, the mass of the undeformed cellular material moves with the structural system and must be taken into account. Additionally, until the sacrificial cladding suffers a full compression, the transmitted stress into the structure will take the value of the material's plateau

stress  $\sigma_{pl}$ . Therefore, equation (3.47) is rewritten as equation (3.48) for the current problem.

$$M_e \frac{d^2 y}{dt^2} + K_e y - p(t)A = 0 \quad (3.47)$$

$$\left[ \rho A l - \frac{\rho A}{\varepsilon_d} (u - y) + M_e \right] \frac{d^2 y}{dt^2} + K_e y - \sigma_{pl} A = 0 \quad (3.48)$$

When the foam layer becomes fully compacted, or the velocity of both the front plate and structure become equal, the sacrificial cladding will move together with the equivalent system of the structure. Therefore, the problem's equation of motion can be simplified as:

$$(M_1 + \rho A l + M_e) \frac{d^2 y}{dt^2} + K_e y - p(t)A = 0 \quad (3.49)$$

Lastly, in order to attain an effective structural protection, the properties of the sacrificial cladding solution should relate to that of the structure. Ma and Ye [87] defined a couple of non-dimensional parameters that allow the design of a cladding solution to a given structural element. The relation between the resistance of the structure and the plateau stress of the sacrificial cladding solution is taken into consideration resorting to non-dimensional parameter  $\kappa$ , which was introduced by the authors as,

$$\kappa = \frac{\sigma_{pl} A}{k y_c / 2} \quad (3.50)$$

where  $y_c$  gives the critical deflection. It should be noted that Ma and Ye [87] consider that the critical deflection of the structural element is given by its elastic limit. Therefore, one might conclude that the LCS model assumes that the structural element always deforms under the elastic regime. Alternatively, in order to relate the impulse that the cladding solution transmits to the protected structural element  $I_0$  and the impulse required to fully compress the crushable core  $I_1$ , non-dimensional parameter  $\tau$  is defined as  $I_1/I_0$ , yielding the following expression:

$$\tau = \frac{\sqrt{(\rho A l + M_1) \frac{l \varepsilon_d}{\sigma_{pl} A}}}{T/2} \quad (3.51)$$

### 3.5.3.4 Material models

According to Sun and team [159], a continuum mechanics model requires the definition of a constitutive relation, usually a stress-strain relation. Several simplifications for the stress-strain relation have been used to simulate the nonlinear behaviour of cellular materials under compaction, e.g. rigid-perfectly plastic-locking (RPPL); elastic-perfectly plastic-rigid (EPPR); elastic-linear hardening plastic-rigid (ELHPR); elastic-perfectly plastic-nonlinear hardening (EPPNHL); and the elastic-nonlinear hardening plastic (ENLHP) simplifications (see Figure 3.40).

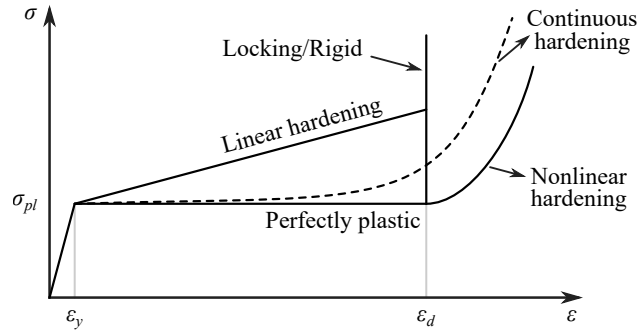


Figure 3.40: Commonly used simplified constitutive relations for cellular materials (Adapted from [159])

The initial compressive response may be assumed as either linear elastic or as rigid, since it is considered that both approximations are acceptable if large deformations are expected. The plateau stress  $\sigma_{pl}$ , in combination with the respective strain  $\varepsilon_y$ , mark the beginning of the plastic regime. As illustrated in Figure 3.40, the plastic behaviour of the cellular material may be idealised as perfect or characterised by a linear or nonlinear hardening. It should be noted that the plateau and densification regimes are usually taken into account separately. Consequently, the correct definition of the densification initiation strain  $\varepsilon_d$  is considered to be paramount. Lastly, the densification stage is commonly simplified with locking/rigid or through a nonlinear hardening.

While the linear hardening approximation only requires the definition of a hardening modulus, e.g.  $E_p$ , the nonlinear hardening simplification is commonly given as a function of strain. Although several functions have been proposed, see Sun et al. [159], the present study only reviews the one introduced by Zheng and co-workers [186], in which the stress-strain curve is given by the following expression:

$$\sigma = \sigma_o + \frac{C \varepsilon}{(1 - \varepsilon)^2} \quad (3.52)$$

where  $\sigma_o$  is the initial crushing stress, and  $C$  is the strain hardening parameter.

### 3.6 Conclusions

A brief state of the art on traditional strengthening techniques was presented in the current chapter. However, these techniques greatly increase the construction costs both during the strengthening process and due to retrofit if damaged. Therefore, alternative methods to improve the blast resistance capabilities of structural elements were reviewed, such as the use of externally bonded steel plates and composite materials.

More recently, the scientific community focused on the use of protective solutions with reduced mass and high energy absorption. These solutions, which are usually referred to as sacrificial claddings, are mounted to the outer surface of an already existent

structural element in order to mitigate the effects of a blast load. Amongst several candidate materials, cellular solids have been reported in the literature as one of the most reliable. A brief definition of these solutions and the analysis of their typical compressive stress-strain curve and resulting energy absorption capabilities were presented in the current chapter. Subsequently, the state of the art on additively manufactured solutions for energy absorption was reported. The chapter finished with a revision of related simplified numerical models proposed by Hanssen et al. (2002), which assumes the structural element to be protected as rigid, and by Ma and Ye (2007), which takes into account the behaviour of the structural element on the design of sacrificial cladding solutions whose crushable core is materialised with a cellular material.

Sacrificial claddings need to be customised according to each particular scenario and produced with flexibility and precision. Consequently, a rapid growth on the use of 3D printing as a manufacturing technique has been registered over the last years. These protective solutions are typically based on thin walled structures [1, 7, 19, 71] and, as a result of their dimensions, the successive layers of these walls are usually 3D printed in the same direction, yielding anisotropic mechanical behaviour of the constitutive materials. Moreover, the reported state of the art revealed that finite element (FE) modelling is considered to be a valuable tool to study the energy absorption capabilities of protective systems [1, 7, 19, 71, 145]. However, despite the known anisotropic behaviour of 3D printed materials, most of the studies resort to a homogeneous and isotropic constitutive relation. This approach represents a major drawback for these numerical models. Consequently, it is essential to understand and quantify the influence of the FDM technique on the mechanical behaviour of bulk materials.





# Chapter 4

## Experimental testing

### 4.1 Introduction

The mechanical properties of 3D printed components are different from that of the polymer filament and may vary with the loading direction due to their layered microstructure [18, 27, 36, 44] and present tension/compression asymmetry [8, 157].

The current chapter presents the experimental testing conducted to attain the mechanical characterisation of unidirectional 3D printed samples with special focus on anisotropy and asymmetry under quasi-static regime and their strain rate sensitivity. Firstly, the generic sample preparation (constant throughout the entire study) is briefly introduced, followed by the experimental tests performed using a modified electromagnetic compressive split-Hopkinson bar [150–152]. The preference for a compressive split-Hopkinson bar apparatus over alternative solutions derives from its flexibility to incorporate a hydraulic actuator, which allows the authors to perform quasi-static and high strain rate tests using the same experimental apparatus. Tensile tests were also conducted on a universal testing machine, allowing for a better understanding of the anisotropy and asymmetry behaviour of the specimens.

Subsequently, the nonlinear response of 3D printed PLA honeycomb structures is experimentally investigated in order to analyse their energy absorption capacity when used as the crushable core of a sacrificial cladding solution. The proposed sacrificial cladding is composed by a crushable core (PLA honeycomb structure of a given relative density and height, in combination with two PLA solid plates) and an aluminium front plate. Its dynamic response is obtained resorting to a previously developed and validated explosive driven shock tube [119, 120].

The results of this chapter allow the calibration of the constitutive model to be used in the numerical simulations presented in Chapter 5.

## 4.2 Sample preparation

A FDM 3D printer [128] (see Figure 4.1) was used to manufacture all the samples used in the present work. According to Dizon and co-workers [30], FDM is currently the most popular technology for consumer-level 3D printers, in which the polymeric filament is melted and extruded through a heated nozzle that deposits the material onto a two-dimensional layer on top of another, leading to a three-dimensional object. Figure 4.2 shows a schematic representation of the described manufacturing process.

Polylactic acid, commonly referred to as PLA, is usually the material of choice for 3D printing over acrylonitrile-butadiene-styrene (ABS) due to its higher mechanical resistance and lower thermal expansion coefficient, the latter yielding better printability as a result of reduced warping. Moreover, the former is readily available on the market and it

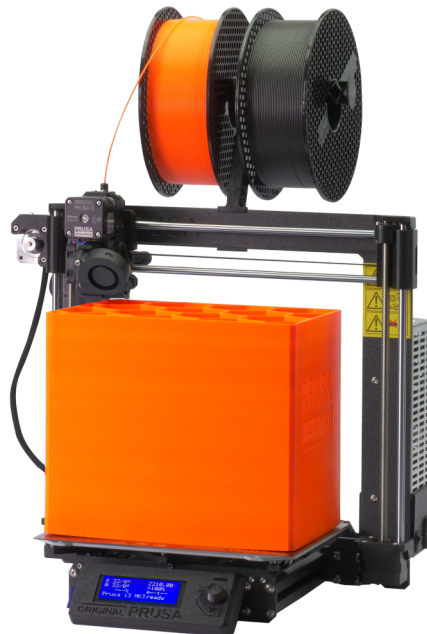


Figure 4.1: Prusa Mk3 3D printer [128]

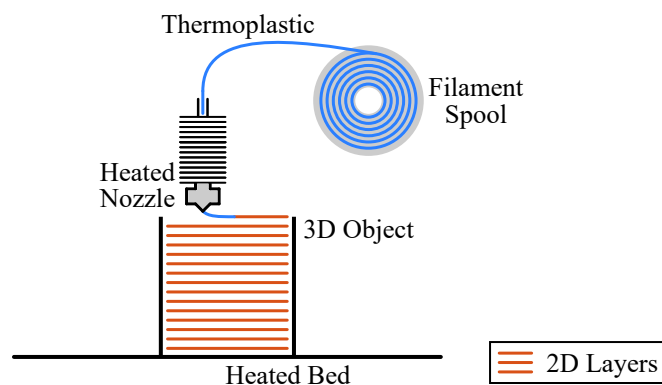


Figure 4.2: Schematic of a Fused Deposition Modelling 3D printer

is relatively cheap when compared with other filaments. Therefore, PLA filament, whose original diameter is 1.75 mm, was extruded through a 0.4 mm diameter heated nozzle and deposited layer by layer according to a user defined pattern, yielding the desired three-dimensional specimen.

The mechanical properties of components manufactured with FDM vary according to several parameters identified and studied by the scientific community, namely the layer deposition height, the extrusion temperature, the feed rate and the presence and configuration of external contours [18, 30, 72, 85, 101, 102, 157]. Therefore, the printing parameters employed in the present work, see Table 4.1, were maintained constant and defined according to the manufacturer's recommendations (nozzle extrusion temperature and heated bed temperature) and user experience (printing speed) as to avoid imperfections.

Furthermore, as a result of the layered microstructure of the manufactured components, the mechanical properties of 3D printed parts depend on the two-dimensional deposition orientation with respect to the loading direction [18, 27, 30, 36, 44]. On traditional composites, the bond between their matrix and fibres may have different mechanical properties from those of its constituent materials. Correspondingly, in the case of 3D printed components, the mechanical properties of the interface between the layers are different than the properties of the extruded filament. For that reason, it is possible to conclude that the mechanical response of 3D printed components portrays both anisotropy and tension/compression asymmetry [8, 157].

Table 4.1: Printing parameters

Parameter	Value
Nozzle extrusion temperature	210 °C
Heated bed temperature	60 °C
Layer height	0.1 mm
Printing speed	30 mm/s
Number of outer shells	2

### 4.3 Material characterisation

The present section reports the experimental characterisation of 3D printed PLA components conducted on the Mechanical Testing Laboratory of IDMEC<sup>1</sup>. The printed specimens were subjected to uniaxial loading ranging from quasi-static to high strain rate regimes.

Although 3D printers have the ability to manufacture components where successive layers may have orthogonal deposition directions, which would yield specimens with an isotropic mechanical behaviour, the energy dissipation solutions that resort to this

<sup>1</sup>The author gratefully acknowledges the collaboration with Dr. Pedro A. R. Rosa and Eng. Afonso Gregório from the Mechanical Testing Laboratory of IDMEC.

manufacturing technique are based on thin walled structures [1, 7, 19, 71]. Due to their dimensions, the successive layers of these walls are commonly deposited in the same direction. Consequently, only the mechanical properties of unidirectional 3D printed specimens were obtained. As depicted in Figure 4.3, three different configurations were considered, in which the printing orientation makes an angle of  $0^\circ$ ,  $90^\circ$  and  $45^\circ$  with respect to the loading direction.

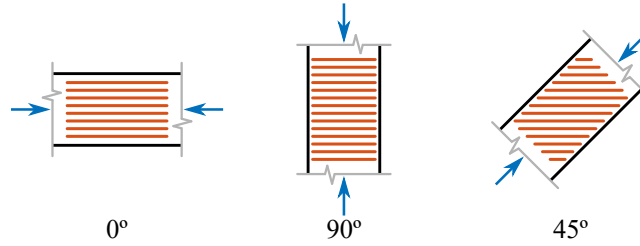


Figure 4.3: Angle between 3D printing orientation (red lines) and loading direction (blue arrows)

A preliminary study, which aimed to verify the existence of scale effects and ensure the correct determination of the mechanical response, subjected cylindrical specimens manufactured with a  $90^\circ$  orientation to a compressive load. No evidence of scale effects was identified, as clearly visible in the true stress-true strain curves shown in Figure 4.4, for the considered dimensions of the cylindrical specimens having initial diameters of 3.0, 6.0 and 12.0 mm and initial heights of 3.2, 6.4 and 12.8 mm, respectively.

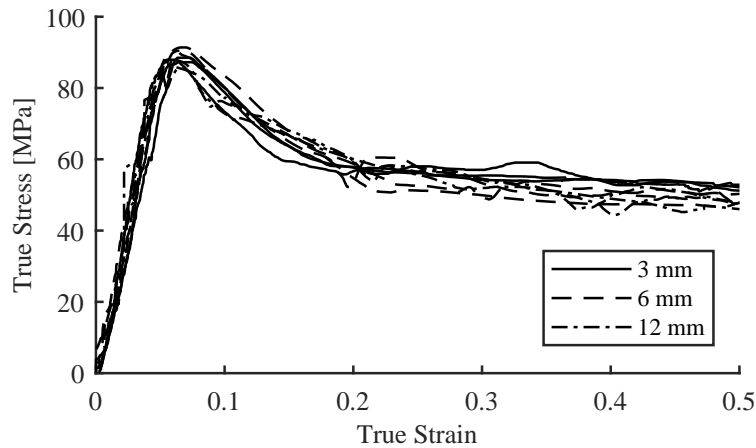


Figure 4.4: True stress-true strain curves for specimens of different diameters

Therefore, all subsequent tests (see Section 4.3.1) were performed on samples with a 6.0 mm diameter gauge section. The compression tests resorted to cylinders with a diameter/height of 6.0/6.4 mm ( $0^\circ$  and  $90^\circ$  orientations), as depicted in Figure 4.5(a), while the tensile tests utilised dogbone inspired specimens whose geometry, characterised by a 6.0 mm gauge section, is defined in Figure 4.5(b) ( $0^\circ$ ,  $90^\circ$  and  $45^\circ$  orientations). A minimum of three specimens were subjected to each of the considered combinations of

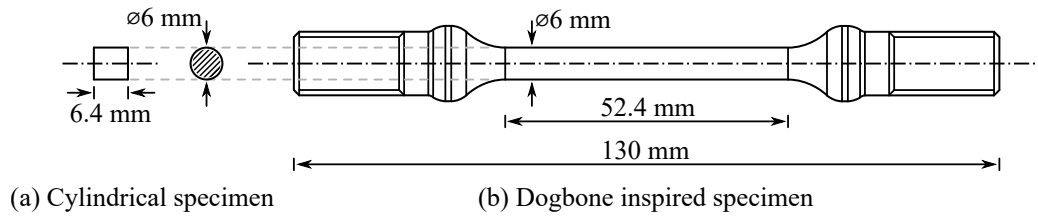


Figure 4.5: Geometry of the tested specimens

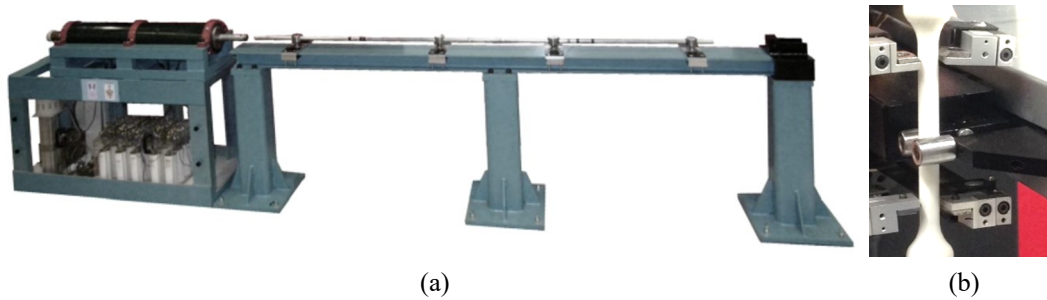


Figure 4.6: Mechanical characterisation of the commercial PLA: (a) compression tests using a split-Hopkinson bar apparatus; (b) tensile tests using a universal testing machine Instron 4507

loading (compressive/tensile), configuration and strain rate.

### 4.3.1 Mechanical testing

A split-Hopkinson bar apparatus was used to carry out the compression tests under high strain rate conditions. An overall view and a schematic representation of the employed compressive testing apparatus is illustrated in Figures 4.6(a) and 4.7, respectively. As depicted in Figure 4.7, the main components of the testing apparatus may be divided into impact bench and actuator. The former comprises the basic structural components, a load cell and a displacement transducer, which are independent of the strain rate conditions, while the latter will vary according to the desired strain rate range. An electromagnetic gun is used as actuator for high strain rate conditions [150–152]. This electromagnetic actuator consists of electrical circuits for charging and firing of an energy storage bank and a series of coils that generate the pressure to accelerate the striker bar into the incident bar. Note that the amount of stored energy controls the velocity of the striker bar and, consequently, the compressive strain rate. Alternatively, quasi-static conditions are achieved by means of a hydraulic actuator, in combination with an electric pump that supplies the required fluid at the required flow and pressure. Due to the use of interchangeable actuators, the compression tests were performed in strain rate conditions ranging from  $10^{-1}$  to  $10^3 \text{ s}^{-1}$  while resorting to the same data acquisition elements. Lastly, it is important to refer that a zinc stearate lubricant was employed in order to ensure homogeneous deformation of the cylindrical specimens.

An Instron 4507 testing machine, see Figure 4.6(b), was used to perform the tensile

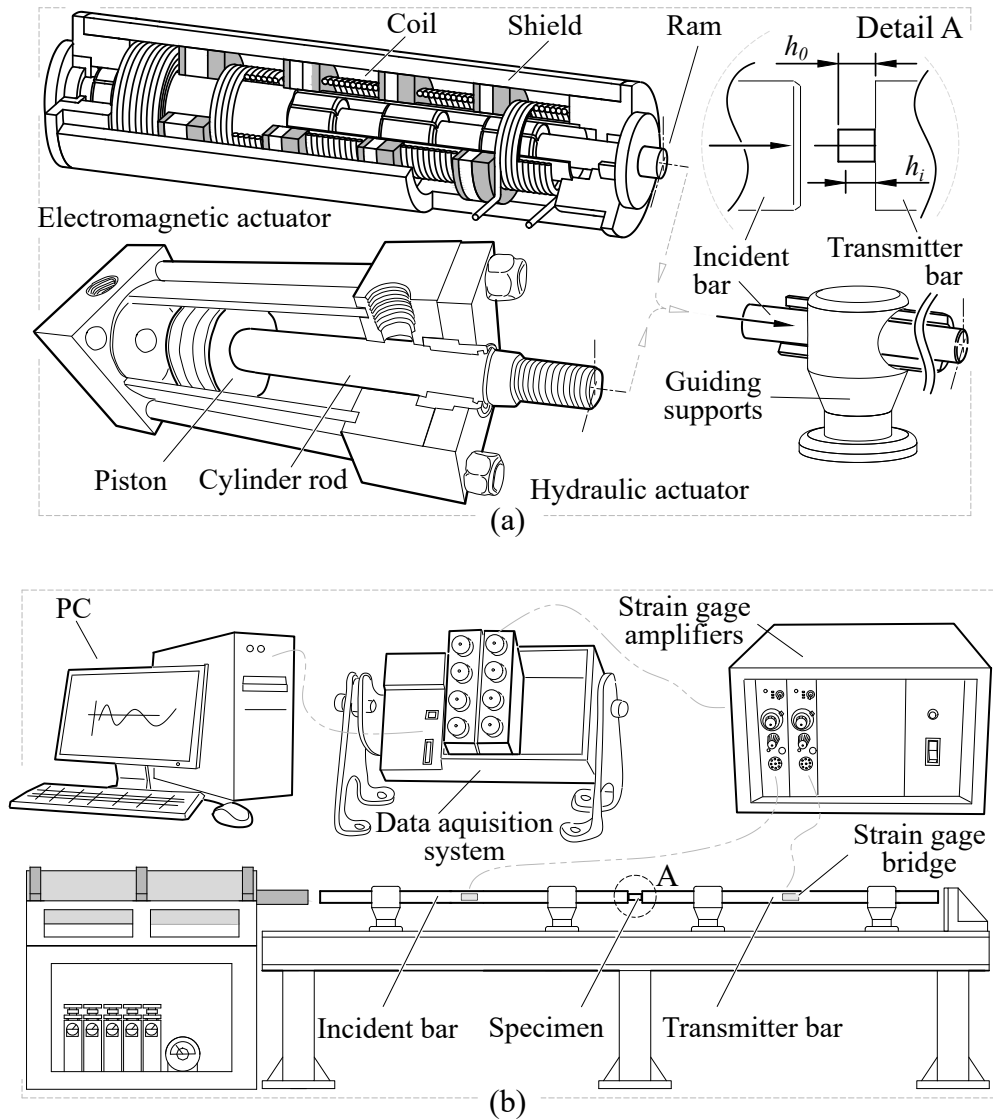


Figure 4.7: Schematic representation and nomenclature of the specially designed split-Hopkinson bar apparatus that allows quasi-static and high strain rate testing conditions by using (a) replaceable electromagnetic and hydraulic actuators, (b) assembled on the same platform as the downstream data acquisition elements [Image credit to Eng. Afonso Gregório from IDMEC]

tests at a deformation rate of approximately  $10^{-1} \text{ s}^{-1}$ . Although, as illustrated in Figure 4.5(b), the distance between shoulders is 52.4 mm, the referred tests were performed considering a gauge length of 24 mm.

The average Young's modulus and maximum strength, as computed from the results of the compression and tensile tests, are summarised in Table 4.2. Analysing the referred table, it is possible to infer a 20% increase in the maximum stress when the specimen is compressed perpendicularly to the printing direction ( $90^\circ$  orientation). On the contrary, for tensile loading, both the Young's modulus and ultimate strength reach maximum values when the loading direction is aligned with the printing orientation ( $0^\circ$  orientation). As expected, the mechanical properties attained when the samples were subjected to tensile loads with a  $45^\circ$  orientation lie within the values obtained for the other orientations.

Table 4.2: Summary of the measured mechanical properties for all considered orientations

T/C	Orientation	$E$ [GPa]	$\sigma_{max}$ [MPa]
C	$0^\circ$	$1.73 \pm 0.17$	$72.94 \pm 2.83$
	$90^\circ$	$2.16 \pm 0.34$	$90.05 \pm 3.54$
T	$0^\circ$	$3.94 \pm 0.23$	$66.04 \pm 2.31$
	$90^\circ$	$2.38 \pm 0.09$	$26.07 \pm 2.05$
	$45^\circ$	$2.73 \pm 0.01$	$37.31 \pm 3.73$

To analyse the strain effects, cylindrical specimens, whose rasters were perpendicular to the loading direction ( $90^\circ$  orientation), were subjected to compressive loads with three strain rates (500, 2500 and 5000  $\text{s}^{-1}$ ). These strain rate values were chosen in order to fall within the range of high velocity impact and blast loads. Figure 4.8 illustrates the maximum strength as a function of strain rate. A power regression function, defined through equation (4.1), was applied to the experimental data, yielding a coefficient of determination ( $R^2$ ) close to unity. Additionally, the prediction bounds for the fitted function with a 95% level of confidence are also shown.

$$\sigma_d(\dot{\epsilon}) = -4.708 \dot{\epsilon}^{0.2873} + 90.71 \quad [\text{MPa}] \quad (4.1)$$

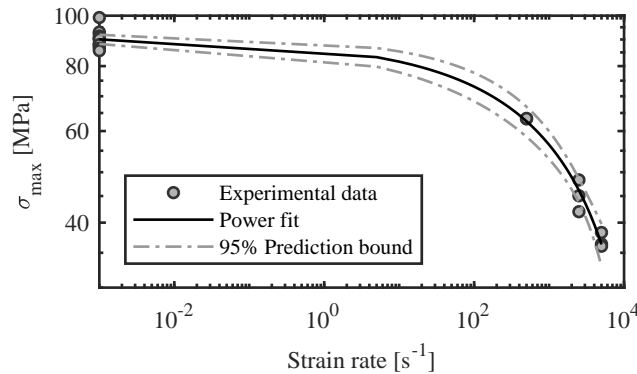


Figure 4.8: Maximum stress of PLA as a function of the strain rate

A three-dimensional surface, which allows for a better understanding of the influence of both strain and strain rate on the nonlinear behaviour of 3D printed PLA, was constructed and presented in Figure 4.9. Analysing the referred figure, one might verify that the maximum stress is inversely proportional to strain rate. Nonetheless, with the increase of strain, the resulting stress seems to tend to a constant value, regardless of strain rate, corresponding to approximately a 25% reduction, when compared with the quasi-static stress at the same true strain.

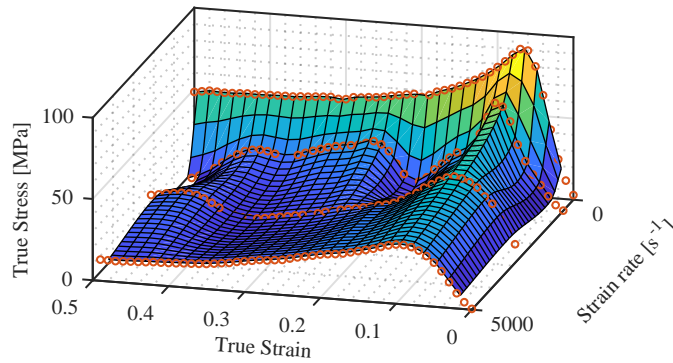


Figure 4.9: 3D printed PLA stress response with respect to strain and strain rate

#### 4.4 Blast testing

The experimental campaign conducted during the present work, aimed to obtain the nonlinear response of a sacrificial cladding solution composed by a 3D printed crushable core and an aluminium front plate, was performed using an explosive driven shock tube (EDST). As depicted in Figure 4.10, experimental samples, with  $8 \times 8 \times 9.4$  cm, were used to determine the dynamic behaviour of the 3D printed crushable core. The proposed crushable core is composed by a honeycomb structure with a height of 9 cm and two solid plates with a thickness of 2 mm. As referred in Section 3.5.2, the relative density is considered as the most relevant property of a cellular solid. Therefore, three different relative densities were considered, as presented in Table 4.3. The wall thickness (0.43 mm) was maintained constant, while the edge length was varied in order to obtain relative densities of 5, 7.5 and 10% (see Figure 4.11). The solid plates were manufactured with the same material and parameters as the honeycomb structure and improved the bonding between the honeycomb structure and the front aluminium plate.

Table 4.3: Properties of the regular hexagon honeycomb

Type	$t$ [mm]	$l$ [mm]	$t/l$	$\bar{\rho}$ [%]	No. of cells	Mass [g]
1	0.43	9.90	0.043	5	$5 \times 5$	79.3
2	0.43	6.59	0.065	7.5	$7 \times 7$	100.7
3	0.43	4.95	0.087	10	$9 \times 9$	122.6



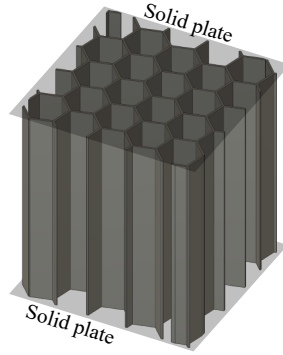


Figure 4.10: Experimental sample of the 3D printed crushable core

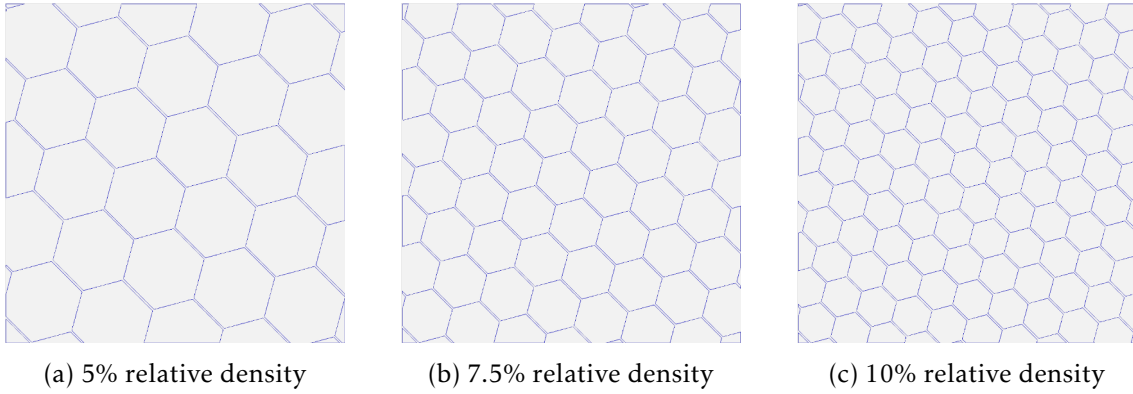


Figure 4.11: Specimens' cross section

#### 4.4.1 Preliminary quasi-static tests

Preliminary quasi-static ( $\dot{\epsilon} = 10^{-3} \text{ s}^{-1}$ ) compression tests were performed with the loading direction aligned with the honeycomb tubes to verify the influence of relative density on the samples' nonlinear response. The resulting stress-strain curves are presented in Figure 4.12, while Table 4.4 collects the associated mechanical properties. Analysing both the referred figure and table, one can readily observe that the plateau stress ( $\sigma_{pl}$ ) and the absorbed ( $U_{pl}$ ) and specific ( $SEA$ ) energies increase proportionally with the relative density.

Table 4.4: Summary of 3D printed honeycomb mechanical properties under quasi-static loading

$\bar{\rho}$ [%]	$\sigma_{pl}$ [MPa]	$\epsilon_d$	$U_{pl}$ [J]	$SEA$ [J/g]
5	0.947	0.594	313.5	11.1
7.5	2.215	0.633	774.8	17.7
10	3.778	0.648	1,302.3	22.1

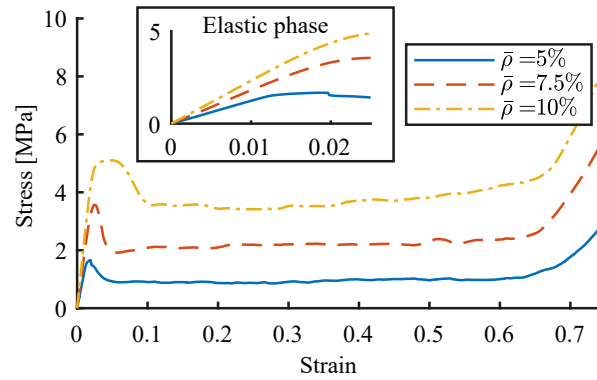


Figure 4.12: Quasi-static stress-strain curve dependence on the relative density

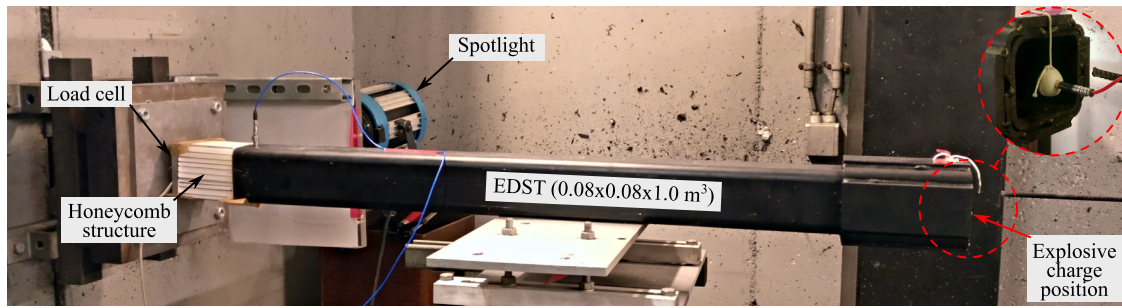
#### 4.4.2 Experimental set-up

The experimental campaign, conducted in the Laboratory for the Analysis of Explosive Effects at the Royal Military Academy in Brussels<sup>2</sup>, employed the small-scale experimental set-up illustrated in Figure 4.13. A square section (SHS 80×3 mm) explosive driven shock tube was used to generate a planar blast load at its end, resulting from the detonation of a given explosive charge, positioned at a definite distance from, or at, its entrance [119] (see Figure 4.13(a)). A schematic representation of the set-up is shown in Figure 4.13(b), in which it is possible to observe that the front plate of the blast absorption solution, whose mass (87 g) was maintained constant throughout the whole experimental campaign, was positioned 2 mm away from the opposite end of the EDST. Double-sided bonding tape was used to bond the crushable core to both the 5 mm front plate and the set-up. A PCB 203B force load cell was placed between the rear plate and the remainder of the set-up to measure the transmitted load with a 1 MHz acquisition rate. A Photron Fastcam SA5 high speed camera was used at a frame rate of 10,000 frames per second and a resolution of 1024 by 640 pixel, which yields an imaging magnification of 0.19 mm/pixel when measuring the displacement of the front plate. Note that, although the images were captured with 10,000 frames per second, an exposure duration of 1/40,000 s was chosen in order to avoid the presence of “motion blur” on the recorded frames. Lastly, it is important to refer that all the obtained measurements were synchronised using a light intensity sensor.

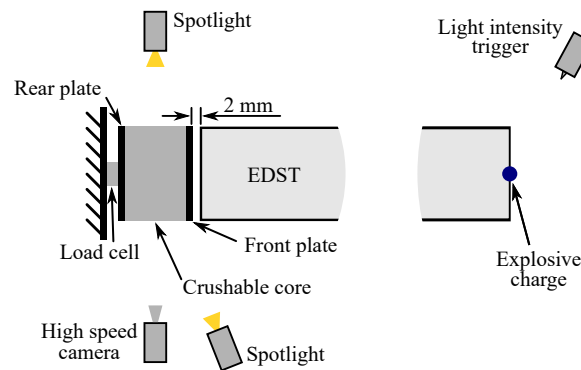
#### 4.4.3 Instrumentation

The present section introduces in more detail the instrumentation used during the experimental blast tests.

<sup>2</sup>The author gratefully acknowledges the collaboration with the research team from the Department of Civil and Materials Engineering of RMA.



(a) Overview



(b) Schematic representation

Figure 4.13: Experimental set-up

#### 4.4.3.1 Force load cell

A PCB 203B force load cell, whose specifications are presented in Table 4.5, was positioned between the rear plate and the remainder of the set-up in order to record the load transmitted by the sacrificial cladding solution. The referred sensor is classified as an integrated circuit piezoelectric (ICP) quartz force ring, which is well suited for dynamic force measurement applications, and includes built-in microelectronic amplifiers that convert the high-impedance electrostatic from the quartz crystals into a low-impedance voltage output signal. When the sensor is loaded, the quartz crystals generate an electrostatic charge proportional to the applied force. In order to guarantee a correct contact between the sensor and the plates, ensure a linear variation of voltage with force and enable tensile force measurements, a preload must be applied to the sensor and, consequently, to the crystals. Lastly, an anti-friction washer is used to mitigate damage to the sensor's surface during preload application [45].

Table 4.5: Specification of PCB 203B force load cell [125]

Sensitivity [mV/kN]	Measurement range (Comp.) [kN]	Preload [kN]	Stiffness [kN/ $\mu\text{m}$ ]
56.2	88.96	17.793	4.0

#### 4.4.3.2 Pressure sensor

A pressure transducer (PCB 102B) was used to measure the reflected overpressure on a rigid and fixed boundary. The corresponding specifications of this sensor are given in Table 4.6. Similarly to the force load cell, the pressure transducer has a piezoelectric element, which generates an electric charge when pressure is applied, and an ICP source follower amplifier that converts the referred charge to a low impedance voltage output. This pressure transducer possesses a very high natural frequency (beyond 500 kHz), which yields a wide usable frequency range and a fast rise time (less or equal to 1  $\mu$ s), resulting in minimal overshoot and/or ringing.

Table 4.6: Specification of PCB 102B force load cell [124]

Sensitivity [mV/kPa]	Measurement range ( $\pm 5V$ ) [kPa]	Max. pressure [kPa]	Rise time [ $\mu$ s]
0.15	34,500	103,000	$\leq 1.0$

#### 4.4.3.3 High speed camera

The deformation of the sacrificial cladding was obtained resorting to a Photron Fastcam SA5 high speed camera, which was placed perpendicularly to the loading direction, guaranteeing a minimization of errors due to out-of-plane movements on the two-dimensional projection of the compression process. As illustrated in Figure 4.13, two spotlights were placed on either side of the specimen. A white screen was placed in front of the light which was positioned behind the set-up and pointed at the high speed camera (see Figure 4.13(a)) to obtain a more homogeneous background. Figure 4.14 shows the two-dimensional projection of the sacrificial cladding solution on the high speed camera during the experimental campaign. Three steps are required to measure the displacement of the front plate, namely calibration, processing and post-processing. On the calibration step, the imaging magnification is computed resorting to an object of known dimensions. As illustrated in Figure 4.14, three different measurements (C1 to C3) were performed for all tests of the experimental campaign (total of 30 measurements), yielding an average imaging magnification of 0.19 mm/pixel. During the processing step, two  $x$  coordinates (X1 and X2) were recorded at each frame. Subsequently, the average displacement of the front plate may be computed by means of the difference between the initial and corresponding  $x$  coordinate. During the post-processing phase, the image magnification is used to convert the displacement of the plate, while the frame rate enables the conversion of the frame numbers into a time scale. Lastly, the velocity of the front plate is approximated via a typical central difference scheme.

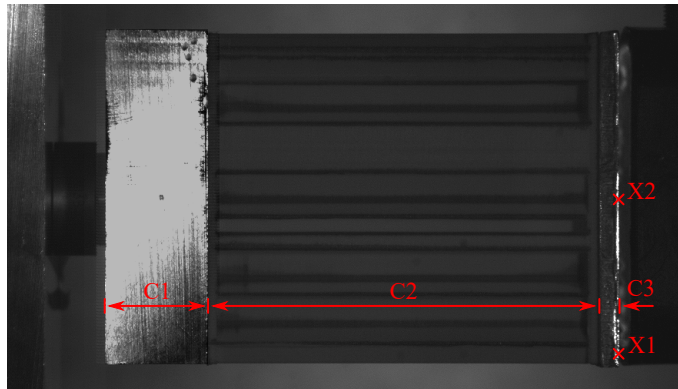


Figure 4.14: Two-dimensional projection of SC solution on HSC

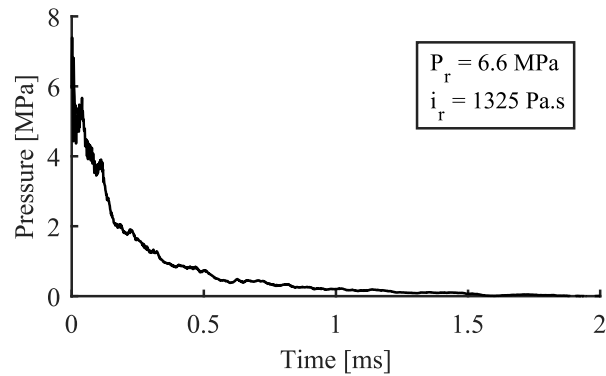
#### 4.4.4 Blast load on rigid and fixed boundary

In order to correctly obtain the reflected pressure-time history, a set of preliminary tests were performed on a rigid and fixed boundary, on which a PCB 102B pressure sensor was placed centred at a distance of 50 mm from the end of the EDST. Resorting to 10 g of C4 positioned at a distance of 50 mm and at the entrance of the EDST, one obtains the average pressure-time histories shown in Figure 4.15. The former may be characterised by a 6.6 MPa and a 1325 Pa·s reflected overpressure and impulse, respectively, while the latter yields a peak reflected overpressure of 20 MPa and a reflected specific impulse of 2600 Pa·s. Both blast scenarios were used on the preliminary tests of the experimental set-up, while 10 g of C4 was placed at the entrance of the EDST for the sacrificial cladding's experimental campaign. Note that, the mass and position of the explosive charge were maintained constant for the entirety of the reported experimental campaign. The recorded pressure-time histories will be used in the numerical models presented in Chapter 5.

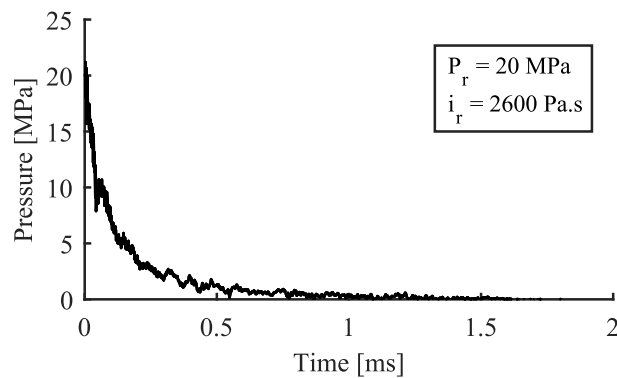
The planarity of the blast wave has been previously verified by Ousji and team [119]. They concluded that planarity of the blast wave inside an EDST is achieved when length to diameter ratio is larger than 4.5. Taking into account the dimensions of the EDST used during the current work, this ratio is 12.5 and therefore, the blast wave may be considered as planar.

#### 4.4.5 Preliminary tests on the experimental set-up

Although the experimental set-up has been previously used and verified by Ousji and co-workers [120], an additional preliminary set of experimental tests was conducted, with the blast load directly applied to two different set-ups, to verify their influence on the force recorded by the PCB 203B load cell. The geometry of the first set-up, which was based on the set-up developed by Ousji, is illustrated in Figure 4.16(a) and it was materialised with steel elements. Note that the steel plate with 200x200x10 mm, to which the load cell is fixed, is only bolted to the large steel mass, whose dimensions are



(a) 10 g of C4 set at 50 mm from the entrance of the EDST



(b) 10 g of C4 set at the entrance of the EDST

Figure 4.15: Average reflected overpressure-time history measured on rigid and fixed boundary

250x250x50 mm. The second set-up was materialised on aluminium with the geometry depicted in Figure 4.16(b).

A schematic illustration of the force sensor's installation is depicted in Figure 4.17. Set-up 1 resorted to a typical installation (see Figure 4.17(a)), in which a Beryllium Copper (BeCu) mounting stud was used to clamp and prestress the quartz crystal. According to the sensor's installation manual [125], part of the force transmitted between the two plates is shunted through the mounting stud. Consequently, the material of the stud influences the amount of force shunted through it (up to 5% of the total force with the BeCu stud). However, the preload application is not straightforward, since the rear plate was positioned without any knowledge of the applied torque. Alternatively, a M10 threaded rod was used in combination with a nut and washer, enabling the use of a torque wrench to apply a 40 N·m torque, which approximately corresponds to the 20 kN preload recommended by the manufacturer [125]. Observing Figure 4.17(b), it is possible to verify that, during compression and tensile forces up to 20 kN, no force is shunted through the steel threaded rod, since the rod is not directly connected to the leftmost plate.

Comparing the force-time histories presented in Figures 4.16(a) and 4.16(b), obtained when both set-ups are subjected to the blast load illustrated in Figure 4.15(a), it is possible

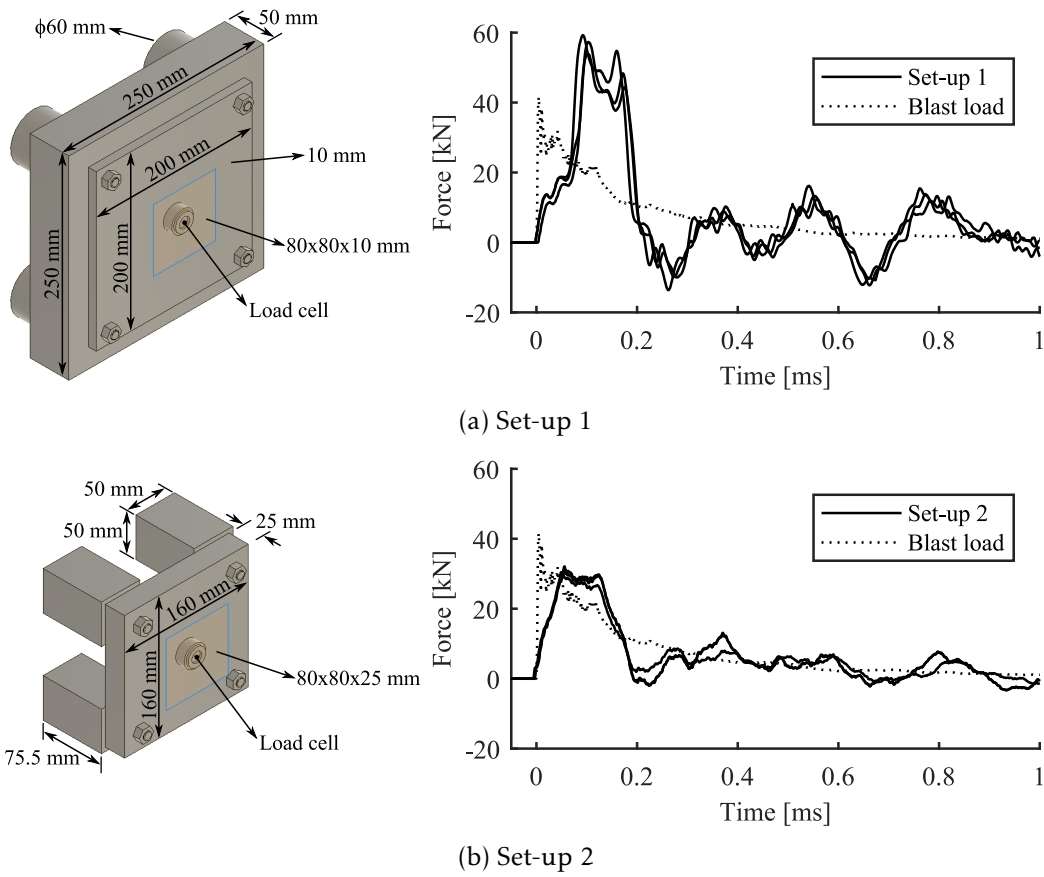


Figure 4.16: Schematic representation of the remainder of the experimental set-up and corresponding force-time history

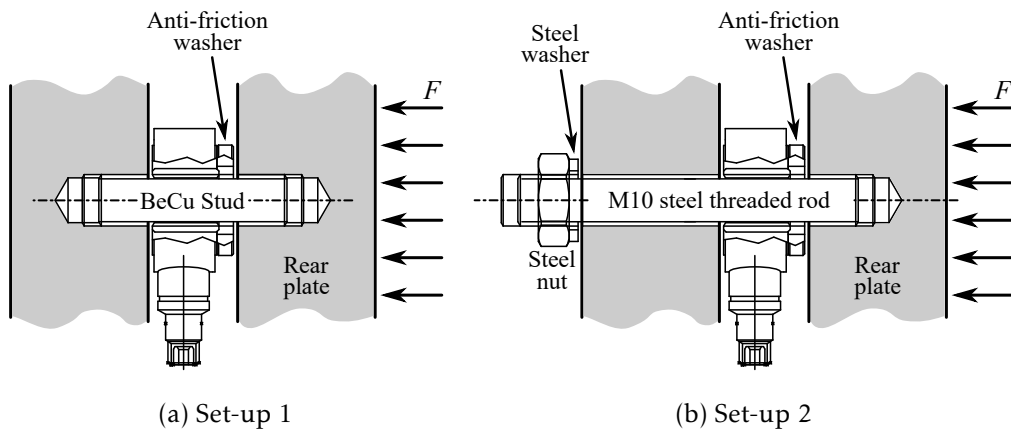


Figure 4.17: Schematic representation of the PCB 203B load cell installation

to observe that the force-time history recorded for set-up 2 follows the applied pressure-time history. Additionally, a greater repeatability of the results and a high frequency vibration reduction are visible when set-up 2 is used. Therefore, set-up 2 will be used for the remainder of the experimental campaign.

An additional preliminary set of experimental tests was conducted, with the blast load resulting from a 10 g C4 charge placed at the entrance of the EDST applied directly to set-up 2. Figure 4.18 depicts the experimental records of both the force sensor and the pressure transducer. Similarly, vibrations are readily observable in the experimental force sensor's measurements when compared with the pressure-time history. Consequently, one might conclude that the set-up influences the transmitted force-time history recorded during the remainder of the experimental campaign. Nonetheless, when the impulses of both sensors are compared, no significant difference was verified, i.e. no energy loss was recorded.

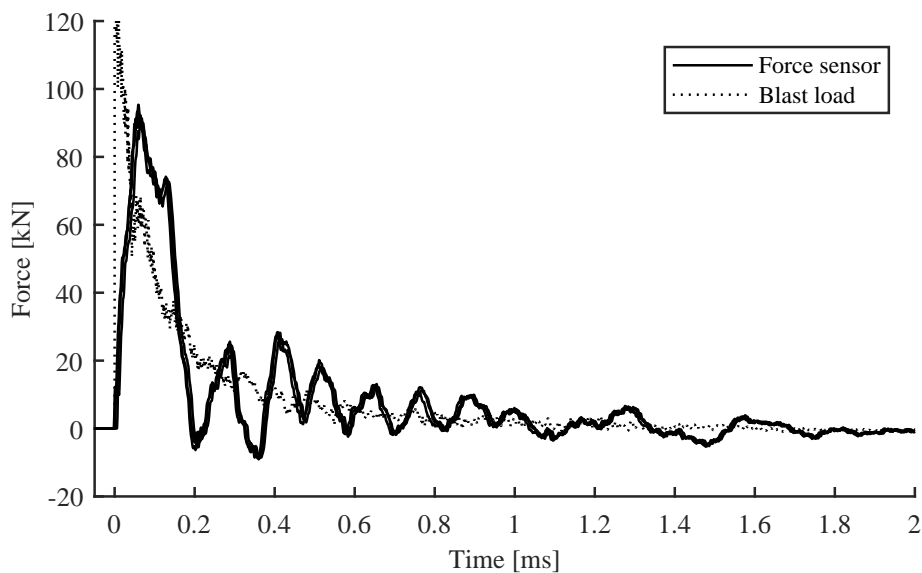


Figure 4.18: Force-time history on rigid and fixed boundary

#### 4.4.6 Sacrificial cladding

The dynamic behaviour observed when the sacrificial cladding solutions with different relative densities are subjected to a blast load will be subjected to both a qualitative and a quantitative analysis. It should be noted that the current section aims to present an initial analysis of the results, while a more complete analysis will be reported in Chapter 5.

Photographs of the crushable core after the experimental tests are shown in Figure 4.19, from which one can readily observe that the sacrificial cladding solution characterised by a 5% relative density was completely destroyed, while some material remained attached to back solid plate of the 7.5% relative density core. Contrarily, the crushable



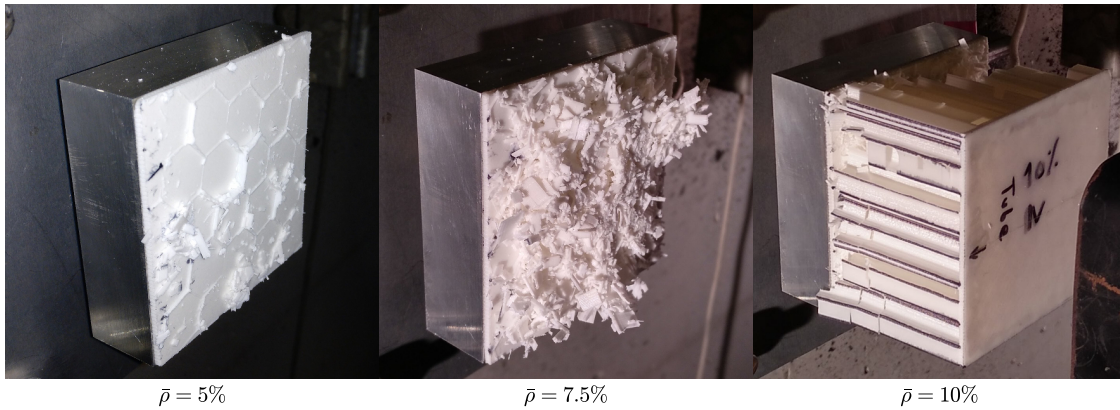


Figure 4.19: Photo of the specimens after being subjected to blast load

core with a 10% relative density was not fully compressed and therefore, relatively intact honeycomb structure is still visible in Figure 4.19.

The average maximum displacement ( $d_{max}$ ), first peak force ( $F_{max}$ ), transmitted impulse ( $i_s^t$ ), efficiency ( $e$ ) and applied work ( $W$ ) are summarised in Table 4.7 for the three relative densities ( $\bar{\rho}$ ), as resulting from the experimental tests. Analysing the values in Table 4.7, it is possible to verify that both the peak force and efficiency tend to increase with relative density. However, in the case of 10% relative density, the crushable core's height was oversized for the given blast load (only partial compression was verified) and therefore, it did not mobilised its full energy dissipation potential. The decrease in the maximum displacement with the increase of relative density (note that similar blast loads were applied to all specimens) yields, as expected, a corresponding decrease of applied work.

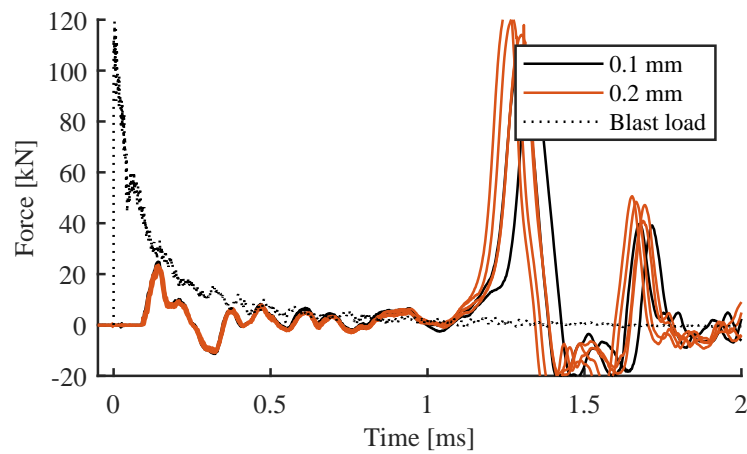
Table 4.7: Summary of the experimental results

$\bar{\rho}$ [%]	$d_{max}$ [mm]	$F_{max}$ [kN]	$i_s^t$ [Pa·s]	$e$ [-]	$W$ [J]
5	88.3	24.8	2,334	0.11	716
7.5	83.1	39.5	2,005	0.20	628
10	39.1	59.4	2,172	0.17	441

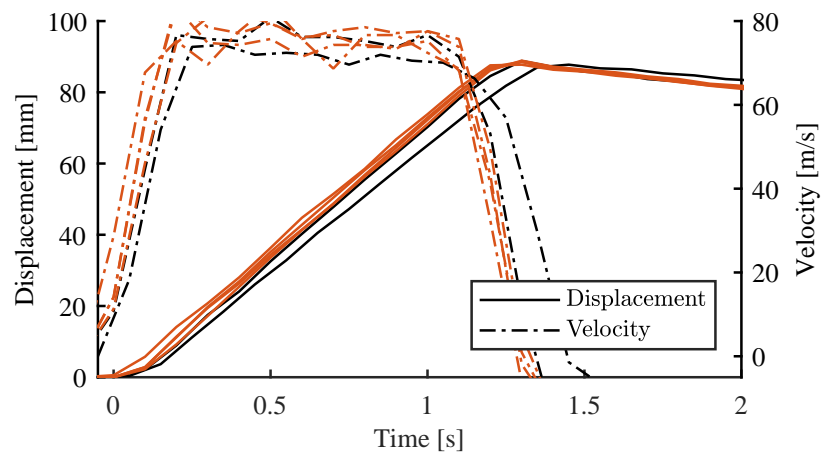
#### 4.4.6.1 Influence of the 3D printing layer height

The influence of the layer height on the energy absorption capabilities of the proposed 3D printed structure was verified. This verification was achieved by maintaining all the properties of the material, the geometry of the honeycomb pattern ( $\bar{\rho} = 5\%$ ), the experimental set-up and applied blast load, while changing the layer height from 0.1 to 0.2 mm during the specimen's manufacturing. Two specimens with a layer height of 0.2 mm were subject to the blast load resulting from a 10 g C4 charge placed at the entrance of the EDST (see Figure 4.15(b)), while four specimens with a layer height of 0.1 mm were experimentally tested. Figure 4.20(a) illustrates the experimental force-time

curves measured with the force sensor for both layer heights, while both the displacement and velocity-time histories, computed resorting to the high speed camera, are shown in Figure 4.20(b). Through the analysis of the referred curves, no influence is observed on the nonlinear response of the proposed sacrificial cladding solution due to 3D printing layer height. Therefore, one might conclude that the proposed crushable core might be manufactured with a 0.2 mm layer height. This options allows for a significant reduction of the manufacturing time.



(a) Force-time history



(b) Displacement and velocity-time histories

Figure 4.20: Influence of layer height on nonlinear reponse of the proposed sacrificial cladding solution

## 4.5 Conclusions

The current chapter reviewed the experimental campaign conducted to attain the mechanical characterisation of unidirectional 3D printed samples with special focus on anisotropy and compression/tension asymmetry under quasi-static regime and their strain rate sensitivity. Firstly, the generic sample preparation (constant throughout the entire study) was briefly presented, followed by the experimental research work performed in a modified electromagnetic compressive split-Hopkinson bar. Tensile tests were also conducted resorting to a universal testing machine, allowing for a better understanding of the anisotropy and asymmetry behaviour of specimens manufactured via the FDM technique.

As expected, the mechanical behaviour of unidirectional 3D printed FDM samples presented significant anisotropy and compressive/tensile asymmetry. Under compressive loads, a difference up to 20% was attained in terms of maximum stress when the angle between the loading direction and the manufacturing direction is considered as either 0 or 90°. Alternatively, for tensile loading, larger differences were found between the inferred maximum stresses, namely when the 0 and 90° values were compared. When the loading direction is aligned with the manufacturing direction (0° orientation), the observed maximum stress was found to be approximately 2.5 times larger than its 90° counterpart. Predictably, the maximum stress recorded when the samples were subjected to tensile loads with a 45° orientation was contained within the values obtained for the other orientations.

The influence of strain rate on the behaviour of 3D printed FDM PLA was evaluated resorting to a split-Hopkinson bar apparatus. Subjecting the cylindrical specimens to compressive loads with three different strain rates (500, 2500 and 5000 s<sup>-1</sup>), it was possible to conclude that the mechanical behaviour of the material greatly depends on the applied strain rate, namely, the maximum stress is inversely proportional to strain rate. A reduction up to 60% was attained when comparing the maximum stresses attained by imparting a quasi-static and dynamic compressive loads on the specimens. Additionally, it was found that, with the increase of strain, the resulting stress seems to tend to a constant value, regardless of strain rate, corresponding to approximately a 25% reduction, when compared with the quasi-static stress at the same true strain.

Subsequently, the nonlinear response of a sacrificial cladding solution was experimentally evaluated in order to analyse its energy absorption capacity. The sacrificial cladding solution, materialised with a 3D printed crushable core and an aluminium front plate, was subjected to a given blast load resorting to an explosive driven shock tube. Three different relative densities were considered in the present study (5, 7.5 and 10%) to evaluate their influence on the nonlinear response under study. Firstly, the reflected pressure-time histories, resulting from two blast scenarios (10 g of C4 positioned at a distance of 50 mm and at the entrance of the EDST), were imparted on a rigid and fixed boundary and recorded resorting to a pressure transducer. The recorded pressure-time

histories will be used in the numerical and simplified models presented in Chapter 5.

An additional preliminary set of experimental tests was conducted to investigate the set-up's influence on the force-time histories recorded by the load cell. Comparing the force-time histories obtained when both set-ups were subjected to the same blast load, one might conclude that the force-time history recorded for set-up 2 follows the applied pressure-time history more closely than the one measured for set-up 1. Additionally, a greater repeatability of the results was verified and a high frequency vibration reduction was visible when the second set-up was used. Therefore, it was concluded that improvements were attained and that the second set-up should be used on the remainder of the experimental campaign.

The sacrificial cladding solutions were then mounted on the second experimental set-up, subjected to a constant blast load and an initial analysis of the attained results was reported. Photographs of the crushable core after the experimental tests clearly shown that the sacrificial cladding solution characterised by a 5% relative density was completely destroyed, while some material remained attached to the back solid plate of the 7.5% relative density core. Contrarily, the crushable core with a 10% relative density was not fully crushed and therefore, relatively intact honeycomb structure was still visible after the experimental test. It was possible to verify that both the peak force and efficiency tend to increase with relative density.

Lastly, the influence of the manufacturing layer height on the energy absorption capabilities of the proposed 3D printed crushable core was verified. Layers heights of 0.1 and 0.2 mm were considered and no influence was observed on the nonlinear response of the proposed sacrificial cladding solution due this manufacturing parameter. Consequently, one might conclude that a significant reduction in manufacturing time might be attained using a 0.2 mm layer height.

## Chapter 5

# Development, verification and validation of numerical models

### 5.1 Introduction

The experimental campaigns reported in the last chapter allow the development, verification and validation of the numerical models described in the current chapter.

The characterisation of the 3D printed PLA's anisotropy and compressive/tensile asymmetry was attained by means of an experimental campaign. These experimental results allow the calibration of one of the anisotropic constitutive models available in the finite element program LS-DYNA [83]. The chosen anisotropic constitutive model, namely the Laminated Composite Fabric is introduced and, based on the experimental results, its properties calibrated for 3D printed FDM PLA. Lastly, in order to verify that a proper calibration was attained, the numerical true stress-true strain curves are compared with the ones obtained experimentally.

The results attained during the previously presented blast testing experimental campaign are used to validate a FE numerical model and a simplified model similar to the one presented by Hanssen and team [51]. The development of both models, which is reported in the current chapter, was achieved resorting to the explicit finite element code LS-DYNA and to the commercial software MATLAB [96], respectively. Additionally, the FE numerical model allows further insights on the nonlinear behaviour of 3D printed crushable cores, specifically on the crushing mechanisms observed in their interior.

### 5.2 Material model calibration

The simulation of the nonlinear behaviour of composite materials throughout the elastic, failure and post-failure phases may be achieved through the use of several material models available in LS-DYNA.

### 5.2.1 Laminated Composite Fabric material model

The Laminated Composite Fabric material model (MAT\_058) can simulate the nonlinear behaviour of composites with unidirectional layers, complete laminates and woven fabrics [83] through a continuum damage mechanics model. This material model was firstly developed by Matzenmiller and co-workers [97] and subsequently implemented in LS-DYNA by Schweizerhof and team [146]. This material model is formulated for plane stress conditions, which corresponds to the state of stress assumed in shell elements.

This material model simulates the nonlinear behaviour of composites by means of three different failure surfaces: a smooth failure surface with a quadratic criterion for both the longitudinal and transverse directions (complete laminates and fabrics); a smooth failure surface in the transverse direction with a limiting value in the longitudinal direction (unidirectional layered composites); and a faceted failure surface (complete laminates and fabrics). Taking into account the manufacturing process of 3D printed walls, it is considered that the smooth failure surface in the transverse direction with a limiting value in the longitudinal direction is the most adequate to model the nonlinear behaviour of these walls. It is assumed that the material model's longitudinal direction is aligned with the manufacturing direction.

#### 5.2.1.1 Lamina behaviour under loading

The behaviour of the composite lamina must be defined both in the longitudinal (fibre) and transverse direction. The longitudinal direction is aligned with the manufacturing direction and, therefore, the stresses in this direction are mainly transmitted through the 3D printed rasters, since no traditional matrix material exists in 3D printed components. Nonetheless, the matrix of these components may be conceptualized as the interlayer adhesion, which will greatly influence the nonlinear behaviour on the transverse direction.

The transmission of tensile loads in the longitudinal direction is not influenced by the state of damage of the interlayer adhesion due to the straightening of the fibres. However, this straightening might contribute to "matrix" damage if the "fibres" damage is absent. Contrary to the observed under tensile loading, the effective stiffness and strength of the interlayer adhesion greatly affects the behaviour of the rasters when carrying compressive loads. Additionally, both failure and buckling of "fibres" under tensile and compressive loads, respectively, cause the appearance of damage on the interlayer adhesion.

Both normal (transverse direction) and shear stresses are transmitted through both constituents of the 3D printed component. Damage is usually observed on the interlayer adhesion, mainly under tensile loading in transverse direction, due to the layered microstructure resulting from the manufacturing process. As expected, the tensile load-carrying capacity of the rasters in the longitudinal direction is not influenced by the transverse and shear stresses. Consequently, their limited contribution to tensile "fibre" damage is neglected by the material model.

### 5.2.1.2 Constitutive assumptions

The constitutive model proposed by Matzenmiller and co-workers [97] is based on several mechanical idealisations, as summarized:

- The theoretical basis of this constitutive model, in the case of unidirectional lamina, is provided by a homogenized continuum, in combination with plane stress conditions;
- Linear elasticity is assumed to hold until a change in the damage state is verified, which implies linear elastic unloading and reloading in the stress-strain space;
- The nonlinear effects are a result of damage, and therefore no plastic deformations are supposed to develop;
- The lamina's orthotropic nature as a homogenized continuum does not change with the increase of damage. Therefore, the symmetry class of the unidirectional lamina remains the same regardless of the damage state.

### 5.2.1.3 Failure modes and criteria

The present material model uses the methodology proposed by Hashin [55] to determine the failure criteria of the corresponding modes. Primarily, the failure modes may be categorized into fibre (*I* and *II*) and matrix (*III* and *IV*) failure modes. The failure planes, on which normal and shear stresses act, are considered to be perpendicular to the fibres for their failure modes, whereas the matrix modes occur in planes tangential to the fibres, as depicted in Figure 5.1.

Considering a three-dimensional transversely isotropic continuum, whose fibres are align with the  $e_1$  axis, the failure criterion must be invariant for every rotation of the  $e_2, e_3$  axes around  $e_1$ . Therefore, the general form of a failure criterion can be at most a function of the stress invariants under such rotations (see Hashin [55] for more details). The failure criterion is considered to be approximated by a complete quadratic polynomial in terms of such invariants, split into four independent criteria according to the

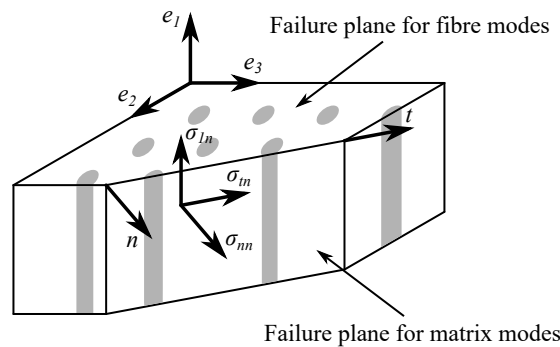


Figure 5.1: Failure planes of the lamina (Adapted from [97])

previously defined failure planes, which may be subsequently subdivided into tensile and compressive modes. The coefficients of the quadratic polynomials may be related to four strength parameters  $X_{c,t}$ ,  $Y_{c,t}$ , where  $X$  and  $Y$  refer to the fibre and matrix loading direction, respectively, and subscripts  $c$  and  $t$  indicate either compressive or tensile loading, respectively. The material model assumes that the transverse and axial shear strength may be considered as equal and denoted by  $S_c$ . Applying plane stress conditions ( $e_1$ - $e_2$  plane) to the four failure criteria, one obtains the following:

Tensile fibre mode *I* ( $\sigma_{11} \geq 0$ ):

$$e_m^2 = \left( \frac{\sigma_{11}}{X_t} \right)^2 - 1 \quad \begin{cases} \geq 0 & \text{failed} \\ < 0 & \text{elastic} \end{cases} \quad (5.1a)$$

Compressive fibre mode *II* ( $\sigma_{11} < 0$ ):

$$e_c^2 = \left( \frac{\sigma_{11}}{X_c} \right)^2 - 1 \quad \begin{cases} \geq 0 & \text{failed} \\ < 0 & \text{elastic} \end{cases} \quad (5.1b)$$

Tensile matrix mode *III* ( $\sigma_{22} \geq 0$ ):

$$e_c^2 = \left( \frac{\sigma_{22}}{Y_t} \right)^2 + \left( \frac{\tau}{S_c} \right)^2 - 1 \quad \begin{cases} \geq 0 & \text{failed} \\ < 0 & \text{elastic} \end{cases} \quad (5.1c)$$

Compressive matrix mode *IV* ( $\sigma_{22} < 0$ ):

$$e_d^2 = \left( \frac{\sigma_{22}}{Y_c} \right)^2 + \left( \frac{\tau}{S_c} \right)^2 - 1 \quad \begin{cases} \geq 0 & \text{failed} \\ < 0 & \text{elastic} \end{cases} \quad (5.1d)$$

The failure criteria, which is valid for unidirectional layered composites, is interpreted as a ‘‘loading’’ criteria (using strain space plasticity terminology) which establishes the threshold variables in the damage model. According to classical continuum mechanics, only the undamaged part of a cross section, commonly referred to as net area, is able to transmit stresses. Therefore, the stresses  $\sigma_{ij}$  used by the above criteria should be interpreted as effective stresses  $\hat{\sigma}_{ij}$ , with respect to the net area. The relation between effective and nominal (true) stresses may be found in equation (5.2) as a function of a set of damage parameters  $\omega$ . One should note that damage parameters  $\omega_{11}$  and  $\omega_{22}$  take different values for tensile and compressive load, allowing the consideration of the tension/compression asymmetry observed in several materials. On the contrary, the shear damage parameter  $\omega_{12}$  is independent of the sign of  $\tau$ .

$$\begin{bmatrix} \hat{\sigma}_{11} \\ \hat{\sigma}_{22} \\ \hat{\tau} \end{bmatrix} = \begin{bmatrix} \frac{1}{1-\omega_{11}} & 0 & 0 \\ 0 & \frac{1}{1-\omega_{22}} & 0 \\ 0 & 0 & \frac{1}{1-\omega_{12}} \end{bmatrix} \begin{bmatrix} \sigma_{11} \\ \sigma_{22} \\ \tau \end{bmatrix} \quad (5.2)$$

The constitutive tensor  $\mathbf{C}$  used by the material model (see definition (5.3)) is defined by means of the undamaged lamina’s material parameters and damage parameters  $\omega$ , with



$D = 1 - (1 - \omega_{11})(1 - \omega_{22})\nu_{12}\nu_{21} > 0$ . Note that, normal stress contributions, that arise from Poisson effect, vanish as either of the damage variables  $\omega_{11}$  and  $\omega_{22}$  approaches unity.

$$\mathbf{C}(\boldsymbol{\omega}) = \frac{1}{D} \begin{bmatrix} (1 - \omega_{11})E_{\parallel} & (1 - \omega_{11})(1 - \omega_{22})\nu_{21}E_{\perp} & 0 \\ (1 - \omega_{11})(1 - \omega_{22})\nu_{12}E_{\parallel} & (1 - \omega_{22})E_{\perp} & 0 \\ 0 & 0 & D(1 - \omega_{12})G \end{bmatrix} \quad (5.3)$$

The current state of damage suffers no change if the stress state lies inside the elastic range defined by the loading criterion in stress space  $f(\boldsymbol{\sigma}, \boldsymbol{\omega}, \mathbf{r})$  in terms of the stresses  $\boldsymbol{\sigma}$ , the damage variables  $\boldsymbol{\omega}$  and the damage thresholds  $\mathbf{r}$ , which measure the size of the elastic region. The required loading surfaces may be defined in the space of effective stresses if stress components  $\sigma_{ij}$  in the failure criteria (equations (5.1a) to (5.1d)) are replaced resorting to equation (5.2). Subsequently, loading surfaces  $f_{\parallel}$  (fibre modes *I* and *II*) and  $f_{\perp}$  (matrix modes *III* and *IV*) are as follows:

$$f_{\parallel} = \frac{\sigma_{11}^2}{(1 - \omega_{11c,t})^2 X_{c,t}^2} - r_{\parallel c,t} = 0 \quad (5.4)$$

$$f_{\perp} = \frac{\sigma_{22}^2}{(1 - \omega_{22c,t})^2 Y_{c,t}^2} + \frac{\tau^2}{(1 - \omega_{12})^2 S_c^2} - r_{\perp c,t} = 0 \quad (5.5)$$

Figure 5.2 illustrates the previously defined loading criterion, clearly composed by different surfaces, in the effective stress space.

#### 5.2.1.4 Damage evolution

Once the state of stress lies outside of the failure criteria, it is assumed that the state of damage will change. Several evolution laws may be used to control the change of the damage parameters (see Matzenmiller et al. [97] for more details). The Laminated Composite Fabric material model, with a smooth failure surface in the transverse direction

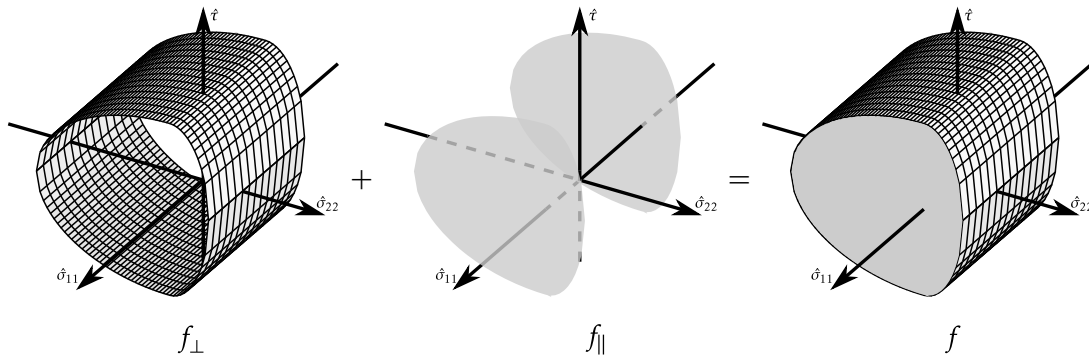


Figure 5.2: Multisurface  $f$ , formed by  $f_{\perp}$  and  $f_{\parallel}$  in the effective stress space

and a limiting value in the longitudinal direction, uses the following evolution law,

$$\omega_i = 1 - e^{-\frac{1}{m_i} \left( \frac{\varepsilon_i}{\varepsilon_f} \right)^{m_i}} \quad (5.6)$$

where  $\varepsilon_f$  is the nominal failure strain:

$$\varepsilon_{f\parallel} = \frac{X_{c,t}}{E_{\parallel}}; \quad \varepsilon_{f\perp} = \frac{Y_{c,t}}{E_{\perp}} \quad (5.7)$$

The presented evolution law yields a smooth increase of damage, i.e. no sudden change of behaviour is observed. Parameters  $m_i$  control the evolution of the different failure modes such as tension, compression and shear in the various directions depending on the strains. Subsequently, a damage parameter  $\omega_i$  is determined for each direction and a stress-strain relation may be computed. Note that a unitary value of  $\omega_i$  corresponds to complete damage.

Nonetheless, in order to avoid localization effects on FE analysis, Schweizerhof and co-workers [146] implemented a simple modification to the damage evolution law. The modification introduces a threshold value, referred to as the limit stress, such that the stress does not go under the defined value. The evolution law shown in equation (5.6) is used until this limit stress is attained. Then the evolution law for damage parameter  $\omega_i$  becomes:

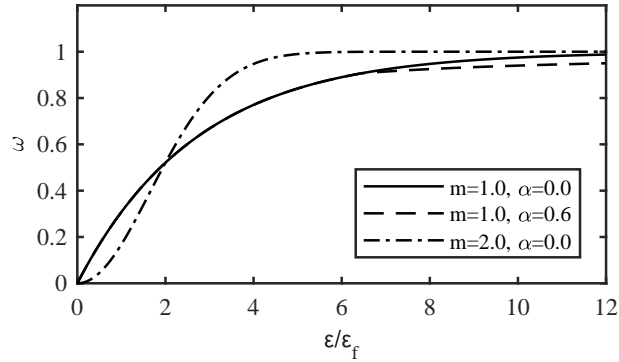
$$\omega_{i\parallel} = 1 - \frac{\alpha X_{c,t}}{E_{\parallel} \varepsilon}; \quad \omega_{i\perp} = 1 - \frac{\alpha Y_{c,t}}{E_{\perp} \varepsilon} \quad (5.8)$$

Parameter  $\alpha$  ( $0 \leq \alpha \leq 1$ ) characterizes the relation between the threshold value and the corresponding strength value ( $X_{c,t}$  and  $Y_{c,t}$ ). It is important to refer that, when  $\alpha < 1$ , localization effects are still present and, consequently, damage growth is only present in the first damaged elements. Nonetheless, if no softening is considered ( $\alpha = 1$ ), this effects disappear.

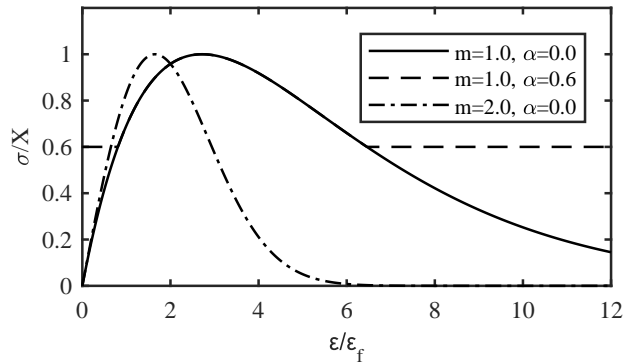
Figure 5.3 depicts the graphical representation of the damage evolution laws as a function of the normalized strain  $\varepsilon/\varepsilon_f$ . Specifically, in Figure 5.3(a), it is possible to observe the influence of  $m$  on the evolution of damage parameter  $\omega$  when the modified evolution law is not considered ( $\alpha = 0$ ). Additionally, analysing the normalized stress-strain curves presented in Figure 5.3(b), one might verify that, when no limit value is specified, the stress values diminish until a null stress is reached ( $\omega = 1$ ). Contrarily, despite the increase of damage visible in Figure 5.3(a), the modified evolution law yields a constant stress ( $0.6X$  for the present example) after the defined limit value has been reached, as shown in Figure 5.3(b).

### 5.2.1.5 Typical stress-strain curve definition

The typical stress-strain curve for both longitudinal and transverse directions, subjected to either compressive or tensile uniaxial loading, is depicted in Figure 5.4, allowing the



(a) Damage parameter



(b) Normalized stress-strain diagram

Figure 5.3: Damage evolution law

analysis of its correlation with the input required by LS-DYNA. The initially elastic response of the material in the longitudinal ( $A$ ) and transverse ( $B$ ) directions is defined via the corresponding initial Young's modulus  $E_A$  and  $E_B$ . This response is followed by a nonlinear response, according to the previously presented material model, until the maximum strength is reached, at which the longitudinal and transverse strain at maximum strength  $E_{11}$  and  $E_{22}$  is verified, respectively. Subsequently, a softening response is verified until a limit stress, defined by the "stress limiting factor"  $S_{LIM}$ , is attained and the strength is kept constant until the element layer failure strain ( $ERODS$ ) is reached.

As a result of the use of a smooth failure surface in the transverse direction with a limiting value in the longitudinal direction, the shear stress versus strain response is considered to be similar to the one illustrated in Figure 5.4. Following an initially elastic response, defined by  $G_{AB}$ , the nonlinear strength is capped at the maximum shear strength  $S_C$ , in combination with the corresponding shear strain  $GMS$ . Similarly, once the maximum shear strength is reached, a reduction on the shear stress, resorting to the "shear stress limiting factor", is observed. Lastly, the deletion of the element layer is performed at the strain parameter  $ERODS$ .

The material model accounts for strain rate effects on both the maximum strength and the corresponding strain through an input curve. This effect on the referred material

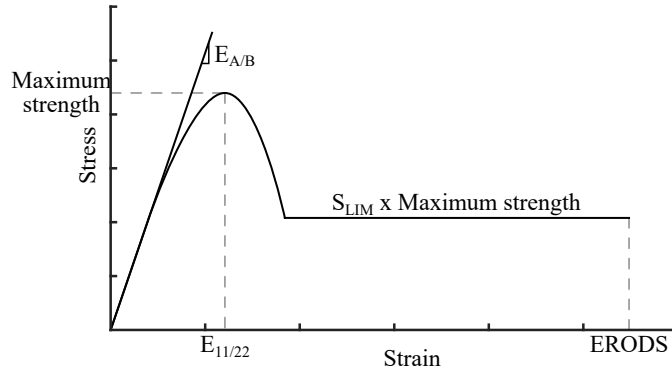


Figure 5.4: Typical MAT058 stress-strain curve for longitudinal and transverse directions (compression/tension)

properties is independent on the five considered directions, i.e. a unique tensile and compressive curve for the longitudinal and transverse directions may be defined, while the shear behaviour only requires a single curve.

#### 5.2.1.6 Material model properties for PLA

The complete set of properties that define the MAT058 material model, as used in the present study to simulate the nonlinear response of anisotropic 3D printed PLA, are listed in Tables 5.1 and 5.2. The alignment of the material axes is achieved by means of the *AOPT* parameter, in combination with the cross product of a vector (user defined) and the shell elements' normal.

Table 5.1: Material model properties for PLA

Material property	Value	Unit
Density	1,250	kg/m <sup>3</sup>
Longitudinal Young's modulus, $E_a$	2.84	GPa
Transverse Young's modulus, $E_b$	2.26	GPa
Poisson's ratio, $\nu_{ba}$	0.26	-
Shear modulus, $G_{ab}$	0.908	GPa
Longitudinal compressive strength, $X_C$	72.94	MPa
Longitudinal tensile strength, $X_T$	39.63	MPa
Transverse compressive strength, $Y_C$	90.05	MPa
Transverse tensile strength, $Y_T$	26.42	MPa
Shear strength, $S_C$	58.24	MPa
Strain at longitudinal compressive strength, $E_{11C}$	0.053	-
Strain at transverse compressive strength, $E_{22C}$	0.063	-

Table 5.2: Nonphysical parameters for material model

Material property	Value	Unit
Material axes option, $AOPT$	3	-
Time step for automatic element deletion, $TSIZE$	$5 \times 10^{-9}$	s
Maximum strain for layer failure, $ERODS$	2.0	-
Stress limit factor under longitudinal compression, $S_{LIMC1}$	0.65	-
Stress limit factor under transverse compression, $S_{LIMC2}$	0.54	-

### 5.2.2 Numerical model

In order to verify the behaviour of the MAT\_058 material model, compressive and tensile tests were simulated on single square elements with two orientations (0 and 90°), see Figure 5.5. The yielding true stress-true strain response was compared with the experimental results reported in Chapter 4 to check the proper calibration of the model's parameters.

Belytschko-Wong-Chiang shell elements with a 2.5 mm edge ( $l_0$ ) and one integration point on the thickness (0.43 mm) were used. Their out-of-plane displacement was constrained, together with the boundary conditions and loading velocity depicted in the referred figure. The quasi-static response of the material was obtained through the application of a 0.4 m/s loading velocity, while no strain rate sensitive parameters were introduced in the material model. The inertial effects may be disregarded due to reduced mass of the element<sup>1</sup>. The high strain rate response of the material model was attained by applying a constant true strain rate  $\dot{\epsilon}$  to the square element, which is achieved by applying the following loading velocity:  $v(t) = \dot{\epsilon} l_0 \exp(-\dot{\epsilon} t)$ . The presented true stress and strain may be obtained either directly from the integration point of the FE, or computed from the obtained reaction forces at the bottom nodes and the displacements at the top nodes.

#### 5.2.2.1 Belytschko-Wong-Chiang shell element (ELFORM 10)

The Belytschko-Lin-Tsay shell element (ELFORM 2) is commonly the shell element of choice for explicit calculations due to its computational efficiency. This shell element is based on a combined co-rotational and velocity-strain formulation [50]. These two kinematic simplifications yield several mathematical simplifications and, consequently, lead to the efficiency of the element. The co-rotational part of the element formulation allows the avoidance of the complexities resulting from nonlinear mechanics through the use of a local coordinate system in the element. Additionally, the velocity-strain formulation simplifies the constitutive evaluation, since the conjugate stress is the physical Cauchy stress.

The mid-surface of the quadrilateral shell element, commonly referred to as reference surface, is determined by the nodal coordinates of the element. The embedded element

<sup>1</sup>The FE estimates for the inertial effect yielded maximum stresses less than 1% when compared to the ones resulting from the loading (see Figures 5.6 and 5.7).

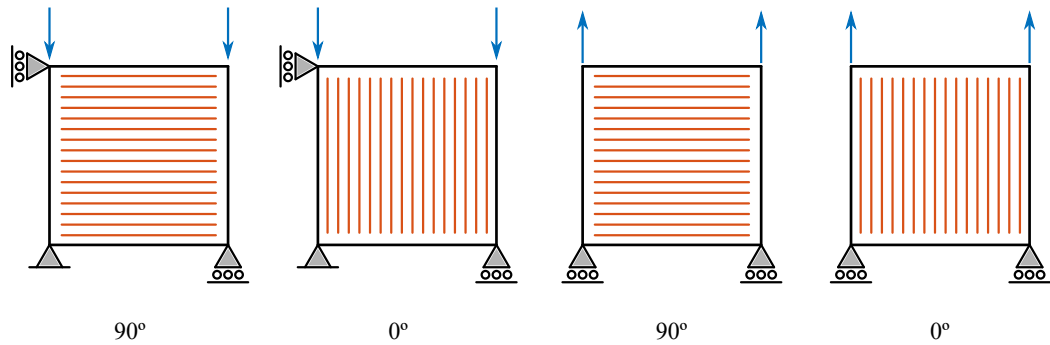


Figure 5.5: Schematic of the single element compression/tension simulations

co-rotational coordinate system, which is tangent to this surface and deforms with the element, serves as a local coordinate system. The velocity-strain of a given point in the shell's reference surface is defined in terms of the velocity of the mid-surface and the angular velocity vector using the Mindlin-Reissner theory of plates and shells. Since the velocity-strain relations need to be evaluated at the location of the quadrature points, a standard bilinear nodal interpolation is used. Subsequently, Cauchy stresses are determined in the co-rotational system from the velocity-strain and the suitable constitutive model, allowing their integration through the thickness of the shell to attain local resultant forces and moments. The force and moment resultants at the centre of the element are related to the local nodal forces and moments through the principle of virtual work and integrating with a one-point quadrature.

The Belytschko-Lin-Tsay shell element, despite performing well for most practical applications, performs poorly when warped since it is based on a flat geometry. To overcome this limitation, additional terms are implemented into the strain-displacement equations and a shear projection is used to compute the transverse shear. These improvements are referred to as Belytschko-Wong-Chiang improvements hence, the shell element's designation (ELFORM 10).

### 5.2.3 Results

Figures 5.6 and 5.7 illustrate the experimental and numerical results of the quasi-static uniaxial tests. Analysing the referred figures, one can readily conclude that a good correlation between the experimental and numerical results was attained for the anisotropic response of 3D printed specimens under unidirectional quasi-static loading.

The behaviour of the material under compressive loading is characterized by an initial elastic phase, followed by a nonlinear response up to the maximum stress. The increase of approximately 20% in the maximum stress when the specimen is loaded perpendicularly to the printing direction as opposed to parallel is correctly recovered by the material model. When the maximum stress is reached, a softening phase follows until the stress drops to the specified limit. The angle between the printing and loading directions seems

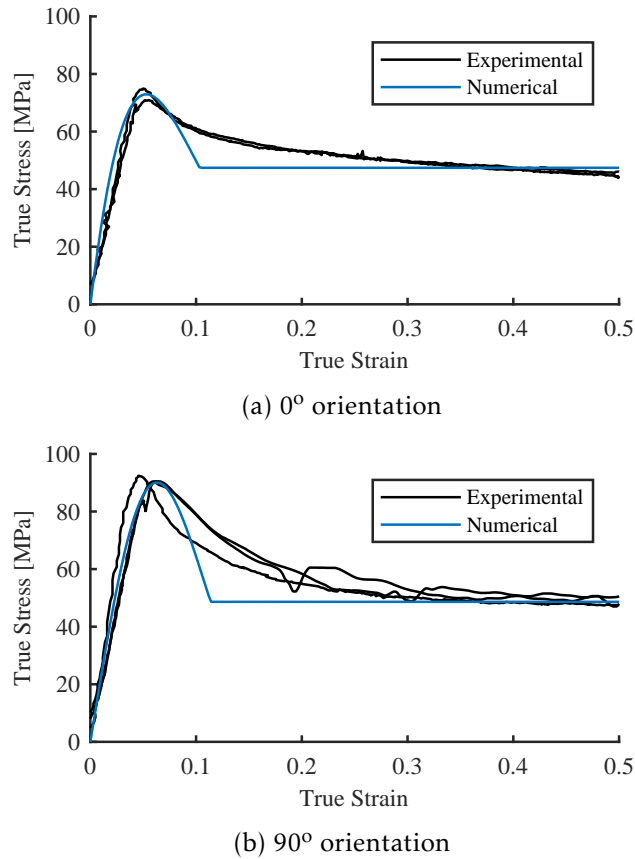


Figure 5.6: Experimental and numerical stress-strain curves under compressive loading

to be less important with the increase of strain, as clearly noticeable in Figure 5.6. Observing the stress-strain curves depicted in Figure 5.7(b), an elastic behaviour is evident on the tensile behaviour of PLA up to a brittle failure, regardless of the printing orientation.

A large difference between the experimental and numerical initial elastic response of the material under compressive and tensile loading, when the loading direction is aligned with the manufacturing orientation, is verified through the observation of Figures 5.6(a) and 5.7(a). This difference results from the inability of the material model to distinguish between compressive and tensile loading when defining the stiffness properties of the composite material. The maximum strength was still correctly modelled when the specimens are subjected to both compressive and tensile loading with an angle of  $0^\circ$  with respect to the manufacture orientation.

Figure 5.8 presents the experimental and numerical true stress-true strain curves obtained when the bulk material, considering a  $90^\circ$  orientation, is subjected to compressive high strain rate loads. In the referred figure, one may verify that the maximum strength of the material is correctly simulated for the considered strain rates. Nonetheless, two limitations may be identified for the material model: firstly, contrary to the observed on the experimental data, the elastic properties of the material remain constant under any strain rate; secondly, despite scaling the maximum strength according to the input curve,

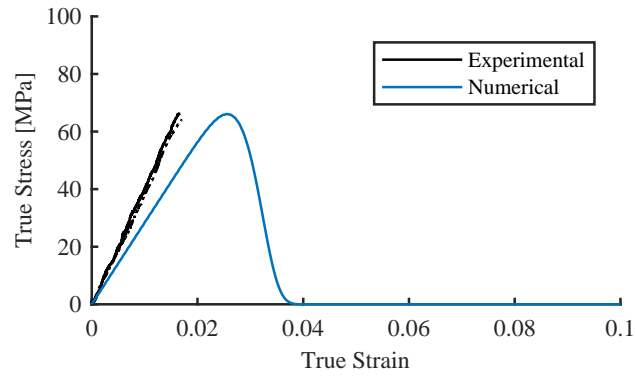
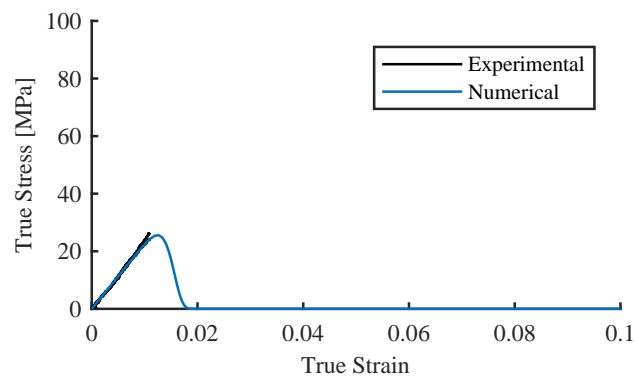
(a)  $0^\circ$  orientation(b)  $90^\circ$  orientation

Figure 5.7: Experimental and numerical stress-strain curves under tensile loading

the material model does not consider the influence of strain rate on the “stress limiting factor”. Consequently, the plateau stress after softening follows the maximum strength curve multiplied by the referred factor, leading to a slight overestimation of this stress, when compared with experimental values.

It should be noted that, although the material model has the ability to consider strain rate effects on the maximum strength and corresponding strain, due to the lack of experimental results for all the five possible directions, strain rate effects will not be taken into account in the following section.



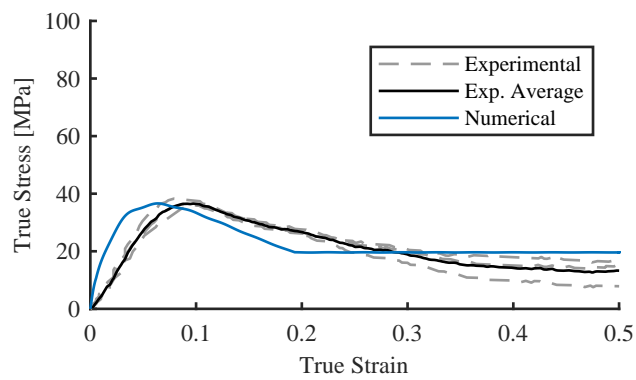
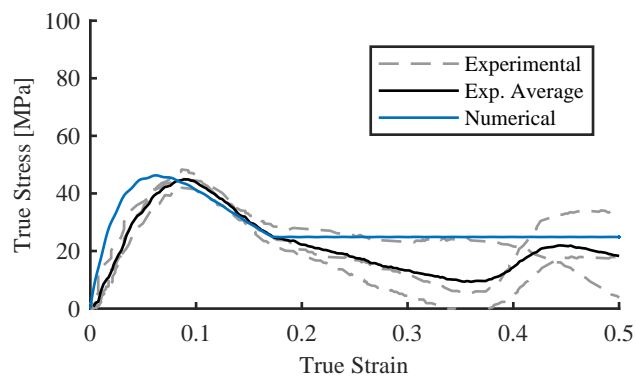
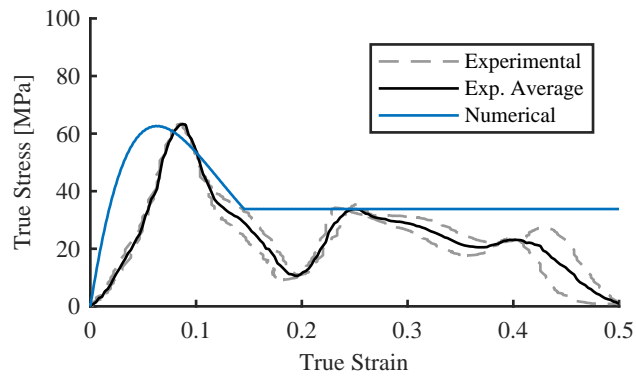


Figure 5.8: Experimental and numerical stress-strain curves under high strain rate compressive loading

### 5.3 Blast testing

The current section aims to present the development of a FE numerical model and a simplified model similar to the one presented by Hanssen and team [51], which will be used to simulate the nonlinear response of the 3D printed crushable core under blast loading. The results obtained with both models will be compared with the ones recorded during the blast testing experimental campaign in order to verify their validity.

#### 5.3.1 FE numerical model

According to the preliminary test results presented in Section 4.4.5, the set-up clearly influences the force-time history recorded by the force sensor. Therefore, the complete set-up must be taken into account for the numerical simulation of the nonlinear response of the 3D printed crushable cores.

Figure 5.9 illustrates the numerical model used to take into account the effects of the set-up on the obtained results. The PCB force sensor was discretised with a set of translational springs, which are assumed to be massless [50]. As shown in the referred figure, these springs are two-node elements that connect the face nodes of the aluminium components (one node on each component). The aluminium components that were in contact with the force sensor were modelled using fully integrated solid elements (see Section 5.3.1.1) due to the presence of concentrated loads, which result from the translational springs. All the remaining aluminium components were simulated resorting to constant stress solid elements (see Section 5.3.1.1). The fixation of the supports to the wall, which is considered as rigid, and the fastening of the aluminium rear plate, force sensor and the remainder of the set-up (see Figure 4.17(b) for more details) was materialised with M10 steel bolts, which were modelled with spotweld beam elements (see Section 5.3.1.2) on the present study. Lastly, the steel washers were simulated using Belytschko–Tsay shell elements (see Section 5.2.2.1) with a thickness of 2 mm and 2 integration points on the thickness.

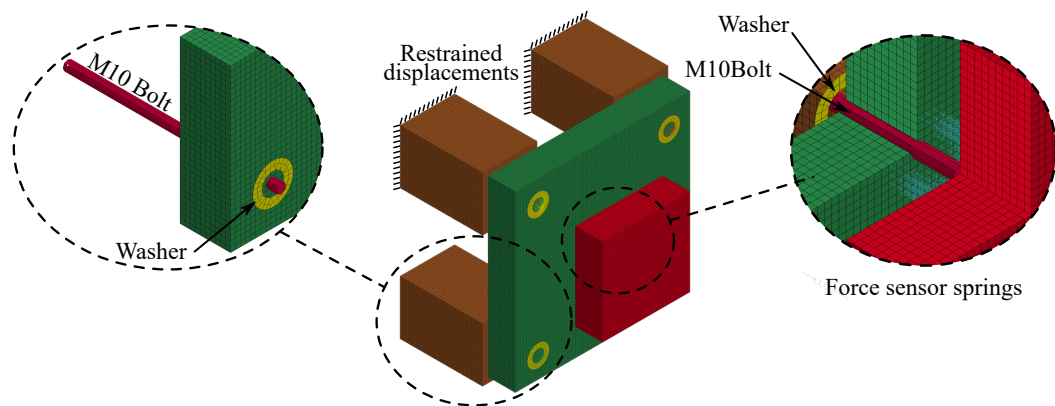


Figure 5.9: FE model of the set-up

As schematically represented in Figure 5.9, the displacements at the end of the supports and the M10 bolts, which fixed the remainder of the set-up to the wall, were restrained in all directions. To ensure the correct transmission of loads between the bolts and the washers, a `NODAL_RIGID_BODY` constrain was defined for each bolt and washer set, while an `AUTOMATIC_SURFACE_TO_SURFACE` contact guaranteed the correct interaction between the washers and the aluminium components of the set-up.

The numerical model of the several components of the sacrificial cladding solution is depicted Figure 5.10, from which one may verify that both shell (crushable core) and solid (front plate) elements were used. The crushable core, composed by the honeycomb structure (0.43 mm thickness) and the top and bottom plates (2 mm thickness), was modelled using Belytschko-Wong-Chiang shell elements (`ELFORM 10`) with 5 integration points on the thickness.

Several contact algorithms were used to correctly transmit loads throughout the several components. A `TIED_SURFACE_TO_SURFACE` contact with a soft constrain formulation was defined between both top and bottom 3D printed solid plates and the front and rear plate, respectively. According to LS-DYNA's theory manual [50], the soft constrain formulation is recommended for cases with a large difference of elastic bulk moduli, aluminium and PLA in the present study. An `ERODING_SURFACE_TO_SURFACE` contact was used to ensure the correct simulation of the interaction between the 3D printed solid plates and the honeycomb structure, while the interaction of the latter with itself was achieved via an `AUTOMATIC_SINGLE_SURFACE` contact.

Considering the geometry of the explosive driven shock tube, the overpressure profile depicted in Figure 4.15(b), obtained when the blast load is applied to a rigid and fixed boundary, is applied to a specific area of  $75 \times 75 \text{ mm}^2$  on the front plate by means of the `LOAD_SEGMENT_SET` keyword.

As recommended by the LS-DYNA's user manual [83], second order objective stress

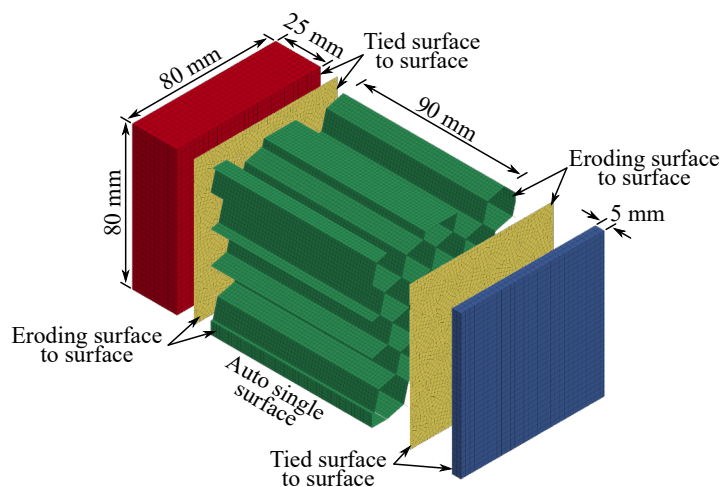


Figure 5.10: FE model of the sacrificial cladding solution

update was activated, since large strains are expected in a number of time steps. Additionally, due to the presence of shells with anisotropic materials on the numerical model and the likelihood of element distortion, the invariant node numbering for shell elements was prompted.

FE software LS-DYNA resorts to a modified central difference method to perform time integration. Despite being a fast and simple method, the time step used with this explicit method must satisfy the Courant's condition in order to converge to a stable solution [50]. LS-DYNA automatically computes the required time step as a function of the local speed of sound of every FE, i.e. the resulting time step size roughly corresponds to the time required by an acoustic wave to travel across each element (considering the shortest characteristic distance). Subsequently, this time step is multiplied by scale factor TSSFAC, which was set to 0.6 in the present study since the effects of high explosives are present in the numerical model [83].

#### 5.3.1.1 Solid elements

The default solid element formulation in LS-DYNA is a 8-node hexahedron with one-point integration (ELFORM 1). This allows substantial savings in computational time, due to an anti-symmetry of the strain matrix, savings on the strain and element nodal force computations and, lastly, only one constitutive evaluation is required. Therefore, the element may be classified as a sub-integrated constant stress solid element, which is efficient, accurate and performs well under severe deformations. However, as a result of the sub-integration, zero energy modes, which are commonly referred to as hourglass modes, may arise. Consequently, the undesirable zero energy modes must be controlled by means of a hourglass formulation, usually composed by viscous damping or small elastic stiffness that stops the development of the referred modes, while having a negligible effect on the global response. Alternatively, the fully integrated solid element (ELFORM 2) uses selectively reduced integration in order to alleviate volumetric locking, while not requiring any form of hourglass control. However, its response is regarded as too stiff as a result shear locking when it possesses a poor aspect ratio [50].

#### 5.3.1.2 Hughes-Liu beam element (ELFORM 1)

The Hughes-Liu beam element formulation, on which the spotweld beam formulation beam (ELFORM 9) is based, is based on a degeneration of the isoparametric 8-node solid element. According to the LS-DYNA's theory manual [50], it possesses several qualities, such as being incrementally objective (rigid body rotations do not create strains); being simple, which commonly yields computational efficiency and robustness; being compatible with 8-node solid elements; and the inclusion of finite transverse shear strains with an insignificant increase of computations. The computation of the beam's internal forces is performed with one integration point along the beam's axis and a  $2 \times 2$  Gauss quadrature rule in the cross section.

### 5.3.1.3 Hourglass control

To suppress zero energy modes that arise from the use of one-point quadrature, both in solid and shell elements, hourglass forces are added to the physical forces at the local element level. Hourglass control may be subdivided into viscous and stiffness forms. The former considers that hourglass forces are proportional to components of nodal velocities that contribute to hourglass modes, while the latter computes them as a function of the relevant nodal displacement components. Viscous form of hourglass control prevents the increase of hourglass deformation. However, it is not able to remove previously acquired deformation. On the other hand, stiffness forms are able to reduce previously accumulated deformation but may stiffen structural response if not used with care.

According to the LS-DYNA's user manual [83], six different forms of hourglass control are applicable to solid elements:

- Standard LS-DYNA viscous form (IHQ = 1);
- Flanagan-Belytschko viscous form (IHQ = 2);
- Flanagan-Belytschko viscous form with exact volume integration (IHQ = 3);
- Flanagan-Belytschko stiffness form (IHQ = 4);
- Flanagan-Belytschko stiffness form with exact volume integration (IHQ = 5);
- Belytschko-Bindeman assumed strain co-rotational stiffness form (IHQ = 6).

By default, the Flanagan-Belytschko viscous form is used, in combination with a hourglass coefficient (QM), which scales the hourglass forces, of 0.1. However, according to Schwer and team [147], only the hourglass control formulations that use exact volume integration are able to pass the performed three-dimensional patch test. Additionally, it is known that, although they may artificially stiffen the response, stiffness forms of hourglass are more efficient than their viscous counterparts. Therefore, in order to minimize stiffening of the response, it is recommended to reduce the hourglass coefficient to a value in the range of 0.03 to 0.05 [83].

On the other hand, a single viscous and stiffness form of hourglass control is available in LS-DYNA for shell elements. Flanagan-Belytschko stiffness form with exact volume integration (IHQ = 5) was used in the numerical model of both the set-up and the sacrificial cladding solution. Special care was employed to ensure that the hourglass energy was inferior to 10% of internal energy in the entire model and for each part.

### 5.3.1.4 Contact modelling

Three different methods have been implemented in LS-DYNA to handle sliding and impact along interfaces: the kinematic constraint, the penalty and the distributed parameters methods. The interfaces to be considered are usually composed by a set of triangular

and/or quadrilateral segments on each side, which are categorised as the slave and the master. Automatic contact definitions are commonly used nowadays due to the internal generation of the slave and master surfaces from the part ID's given for each surface.

The penalty method was used in the present study to ensure the correct simulation of sliding and impact between the several components of the numerical model. The method places normal interface springs between all penetrating nodes and the contact surface. The standard penalty formulation automatically determines a unique stiffness, such as to be approximately the same order of magnitude as the stiffness of the interface element (normal to the interface). Contrarily to the kinematic constraint method, the penalty method does not significantly excites hourglass modes, as a result of the symmetry of the approach. Additionally, the imposing of impact and release conditions, required by the kinematic constraint method to insure momentum conservation, do not need to be used since the penalty method exactly conserves momentum. Lastly, the implementation of the penalty method is greatly simplified, since no further treatment of the intersecting interfaces is required.

Closure and separation of the contact interface is automatically considered by the penalty method, since each slave node is checked for penetration across the master surface. If no penetration is observed, no action is required. On the contrary, an interface force, whose magnitude is proportional to the amount of penetration (interface spring), is applied between the slave node and its contact point. As previously referred, the method automatically computes the penalty stiffness value based on the stiffness of the interface element. More specifically, the standard penalty method resorts to the minimum of the master segment and slave node stiffness. Nonetheless, when the materials in contact possess a considerable difference in bulk moduli, an excessively small stiffness may be used and yield excessive penetration. Alternatively, for such cases, the soft constrain penalty formulation is recommended by LS-DYNA's user manual [83]. In addition to the previously referred stiffness values, a third one is computed, based on the stability (Courant's criterion) of the local system, which is composed by two masses (segments) connected by a spring. Subsequently, the contact stiffness values computed by the standard and soft constrain penalty formulations are compared and, in general, the larger of the two is taken [50].

### 5.3.1.5 Material modelling

An elastic material model was considered for the constitutive relation of the aluminium components, the steel washers and the 3D printed top and bottom PLA plates, since no damage was observed during the reported experimental blast testing campaign. The material properties used for aluminium and steel are shown in Table 5.3, while the PLA elastic properties were based on the average elastic properties used for the Laminated Composite Fabric material model (see Table 5.1). The force sensor was considered to have an elastic behaviour with a stiffness computed as the total stiffness of the sensor,

Table 5.3: Material properties for aluminium and steel

Material	Density [kg/m <sup>3</sup> ]	Young's modulus [GPa]	Poisson's ratio
Aluminium	2,760	72	0.34
Steel	7,860	210	0.30

4 kN/ $\mu\text{m}$  [125], divided by the number of strings used in the FE model.

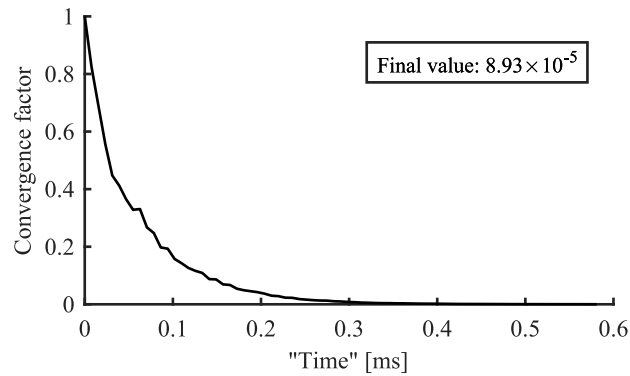
The M10 steel bolts were modelled using the SPOTWELD material model, whose elastic properties are those of steel and the nonlinear behaviour is based on an isotropic hardening plasticity coupled to two failure models, which were not activated in the present study. Since no plastic behaviour was observed on the bolts during the experimental campaign, the initial yield stress was considered to be 1% of the Young's modulus, i.e. 2.1 GPa.

#### 5.3.1.6 Dynamic relaxation

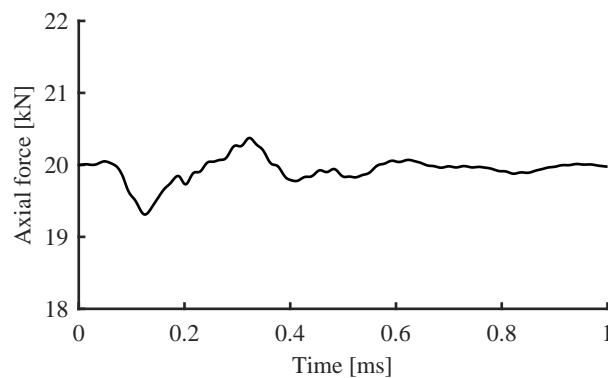
Dynamic relaxation is available in LS-DYNA to approximate solutions (stress and displacement fields) to linear and nonlinear static or quasi-static processes during the initialization phase of a numerical model. In the referred phase, only the specified loads curves are used to apply the quasi-static loads like a normal explicit LS-DYNA computation but with the inclusion of damping to the displacement field update. Therefore, a damping coefficient factor must be selected in order to obtain convergence to the quasi-static solution in minimal time. The relaxation process continues until a convergence criterion, which is based on the global kinetic energy and a tolerance, is met. Note that, rigid body components are excluded when the kinetic energy is computed [50].

As referred in Section 4.4.2, a 20 kN preload was applied to all M10 bolts. This preload was applied to all the bolts present on the numerical model by means of dynamic relaxation and the INITIAL\_AXIAL\_FORCE\_BEAM keyword. A value of 0.995 was used as the damping coefficient factor, while a  $10^{-4}$  convergence tolerance was considered. The preload was applied linearly until a value of 20 kN is reached and, maintained constant during the remainder of the relaxation process, i.e. until convergence was achieved. Subsequently, the stress and displacement fields are saved, time is reset back to 0 and the transient analysis begins.

Figure 5.11(a) shows the convergence factor of the conducted dynamic relaxation process. As expected, convergence was considered as attained when the convergence factor is lower than  $10^{-4}$ . The axial force, recorded in the M10 bolts that fix the remainder of the set-up to the wall during a transient analysis, is illustrated in Figure 5.11(b). Analysing the axial force-time curve depicted in the referred curve, it is possible to verify that the 20 kN preload was correctly applied and the dynamic vibrations of the set-up lead to axial force values that vary around this value.



(a) Convergence factor



(b) Bolt's axial force during transient analysis

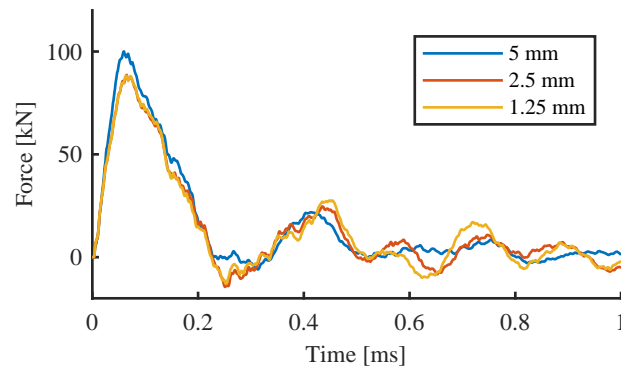
Figure 5.11: Dynamic relaxation verification

### 5.3.1.7 Convergence

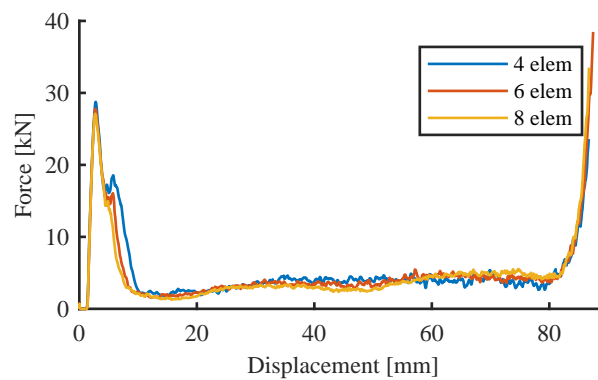
The optimization of a numerical model is both related to the reliability and accuracy of the obtained results and to the computational effort and time of analysis required to obtain them. Therefore, a mesh sensitivity analysis was independently performed for the numerical model of both the set-up and the sacrificial cladding solution, as the correct transmission of loads between them was verified for all the performed analyses. In the case of the set-up, solid elements with edges of 5, 2.5 and 1.25 mm were considered, while the shell elements used to model the steel washers were generated accordingly, resorting to the LS-PrePost AutoMesh tool. The convergence analysis of its dynamical response yielded stable results for a FE mesh with a 2.5 mm edge size, as illustrated in Figure 5.12(a). Table 5.4 presents the solid element's edge size, the resulting number of nodes on the numerical model, the maximum observed total force on the sensor springs and the required time to compute the analysis up to an analysis time of 0.001 s. Analysing the referred table, it is possible to confirm that resorting to the mesh with a 2.5 mm edge size yields reliable and accurate results with reasonable computational effort and time of analysis.

It was observed that the simulated response of the 3D printed honeycomb is more sensitive to the number of elements along the edge of the cell walls than to the absolute





(a) Set-up



(b) Sacrificial cladding solution (5% relative density)

Figure 5.12: Mesh sensitivity analysis

Table 5.4: Mesh sensitivity analysis of the set-up

Edge size [mm]	No. of nodes	Max. sensor force [kN]	Time [s]
5	16,354	100.06	102
2.5	113,468	88.66	703
1.25	849,505	88.25	7471

value of the mesh size, regardless of the considered relative density. Therefore, meshes with 4, 6 and 8 elements along the referred length were considered for the present mesh sensitivity study. The FE mesh of the honeycomb structure and the top and bottom plates was created using the LS-PrePost AutoMesh tool, while solid elements with a 2.5 mm edge size were used to simulate the front aluminium plate. The overall response was very similar, as illustrated in Figure 5.12(b), with subtle differences on the maximum peak force and compaction speed. Table 5.5 presents the mesh sensitivity analysis of the sacrificial cladding solution, composed by a 5% relative density honeycomb structure and a front plate. Observing the similarities between all the force-time curves depicted in Figure 5.12(b) and the maximum peak force values presented in the referred table, no significant differences were observed between the FE estimates obtained with 6 and 8 elements along the walls of the honeycomb structure. Additionally, considering the most

Table 5.5: Mesh sensitivity analysis of sacrificial cladding solution (5% relative density)

No. of elements	No. of nodes	Max. peak force [kN]	Time [s]
4	16,937	28.75	356
6	34,169	27.77	1177
8	58,601	27.11	3402

severe case ( $\bar{\rho}=10\%$ ), the use of 6 elements per cell wall results in 228,616 shell elements that already requires almost 9h of computing time to simulate 0.002 s. Consequently, all the numerical models of the considered sacrificial cladding solutions were meshed with 6 elements along the cell wall, resulting on FE meshes with 32,620, 100,492 and 228,616 shell elements (edge size of 1.650, 1.098 and 0.825 mm) for the 5, 7.5 and 10% relative density, respectively.

### 5.3.2 Simplified model

The use of the presented FE numerical model requires, just for the sacrificial cladding solution, almost 9h of computing time if a 10% relative density is considered. This large computational effort and, consequently time, might become impractical if a large number of analysis is required. Therefore, the nonlinear behaviour of the proposed sacrificial cladding was also investigated resorting to a simplified model in order to verify its applicability. The schematic representation of the considered one-dimensional simplified model is illustrated in Figure 5.13(a). The considered model is very similar to the one proposed by Hanssen and co-workers [51] (see Section 3.5.3.2). Similarly, the honeycomb structure is attached to a front plate and to a rigid and fixed structure at its ends. Contrarily, the mass of the front plate  $M_1$  is considered to be the sum of the aluminium front plate and the top solid plate masses. The properties of the honeycomb structure are given by its length  $l$ , cross-sectional area  $A$  and total mass  $\rho Al$ . The front plate is assumed to be rigid, while the nonlinear behaviour of the 3D printed cellular structure is idealised

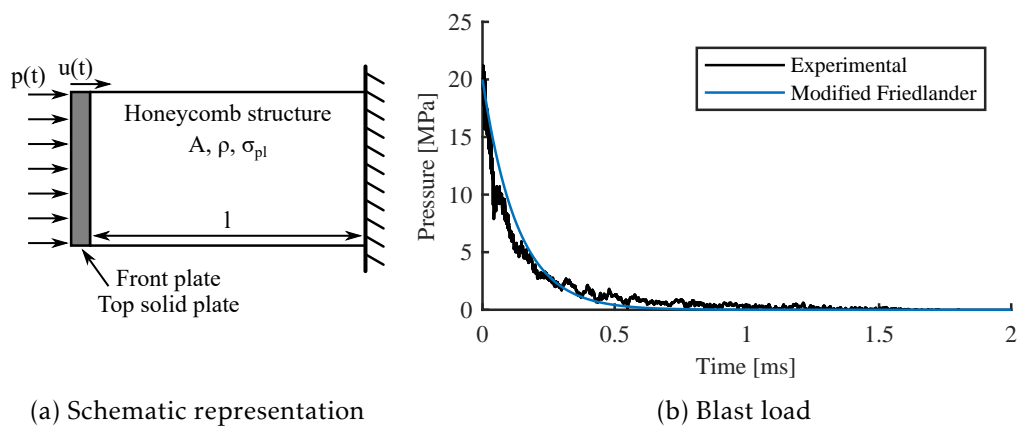


Figure 5.13: One-dimensional simplified model

with the RPPL material model, characterised by a plateau stress of  $\sigma_{pl}$  and a densification strain of  $\varepsilon_d$ . Lastly, it is important to refer that the movement of the front plate and deformation of the honeycomb structure are expressed by  $u(t)$ .

A uniform blast load ( $p(t)$ ) is applied to a specific area of  $75 \times 75 \text{ mm}^2$  on the front plate. Although the model proposed by Hanssen et al. [51] considers a triangular pressure-time history, the overpressure profile obtained from the blast load on a rigid and fixed boundary (see Figure 4.15(b)) is approximated by the modified Friedlander equation as depicted in Figure 5.13(b).

The ordinary differential equation (ODE) is solved numerically with a fourth/fifth-order explicit Runge-Kutta method available in the MATLAB ODE suite [96], using the `ode45` function. This function integrates a system of first-order ODE's over a certain time span and with given initial conditions. Consequently, the second-order ODE must be rewritten as a system of first-order ODE's as:

$$\begin{bmatrix} \frac{du}{dt} \\ \frac{dv}{dt} \end{bmatrix} = \begin{bmatrix} v \\ - \left[ A \left( \frac{\rho v^2}{\varepsilon_d} + \sigma_{pl} - p(t) \right) \right] / \left( M_1 + \frac{\rho A}{\varepsilon_d} u \right) \end{bmatrix} \quad (5.9)$$

In the present study the system is considered to be at rest when the blast load is applied and, therefore, the initial conditions are set to zero. Although the `ode45` function integrates the system of first-order ODE's over a user-defined time span, it may be necessary to stop the numerical method when a certain "event" takes place. For the simplified model in question, the integration should terminate when either the honeycomb structure becomes fully compressed or the velocity of the front plate becomes null. Nonetheless, these "events" will occur at a specific time, which is not known *a priori*, and their accurate and efficient detection is paramount. Two user-defined functions were used on the present study (see equation (5.10)) to terminate the `ode45` function.

$$\begin{bmatrix} \frac{u}{l\varepsilon_d} - 1 \\ v \end{bmatrix} = \begin{bmatrix} 0 \\ 0 \end{bmatrix} \quad (5.10)$$

Figure 5.14 illustrates the logical diagram of the implemented procedure. A Main MATLAB script is used to initiate the procedure with the definition of the sacrificial cladding parameters, the blast scenario defined in terms of peak reflected overpressure  $P_r$ , impulse  $i_r$  and decay parameter  $b$ , the initial conditions of the system and the time span. Subsequently, the time integration of the first-order ODE's is performed inside the `SCResponse` function, which verifies if compaction of the crushable core will take place and, if true, resorts to `ode45` function to integrate the ODE's system over  $t_{span}$ , with zero initial conditions  $y_0$ . The system of ODE's to be integrated and the events that may stop the numerical integration are passed onto the `ode45` function by means of function handles `@ODE` and `@ODEEnd`, respectively. These functions are nested inside the `SCResponse` function, which allows variables to be shared between them reducing

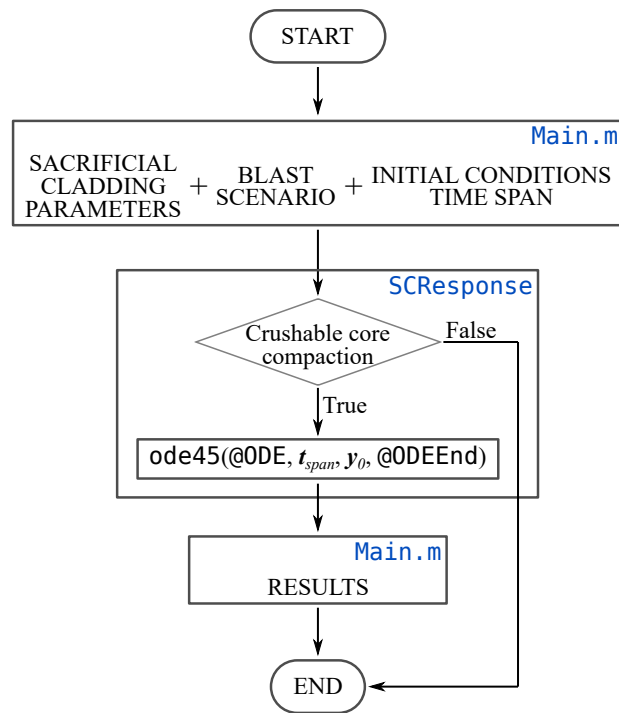


Figure 5.14: Logical diagram of MATLAB implementation for the simplified model

the number of input variables, and define the system of first-order ODE's (@ODE function according to equation (5.9)) and the event expressions that stop the analysis (@ODEEnd function according to equation (5.10)). When either the termination time or an event is triggered, the SCResponse function returns the displacement and velocity time histories into the Main MATLAB script, allowing a post-processing of the results.

### 5.3.3 Results of FE numerical model

The current section reports the results obtained with FE numerical models of the blast test. Initially, only the FE model of the set-up is subjected to a blast load and the resulting force-time history is compared with the one obtained during the previously reported preliminary tests on the experimental set-up. Next, the FE numerical model of the sacrificial cladding solution is added to the FE model of the set-up in order to model the experimental blast testing of the 3D printed crushable core. The numerical results obtained resorting to this model will be presented and compare with the experimental ones in the current section. Additional insights regarding the nonlinear response of the crushable core are attained by means of the numerical results.

#### 5.3.3.1 Preliminary tests on the experimental set-up

A preliminary set of experimental tests was performed with no sacrificial cladding, i.e. the blast load was directly applied to the set-up, in order to verify its influence on the obtained results, namely on the force-time curve recorded by the force sensor. Figure 5.15

illustrates the experimental records of both the force sensor and the pressure transducer, together with the numerically simulated response of the force sensor. As previously referred, the influence of spurious vibrations of the set-up on the force sensor's measurements is readily observable in the experimental force-time curve (black line in the referred figure). Nonetheless, a good agreement between the experimental and numerical curves was obtained.

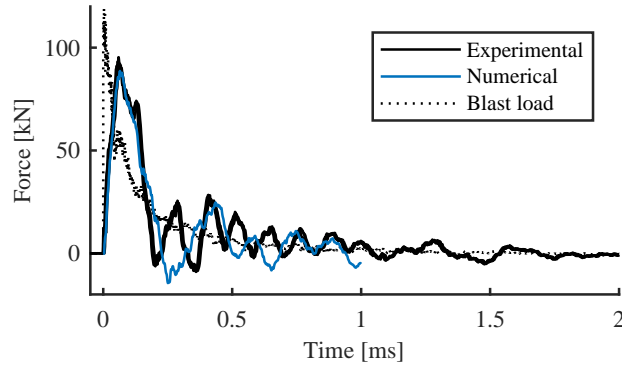


Figure 5.15: Force-time history on rigid and fixed boundary

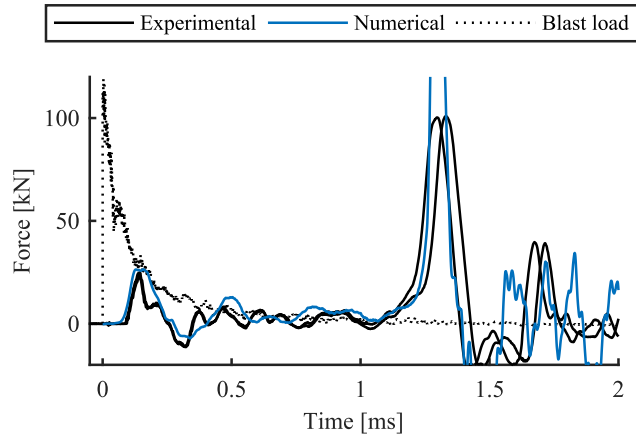
### 5.3.3.2 Sacrificial cladding

A quantitative and a qualitative analysis of the experimental tests performed on the sacrificial cladding with different relative densities, as well as of the associated numerical simulations, is presented in the following sections. Additionally, the evolution of the crushing mechanism, inside the 3D printed crushable cores, is analysed.

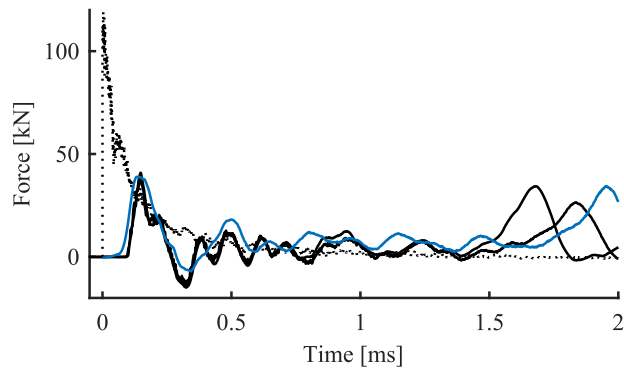
#### Quantitative analysis

Two experimental specimens were tested for each considered relative density. Figure 5.16 illustrates the force-time curves recorded by the force sensor during the experimental campaign, together with the applied blast load and the numerically simulated time history of the total force present on the discrete springs.

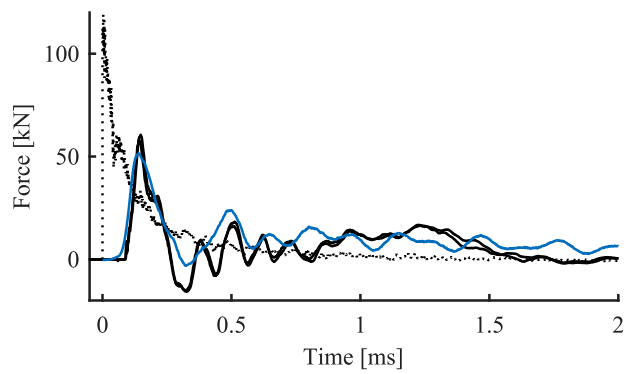
Digital processing of the images recorded by the high speed camera (see Section 4.4.3) yields the displacement and, by means of post-processing, the velocity-time histories shown in Figure 5.17. Analysing the depicted velocity-time histories, it is possible to observe that when the blast load is applied to the front plate ( $t = 0$ ), the latter attains an initial compaction velocity that greatly depends on the relative density of the honeycomb structure. This result was not expected due to the constant front plate's mass and applied blast load since, generally, it is considered that the initial velocity  $v_0$  only varies with the applied reflected impulse  $I_r$  and the mass of the front plate  $M$  according to the following expression:  $v_0 = I_r/M$ , which would yield a similar initial velocity throughout the entire experimental campaign.



(a) 5% relative density



(b) 7.5% relative density



(c) 10% relative density

Figure 5.16: Force-time history dependence on the relative density

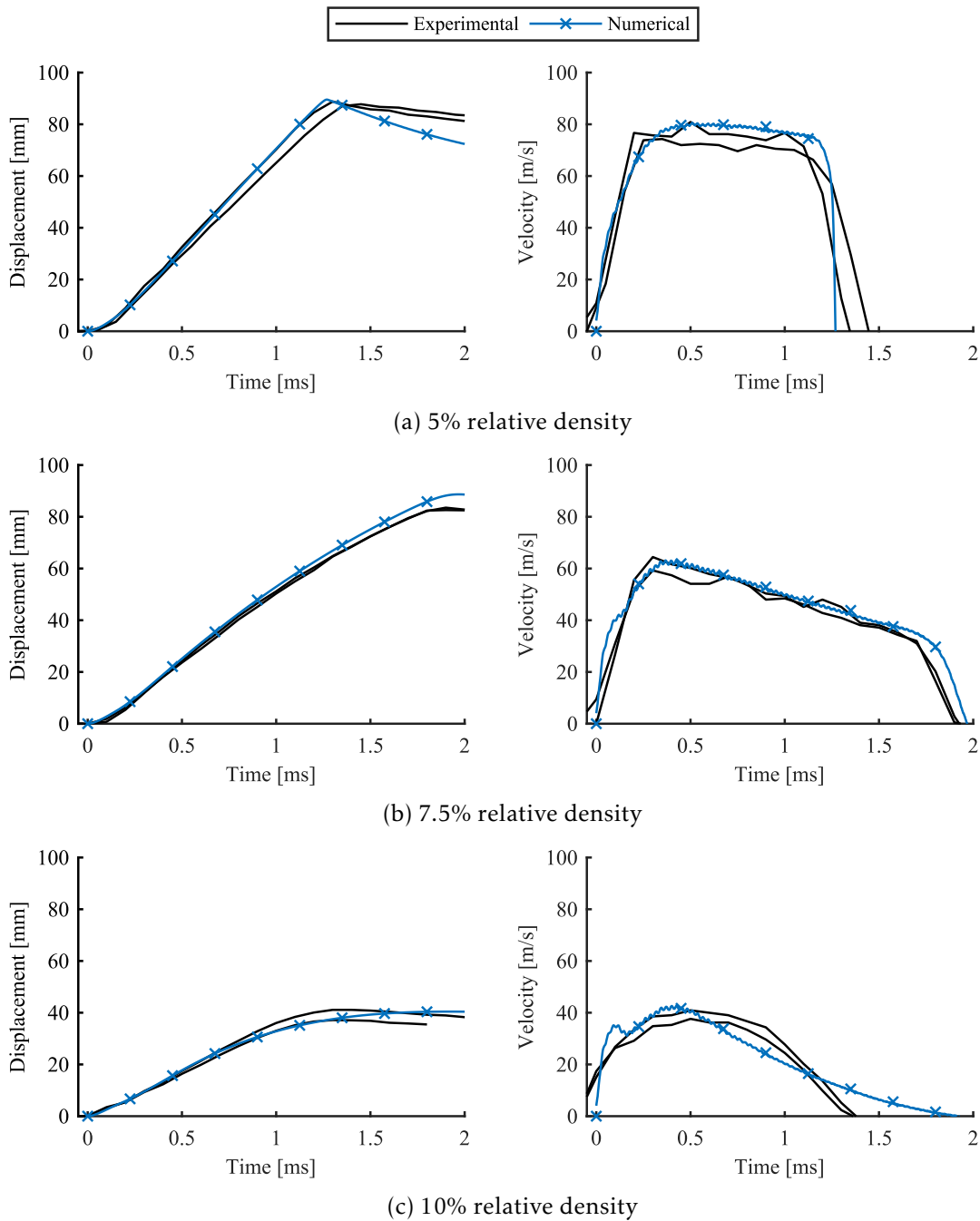


Figure 5.17: Displacement and velocity-time histories dependence on the relative density

A full compaction of the crushable core with a 5% relative density honeycomb structure is clearly observable in Figures 5.16(a) and 5.17(a), evidenced by the excessive secondary force peak and the 90 mm maximum displacement, respectively. Therefore, one may conclude that the crushable core was not able to fully absorb the applied blast load.

On the other hand, the proposed solution characterised by the 10% relative density only underwent a partial compression, with a maximum displacement of approximately 40 mm, as illustrated in Figure 5.17(c). Moreover, the referred crushable core fully absorbed the applied reflected impulse before undergoing a full compression, since no secondary peak was detected both experimental and numerically. Nonetheless, since the observed maximum displacement is way under the dimension of the crushable core, it is considered that the height of the protective cladding is oversized for the given blast load.

The curves related to the 7.5% relative density, Figures 5.16(b) and 5.17(b), demonstrate that the proposed solution stopped the front plate before suffering a full compression ( $d_{max} = 83.1$  mm), while reaching the densification stage. Consequently, a secondary peak, despite being less severe than the one recorded with a 5% relative density crushable core, is clearly visible in Figure 5.16(b).

Comparing the experimental and numerical force, displacement and velocity-time histories depicted in Figures 5.16 and 5.17, one might conclude that a good agreement between them was attained. Therefore, it is considered that the FE numerical model is valid when used to simulate the nonlinear response of the proposed 3D printed crushable core under blast loading.

### Qualitative analysis

Figure 5.18 illustrates a side view of the damage evolution in the analysed PLA crushable cores' exterior during blast loading. For each set of images, the top line presents frame stops recorded with the high speed camera at significant time moments, while the corresponding numerical simulations, which are in good agreement with the experimental results, are given in the bottom lines. As depicted in the referred figure, the fracture pattern is initiated by the crushing of the layers near the top and bottom solid plates, while maintaining relatively intact cells on the lateral surfaces. Further analysis of the deformation mechanisms is performed in Section 5.3.3.2 to investigate their evolution in the interior of the samples. Note that the loose particles, visible in high speed camera frame stops, are not visible in the numerical simulations due to the deletion of the elements during the analysis by the activated eroding algorithm.

### Evolution of the crushing mechanism

The post-processing of the numerical simulations, allows to analyse the evolution of the crushing mechanism inside the 3D printed honeycomb structures, by inspecting the deformation patterns revealed by a vertical cut at mid section of the specimens. The contact force between the bottom 3D printed solid plate and the rear aluminium plate is



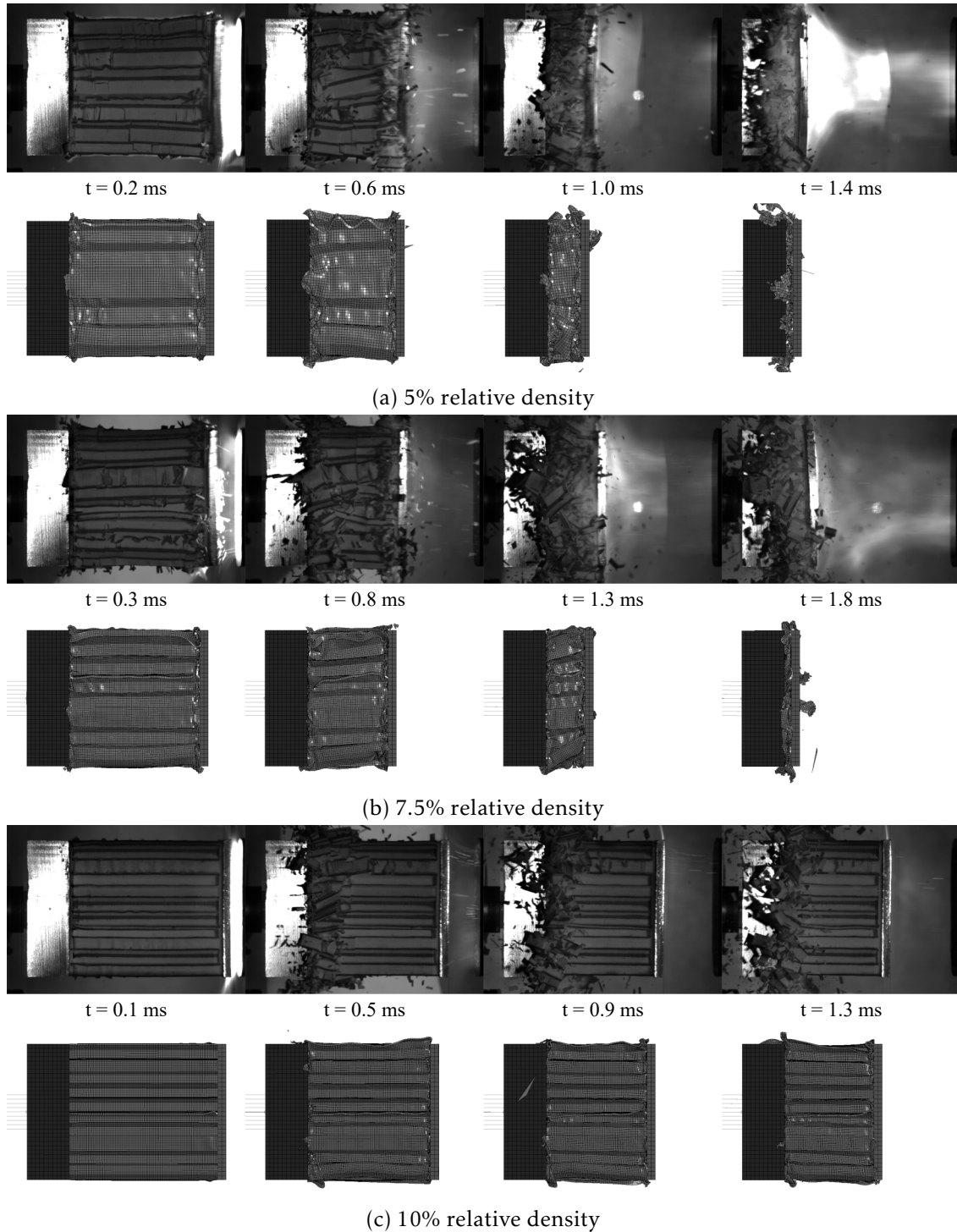


Figure 5.18: Side view of the sacrificial cladding solutions under dynamic compression

used, together with the displacement of the front plate to compute the numerical stress-strain curve of the crushable core (5% relative density), shown in Figure 5.19. In this graph, several key instants are highlighted corresponding to zero stress (*I*), maximum stress and the buckling initiation of the exterior walls (*II*), evolution of the buckling in the interior of the sample (*III* and *IV*) and, finally, the plateau region (*V* and *VI*). The related interior deformation patterns are depicted in Figure 5.20. Similarly, the stress-strain curves obtained when a crushable core with 7.5 and 10% relative densities are subjected to a blast load are presented in Figures 5.21 and 5.23, respectively. The corresponding deformation patterns are given in Figures 5.22 and 5.24. Similarities between the stress-strain curves obtained for all the considered relative densities is clearly evident through

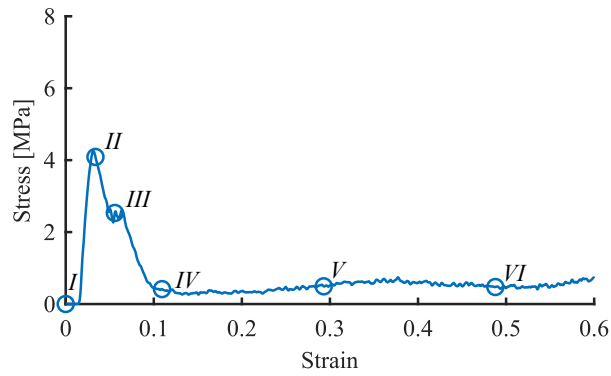


Figure 5.19: Stress-strain curve ( $\bar{\rho} = 5\%$ )

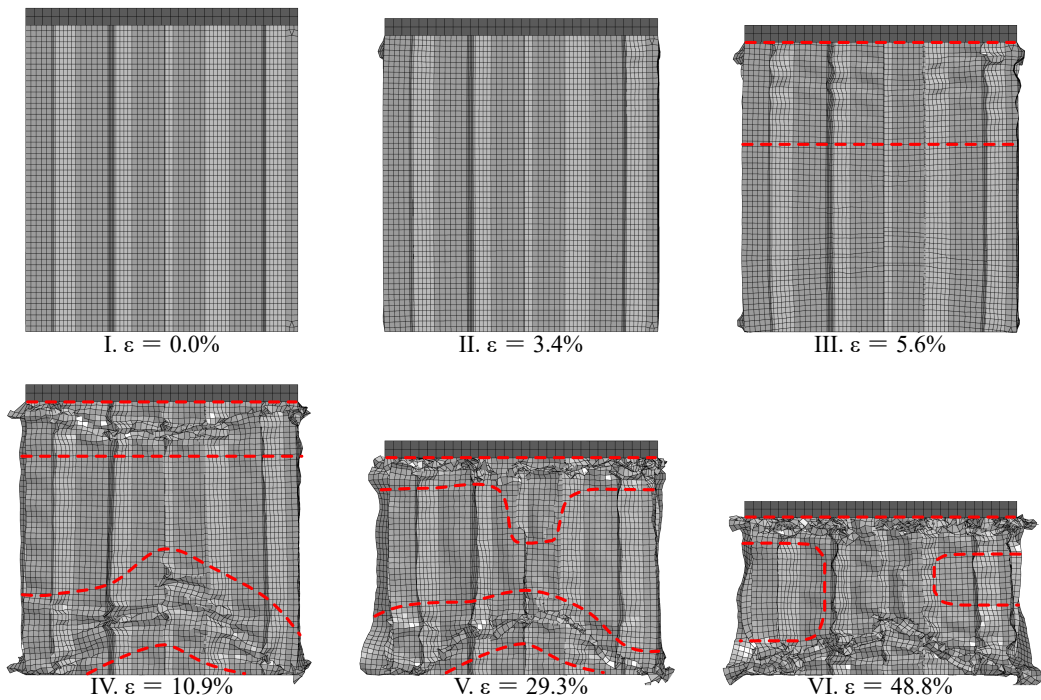


Figure 5.20: Evolution of the crushing mechanism in the PLA honeycomb ( $\bar{\rho} = 5\%$ )

the analysis of Figures 5.19, 5.21 and 5.23.

Analysing the evolution of the obtained patterns, one may observe that the triggering of the crushing varies with relative density. Although different relative densities also imply different loading velocities (taking into account that the experimental campaign was conducted with constant blast load and front plate), according to Karagiozova and Alves [63], the crushing pattern of aluminium honeycombs, when subjected to out-of-plane loading, is independent of the loading velocity. Assuming this is also valid for 3D printed PLA honeycomb structures, the evolution of the crushing patterns can be considered as mainly controlled by the relative density of the core. For example, while the buckling of the cell walls initiates near the top plate for 5 and 7.5% relative densities

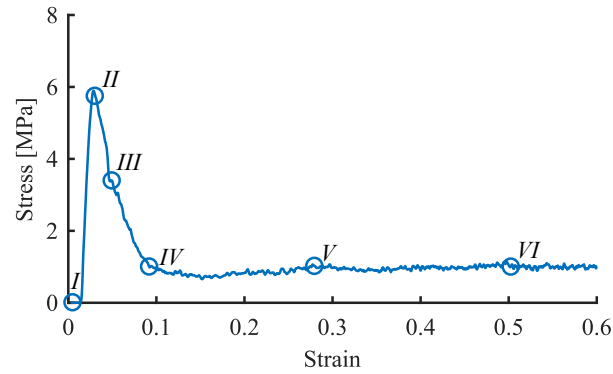


Figure 5.21: Stress-strain curve ( $\bar{\rho} = 7.5\%$ )

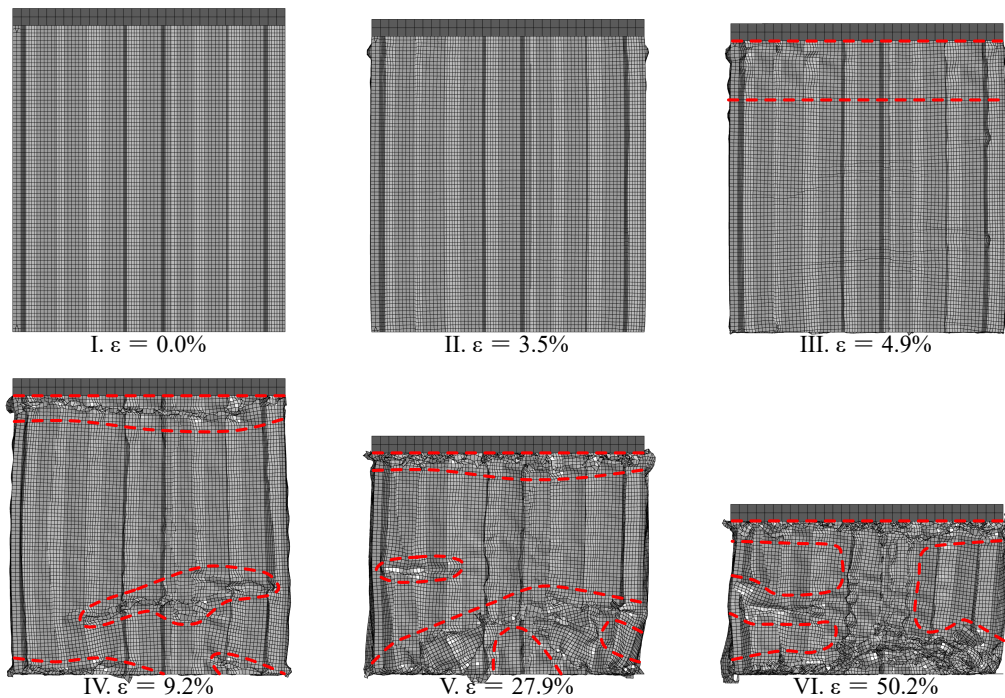


Figure 5.22: Evolution of the crushing mechanism in the PLA honeycomb ( $\bar{\rho} = 7.5\%$ )

(see instant *III* in Figures 5.20 and 5.22), it starts in the centre of the specimen for the 10% relative density, as clearly visible at instant *III* in Figure 5.24.

The initial localised crushing shown in Figures 5.20 and 5.22 is further developed between instants *III* and *IV*. Additional regions of localised deformations are observable at later instants for all the considered relative densities. They appear at the bottom and middle (5 and 7.5%) and at the top and bottom of the specimen (10%) of the crushable core. Observing the vertical cuts given in Figure 5.20, it is possible to verify that, in the case of the 5% sacrificial cladding solution, further compression of the localised deformation regions develops as the nonlinear response progresses through the plateau region (instants *V* and *VI*), culminating with the general collapse of the sample.

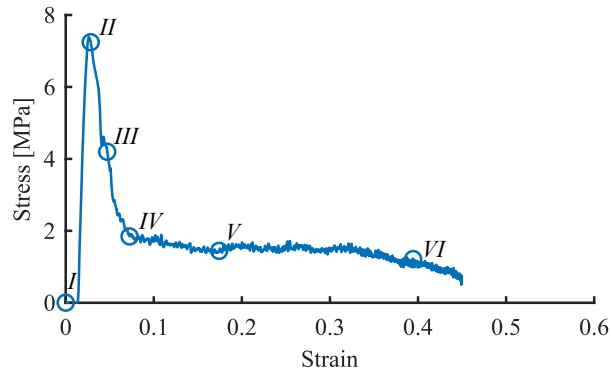


Figure 5.23: Stress-strain curve ( $\bar{\rho} = 10\%$ )

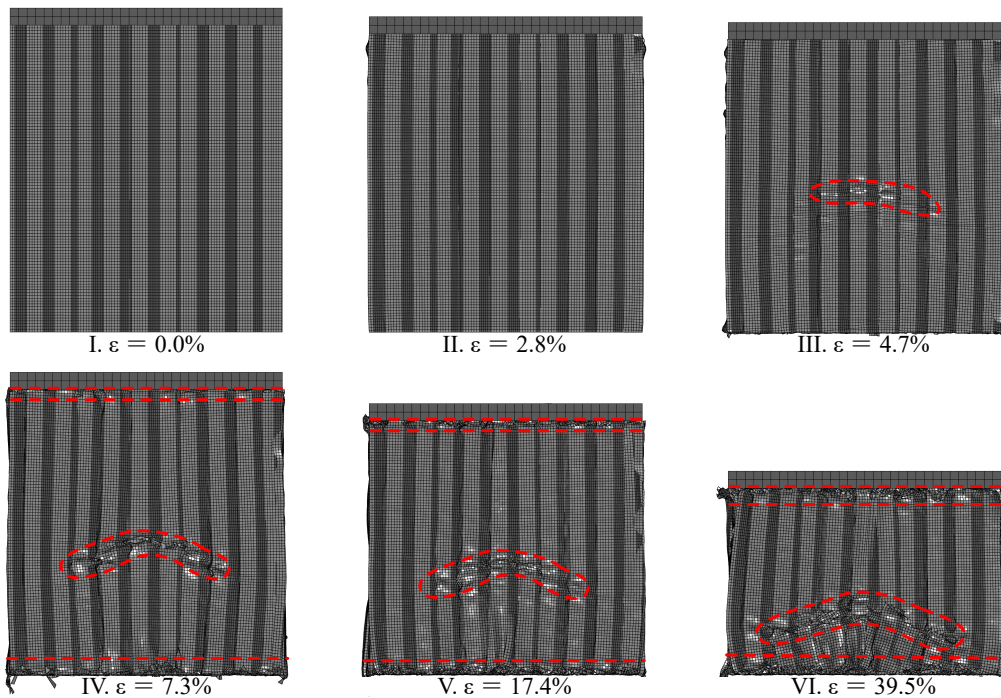


Figure 5.24: Evolution of the crushing mechanism in the honeycomb ( $\bar{\rho} = 10\%$ )

The evolution obtained for the 7.5% relative density crushable core plotted in Figure 5.22 attains a third localised crushed zone in the middle of the specimen (instant  $V$ ), while the final collapsed pattern exhibits similarities when compared with the 5% sacrificial cladding solution.

As illustrated in Figure 5.24, the evolution of the crushing mechanism ( $\bar{\rho} = 10\%$ ), despite growing with strain, led to a final pattern with a large intact zone in the core of the sample. This undeformed area confirms that the solution was oversized, as already previously stated.

### Summary of the obtained results

The average maximum displacement ( $d_{max}$ ), first peak force ( $F_{max}$ ), transmitted impulse ( $i_s^t$ ), efficiency ( $e$ ) and applied work ( $W$ ) are summarised in Table 5.6 for the considered relative densities ( $\bar{\rho}$ ), as resulting from the experimental tests and associated numerical simulations. Analysing the values presented in the referred table, one can readily observe that the numerical estimates for the maximum displacement and the applied work are in relatively good agreement with the experimental data with a maximum error below 5%. However, as seen in Section 5.3.3.2, the numerical simulation overestimates the secondary force peaks leading to higher transmitted impulses. Consequently, the numerical analyses yield lower efficiency ratios when compared to the experimental ones.

Nonetheless, when the specimen is fully compressed, both the experimental values and the corresponding numerical estimates show that efficiency tends to increase with relative density. Lastly, since the same blast load was applied to all specimens, a decrease in the maximum displacement, resulting from an increase of the relative density, yields a corresponding decrease of the applied work.

Resorting to the stress-strain curves presented in the last section (see Figures 5.19, 5.21 and 5.23), which were computed by means of the contact forces between the crushable core and the aluminium rear plate, the average value of the plateau stress ( $\sigma_{pl}$ ), the densification initiation strain ( $\varepsilon_d$ ), the transmitted energy ( $U_{pl}$ ), the associated absorption capacity ( $Ab_{cap}$ , defined as  $U_{pl}/W$ ), as well as the energy absorbed per unit mass ( $SEA$ ) were determined according to Section 3.5.2.1 and presented in Table 5.7. Note that, since the 10% relative density was not fully crushed, all the referred parameters were computed between the elastic strain and the strain that corresponds to a null velocity of the front plate.

Table 5.6: Summary of the experimental/numerical results

$\bar{\rho}$ [%]	$d_{max}$ [mm]	$F_{max}$ [kN]	$i_s^t$ [Pa·s]	$e$ [-]	$W$ [J]
5	88.3/89.5	24.8/25.5	2,334/2,600	0.11/0.00	716/740
7.5	83.1/88.7	39.5/37.0	2,005/2,440	0.20/0.06	628/647
10	39.1/40.4	59.4/48.9	2,172/2,423	0.17/0.07	441/439

Table 5.7: Additional numerical estimates

$\bar{\rho}$ [%]	$\sigma_{pl}$ [MPa]	$\varepsilon_d$	$U_{pl}$ [J]	$Ab_{cap}$ [%]	$SEA$ [J/g]
5	0.695	0.85	327.6	45.8	8.1
7.5	1.054	0.90	527.1	83.9	8.5
10	1.709	N.A.	416.8	94.5	10.2

The obtained numerical estimates show that, when the crushable core is completely compressed by the blast load (5 and 7.5% relative densities), both the plateau stress and the transmitted energy are proportional to the relative density of the honeycomb structure, which agrees with the results obtained with the preliminary quasi-static compression tests reported in Section 4.4.1. Comparing the plateau stress values obtained via blast testing with the ones resulting from the quasi-static tests, a slight reduction is verified, as a result of the stress decrease of the PLA material with increasing strain rates (see Section 4.3).

The transmitted energy and absorption capacity values depicted in Table 5.7 show that, when the compression of the crushable core reaches the densification phase at the end of the blast loading, the transmitted energy and, consequently, the absorption capacity of the sacrificial cladding solution increase for larger relative densities. Moreover, when a honeycomb structure with a 10% relative density is used as the crushable core, its resulting absorption capacity is close to 100%, further demonstrating that the sacrificial cladding solution was able to mitigate the applied blast load. Assuming a maximum strain of 0.9 and taking into account the 1.709 MPa plateau stress (Table 5.7), its theoretical absorption capacity yields 860.4 J (SEA = 10.5 J/g).

### FE numerical model with rigid boundary

An additional FE model was created for the simulation of the nonlinear response of the sacrificial cladding solution, composed simply by the front plate, the top and bottom 3D printed solid plates and honeycomb structure. This model attained all the geometric, material, contact and load properties of the original FE model, presented in Section 5.3.1, for the correct simulation of the considered parts of the complete model. The only change was the implementation of a rigid boundary on the bottom PLA solid plate, achieved by restraining the displacements of the nodes. Figure 5.25 shows the contact force, from the full numerical model, and the reaction force, determined with the “independent” FE model, time histories, from which it is possible to observe that the results are in good agreement. Therefore, one can conclude that, although the set-up influences the force-time curve recorded by the force sensor, the response of the sacrificial cladding solution is not influenced by the experimental set-up and can be numerically obtained with an “independent” model.

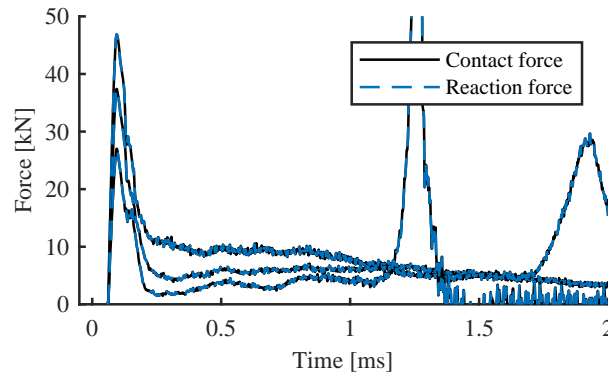


Figure 5.25: Comparison of force-time histories obtained with full and “independent” model

### 5.3.4 Results of simplified model

The objective of the current section is to present the results obtained when a simplified model (see Section 5.3.2) is used to simulate the nonlinear response of 3D printed crushable cores subjected to blast loads. Comparing the numerical results with the experimental ones, it is possible to verify the applicability of the simplified model for the intended purpose.

#### 5.3.4.1 Original simplified model

Comparing the velocity-time histories determined by means of the simplified model with the ones obtained during the previously presented experimental campaign, one may verify that the maximum velocity attained by the front plate is overestimated when the simplified model is used. Consequently, when the analysis is not terminated as a result of the full compaction of the crushable core, the corresponding maximum displacement is larger than the experimental one (see Figure 5.26(c)). Additionally, for the honeycomb structures with 5 and 7.5% relative density, the slope of the descending part of the velocity curve seems to be excessively high. Due to the observed differences, it is considered that the simplified model proposed by Hanssen and team [51] is not able to correctly predict the nonlinear behaviour of the proposed 3D printed honeycomb structures subjected to blast loads.

#### 5.3.4.2 Improved simplified model

In order to improve the comparability between the simplified model predictions and the nonlinear compaction behaviour observed during the experimental campaign, a couple of modifications are proposed to the simplified model. The contact stress between the aluminium front plate and the 3D printed solid top plate, as estimated by the FE analysis, is used to verify the existence of a fully densified region on the top part of the crushable core, which moves with the same velocity as the front plate. Figure 5.27 presents this

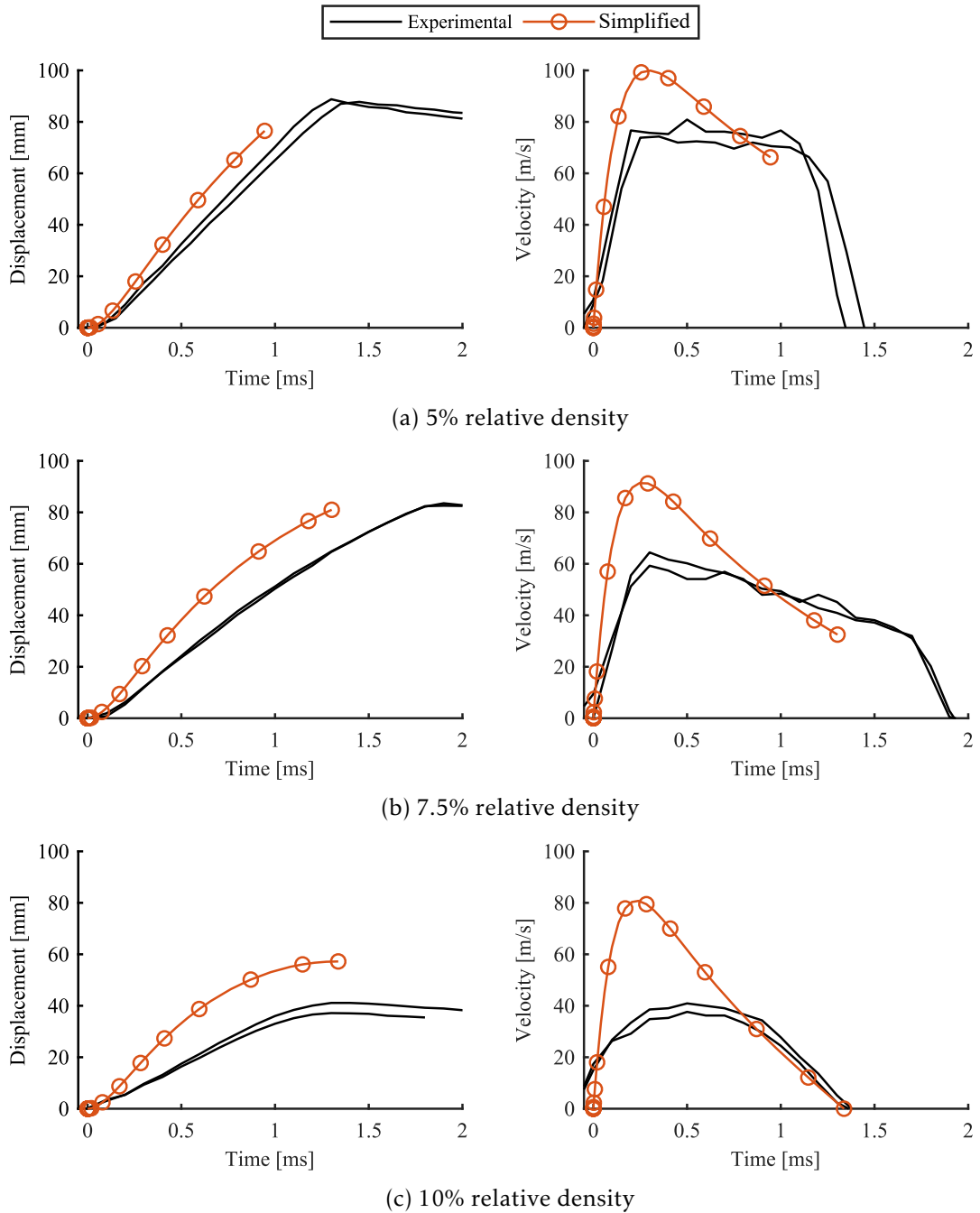
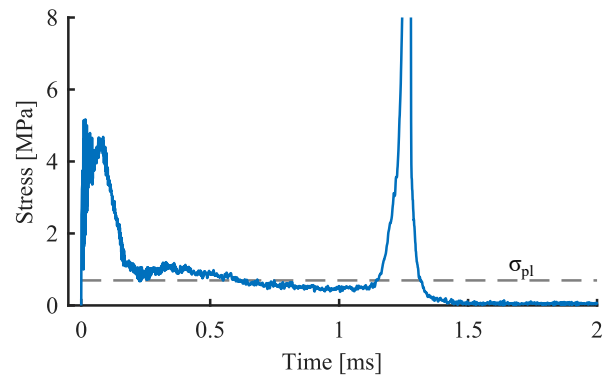
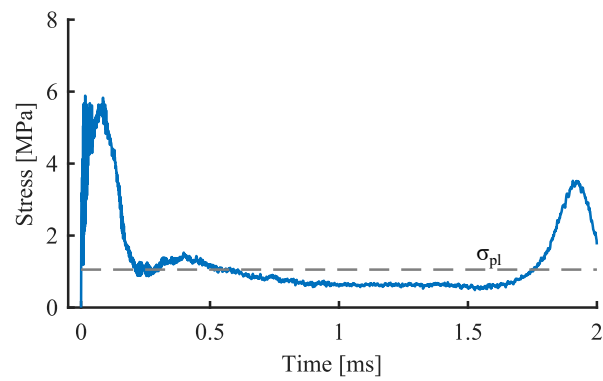


Figure 5.26: Displacement and velocity-time histories obtained with the simplified model

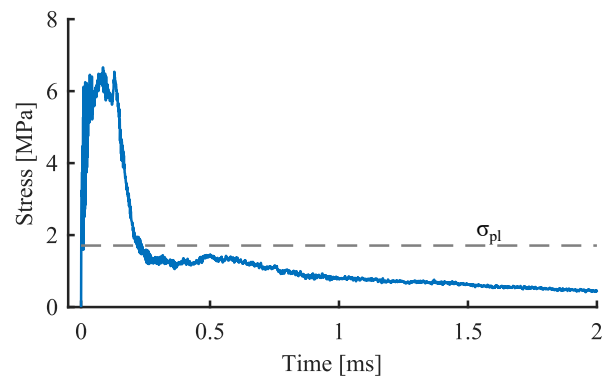




(a) 5% relative density



(b) 7.5% relative density



(c) 10% relative density

Figure 5.27: Numerical contact stress between aluminium front plate and 3D printed solid plate

contact stress-time history dependence on the relative density of the honeycomb structure, together with the plateau stress depicted in Table 5.7. According to Hanssen and co-workers [51], the formation of the fully densified region leads to an increase in stress inside this region, which is a function of the front plate's velocity. However, analysing the curve shown in the referred figure, one may observe that the contact stress between the crushable core and the front plate, after the initial peak and development of the plateau stress, is either close or lower than the plateau stress of the honeycomb structure until its full compaction is observed.

The original simplified model considers that only the compacted crushable core contributes for the mass of the system, acting as a free body together with the front plate. However, observing the image frames recorded with the high speed camera and the results computed using the FE numerical model, one might verify a different behaviour for this particular case. Both the acceleration distribution over the specimen's side (left side) and the resultant acceleration-time histories of the front plate and the honeycomb structure (right side) are shown in Figure 5.28 for all the considered relative densities. Comparing the resultant acceleration curves of the sacrificial cladding solution's components (front plate and honeycomb structure), it is possible to verify that, despite some differences on the initial response, the overall behaviour is similar. Additionally, the acceleration distribution over the side of the specimens seems to be relatively constant.

Taking into account these findings, two modifications are proposed to the idealised behaviour considered by the original simplified model. Firstly, it is assumed that the formation of a fully compacted region may not be explicitly considered and, consequently, only the plateau stress is applied on the dynamic system. Secondly, the honeycomb structure, although it does not move with the same displacement as the front plate on the numerical results, its acceleration is considered to be the equal to the front plate's acceleration. Consequently, the honeycomb structure contributes as a whole to the mass of the dynamic system. Considering the proposed modifications, the system of first-order ODE's to be integrated becomes:

$$\begin{bmatrix} \frac{du}{dt} \\ \frac{dv}{dt} \end{bmatrix} = \begin{bmatrix} v \\ -[A(\sigma_{pl} - p(t))] / (M_1 + \rho Al) \end{bmatrix} \quad (5.11)$$

Additionally, following the work presented by Zheng and team [186], a rate independent rigid-plastic hardening (RPH) idealisation was implemented. As reviewed in Section 3.5.3.4, the stress-strain curve is defined by the following expression:

$$\sigma = \sigma_o + \frac{C \varepsilon}{(1 - \varepsilon)^2} \quad (5.12)$$

where  $\sigma_o$  is the initial crushing stress, considered to be equal to the plateau stress  $\sigma_{pl}$  on the present study, and  $C$  is the strain hardening parameter, which took a value of 2.5 kPa. It should be noted that this value was computed based on the FE estimates presented in Section 5.3.3.2.

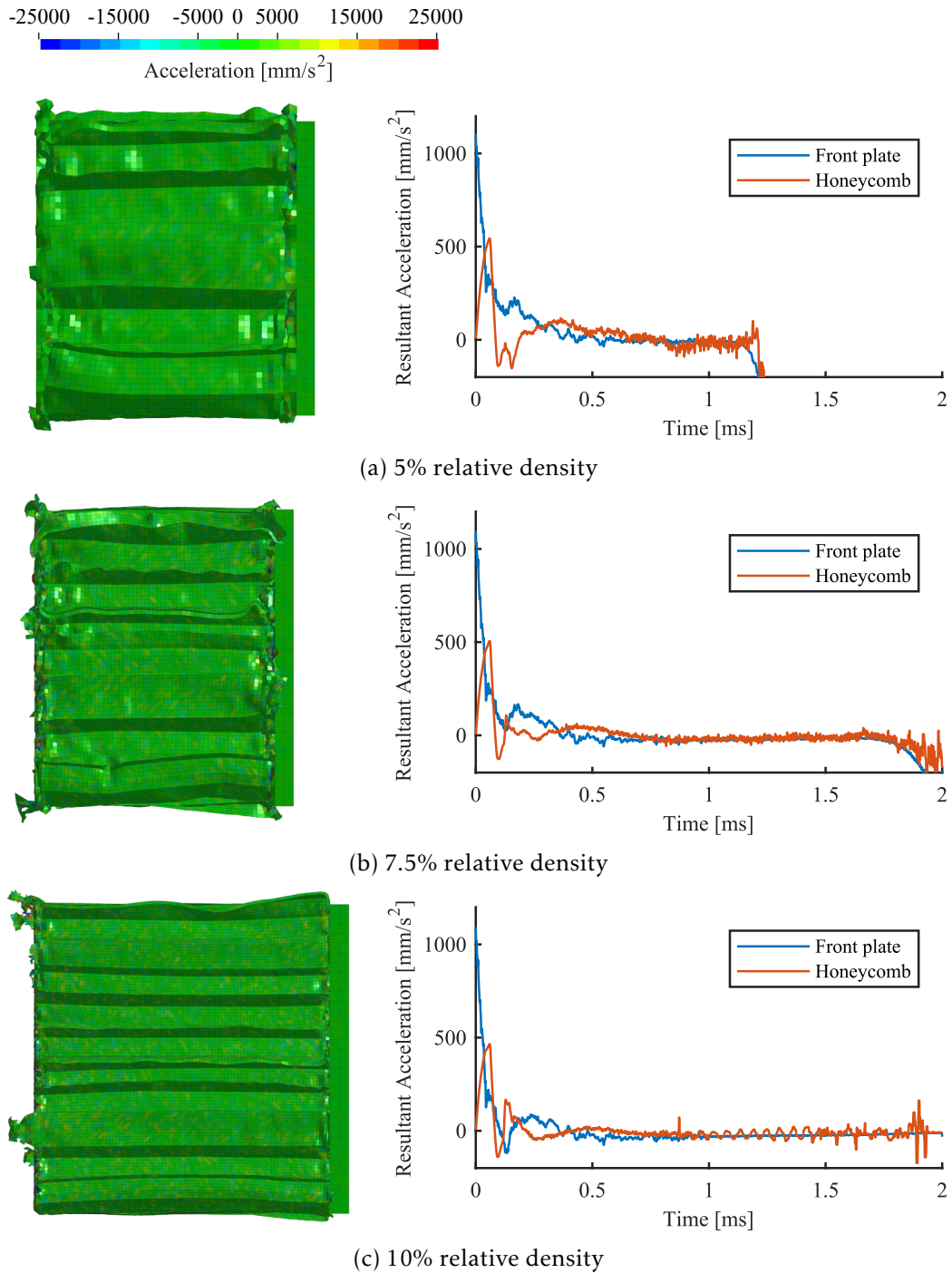


Figure 5.28: Acceleration distribution over the specimen's side and resultant acceleration-time histories of the front plate and the honeycomb structure

Figure 5.29 illustrates the displacement and velocity-time histories determined resorting to the modified system of differential equations for all the considered relative densities, together with the experimental ones. A good agreement was attained between the experimental and improved simplified model's results, as further evidenced by the summary presented in Table 5.8, which presents a maximum difference of 6% in terms of maximum displacement. For both the 7.5 and 10% relative densities, the crushable

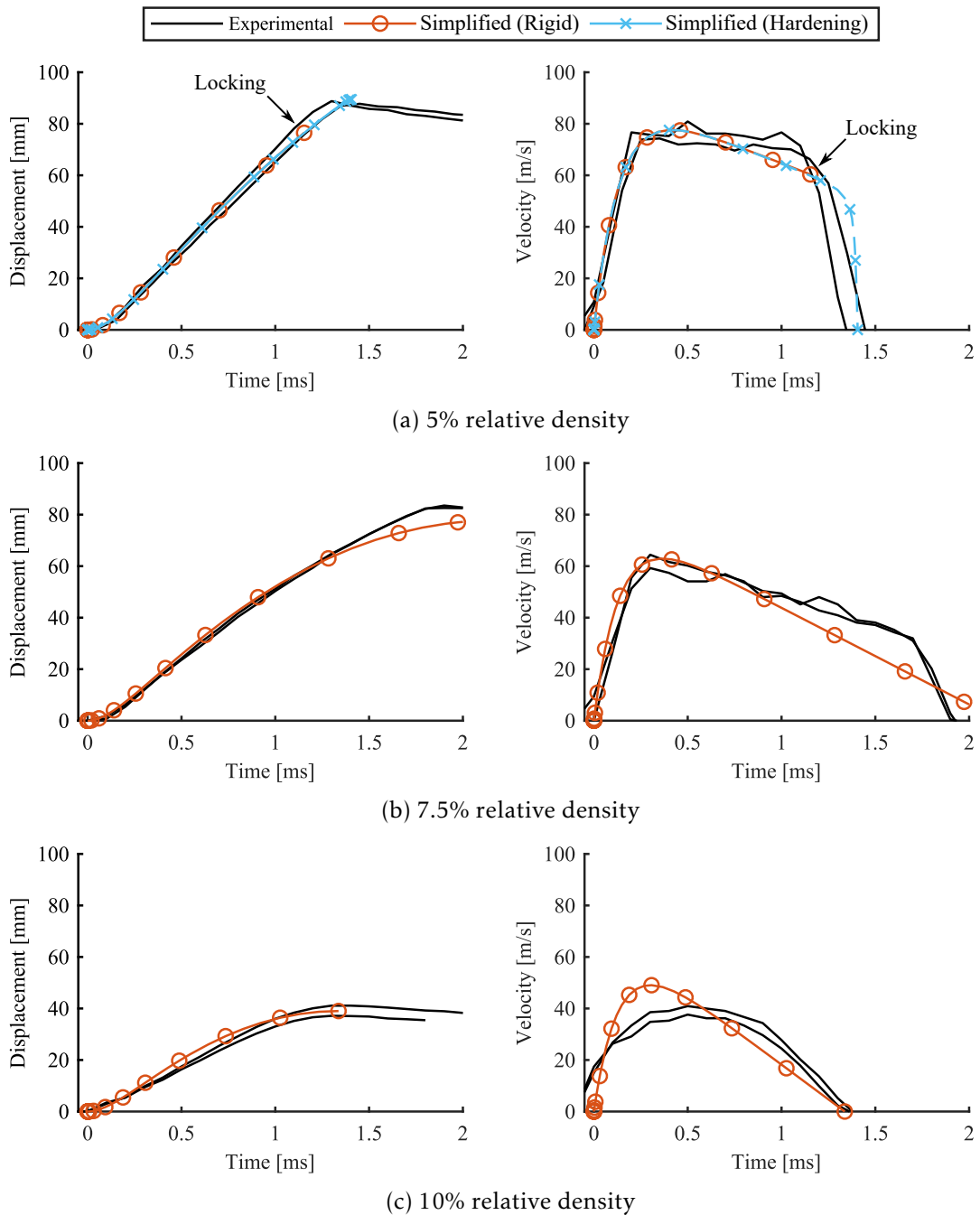


Figure 5.29: Displacement and velocity-time histories obtained with the modified simplified model

Table 5.8: Summary of the experimental and simplified results (Diff. [%])

$\bar{\rho}$ [%]	$d_{max}$ [mm]		
	Experimental	Locking	Hardening
5	88.3	76.5 (13%)	89.5 (1%)
7.5	83.1	77.7 (6%)	76.9 (7%)
10	39.1	39.0 (0%)	39.0 (0%)

core was not fully compacted, while the honeycomb structure with a relative density of 5% was, which agrees with the findings of the experimental tests. Despite the larger descending slope after the maximum velocity, the general profile of the simplified model's velocity-time curves agree with the ones recorded by the high speed camera. Analysing the referred table, a 13% difference may be observed in terms of maximum displacement for the sacrificial cladding solution which resorts to a crushable core with a 5% relative density. This difference arises from the 0.85 densification strain, computed based on the load transmitted by the sacrificial cladding solution, that triggers an event and, subsequently, terminates the numerical time integration prematurely. Resorting to the RPH idealisation to model the nonlinear compressive behaviour of the 5% relative density honeycomb structure, one might observe from Table 5.8 that a smaller difference is obtained (1%). Additionally, Figure 5.29(a) clearly shows that, up to densification, the results obtained with either material idealisation might be considered as equal, both in terms of displacement and velocity. As expected, the RPH idealisation is able to model the movement of the front plate until its velocity becomes null, since locking at the densification strain is not considered.

## 5.4 Conclusions

The experimental campaigns reported in the Chapter 4 allowed the development, verification and validation of the numerical models described in the current chapter.

Resorting to the commercial finite element software LS-DYNA [83], a FE numerical model, composed by a single square element, was developed to simulate the mechanical behaviour of 3D printed PLA manufactured via the FDM technique. Amongst the available material models in LS-DYNA, the applicability of the Laminated Composite Fabric material model (MAT\_058) was verified resorting to the experimental characterisation of the anisotropy of the stress-strain behaviour. The material model properties were calibrated for 3D printed FDM PLA and a comparison between the experimental and numerical behaviour was performed in order to verify if proper calibration was achieved.

The anisotropic and tension/compression asymmetry was correctly recovered by the material model when the maximum stress is of interest. However, due to the inability of the material model to distinguish between compressive and tensile loading when defining the stiffness properties of the composite material, a large difference between

the experimental and numerical initial elastic response of the material under quasi-static compressive and tensile loading ( $0^\circ$  orientation) was verified.

Comparing the experimental and numerical results obtained when the material is subjected to high strain rate compressive loading ( $90^\circ$  orientation), it was possible to verify that the maximum strength of the material were correctly simulated for the considered strain rates (500, 2500 and  $5000 \text{ s}^{-1}$ ). However, two limitations were identified for the material model when used to simulate the dynamic behaviour of 3D printed PLA. Firstly, contrary to the observed on the experimental data, the elastic properties of the material are strain rate independent. Secondly, the “stress limiting factor” was also found to be strain rate independent. Therefore, the plateau stress after softening follows the maximum strength curve multiplied by the referred factor, which led to a slight overestimation of this stress, when compared with experimental values.

Despite the identified limitations, it is concluded that the Laminated Composite Fabric material model (MAT\_058) is able to adequately simulate the mechanical behaviour of 3D printed PLA manufactured via the FDM technique.

The results attained during the experimental blast testing campaign were used to validate two numerical models. The first one was achieved resorting to the explicit finite element code LS-DYNA, while the second one was implemented in the commercial software MATLAB.

The experimental curves and the FE numerical simulations allowed to conclude that both the force peak and plateau stress are directly proportional to the relative density of the 3D printed crushable core, which controls the crushing of the top and bottom layers and the buckling of the interior cell walls. Additionally, contrary to what is commonly considered, i.e. that the initial velocity of the front plate only varies with the applied reflected impulse, it was found that the front plate initial velocity depends not only on its mass and the applied reflected impulse, but also on the relative density of the crushable core.

The use of the reported FE numerical model required, just for the sacrificial cladding solution, almost 9h of computing time if a 10% relative density was considered, which might become impractical if a large number of analysis are required. Therefore, the nonlinear behaviour of the proposed sacrificial cladding was investigated resorting to a simplified model (Hanssen et al. [51]) in order to verify its applicability.

In its original formulation, the simplified model considers that only the compacted crushable core contributes for the mass of the dynamic system, acting as a free body together with the front plate. Nonetheless, through the analysis of the experimental (high speed camera) and numerical (LS-DYNA) image frames, a different behaviour was observed for this particular case. When the resultant acceleration curves of the sacrificial cladding solution’s components (front plate and honeycomb structure) were compared, it was possible to verify that, despite some differences on their initial response, the overall behaviour was similar. Additionally, the FE estimate of the acceleration distribution along the specimens seemed to be relatively constant. Consequently, two modifications

were proposed to the original model. Firstly, it was assumed that the formation of a fully compacted region may not be explicitly considered and, consequently, only the plateau stress is applied on the dynamic system. Secondly, it was considered that the honeycomb structure contributes as a whole to the mass of the dynamic system. With the inclusion of these modifications, a good agreement was attained between the experimental and improved simplified model's results.





## Chapter 6

# Design of a sacrificial cladding solution

### 6.1 Introduction

The present chapter reviews the design procedure of a sacrificial cladding solution, based on the findings reported in Chapters 4 and 5.

In order to design the sacrificial cladding taking into account the properties of the structural element to be protected and considering that this element will be subjected to a wide range of blast scenarios, several simplified models are required:

- Numerical procedure to compute pressure-impulse diagrams;
- Nonlinear equivalent SDOF model of a reinforced concrete beam, in combination with the corresponding resistance-deflection curve;
- Load-Cladding-Structure model developed by Ma and Ye [87].

With the implementation of the required simplified models concluded, a case study was selected from the literature in order to illustrate the design procedure of a sacrificial cladding. The implemented procedure to compute the resistance-deflection curve and the resulting equivalent SDOF model are validated resorting to published experimental results. Next, a sacrificial cladding is designed as to increase the blast resistant capabilities of the structural element when subjected to a given blast load. Lastly, a robustness assessment of the designed solution is conducted resorting to an approach in which several key parameters are varied according to a given probabilistic distribution.

### 6.2 Simplified models

The current section presents, firstly, the implementation of a numerical procedure to compute pressure-impulse diagrams, which resorts either to the implementation of an equivalent SDOF model or a simplified method based on the one developed by Ma and

Ye [87], both of which are also reviewed here. Subsequently, a series of modifications are proposed to the model published by Ma and Ye in order to consider the nonlinear behaviour of the structural element and the effects of fluid-structure interaction on the pressure-time history imparted to the structural element.

### 6.2.1 Pressure-impulse diagram

The pivot search proposed by Blasko and team [11] (as cited in [70]) and presented in Section 2.9.5 was implemented in MATLAB. As depicted in Figure 6.1, this method allows the independent computation of the polar coordinates of the PI curve for each angle  $\theta_i$  of the polar coordinate system. Therefore, since the determination of the PI curves involves the extensive use of the bisection method, the implementation took into account the parallelisation capabilities available in MATLAB (parallel for loops). Figure 6.2 shows the logical diagram in which the implementation was based. The Main MATLAB script is used to define the properties of the structural element and, if required, those of the sacrificial cladding solution. Resorting to the properties of the former, the pivot point  $(I_p, P_p)$  is computed by means of the pressure and impulse asymptotes and is defined as the origin of the polar coordinate system. It should be noted that, on the present implementation, only angles between 0 and 90° were considered for the coordinate system. Consequently, the pivot point corresponds to the limit values in terms of impulse and pressure. Subsequently, resorting to parallel computing, the PIDetermination computes the polar coordinates of the PI curve. The computation of each radius  $r_i$  of the PI curve resorts to either the implemented equivalent SDOF system (see Section 6.2.2 for more details) or to the Load-Cladding-Structure model (see Section 6.2.3 for more details) to determine the maximum displacement of the structural element when a given pressure-impulse combination is imparted on it.

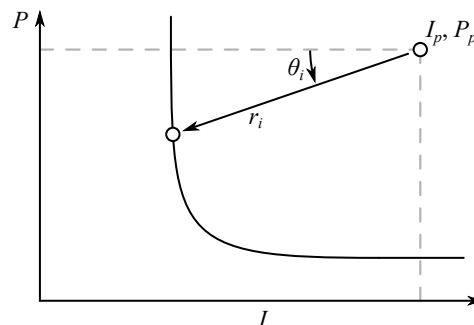


Figure 6.1: Pivot search numerical method to compute pressure-impulse diagrams (Adapted from [70])

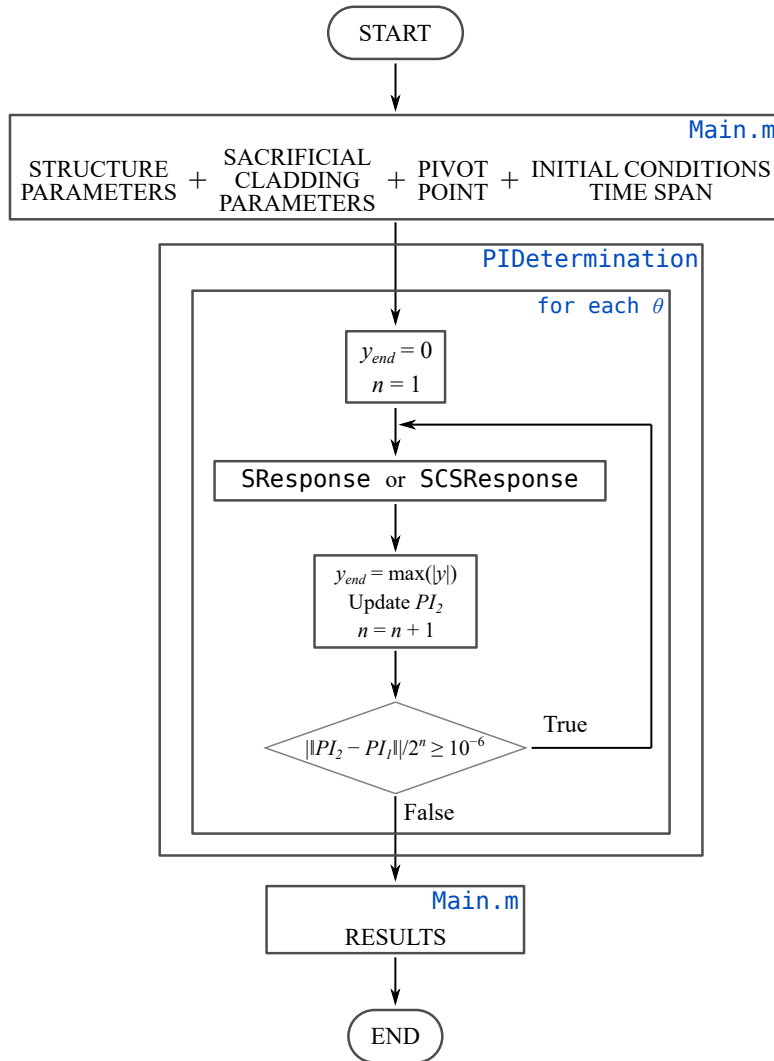


Figure 6.2: Logical diagram of the pivot search numerical method to compute Pressure-Impulse diagrams

## 6.2.2 Structure

An equivalent single-degree-of-freedom (SDOF) system is commonly used to model the dynamic behaviour of a single structural element. As reviewed in Section 2.9.4, the conversion of a structural element with distributed mass, stiffness and load into an equivalent SDOF system is performed by means of transformation factors. Taking into account that its deformation due to blast is mostly dominated by bending modes, it is considered advantageous to define the resistance curve as a function of this deformation.

### 6.2.2.1 Resistance-displacement curve

The development of the resistance-displacement curve for a reinforced concrete (RC) structural element will be detailed in the present section. When subjected to a dynamic

load, a RC structural element deforms elastically (state 1) until the tensile strength of concrete is exceeded and cracking is initiated (state 2) and, consequently, a reduction in stiffness is attained. Subsequently, due to the yielding of the reinforcement bars and the development of a plastic hinge, the stiffness is once again reduced and an accumulation of deformation and damage will occur at the vicinity of the latter (see Figure 6.3(a)). The conversion from the moment-curvature curve to a resistance-displacement curve depends on the properties of the structural element and the loading. Assuming that the structural element of interest is a one-way simply-supported RC structural element with a distributed load, the plastic hinge will form at mid-span and yields the corresponding schematic representation of the resultant resistance-displacement curve, illustrated in Figure 6.3(b).

An appropriate determination of the section's flexural stiffness throughout the entire response is paramount for the correct computation of the RC beam's resistance-displacement curve. Figure 6.4 shows a generic cross-section of a doubly-reinforced concrete beam with height  $h$  and width  $b$ . Firstly, according to Darwin and team [26], it may be assumed that, in elastic regime, the strain in the concrete and steel are equal and, consequently,

$$\varepsilon_c = \varepsilon_s \Leftrightarrow \frac{f_c}{E_c} = \frac{f_s}{E_s} \Leftrightarrow f_s = \frac{E_s}{E_c} f_c = \alpha_e f_c \quad (6.1)$$

where  $f_c$  and  $f_s$  are the concrete and steel's stresses, respectively,  $E_c$  and  $E_s$  are the concrete and steel's Young's modulus, respectively, and  $\alpha_e$  is commonly referred to as the modular ratio.

Resorting on the method of the transformed section, in which the steel is replaced by a given quantity of concrete so that the resultant force remains constant, the equivalent area of fictitious concrete becomes  $\alpha_e A_s$  and  $\alpha_e A'_s$ . Subsequently, the distance between the top of the cross-section and the neutral axis position, denoted as  $x_I$  (see Figure 6.4),

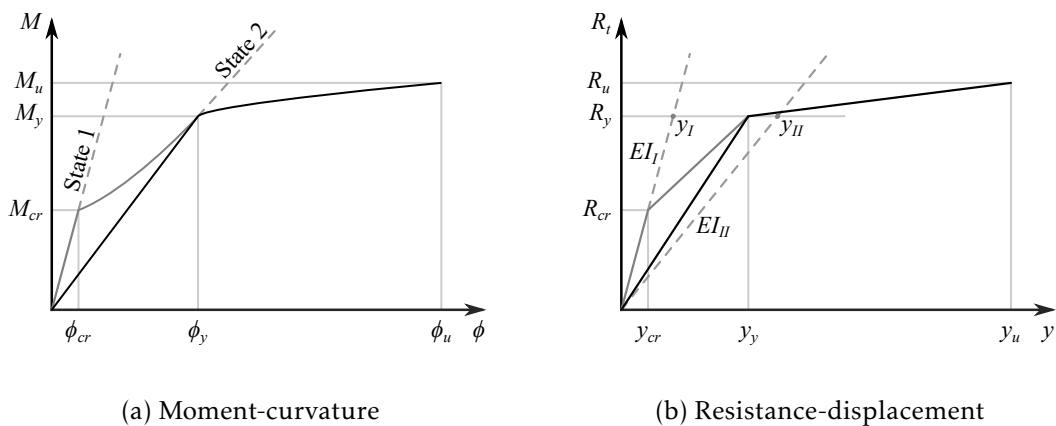


Figure 6.3: Response of a reinforced concrete structural element

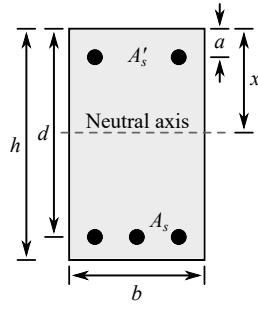


Figure 6.4: Generic RC cross-section

is given by the following expression,

$$x_I = \frac{(bh^2/2) + d(\alpha_e - 1)A_s + a(\alpha_e - 1)A'_s}{bh + (\alpha_e - 1)(A_s + A'_s)} \quad (6.2)$$

where  $a$  and  $d$  are the distance between the top fibre of the cross section and the top and bottom reinforcements' centre of gravity, respectively. Usually the area of the reinforcement steel bars is simply multiplied by  $\alpha_e$  and summed to the concrete's gross cross-sectional area. However, this procedure induce small errors in the analysis which may be avoided by using the steel reinforcement's area multiplied by  $(\alpha_e - 1)$ , since the concrete's gross cross-sectional area is being used instead of the net area. The moment of inertia of the cross-section under elastic regime, computed about the previously referred neutral axis, may be determined according to equation (6.3).

$$I_I = \frac{bh^3}{12} + bh\left(x - \frac{h}{2}\right)^2 + (\alpha_e - 1)A_s(d - x)^2 + (\alpha_e - 1)A'_s(x - a)^2 \quad (6.3)$$

According to [26], when an homogeneous section is subjected to pure bending, the stress values (normal to the section) increase proportionally with the distance from the neutral axis to the point of interest, taking the maximum value at extreme fibres. Therefore, the stress  $f$  at a given point is a function of the bending moment  $M$ , the distance from the neutral axis  $y$  and the moment of inertia  $I$ , according to:

$$f = \frac{My}{I} \quad (6.4)$$

Considering the mid-span section of the beam, it is readily verified that the extreme fibre at its bottom is subjected to the maximum tensile stress and, therefore, constitutes the limiting value for the computation of the cracking moment, whose expression is defined as,

$$M_{cr} = \frac{f_{ctm}I_I}{y_t} \quad (6.5)$$

where  $f_{ctm}$  defines the average tensile strength of concrete and  $y_t$  depicts the distance between the neutral axis and the bottom extreme fibre. Alternatively, for design purposes, the moment of inertia of the elastic transformed section may be approximated by

that of the gross concrete section  $bh^3/12$ , neglecting the influence of reinforcement [26]. Therefore, an approximated cracking moment is given by:

$$M_{cr} \approx \frac{f_{ctm} b h^2}{6} \quad (6.6)$$

Assuming that a uniform load is impinged upon a simply-supported beam, the resistance value that corresponds to the cracking moment is computed by means of the following expression:

$$R_{cr} = \frac{8M_{cr}}{L} \quad (6.7)$$

Lastly, the displacement at cracking may be computed as a function of the flexural stiffness of a one-way reinforced beam subjected to a distributed load as follows:

$$y_{cr} = \frac{R_{cr}}{k_I} = R_{cr} \frac{5L^3}{384E_c I_I} \quad (6.8)$$

After the development of cracking at the section's extreme fibre, it is assumed that the concrete is not able to transmit tensile stress and that the structural element's resistance is given by the steel reinforcement. Therefore, the bending moment capacity of the considered cross section is characterised by the yield of the reinforcement steel under tensile loading. It should be referred that, in the present study, only the reinforcement steel under tensile stress is considered relevant for the determination of the flexural capacity of the beam. Defining the mechanical reinforcement ratio  $\omega$  as,

$$\omega = \frac{A_s f_y}{f_c b d} \quad (6.9)$$

where  $f_y$  is the yield stress of steel,  $f_c$  is the compressive strength of concrete and  $d$  is the effective depth of the cross-section, the reduced bending moment  $\mu$  is defined as:

$$\mu = \omega(1 - 0.588\omega) \quad (6.10)$$

The bending moment of a given beam (rectangular cross-section) may be computed as follows:

$$M_y = \mu f_c b d^2 \quad (6.11)$$

Accordingly, the resistance associated with the bending moment capacity  $R_y$  is determined by means of equation (6.7), replacing  $M_{cr}$  by  $M_y$ . The deformation at mid-span is computed with the method defined by the Eurocode 2 [35]. This method considers that, in order to accurately model the behaviour of RC structural elements and correctly determine their deflection, a distribution coefficient  $\zeta$  must be defined. It should be noted that this coefficient aims to take into account the contribution of concrete under tensile loads between cracks by means of a simplified approach. The deformation of the structural

element  $y_y$  is considered to be the sum of the deflection of the element if its section is considered to be uncracked (state I) and completely cracked (state II), as follows,

$$y_y = (1 - \zeta) y_I + \zeta y_{II} \quad (6.12)$$

while the distribution coefficient  $\zeta$  is computed by means of the following expression,

$$\zeta = 1 - \beta \left( \frac{M_{cr}}{M} \right)^2 \quad (6.13)$$

where  $\beta$  is a coefficient that takes into account the nature of the loading and  $M$  is the bending moment of interest ( $M_y$  to compute the deflection at yield). Taking into account the aim of the present study,  $\beta$  takes a value of 1, since short duration loadings are of interest [35]. In order to compute the displacement at yield while assuming the completely cracked cross-section, its moment of inertia and neutral axis' position must be computed. Once again, the method of the transformed section is used and the distance between the top of the cross-section and the neutral axis is given by:

$$x_{II} = \frac{-[\alpha_e A_s + (\alpha_e - 1) A'_s] + \sqrt{[\alpha_e A_s + (\alpha_e - 1) A'_s]^2 + 2b[\alpha_e A_s d + (\alpha_e - 1) A'_s a]}}{b} \quad (6.14)$$

It is important to refer that only the compressed concrete zone is considered for the computation of the cracked cross-section's properties. With the known position of the neutral axis, it is possible to determine the moment of inertia of the cross-section about it, as follows:

$$I_{II} = \frac{b x^3}{3} + \alpha_e A_s (d - x)^2 + (\alpha_e - 1) A'_s (d - a)^2 \quad (6.15)$$

Following the computation of the uncracked and cracked cross-sections' properties, one must determine the respective deflections when  $M_y$  is imparted on them:

$$y_I = R_y \frac{5L^3}{384E_c I_I} \quad (6.16)$$

$$y_{II} = R_y \frac{5L^3}{384E_c I_{II}} \quad (6.17)$$

Lastly, the mid-span displacement is computed resorting to equation (6.12).

Taking into account that no hardening was considered for steel in the present study, the resistance-displacement curve, after the yield of the cross-section, becomes constant regardless of the increase of displacement. Additionally, as commonly considered [100, 173], the first state of the RC structural element, characterized by an elastic deformation, is not taken into account. Consequently, a elasto-perfectly plastic behaviour is attained. It should be noted that, for the rebound phase, the reviewed procedure may be used considering that the beam's cross section is mirrored around an horizontal axis located at mid-height.

### 6.2.2.2 Implementation

The SDOF model behaviour is governed by the ordinary differential equation (6.18) which is numerically solved with the fourth/fifth-order explicit Runge-Kutta method with arbitrary initial conditions available in MATLAB [96].

$$M_e \frac{d^2 y}{dt^2} + R_e(y) = F_e(t) \quad (6.18)$$

However, as the Runge-Kutta method only solves first-order ordinary differential equations, the previously presented equation must be re-written as a system of first-order ODEs by means of space-state notation:

$$\begin{bmatrix} \frac{dy}{dt} \\ \frac{dv}{dt} \end{bmatrix} = \begin{bmatrix} v \\ \frac{F_e(t) - R_e(y)}{M_e} \end{bmatrix} \quad (6.19)$$

The resistance-displacement curve  $R_e(y)$  is a piecewise bilinear function and, consequently, the dynamical system becomes a hybrid one, i.e. the system must interact with both continuous and discrete state/algebraic variables [126]. Although the resistance  $R_e$  can be defined as a piecewise function of  $y$ , in this particular case, only four discrete values are admissible (stages *I* to *IV* in Figure 6.5(a)). In order to define the transition between stages, a transition diagram, such as the one depicted in Figure 6.5(b), may be used. “Events” were once again used to terminate the analysis if certain conditions are met. In Figure 6.5(b) one may observe that three different “event” functions were considered to make the transition between stages. These event functions were defined in terms of state variables and, consequently, a third one must be added to the previously presented system of first-order ODEs, which becomes,

$$\begin{bmatrix} \frac{dy}{dt} \\ \frac{dv}{dt} \\ \frac{dR_e}{dt} \end{bmatrix} = \begin{bmatrix} v \\ \frac{F_e(t) - R_e(y)}{M_e} \\ (1 - tag_2) k_E v \end{bmatrix} \quad (6.20)$$

where  $tag_2$  is a stage indicator, that is either 0 (stages *I* and *III*) or 1 (stages *II* and *IV*). The three “event” functions are shown in equation (6.21), from which it is possible to observe that two of them are a function of the displacement, while the other depends on the velocity. “Envelope” function (EnvI\_III) is defined in order to reduce the number of “event” functions required to transition between stages. This function, used for stages *I* and *III*, contains “event” functions 1 and 2, while stages *II* and *IV* only require the use



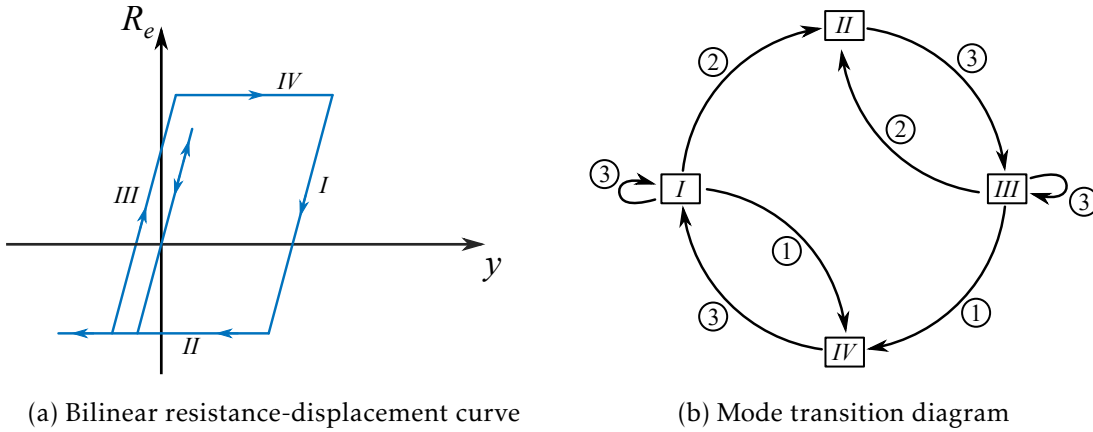


Figure 6.5: Bilinear hysteretic model (Adapted from Pei and team [126])

of the third event function, denoted by  $\text{EnvII\_IV}$ .

$$\begin{array}{l}
 \text{Event \#1: } R_e(y) - R_y = 0 \\
 \text{Event \#2: } R_e(y) + R_y = 0 \\
 \text{Event \#3: } v = 0
 \end{array}
 \left| \begin{array}{l} \\ \\ \\ \end{array} \right.
 \Rightarrow \begin{array}{l}
 \text{EnvI\_III}(t, \mathbf{y}) \\
 \\
 \text{EnvII\_IV}(t, \mathbf{y})
 \end{array}
 \quad (6.21)$$

The logical diagram used for the implementation of the bilinear SDOF system is shown in Figure 6.6. Similarly to that of the sacrificial cladding solution, a `Main` MATLAB script was used on the implementation of the SDOF system. This script starts with the definition of the parameters of the equivalent SDOF system, the blast scenario, which, unless stated otherwise, is a triangular pulse defined as function of  $P_r$  and  $i_r$ , the initial conditions (zero by default) and the time span for the numerical integration. Next, the time integration of the first-order ODEs is conducted by the `ode45` routine inside the `SResponse` function. In order to speed up the computation and limit the number of input variables to the required ODE (`@SODED`) and “event” (`@EnvI_III` or `@EnvII_IV`) functions, the concept of nested functions was used. The `tag2` mode indicator is initialised and the `@EnvI_III` “event” function is initially selected. Subsequently, a while loop is used to guarantee that the numerical integration is performed over the entire time span, since the event function may terminate the analysis before the end time  $t_{end}$  is reached. When an event is triggered, a set of `if` conditions are used to verify which “event” function stopped the analysis and the required variables are updated accordingly. Then, the while loop guarantees that the numerical integration continues until the termination time is reached. The `SResponse` function returns the displacement and velocity-time histories, as well as the resultant force on the SDOF system’s spring, to the `Main` MATLAB script, which allows a post-processing of the results.

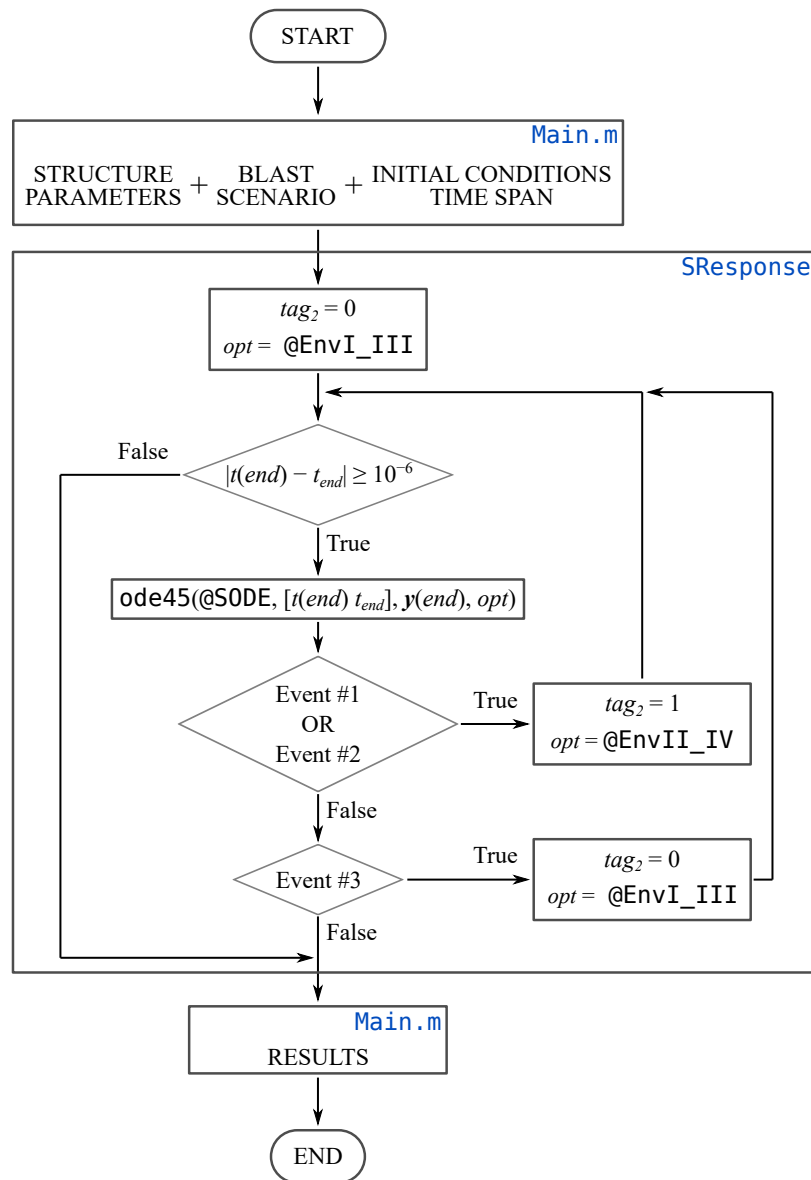


Figure 6.6: Logical diagram of MATLAB implementation for bilinear SDOF system

### 6.2.2.3 Validation

In order to validate the results obtained with the implemented SDOF model, the non-dimensional maximum response of an undamped elastoplastic SDOF due to a triangular load pulse (see Figure 2.15) was used. A non-dimensional SDOF system, whose stiffness, resistance and mass take a unitary value, is considered, resulting in a fundamental vibration period  $T$  of 6.28 s. Afterwards, the peak pressure ( $P$ ) and load duration ( $t_d$ ) of the triangular pulse are varied in order to obtain several non-dimensional combinations, namely 0.2, 0.4, 0.8, 2.0 and 10.0 for  $t_d/T$  and 0.2, 0.4, 0.6, 0.8, 1.0, 1.5 and 2.0 for  $R_y/P$ . The solid lines in Figure 6.7 depict the non-dimensional maximum response determined by Biggs [9], while the crosses shown in the referred figure are the results obtained with

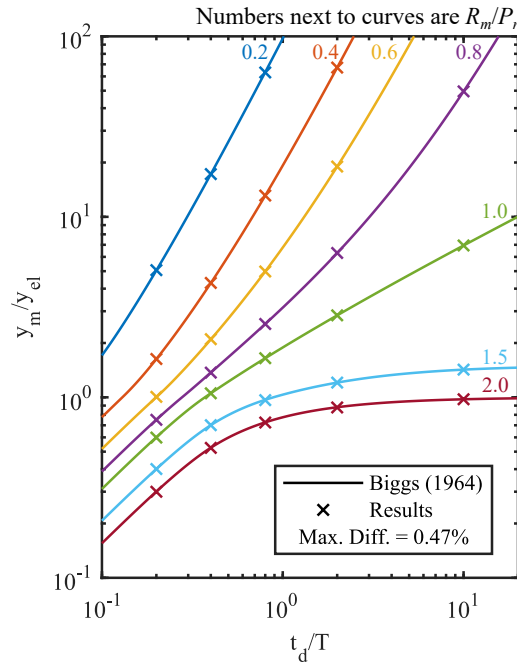


Figure 6.7: Non-dimensional maximum response an undamped elasto-plastic SDOF due to a triangular load pulse

the implemented SDOF model. The implementation is considered to be validated, since the MATLAB code yields, practically, the same non-dimensional maximum displacements as the ones reported by Biggs (error less than 0.5%).

### 6.2.3 Load-Cladding-Structure (LCS) model

As reviewed in Section 3.5.3.3, Ma and Ye [87] developed a simplified model, referred to as the Load-Cladding-Structure (LCS) model, that computes the nonlinear behaviour of a sacrificial cladding, while simultaneously taking into account the behaviour of both cladding and structural element. The following section presents its implementation procedure in MATLAB.

#### 6.2.3.1 Implementation

The LCS model requires the time integration of the ODE's system given in equation (6.22) until either the sacrificial cladding is fully compressed (up to the densification strain) or the velocity of the front plate becomes equal to that of the structural element. Afterwards, the ODE's system is reduced into the equation of motion of the equivalent SDOF system (given by equation (6.23)).

$$\begin{cases} \left[ M_1 + \frac{\rho A}{\varepsilon_d} (u - y) \right] \frac{d^2 u}{dt^2} + \frac{\rho A}{\varepsilon_d} \left( \frac{du}{dt} - \frac{dy}{dt} \right)^2 + [\sigma_{pl} - p(t)] A = 0 \\ \left[ \rho A l - \frac{\rho A}{\varepsilon_d} (u - y) + M_e \right] \frac{d^2 y}{dt^2} + R_e y - \sigma_{pl} A = 0 \end{cases} \quad (6.22)$$

$$(M_1 + \rho A l + M_e) \frac{d^2 y}{dt^2} + R_e y - p(t) A = 0 \quad (6.23)$$

Once again, the MATLAB ode45 function was used to numerically integrate the LCS model with respect to time. Consequently, the previously presented ODE's system was reduced by means of space-state notation into the system of first-order ODEs given by equation (6.24). It should be noted that, although the LCS model considers the structural element always in the elastic regime, the implementation conducted on the present study has the capability to model an elasto-plastic SDOF system, using a piecewise bilinear function  $R_e(y)$ .

$$\begin{bmatrix} \frac{du}{dt} \\ \frac{dv_{FP}}{dt} \\ \frac{dy}{dt} \\ \frac{dv_S}{dt} \\ \frac{dR_e}{dt} \end{bmatrix} = \begin{bmatrix} v_{FP} \\ - \left[ A \left( \frac{\rho (v_{FP} - v_S)^2}{\varepsilon_d} + \sigma_{pl} - p(t) \right) \right] / \left[ M_1 + \frac{\rho A}{\varepsilon_d} (u - y) \right] \\ v_S \\ \left[ A \sigma_{pl} - R_e(y) \right] / \left[ M_e + \rho A l - \frac{\rho A}{\varepsilon_d} (u - y) \right] \\ (1 - tag_2) k_E v_S \end{bmatrix} \quad (6.24)$$

A second system of first-order ODEs is required to simulate the behaviour of the structure after the full compression of the cladding or in the case when the velocity of both the front plate and structure become equal. This system, which is based on equation (6.23), is depicted in equation (6.25).

$$\begin{bmatrix} \frac{du}{dt} \\ \frac{dv_{FP}}{dt} \\ \frac{dy}{dt} \\ \frac{dv_S}{dt} \\ \frac{dR_e}{dt} \end{bmatrix} = \begin{bmatrix} 0 \\ 0 \\ v_S \\ [F_e(t) - R_e(y)] / [M_e + \rho A l + M_1] \\ (1 - tag_2) k_E v_S \end{bmatrix} \quad (6.25)$$

The “event” functions defined in Table 6.1 are used to define the termination criteria for the LCS model. These “event” functions are related to the sacrificial cladding (“event” functions 1 and 2) and to transition between stages of the resistance function  $R_e$  (“event” functions 3 to 5) and may be reduced into four “envelope” functions (ODEEndI, ODEEndII, EnvI\_III and EnvII\_IV). The latter are divided into two groups, each with a couple of “envelope” functions, that are relevant before and after the “events” related to the sacrificial cladding occur (see Table 6.1).

Figure 6.8 illustrates the logical diagram behind the implementation of the reviewed LCS model. The `Main` MATLAB script was employed to define the properties of the sacrificial cladding solution and the structure, the blast scenario and the time integration parameters, i.e the initial conditions of the analysis and the desired time span. Subsequently, the `SCSResponse` function is used as a parent function for the ODE’s and “event” functions nested inside it. Two functions, identified by handles `@ODEI` and `@ODEII`, were numerically solved by the `ode45` function. These functions respectively correspond to the first-order ODE system before and after the “events” related with the sacrificial cladding solution take place.

Firstly, the `SCSResponse` function verifies if compaction of the crushable core will take place, initialises the required variables accordingly and resorts to the `ode45` function to integrate the ODE’s system until an “event” is triggered. When it occurs, it is paramount to correctly identify which “event” function terminated the analysis. Therefore, a series of if conditions are employed to identify it and, subsequently, the required variables are updated. Lastly, if the termination time is reached, the `SCSResponse` function returns the displacement and velocity-time histories of the cladding’s front plate and the equivalent structure and the resultant spring’s force to the `Main` MATLAB script, which performs the post-processing of the results.

Table 6.1: Event functions for the LCS model

“Event” function	Before SC “events”		After SC “events”	
	ODEEndI	ODEEndII	EnvI_III	EnvII_IV
#1: $\frac{u-y}{\varepsilon_d l} - 1 = 0$	x	x		
#2: $v_{FP} - v_S = 0$	x	x		
#3: $R_e(y) - R_y = 0$	x		x	
#4: $R_e(y) + R_y = 0$	x		x	
#5: $v_S = 0$		x		x

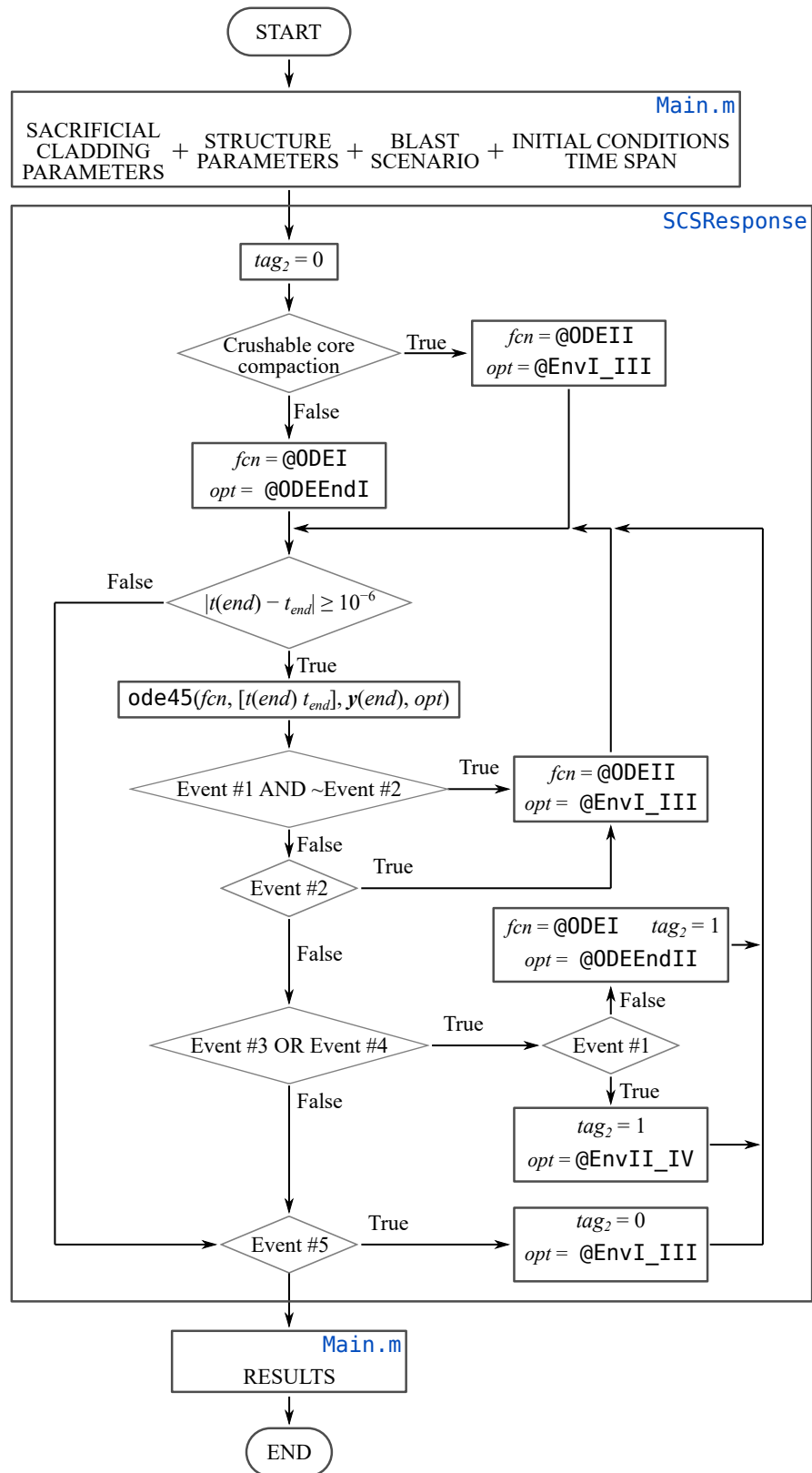


Figure 6.8: Logical diagram of MATLAB implementation for LCS model

### 6.2.3.2 Validation

A fully-clamped steel wide flange I-beam (W14×426) with a 6 m span is to be protected (2.54 m<sup>2</sup> loaded area) [87]. Ma and Ye [87] state that, after the SDOF conversion, the equivalent mass and stiffness of the structure become 2720 kg and 1.12×10<sup>8</sup> N/m, respectively. Therefore, the critical deflection of the beam, i.e. its elastic limit, takes a value of 9.1 mm. The front plate of the sacrificial cladding solution is materialised with steel, yielding a mass of 300.4 kg, while its crushable core is considered to be a foam with a density of 225 kg/m<sup>3</sup> and a 0.8 densification strain. The plateau stress and thickness of the foam were varied according to the non-dimensional parameters in order to obtain a comparison between the results obtained by the authors and the implementation performed in the present study. Two non-dimensional blast scenarios (triangular pulse) were considered to be imparted on the cladding's front plate. This blast scenarios are normalised according to the usual procedure to determine non-dimension pressure-impulse diagrams (see Section 2.9.5 for more details). A constant non-dimensional peak overpressure of 4 was assumed, while the non-dimensional impulse took values of 1.2 and 2.0.

As illustrated in Figure 6.9, Ye and Ma [180] varied the non-dimensional parameters between 0.5 and 2.0 to obtain the corresponding non-dimensional maximum response  $y_m/y_{el}$ . Similarly, in the present work, the same parameters were varied between these values, with a 0.05 spacing, and the obtained results are also depicted in the referred figure (on the right). Comparing the maximum values for both cases, obtained when  $\tau = \kappa = 0.5$ , a maximum relative error of 1% was observed. Additionally, a qualitative comparison between the plotted results in each sub-figure reveals a good agreement between them.

Additionally, in order to verify the validity of the obtained results in terms of maximum response when the protected structural element (considered as elastic) is subjected to a larger range of blast scenarios, non-dimensional P-I diagrams were generated for different combinations of  $\tau$  and  $\kappa$ . Similarly to what was performed for the validation of the bilinear SDOF system's implementation, the results presented by Ye and Ma [180] are illustrated in Figure 6.10 with a solid line, while a cross is used to depict the pressure-impulse combinations obtained with the current implementation. It should be noted that the referred authors defined the non-dimensional pressure as  $p = 2P_r A / (k_E y_E)$ . A maximum relative error of 3% was observed in terms of non-dimensional impulse when a non-dimensional pressure of 14 is considered to be applied to the protected structural element. Analysing the referred figure, one may verify a good agreement between the results across the entire range of blast scenarios, both for the original structural element (computed with the independent SDOF system) and the protected structure, when several combinations of  $\tau$  and  $\kappa$  are considered.

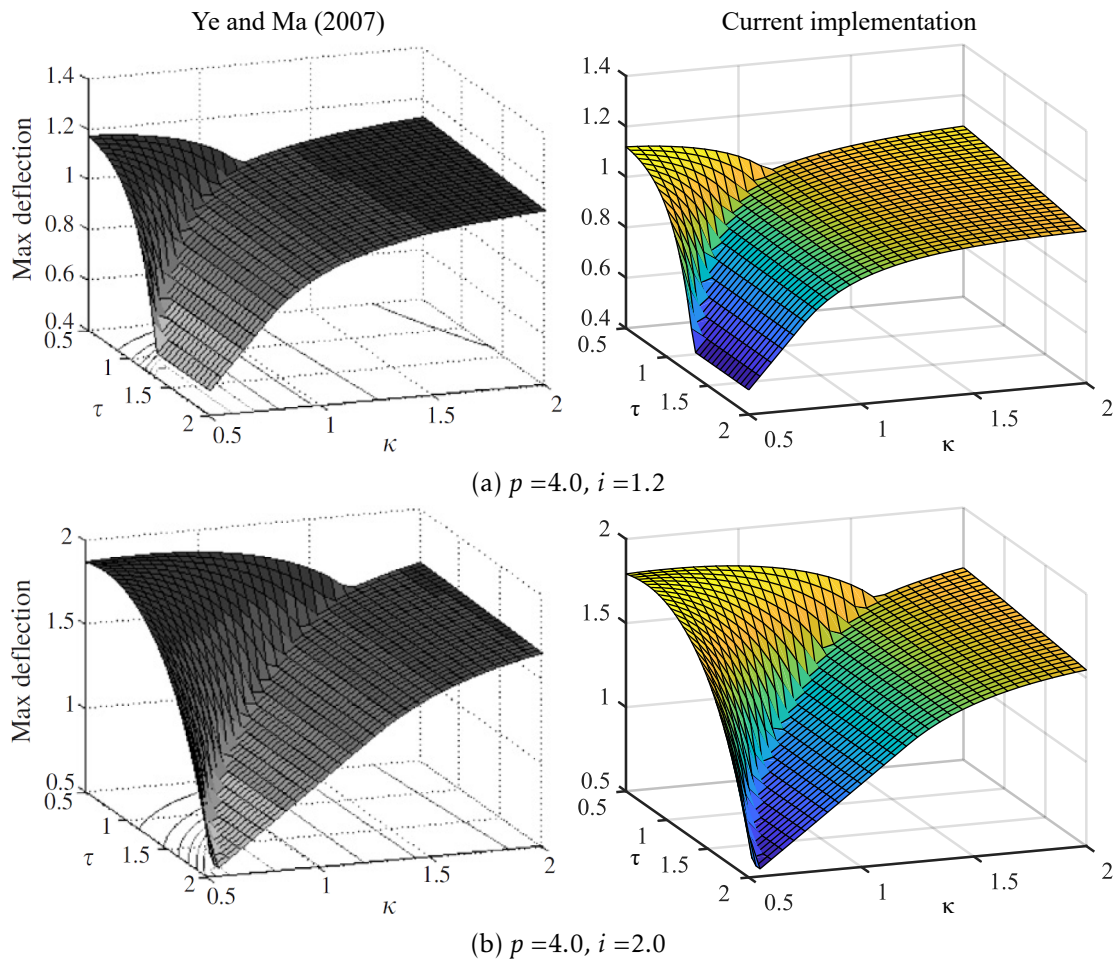


Figure 6.9: Non-dimensional maximum displacement of a structure protected with a foam sacrificial cladding [87]

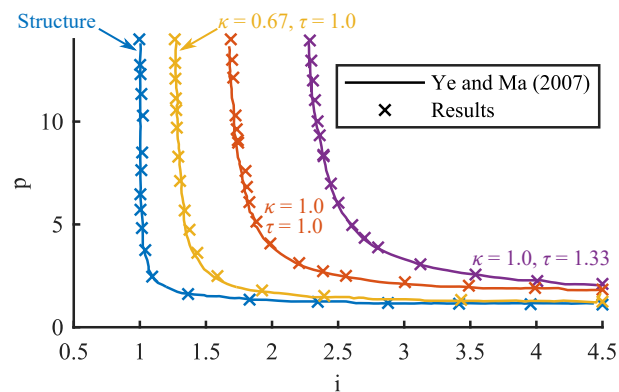


Figure 6.10: Non-dimensional pressure-impulse diagram of the structure [180]

### 6.2.3.3 Modifications to the Load-Cladding-Structure model

Taking into account that the proposed cladding solution is based on 3D printed crushable cores, the improvements presented in Section 5.3.4.2 regarding the nonlinear response of the crushable core are implemented in the Load-Cladding-Structure model.



Besides, the nonlinear behaviour of the structural element will be taken into account, since, as reviewed in Table 2.5, the majority of protection levels allow a maximum deflection larger than its elastic limit. It should be noted that the previously presented implementation has the ability to consider a protected element with an elastoplastic resistance function and, consequently, no further modifications are required. Since non-dimensional parameter  $\kappa$  relates the resistance of the structure with the plateau stress of the cladding, it is readily concluded that no modification is required for the referred parameter because the philosophy behind its development still holds valid even if the structure behaves in a nonlinear fashion. Non-dimensional parameter  $\tau$  assumes that the full compression of the crushable core takes place when the structure reaches its maximum displacement, whose time is given by  $T/2$  when an elastic behaviour is considered. However, if the structure enters the plastic regime, the time required to attain this displacement will vary and a modification to  $\tau$  might be deemed necessary. Although a loss in optimisation might be introduced by not taking this difference into account, the present study assumes that  $T/2$  is a valid approximation for the time at maximum deflection and that the previously presented  $\tau$  is valid for the design of sacrificial cladding solutions, even in cases where the structure's maximum deflection occurs under plastic regime.

As reviewed in Chapter 2, the use of Kingery & Bulmash semi-empirical predictions, in combination with the modified Friedlander equation, is the best practice to define the blast wave parameters and approximate the pressure-time profile of the positive phase. The effects of blast wave clearing and fluid-structure interactions on the original blast wave profile will be taken into account resorting to the method proposed by Hudson and the extended Taylor theory cumulatively. When stated, the referred blast wave profile and the consideration of a non-ideal reflective surface will be considered and applied either directly to the structural element, if no cladding is present, or to the cladding's front plate. Consequently, the computation of the PI diagram must be performed resorting to a charge weight-standoff diagram, which is able to take into account the different effects on the blast wave profile and may be converted into a PI diagram since the resulting pressure and impulse are known for each charge weight-standoff combination. Figure 6.11 illustrates the corresponding logical diagram. The `Main` MATLAB script is used to define the properties of the structural element and, if required, those of the sacrificial cladding solution, and the standoff distances at which the charge weights will be computed. Subsequently, resorting to parallel computing, the `CWSDetermination` determines the charge weights for each standoff by means of the bisection method. When convergence is attained, the charge weight-standoff is converted to the corresponding pressure-impulse diagram by means of the Kingery & Bulmash semi-empirical predictions for surface bursts.

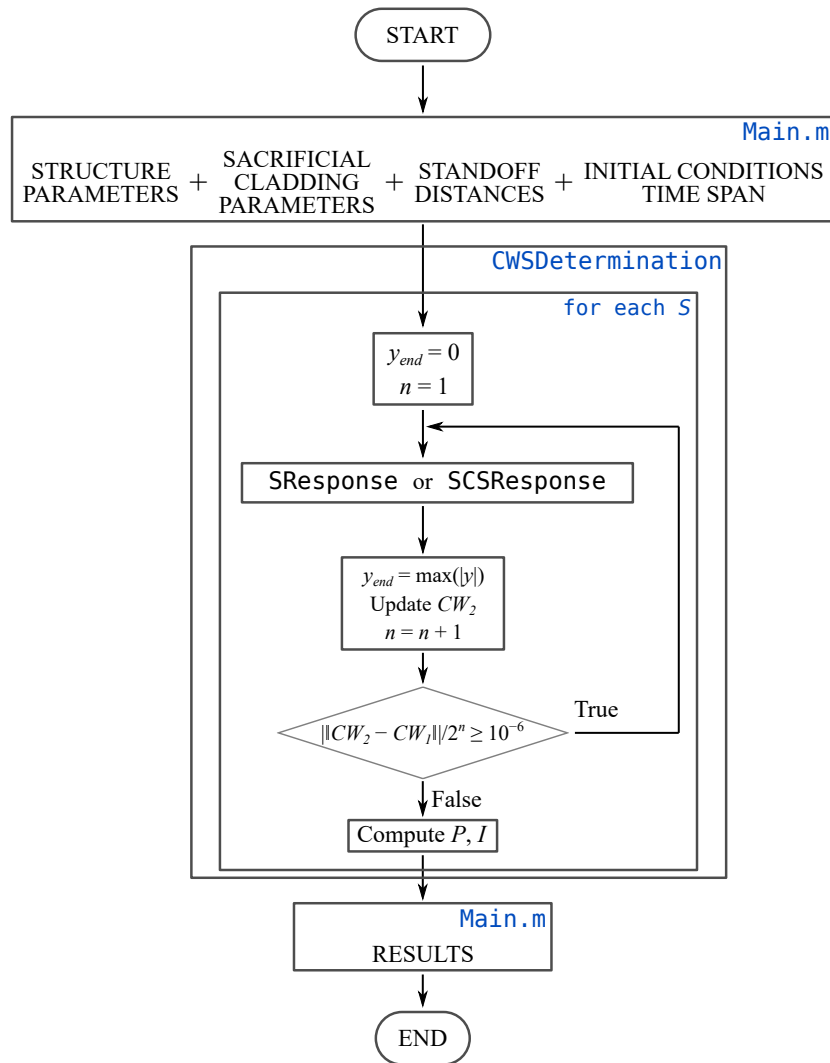


Figure 6.11: Logical diagram of the determination of pressure-impulse diagram resorting to charge weight-standoff diagram

### 6.3 Case study

In order to illustrate the proposed design procedure of the sacrificial cladding, a case study was selected from the available literature. Magnusson [90, 91] conducted an experimental campaign on reinforced concrete beams subjected to quasi-static and air blast loads. A total of 89 concrete beams, with varying strength and reinforcement ratio, were tested by the author under quasi-static and air blast load conditions in order to determine the specimen's load capacity and deflection.

#### 6.3.1 Experimental campaign

The RC beams tested by Magnusson possessed a length of 1720 mm, a height of 160 mm and a width of 290 mm. As illustrated in Figure 6.12, they had a 1500 mm clear span

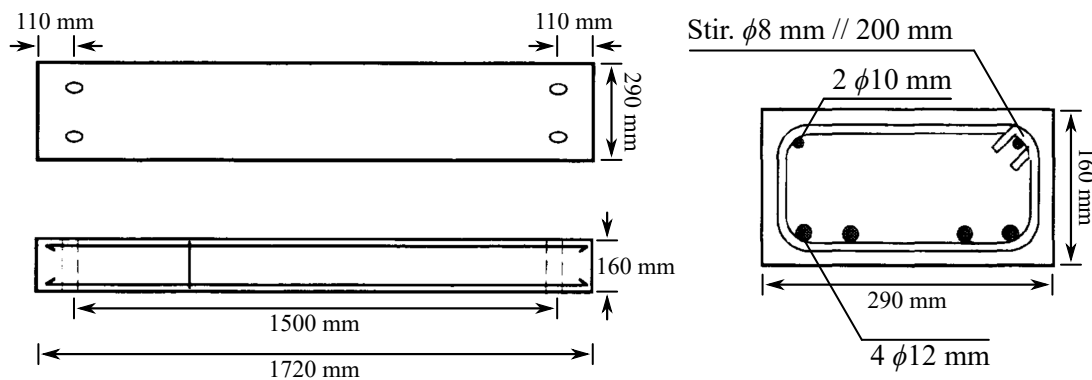


Figure 6.12: Geometry and reinforcement details for one-way RC beams (Adapted from [91])

and their tensile reinforcement was characterised by four 12 mm diameter steel reinforcement, whose yield and ultimate strength and Young's modulus was 580 and 678 MPa and 203 GPa, respectively. Additional rebars consisting of two 10 mm diameter steel compressive reinforcement and stirrups with 8 mm diameters spaced at 200 mm as shear reinforcement were present. A clear cover of 25 mm was used for all the built specimens. Regarding the properties of the concrete, which were determined on the same day as the tests, the author reports a compressive strength, a splitting tensile strength and a Young's modulus of 101, 5.4 MPa and 41.7 GPa, respectively.

The blast load was induced using the shock tube (Tube IV at FOA's testing ground in Märsta, Sweden), schematically represented in Figure 6.13, which had an internal rectangular cross section with 1.6 m height and 1.2 m width. The RC specimen was positioned in a test ring while the explosive charge was centred on the tube's cross section at a distance of 10 m from the specimen and at a distance of 50 m from the open end of the tube. According to the author, this distance allows the resultant shock wave to be considered as uniform when imparted on the specimen. The supports used by the author may be considered as rigid with negligible horizontal displacements and, since the bolts that fixed the specimen had a relatively low flexural strength, the beam was assumed to be simply-supported. The remainder of the shock tube's opening was covered by the test rig (concrete wall covered with steel) which allowed the recording of the applied blast load resorting to two pressure gauges. The resultant support reactions were also recorded during the blast tests with two load cells at each support. Table 6.2 presents the blast load applied to the reinforced concrete specimen and the resultant maximum mid-span displacement.

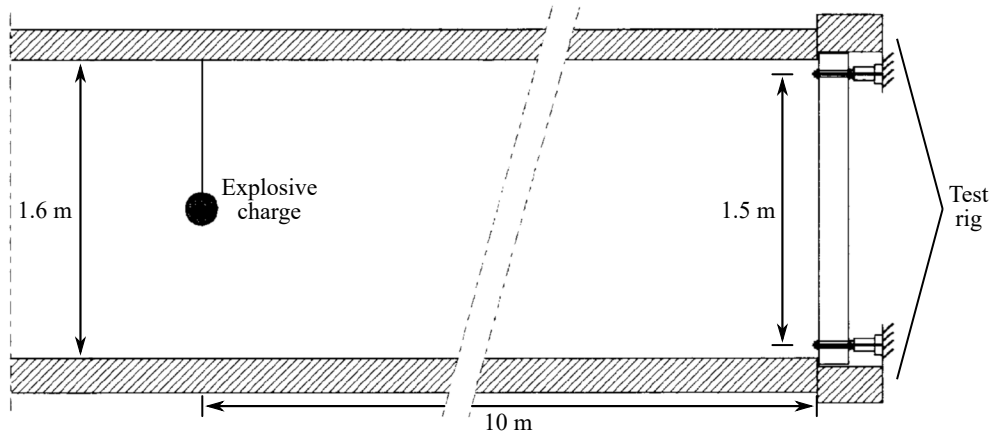


Figure 6.13: Experimental set-up of the RC beam and explosive charge within the shock tube (Adapted from [91])

Table 6.2: Blast wave parameters and experimental results obtained by Magnusson when specimen B100-D2(12) is subjected the effects of a 2.0 kg explosive charge [91]

Blast wave parameters			Experimental results
$P_r$ [kPa]	$t_d$ [ms]	$i_r$ [kPa·ms]	$d_{max}$ [mm]
1059.0	26.0	5910.0	22.9

### 6.3.2 Simplified model

The SDOF model developed during the present study (see Section 6.2.2 for more details) was used to simulate specimen B100-D2(12) from the reviewed experimental campaign [90, 91]. The resistance-displacement curve for the RC beam was computed according to the previously presented procedure, resorting to the concrete and reinforcement steel's properties given by the author, and depicted in Figure 6.14. Comparing the computed curve with the quasi-static experimental one, it is possible to conclude that a good approximation is attained, both during the elastic and plastic response. To account for strain rate effects, a dynamic increase factor of 1.25 was used for the concrete, while the reinforcement steel's yield and ultimate strengths were multiplied by a factor of 1.23 and 1.05, respectively, as defined by the UFC 3-340-02 [173]. This results in an elastic, perfectly plastic behaviour for steel, yielding an elastoplastic behaviour with no hardening for the structure. The SDOF system's properties computed resorting to the procedure reviewed in Section 6.2.2.1 are shown in Table 6.3. The resistance-displacement curve used during subsequent dynamic analysis is equally illustrated in Figure 6.14. The presented mass was then multiplied by the load-mass transformation factor according to Table 2.8.

Figure 6.15 illustrates the experimental displacement-time history, together with the one computed with the implemented SDOF system. Observing the referred figure, it is possible to verify that the maximum displacement predicted by the SDOF model greatly exceeds the experimental value by approximately 40%. In order to improve the numerical estimates, the dynamic increase factors should be corrected based on the actual strain

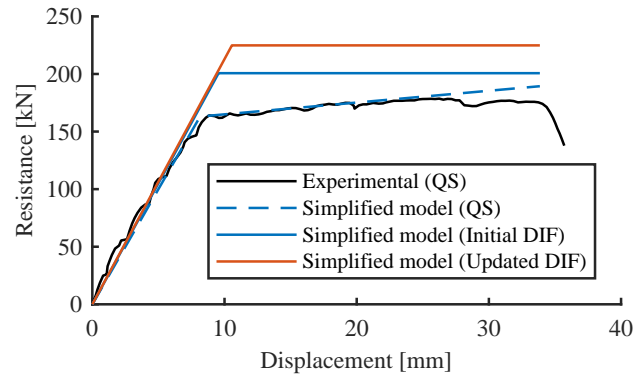


Figure 6.14: Experimental [91] and analytical resistance-displacement curves of a simply-supported RC beam

Table 6.3: SDOF's properties

Specimen	Mass [kg]	$M_y$ [kN·m]	$R_y$ [kN]	$k$ [kN/mm]
B100-D2(12)	174	37.63	200.69	21.01

rate. Taking the resistance at yield and the stiffness of the SDOF system from Table 6.3, one attains a yield displacement of 10.6 mm, which is reached in approximately 3.5 ms. According to the UFC 3-340-02 [173], the average strain rate for both concrete and steel reinforcement may be determined by means of the time to reach yield. Considering the previously computed value, the dynamic increase factors for concrete and steel become 1.35 and 1.38 (1.10 for ultimate strength), respectively. Using the updated DIFs, a new estimate for the resistance-displacement curve is established (see Figure 6.14), which allows the determination of the displacement-time history depicted in Figure 6.15. It should be noted that no further iteration is required because the time to yield did not present any meaningful changes. A significant improvement was attained since the difference between the experimental and numerical results is reduced to 20%. Despite the differences when compared with the experimental results, it is considered that the used SDOF model is able to model the nonlinear behaviour of the experimental specimens within a reasonable level of accuracy both in terms of quasi-static resistance-displacement curve, as in terms of dynamic behaviour.

### 6.3.3 Blast resistant capability

Pressure-impulse diagrams are computed in the present section to illustrate the blast resistant capabilities of the bare structural element. As reviewed, Table 2.6 shows the response limits defined by both the American Society of Civil Engineers [158] and the Protective Design Center of the U.S. Army Corps of Engineers [154] for several types of structural elements subjected to blast loads. Taking into account that the structural element of interest is a double-reinforced beam with shear reinforcement, one may determine the maximum mid-span deflections allowed by each damage level (see Table 6.4).

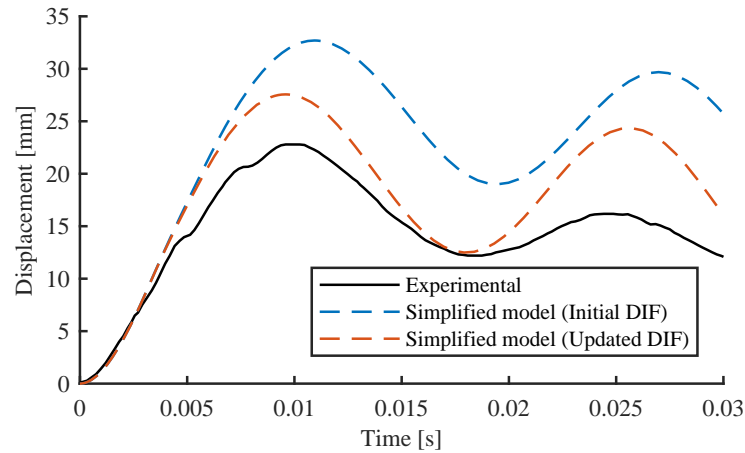


Figure 6.15: Experimental [91] and numerical displacement-time histories of RC beam subjected to a blast load

Table 6.4: Response limits considered for the case study

Damage level	Max. disp [mm]			
	Superficial ( $\mu = 1$ )	Moderate ( $\theta = 4^\circ$ )	Heavy ( $\theta = 6^\circ$ )	Hazardous ( $\theta = 10^\circ$ )
	10.6	52.45	78.83	132.25

Firstly, we investigate the influence of several approximations to the shock wave’s pressure-time history on the pressure-impulse diagrams. Therefore, the pressure-time history is approximated as either a triangular pulse or resorting to the modified Friedlander equation, cumulatively with the influence of blast wave clearing resorting to the method defined by Hudson [57]. Based on the maximum mid-span deflections presented in Table 6.4, two sets of PI curves were determined for each deflection and shown in Figure 6.16. The computation of the first set (depicted with a solid line for each response limit) was conducted resorting to the MATLAB implementation presented in Section 6.2.1 and considering that the pressure-time history may be approximated by a triangular pulse. The second set, which is represented by a dashed line in the referred figure, was determined by means of a charge weight-standoff diagram, which was subsequently converted into the illustrated pressure-impulse diagram, because the modified Friedlander equation was used to approximate the blast wave profile. It should be noted that an additional set of pressure-impulse diagrams was generated resorting to the modified Friedlander equation and taking into account the clearing effects via the Hudson method. Nonetheless, due to the limited range of application of the latter on this particular case, this set was not illustrated in the referred figure. Analysing the illustrated PI diagrams, one might verify that, when compared with a triangular pulse, approximating the blast wave profile with the modified Friedlander equation has little to no influence on the impulsive regime of the pressure-impulse diagram. This result was expected since the maximum deflection of the structural element becomes constant, regardless of the shape of the pressure-time

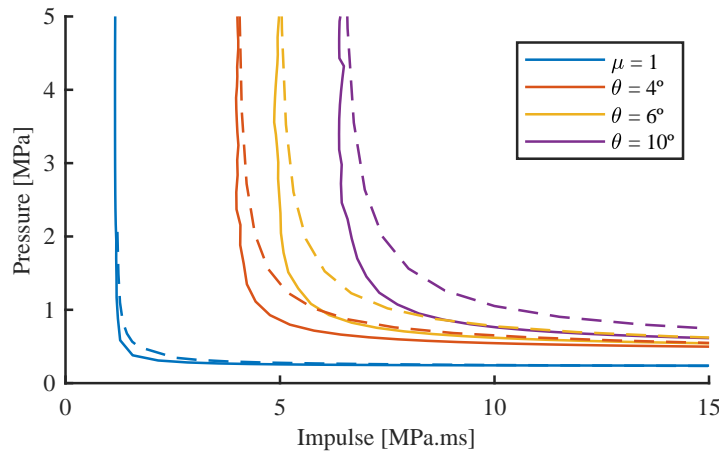


Figure 6.16: Pressure-impulse diagram considering that a triangular pulse (solid line) or the modified Friedlander equation (dashed line) is applied to the structural element

history. The greatest influence is observed when the positive phase duration and the fundamental period of the structure have similar values (dynamic regime) and, consequently, the resultant maximum deflection is highly influenced by the profile of the applied load. One might consider that approximating the blast wave profile with a triangular pulse is conservative since, for each response limit, the resultant pressure-impulse diagram is always on the “safe” side of the other set of PI diagrams. Nonetheless, the objective of the present study is the development and design of a high performance sacrificial cladding solution which should be highly optimised according to the required design specifications. Therefore, the use of the modified Friedlander equation is considered as recommended for the optimisation of the sacrificial cladding solution.

#### 6.3.4 Sacrificial cladding solution design

The current section aims to present the design procedure of a sacrificial cladding to be applied on the surface of the RC beam. The cladding will be designed assuming that the RC beam is classified as a primary structural element and that a moderate damage level, which corresponds to a  $4^\circ$  support rotation, is admissible. Analysing Figure 6.16, one might verify that, for the considered response limit, the bare structural element is able to withstand an impulsive blast load up to approximately 4 MPa.ms reflected impulse. The design of the cladding solution is conducted in order to increase the structural element’s ability to withstand impulsive loads by 50%. Therefore, a 6 MPa.ms impulse is considered to be imparted on it. Taking into account that, since an impulsive load is being applied, the shape of the blast wave profile will not influence the results and, to simplify the analysis, a triangular blast load is used.

The front plate of the cladding solution, considered to be a steel plate with a 2 cm thickness (yielding a mass of 68 kg), was assumed to remain unchanged throughout the entire design process. According to the findings of the experimental campaign, which

are in line with the relevant literature for a cellular solid, the plateau stress of 3D printed honeycomb structure is directly proportional to the relative density. Therefore, since only three different relative densities were tested during the experimental campaign, the relation between both properties is approximated resorting to a quadratic equation that passes through the origin (see Figure 6.17).

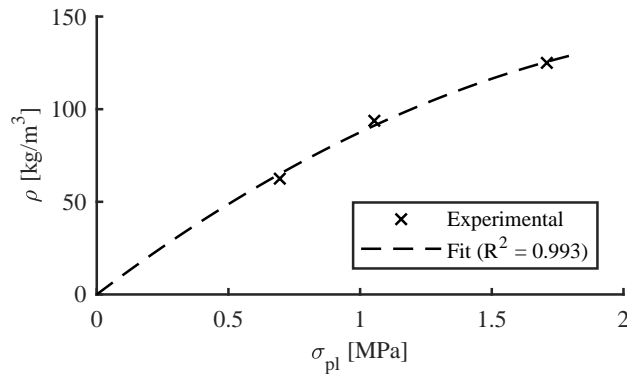


Figure 6.17: Density as a function of plateau stress of 3D printed honeycomb structure

Resorting to the non-dimensional parameters  $\kappa$  and  $\tau$ , as defined by Ma and Ye [87], one might compute the sacrificial cladding's plateau stress and thickness, respectively. These parameters were varied between 0.5 and 2.5 and the resultant plateau stress and thickness were used to determine the maximum displacement of the structural element when the 6000 kPa-ms impulse is imparted on it, yielding the surface depicted in Figure 6.18. This figure presents the ratio between the obtained maximum displacement and the maximum displacement corresponding to the 4<sup>o</sup> support rotation (see Table 6.4) as a function of both  $\kappa$  and  $\tau$ . The contour line corresponding to a unitary scaled displacement is shown on the obtained surface, together with the line when  $\kappa$  takes a value of 2<sup>1</sup>. The crossing of both (coloured) lines was selected as the design of the sacrificial cladding solution, whose plateau stress is 461.36 kPa, which corresponds to a 45.32 kg/m<sup>3</sup> density, and the required thickness takes a value of 15.1 cm.

With the design of the sacrificial cladding concluded, its influence on the structural element's performance, namely on the pressure-impulse diagrams, is evaluated. The pressure-impulse diagrams are generated using charge weight-standoff diagrams and the modified Friedlander equation to approximate the blast wave profile while, simultaneously, taking into account the increased pressure decay due to the velocity of the front plate, according to the extended Taylor theory defined by Aleyaasin and colleagues [2].

Figure 6.19 illustrates the pressure-impulse diagrams computed for each of the RC beam's response limit when the previously designed sacrificial cladding is applied to the RC beam (dashed lines), together with the bare structure's curves (solid lines). It should be noted that, since the objective of the present work is the design of a sacrificial cladding,

<sup>1</sup>This value of  $\kappa$  yields a cladding solution with twice the resistance than the one of the structural element.



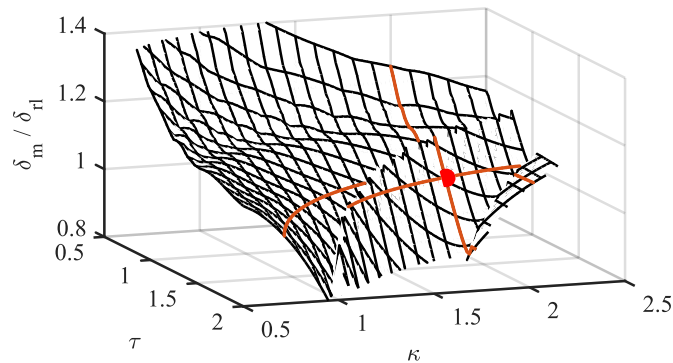


Figure 6.18: Scaled maximum displacement as a function of non-dimensional parameters  $\kappa$  and  $\tau$  when a 6000 kPa·ms impulse is imparted on the case study's structural element

the pressure-impulse diagrams depicted in Figure 6.19 are defined as a function of the reflected overpressure and impulse given by the Kingery & Bulmash's semi-empirical predictions. Therefore, if a given charge weight-standoff combination is considered as the design scenario, the shown pressure-impulse diagrams comprise a simple and fast method to verify if a given response limit is attained.

Analysing the curves corresponding to the moderate damage ( $\theta = 4^\circ$ ), it is possible to verify that the design was successful, since the impulse increased from 4 to 6 MPa·ms, which corresponds to the considered 50% increment in the ability of the structural element to withstand impulsive loads. When comparing the curves obtained for the remainder of the response limits, more specifically under impulsive regime, a similar increase was attained with the addition of the 3D printed sacrificial cladding. Observing the curves depicted in Figure 6.19 for the moderate ( $\theta = 4^\circ$ ), heavy ( $\theta = 6^\circ$ ) and hazardous ( $\theta = 10^\circ$ ) response limits, one may verify that the maximum allowable blast load under dynamic regime, i.e. when the positive phase duration is similar to the fundamental

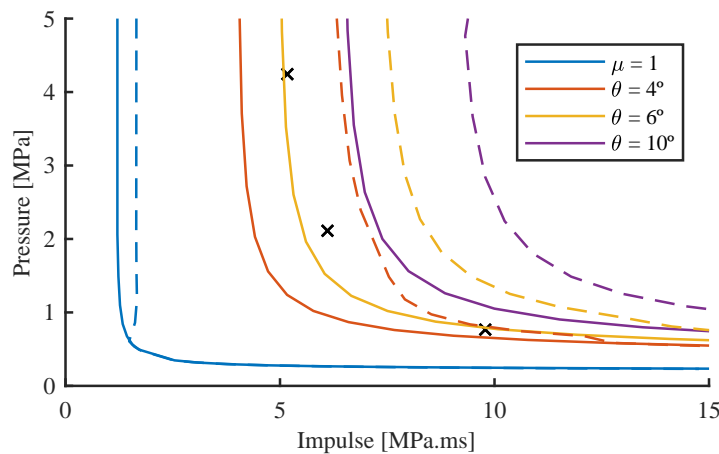


Figure 6.19: Pressure-impulse diagrams of bare RC beam and with 3D printed sacrificial cladding solution

period of the structural element, is also enhanced due to the addition of the cladding solution. Contrarily, due to the large plateau stress of the crushable core when compared with the resistance of the structure ( $\kappa = 2$ ), no enhancement is attained for the elastic limit ( $\mu = 1$ ) under dynamic regime. Similar findings were reported by Ye and Ma [180] (see Figure 10 in [180]). Additionally, as expected, the resistance of the structure under quasi-static regime and when the peak reflected pressure is lower than the crushable core's plateau stress (approximately 0.5 MPa) is not enhanced by the sacrificial cladding solution. Consequently, the curves obtained for the bare RC beam and with the sacrificial cladding overlap.

As an example three different charge weight-standoff combinations are considered as a design scenario. Subsequently, the corresponding reflected overpressure and impulse were computed, resorting to the Kingery & Bulmash's semi-empirical predictions for surface bursts, and illustrated in Figure 6.19 with a black cross. Analysing the referred figure, it is clearly visible that, if no cladding solution is used, the curve corresponding to the heavy damage level ( $\theta = 6^\circ$ ) yields smaller PI combinations than the ones attained for two of the considered design scenarios. The last design scenario exceeds the moderate damage level curve. Alternatively, one might observe that, due to the application of the sacrificial cladding, none of the design scenarios surpasses the curve obtained for a moderate damage level ( $\theta = 4^\circ$ ).

### 6.3.5 Robustness assessment of the designed solution

As previously reviewed, the design of a sacrificial cladding is usually performed in terms of applied impulse, which influences the impulse transmitted to the structure, rather than absolute energy absorption, since a sacrificial cladding with the ability to absorb large amounts of energy might not guarantee an effective protection [188]. Additionally, Zhou and team [188] state that the crushable core should have sufficient thickness to avoid full crushing, since at that instant the transmitted load may increase to values larger than those observed if no sacrificial cladding was used (an experimental example may be found in [51]).

A simplified numerical model, such as SDOF and LCS, is commonly used to perform the design of blast loaded structural elements and/or cladding solutions while assuming that the capacity of the former is deterministic. Several studies presented on the literature have considered a probabilistic approach for the assessment and design of structural components and systems [81, 117, 123].

In the present study, a probabilistic approach is used to assess the impact of the variability of several key parameters of the structural element [60]. Subsequently, a robustness assessment of the designed solution is conducted.

### 6.3.5.1 Uncertainties in material modelling

The simplified model was developed as a function of a certain number of key parameters, whose values have a probabilistic distribution according to [60], which were generated in order to account for physical, mechanical and model uncertainties. The chosen parameters are identified in Table 6.5, in combination with their probabilistic characterisation. The sacrificial cladding's parameters will be assumed as deterministic in the present study.

Figure 6.20 illustrates the probabilistic distribution of the generated key parameters, where the vertical dashed lines, when present, depict the experimental values reported by Magnusson [90, 91].

Table 6.5: Probabilistic characterisation of key parameters

Variable	Distribution	Unit	Mean	Std. deviation
$\rho_c$	Normal	kg/m <sup>3</sup>	2500	75
$f_c$	Lognormal	MPa	101	6.52
$f_y$	Normal	MPa	560	30
SDOF model	Lognormal	-	1	0.05
LCS model	Lognormal	-	1	0.1

#### Concrete's density

According to the Probabilistic Model Code [60], the density of a given structural component has a Gaussian distribution, which takes into account the variability between different structural parts of a given structure and between various structures. The total variability of the concrete's density is accounted for by means of a Gaussian distribution, whose mean value and coefficient of variation are 2500 kg/m<sup>3</sup> and 0.03 (75 kg/m<sup>3</sup>), respectively.

#### Concrete's compressive strength

The distribution related to the concrete's compressive strength is a lognormal distribution in which the mean value is equal to the one obtained experimentally by Magnusson [90, 91], while the standard deviation is given by equation (6.26), as specified in [60]. Although Probabilistic Model Code [60] only defines the required parameters up to a C55 concrete class ( $s' = 0.05$ ,  $n' = 4.00$  and  $v' = 10.0$ ), these values were deemed as applicable to the present case study, yielding the standard variation presented in Table 6.5.

$$\sigma = s' \cdot \sqrt{\frac{n'}{n'-1} \cdot \frac{v'}{v'-2}} \quad (6.26)$$

#### Reinforcement steel's yield stress

Steel is commonly classified according to their yield strength. Taking into account that the reinforcement steel used on the experimental campaign was of grade B500BT,

the Probabilistic Model Code [60] states that the mean value of the normal distribution is given by the steel's grade plus two times the standard deviation, which in turn takes a value of 30 MPa, as shown in Table 6.5.

**Model uncertainties**

The design of structural elements is commonly performed through the use of numerical models, which may not be considered as complete and exact [60]. Model uncertainties are considered in the present study resorting to a lognormal distribution (unitary mean

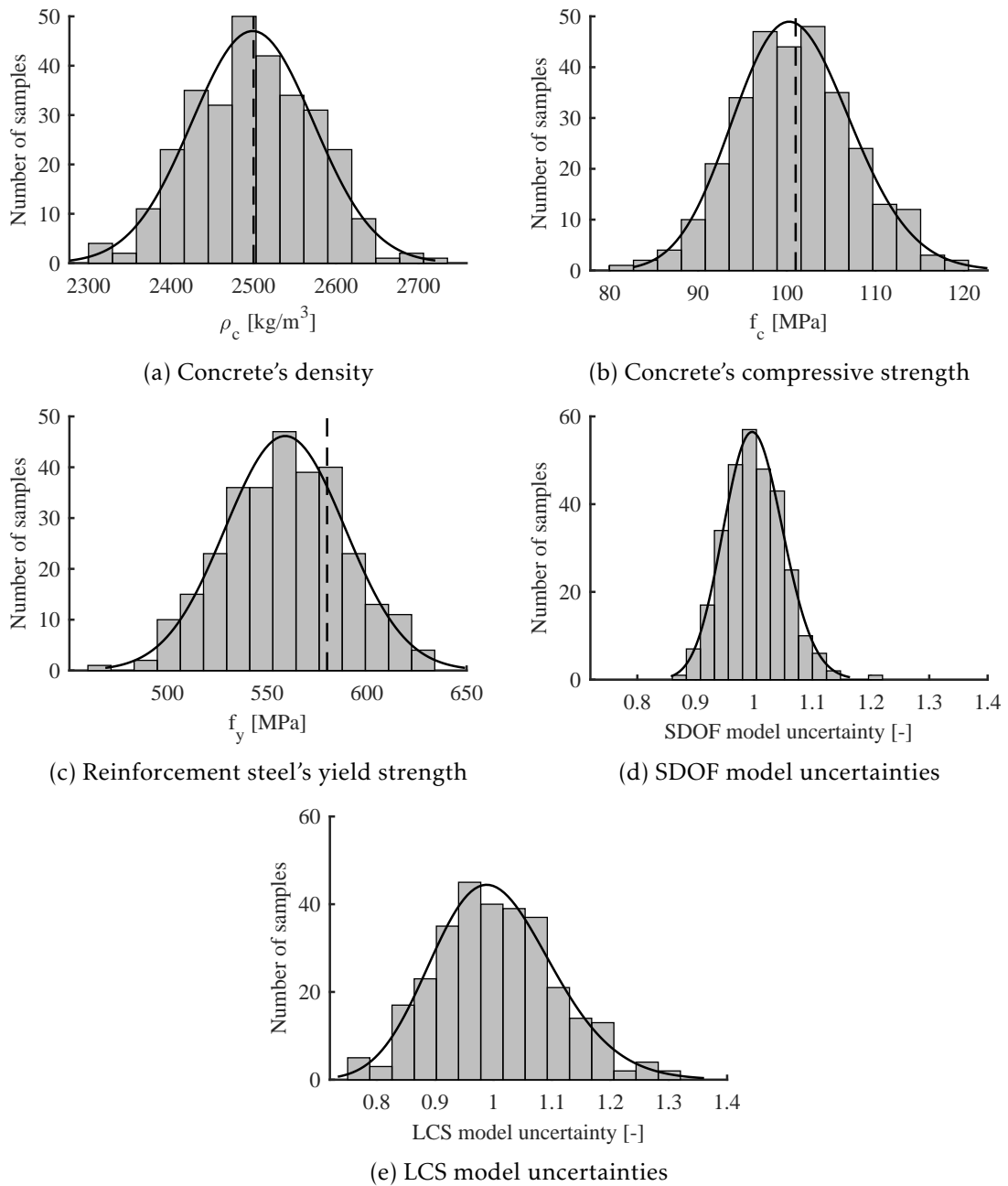


Figure 6.20: Probabilistic distribution of the chosen key parameters

value). Due to the extensive use by the scientific community and industry, the confidence level on the SDOF might be considered as being higher than that of the LCS model, standard deviations of 0.05 and 0.1 were used, respectively. Therefore, the maximum displacement given by the numerical simulations is multiplied by this key parameter.

### Sample space

A critical parameter in probabilist analysis is the number of generated samples, usually referred to as the sample space. The larger the number of samples, more reliable are the obtained results, but with an increasing cost in processing/analysis time. Contrarily, if a small sample space is used, a smaller analysis time will be attained at the expense of a lower confidence level on the results. Therefore, the aim is to generate the minimum number of samples that yields statistically reliable results. To obtain the required sample space, 1000 sample sets, each containing a set of key parameters, were generated and a study of both the evolution of standard deviation and relative error (to the desired standard deviation) was carried out throughout the sample space. Figure 6.21 illustrates the evolution of standard deviation and relative error as a function of the number of samples. Analysing the referred figure, one may verify that both values seem to stabilise when 300 or more samples are generated, which deems the sample space fitting and the results may be considered statistically reliable. Consequently, the probabilistic analysis of the bare RC beam and with the designed sacrificial cladding will be conducted resorting to 300 samples.

#### 6.3.5.2 Pressure-impulse diagrams

Figure 6.22 depicts the pressure-impulse diagrams of bare RC beam for each response limit when the probabilistic variability of key parameters is considered. The value, i.e.

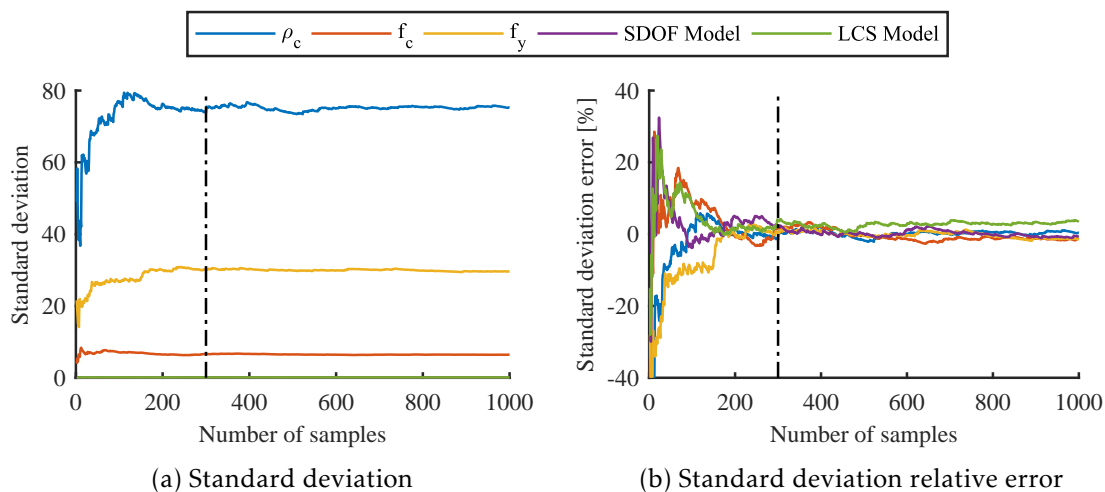
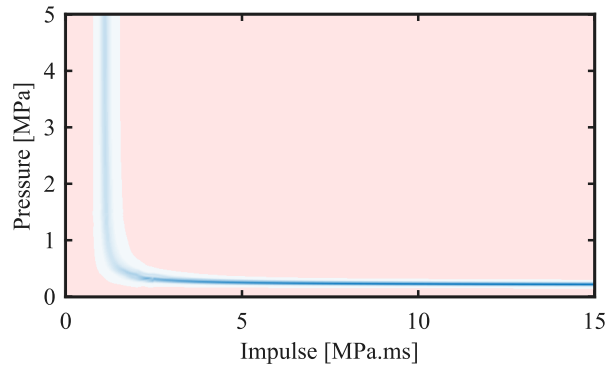
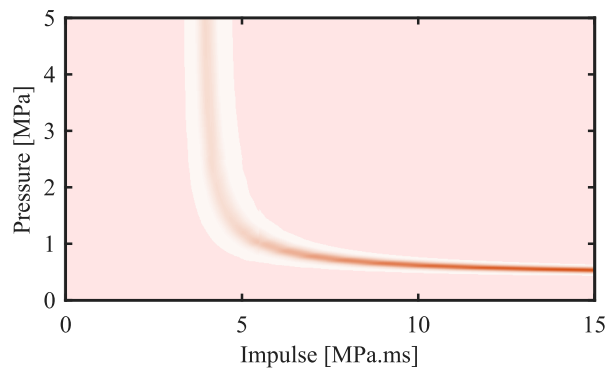


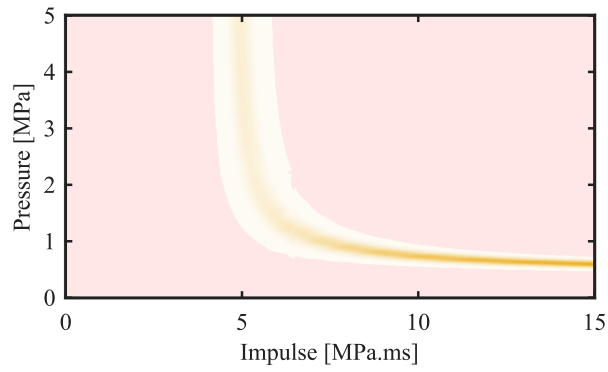
Figure 6.21: Evolution of the standard deviation and its relative error throughout the sample space



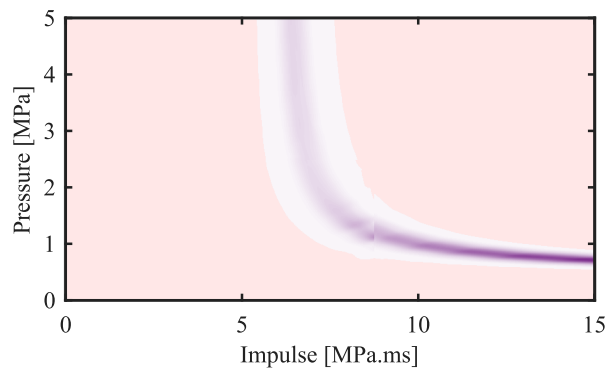
(a) Superficial damage level



(b) Moderate damage level



(c) Heavy damage level



(d) Hazardous damage level

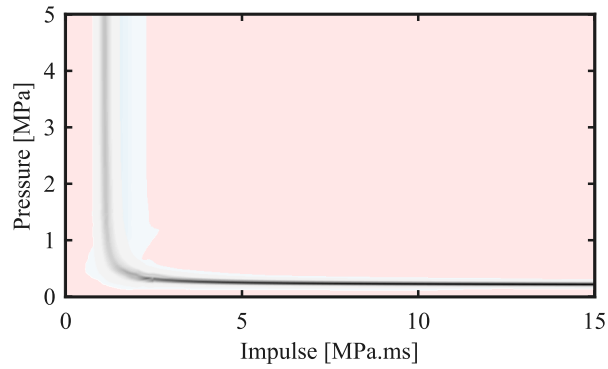
Figure 6.22: Pressure-impulse diagrams of the bare RC beam considering probabilistic variability of key parameters

lightness or darkness, of the colour is directly proportional to the number of samples at a given pressure-impulse combination. Therefore, the lower the value of the colour (closer to white), less samples are present at that given combination. Analysing the referred figure, one might observe that, when the structure is subjected to an impulsive blast load, the variability of the obtained pressure-impulse diagrams increases as a higher response limit is considered due to the growth of the structure's resistance influence on the structural response. Contrarily, when subjected to a quasi-static load, the influence of the structure's mass diminishes and, consequently, the result's variability decreases regardless of the response limit.

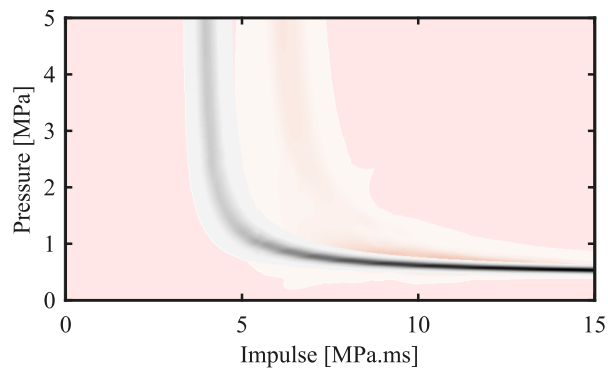
The pressure-impulse diagrams obtained when the previously designed 3D printed sacrificial cladding solution is applied on the face of the RC beam are depicted in Figure 6.23, together with the ones computed for the bare structural component, shown in greyscale in the referred figure. Comparing the pressure-impulse diagrams of the bare structure and with the ones obtained with a cladding solution, a wider variability is visible for the latter under both impulsive and dynamic loading, which results from the lower optimisation of the sacrificial cladding (the structural element is different than the original one to which the cladding was designed for<sup>2</sup>). The application of the sacrificial cladding improves the blast loading capabilities of the structural element for all the response limits when the structural element is subjected to impulsive blast loading. However, observing the plots illustrated in Figures 6.23(a), 6.23(b) and 6.23(c), some regions of the pressure-impulse diagrams obtained with the cladding solution are clearly below the curves computed for the bare structure, specifically at the dynamic and quasi-static responses.

The PI curves generated for the 300 samples were used to compute performance-based pressure-impulse diagrams at several probability levels. The cumulative distribution function of blast resistance was estimated resorting to a kernel smoothing function, which allows the determination of conditional probability of attaining the considered response limit given a certain level of reflected peak overpressure and impulse. Although this conditional probability may be graphically represented as a surface, it is considered that performance-based pressure-impulse diagrams at several probability levels are of a greater interest. Therefore, contour plots at probability levels of 5, 50 and 95% were computed for all response limits and illustrated in Figures 6.24(a) and 6.24(b) for the bare and protected structural element, respectively. It should be noted that, for example, a conditional probability of 5% corresponds to the pressure-impulse combinations that establish the boundary at which 5% of the samples reached a given response limit. Analysing Figure 6.24(a), it is possible to observe that the obtained pressure-impulse diagrams are similar to those determined using a deterministic approach, i.e. they exhibit an impulsive and quasi-static asymptote and a transition phase under dynamic response. The larger

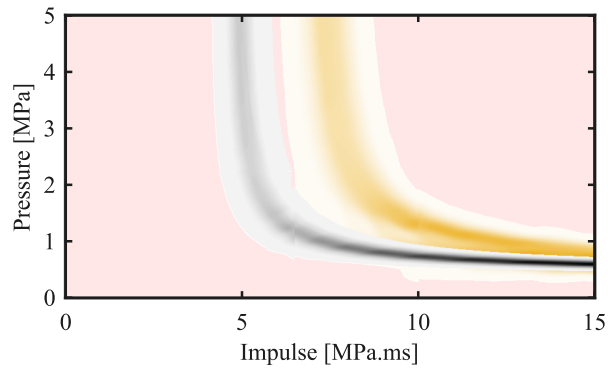
<sup>2</sup>Additional numerical estimates were computed using the same standard deviation as the one used to take into consideration the SDOF model's uncertainties. This analyses revealed a small reduction in variability under impulsive and quasi-static regimes. No reduction was observed under dynamic regime.



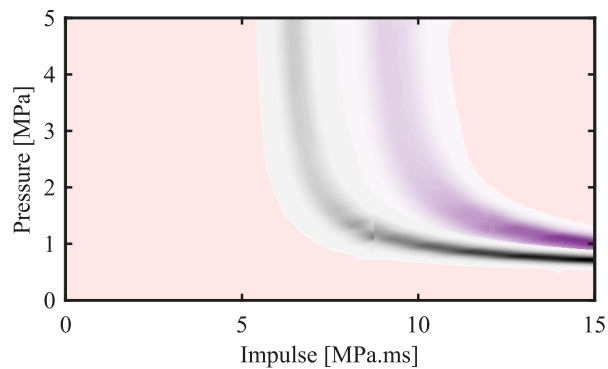
(a) Superficial damage level



(b) Moderate damage level



(c) Heavy damage level



(d) Hazardous damage level

Figure 6.23: Pressure-impulse diagrams of the RC beam with 3D printed sacrificial cladding solution considering probabilistic variability of key parameters



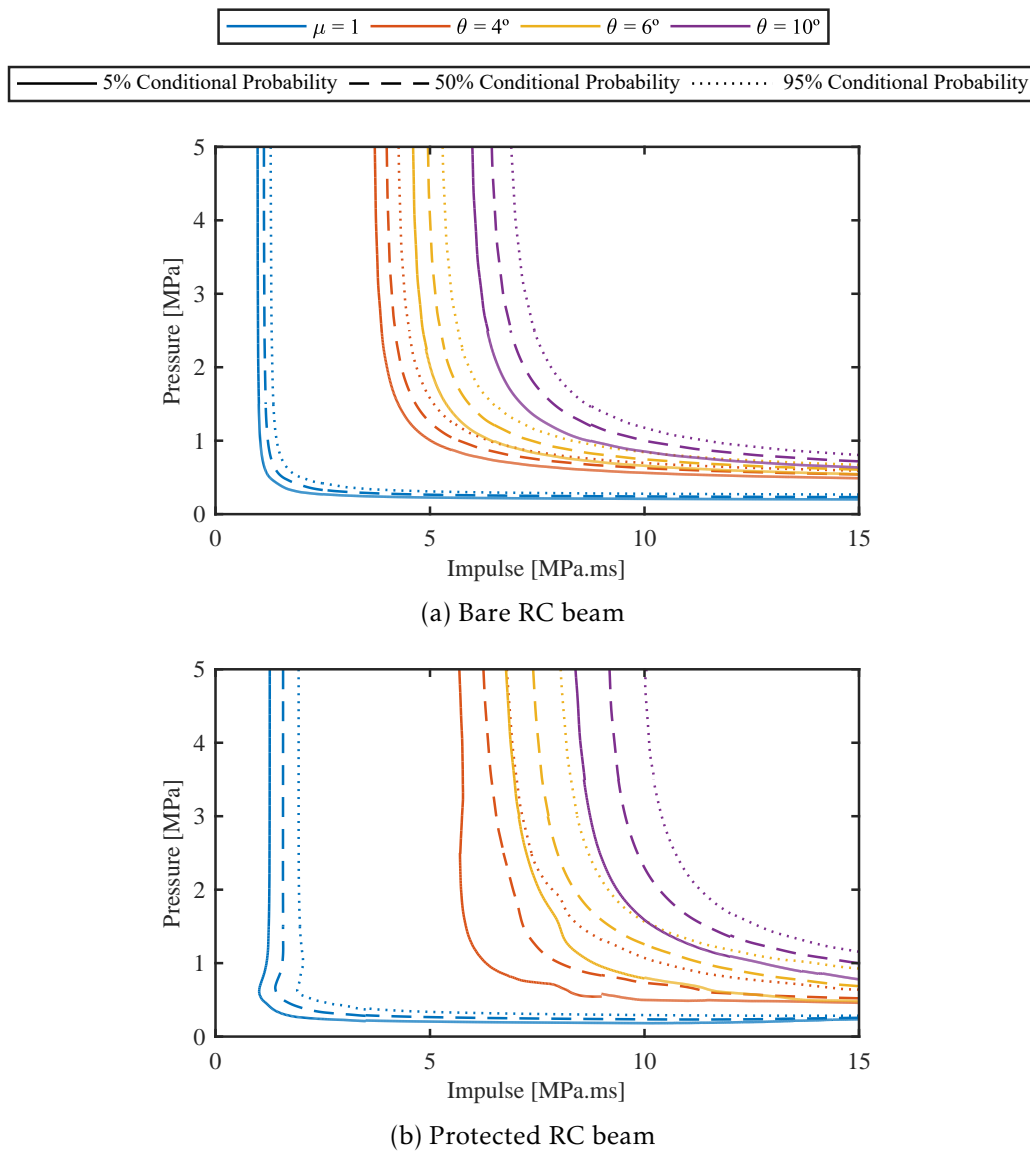


Figure 6.24: Performance-based pressure-impulse diagrams

variability of results when comparing the impulsive and quasi-static responses is also visible in the referred figure. As previously verified, a larger variability is noticeable when the pressure-impulse diagrams of the protected structure (Figure 6.24(b)) are compared with the ones computed for the bare structural component (Figure 6.24(a)), specifically under impulsive and dynamic loading. It is important to refer that, despite not being illustrated in the referred figures, the deterministic pressure-impulse diagrams are contained within the ones computed when the probabilistic variability of key parameters is taken into account.

Figure 6.25 illustrates the 5% conditional probability PI diagrams of both the bare (solid lines) and protected (dashed lines) structures. Similarly to the observed when a deterministic approach was considered, the addition of the designed sacrificial cladding solution improves the blast resistant capabilities of the RC beam, specifically when a

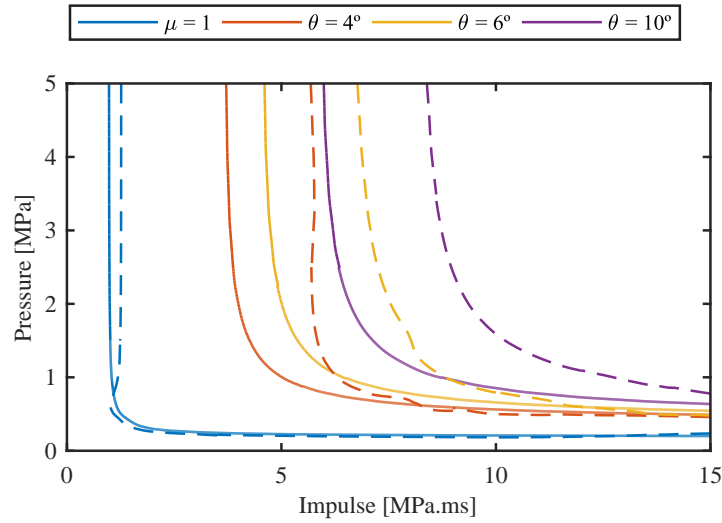


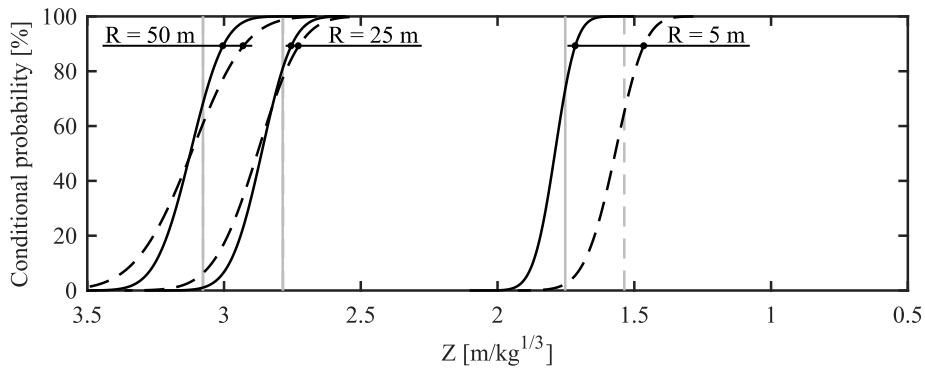
Figure 6.25: Performance-based pressure-impulse diagrams of bare RC beam and with 3D printed sacrificial cladding solution (5% conditional probability)

impulsive blast load is imparted on it. However, when the cladding solution is applied to the RC beam, the curves corresponding to the superficial and moderate damages lie beneath the ones of the bare structure under dynamic and quasi-static loads.

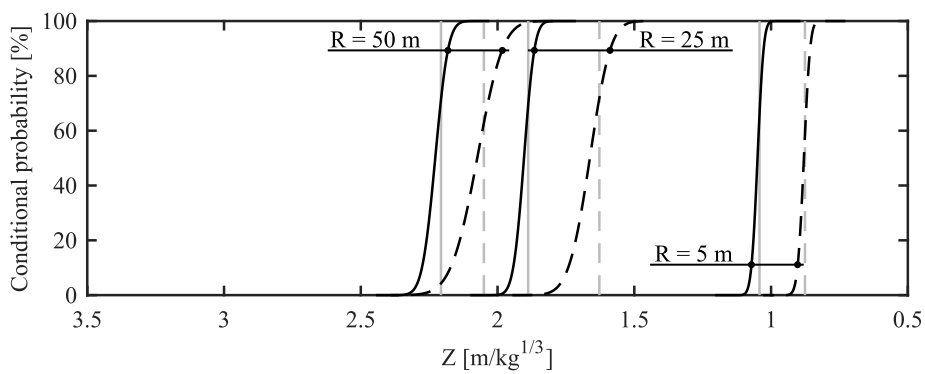
Through the findings of the conducted research, namely the analysis of the PI diagrams illustrated in Figures 6.23 and 6.25, it is possible to conclude that taking into account the probabilistic variability of key parameters is of vital importance when designing sacrificial cladding solutions, since the inclusion of a cladding solution, when not properly designed for the structural element it intends to protect, might negatively impact its blast resistant capabilities. This negative impact is particularly significant under dynamic and quasi-static regimes.

### 6.3.5.3 Fragility curves

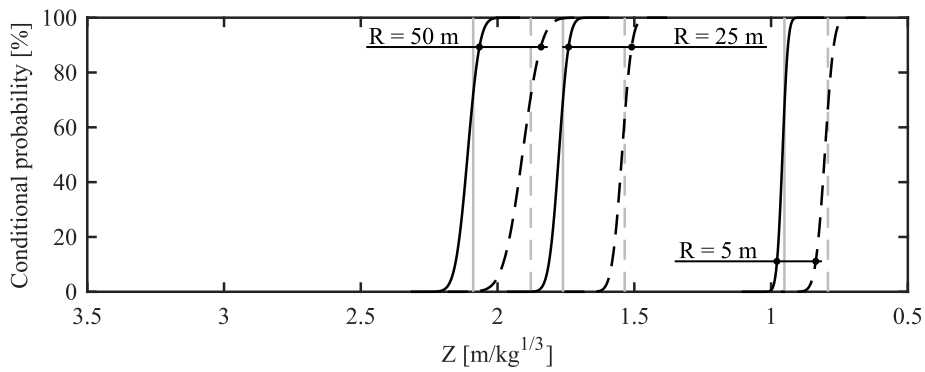
Fragility curves were computed for three different standoff distances (5, 25 and 50 m). For each standoff distance ( $R$ ), the probability density function of scaled distance ( $Z$ ) is determined by fitting the samples with a lognormal distribution and, subsequently, the cumulative density function is determined. Figure 6.26 shows the fragility curves of the bare (solid lines) and protected (dashed lines) structures for the considered values of  $R$ . The values of scaled distance computed resorting to a deterministic approach are also illustrated in the referred figure with grey lines, following the same line type as the depicted fragility curves. Observing the referred figures, namely the conditional probability at which the deterministic values intercept with the corresponding fragility curve, one might verify that this probability is above 50%, regardless of the considered response limit, standoff distance and if the structure is protected or not. Consequently, one might conclude that the admissible scaled distance computed resorting to a deterministic approach is always smaller than the one attained at a conditional probability of



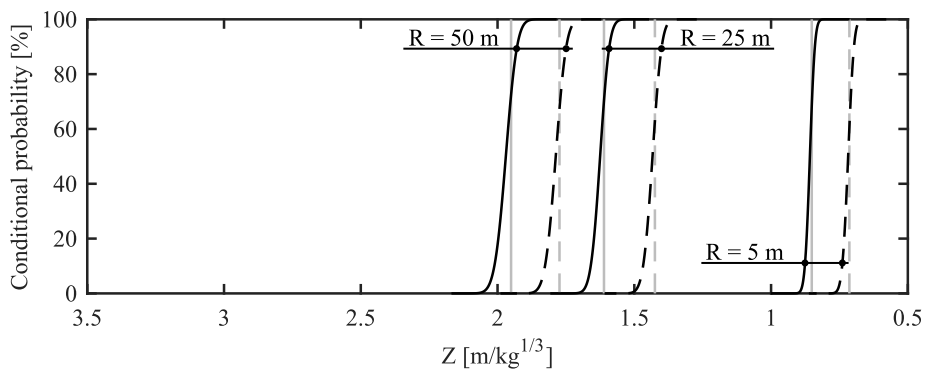
(a) Superficial damage level



(b) Moderate damage level



(c) Heavy damage level



(d) Hazardous damage level

Figure 6.26: Fragility curves for the bare RC beam and with 3D printed sacrificial cladding solution

50%. It is important to refer that, for a constant standoff, a smaller scaled distance yields a larger charge weight and, therefore, the deterministic approach is not on the safety side. Assuming that a value of 5% is admissible for the conditional probability, a comparison between the scaled distances attained at this conditional probability and by means of the deterministic approach may be performed. The maximum reduction between the obtained results took a value of approximately 11%, which corresponds to a 40% increase in admissible charge weight.

The slope of the fragility curves is a good indication of the results' variability with the scaled distance ( $Z$ ). Comparing the slope of the superficial damage curves of the bare RC beam with the ones obtained for the remaining response limits (bare RC beam), one might observe that the former has a lower value regardless of the standoff distance. This observation is a result of the variability of the structural element's elastic limit which, contrarily to the remaining response limits, varies with the considered probabilistic variation. When the cladding solution is applied on the structural element, contrarily to what was previously verified with the PI diagrams, a lower variability is attained as a higher level of damage is considered as admissible (for standoff distances of 25 and 50 m).

Comparing the fragility curves of the bare structure (solid lines in Figure 6.26) with the ones determined when the sacrificial cladding is applied (dashed lines in Figure 6.26), it is possible to verify a global enhancement of the blast resistance capabilities of the RC beam. Assuming that a 5% conditional probability is admissible, the inclusion of the cladding solution reduces the scaled distance up to 15%. This reduction is attained for a 5 m standoff distance while considering a moderate damage as admissible and approximately corresponds to a 70% increase in admissible charge weight. This was to be expected, since the cladding solution was designed to increase the structural element's ability to withstand impulsive loads at a moderate damage level. Additionally, analysing the fragility curves depicted in Figure 6.26(a) for a superficial damage level, namely the curves corresponding to 25 and 50 m standoffs (dynamic and/or quasi-static<sup>3</sup> regimes), one might observe that the sacrificial cladding negatively impacts the blast resistant capability of the RC beam. Therefore, designing a cladding solution for a given blast scenario using a deterministic approach, might hinder the blast resistant capabilities of the protected structural element in the case of a different blast scenario.

## 6.4 Conclusions

The present chapter reviewed the design procedure of a sacrificial cladding solution composed by a 3D printed crushable core of varying relative density and a metallic front plate.

---

<sup>3</sup>For example, the detonation of 3000 kg of TNT at a distance of 50 m yields a positive phase duration of approximately 45 ms, which is three times greater than the natural period of the considered structural element.

The design of cladding solutions is commonly performed for a wide range of blast scenarios. Therefore, the implementation of a numerical procedure to compute pressure-impulse diagrams, which uses an equivalent SDOF model or the LCS model, was reviewed in the current chapter. The procedure used by the author to determine the resistance-deflection curve of a reinforced concrete section was also shown, followed by the implementation and validation of a nonlinear equivalent SDOF model. Subsequently, the implementation and validation of the LCS model was equally reported.

With the implementation of the required simplified models validated, a case study was selected from the literature in order to illustrate the design procedure of a sacrificial cladding. Resorting to the published experimental results, the implementation of the procedure to compute the resistance-deflection curve and the resulting equivalent SDOF model were validated.

The blast resistant capabilities of the bare structural element were evaluated resorting to pressure-impulse diagrams. Firstly, the influence of several approximations to the shock wave's pressure-time history was studied. The pressure-time history was approximated with a triangular pulse and resorting to the modified Friedlander equation. Analysing the obtained PI diagrams, it was possible to conclude that, when compared with a triangular pulse, approximating the blast wave profile with the modified Friedlander equation has little to no influence on the impulsive regime of the pressure-impulse diagram. The greatest influence was observed when the positive phase duration and the fundamental period of the structure have similar values (dynamic regime) and, consequently, the resultant maximum deflection is highly influenced by the profile of the applied load. Although the use of a triangular pulse might be considered as conservative, since the aim of the present study was the design of a high performance cladding solution, the use of the modified Friedlander equation is considered as recommended for the optimisation of the sacrificial cladding.

Next, a sacrificial cladding was designed in order to increase the blast resistant capabilities of the structural element when subjected to an impulsive blast load. Through the analysis of the attained results, namely the computed PI diagrams, one might conclude that the inclusion of the cladding solution increases the blast resistant capabilities of the structural element under impulsive loading regardless of the considered damage level. Under dynamic regime, i.e. when the positive phase duration is similar to the fundamental period of the structural element, an enhancement due to the addition of the cladding solution was only verified for the moderate, heavy and hazardous damage levels. Alternatively, due to the large plateau stress of the crushable core when compared with the resistance of the structure ( $\kappa = 2$ ), no enhancement was attained for the elastic limit under dynamic regime. Lastly, as expected, it was observed that the structure's ability to withstand blast loads, under quasi-static regime, is not enhanced by the sacrificial cladding and the curves obtained for the bare RC beam and with the sacrificial cladding overlap.

A robustness assessment of the designed solution was conducted resorting to a probabilistic approach in which several key parameters were varied according to a given probabilistic distribution. Through the analysis of the evolution of both standard deviation and relative error (to the desired standard deviation), it was verified that a sample space of 300 provides statistically reliable results.

Scatter pressure-impulse diagrams were computed for the structural element with and without the cladding solution. Analysing the PI diagrams of the bare structural element, it was possible to verify that, when subjected to an impulsive blast load, the variability of the obtained pressure-impulse diagrams increased as a higher response limit was considered due to the growth of the structure's resistance influence on the structural response. Contrarily, when subjected to a quasi-static load, the influence of the structure's mass diminishes and, consequently, the result's variability decreased for all response limits.

A wider variability was visible for the PI diagrams obtained when the cladding solution was applied to the structural element, since in a probabilistic approach the properties of the structural element are different than the original ones to which the cladding was designed for. It was found that, under impulsive loading, the cladding solution improved the blast loading capabilities of the structural element for all the response limits. However, some regions of the pressure-impulse diagrams obtained with the cladding solution were clearly below the curves computed for the bare structure, specifically at the dynamic and quasi-static responses.

Performance-based pressure-impulse diagrams were computed at several conditional probability levels. The cumulative distribution function of blast resistance was estimated resorting to a kernel smoothing function, which allowed the determination of conditional probability of attaining the considered response limit given a combination of reflected peak overpressure and impulse. Analysing the 5% conditional probability PI diagrams of both the bare and protected structural elements, similar conclusions were attained. Therefore, it might be concluded that taking into account the probabilistic variability of key parameters is of vital importance when designing sacrificial cladding solutions. When not properly designed for the structural element it intends to protect, the cladding might negatively impact its blast resistant capabilities. This negative impact was particularly significant under dynamic and quasi-static regimes.

Lastly, fragility curves were computed for three different standoff distances (5, 25 and 50 m) resorting to a fit of the samples with a lognormal distribution and, subsequently, computing the cumulative density function as function of scaled distance ( $Z$ ). Analysing the conditional probability at which the deterministic values intercepted with the corresponding fragility curve, it was possible to verify that this probability was always above 50%. A value of 5% was assumed as admissible for the conditional probability and a comparison between the scaled distances attained at this conditional probability and by means of the deterministic approach was conducted. A maximum reduction of 11%, which corresponds to a 40% increase in admissible charge weight, was verified.

Consequently, one might conclude that the deterministic approach is against safety.

Through the comparison of the fragility curves of the bare structure with the ones determined when the sacrificial cladding is applied, a global enhancement of the blast resistance capabilities of the RC beam was verified. Nonetheless, for a superficial damage level, the curves corresponding to 25 and 50 m standoffs presented lower values of  $Z$  when compared with the bare structure's curves. Consequently, for these particular cases, the sacrificial cladding negatively impacts the blast resistant capability of the RC beam.





## Chapter 7

# Conclusions and future research

This chapter presents the a summary and the conclusions of the performed study and some recommendations for future work of interest to the field of study.

### 7.1 Summary and conclusions

The use of improvised explosive devices in terrorist attacks against civil engineering structures increased significantly during the last decades. When such events occur, the associated blast loads may result on the failure of critical load bearing members, with subsequent social disruption and psychological impact to society, as well as high economic and environmental losses. Therefore, the implementation of strengthening or protective techniques is crucial to mitigate the effects of blast loads on structures and to ensure their survivability.

When designing structural elements or protection solutions against blast loads, the correct prediction of the load acting on the target with a given level of accuracy is of vital importance. Chapter 2 presented the basic theory related to shock wave phenomena, as well as a review of the currently available semi-empirical and numerical methods that can be used to evaluate blast loads on an infinite and rigid boundary. Additionally, the state of the art for predicting the effects resulting from blast wave clearing due to a finite target and fluid-structure interaction was also shown in the referred chapter. Finally, a review of the performance criteria of structural components subjected to blast loads, as defined by several standards, was also given, together with available methods for predicting their dynamic response.

A historical survey of important structures subjected to blast loads revealed that, if blast scenarios are considered during their design, reinforced concrete elements behave better than their steel counterparts. Therefore, the traditional structural blast protection methods are based on strengthening with thicker reinforced concrete, ultra high-performance and fibre reinforced concrete structural elements. However, these techniques are time consuming and labour intensive, which leads to an increase in construction cost both during the strengthening process and due to retrofit if damaged, and are

heavy and often difficult to install in existing facilities. Therefore, several alternatives have emerged such as externally bonded steel plates and composite materials. More recently, the use of protection solutions with reduced mass and high energy absorption, which are usually referred to as sacrificial claddings, has risen in interest since they are considered to be advantageous when compared with the traditional strengthening methods. These innovative solutions are composed by a crushable core, commonly materialised by a cellular material or structure, and two skin plates (front and rear).

Chapter 3 began by introducing a brief state of the art on traditional strengthening techniques, followed by an extensive review on the concept of sacrificial cladding solutions and their use as a energy dissipation measure. The simplified numerical models, readily available in the literature, to simulate the nonlinear response of sacrificial cladding were presented in the referred chapter.

Additive manufacturing has recently become a viable manufacturing process as a result of the numerous advantages over traditional subtractive manufacturing techniques when complex geometries are required. Therefore, the use of 3D printing as a manufacturing technique for energy absorption structures has grown in interest in recent years, since it allows tailored properties. A state of the art on additively manufactured solutions for energy absorption was also reported in Chapter 3.

These solutions are of great interest since their properties may be customised according to each particular scenario and produced with flexibility and precision. The state of the art related to additively manufactured protective solutions (see Chapter 3) revealed that these are typically based on thin walled structures and, as a result of their dimensions, the successive layers of these walls are usually 3D printed in the same direction, yielding anisotropic mechanical behaviour of the constitutive materials. However, most of the studies reported in the literature consider the 3D printed material as homogeneous and isotropic. Consequently, an experimental testing campaign was conducted and presented in Chapter 4. This campaign aimed to attain the mechanical characterisation of unidirectional 3D printed samples with a special focus on the characterisation of their anisotropy and compressive/tensile asymmetry under quasi-static regime and strain rate sensitivity.

The literature also showed that experimental testing of 3D printed protective solutions is commonly performed resorting to quasi-static or low velocity impact tests. This might be considered as a limitation and, consequently, the nonlinear response of a sacrificial cladding solution was experimentally obtained by subjecting it to a blast load, which was attained by means of an explosive driven shock tube. This experimental campaign allowed the analysis of its energy absorption capacity. The sacrificial cladding solution under study, introduced in Chapter 4, was materialised with a 3D printed crushable core (PLA honeycomb structure of a given relative density and height, in combination with two PLA solid plates) and an aluminium front plate.

The experimental campaigns allowed the development, verification and validation of the numerical models described in Chapter 5. The finite element (FE) numerical models

developed for the present work use the commercial finite element software LS-DYNA, while the implementation of the simplified model was conducted resorting to MATLAB. Firstly, the calibration of an anisotropic constitutive model available in LS-DYNA was conducted based on the previously obtained experimental results. Subsequently, the results attained during the blast testing experimental campaign were used to validate a FE and a simplified numerical model, when they are used to simulate the nonlinear response of the 3D printed crushable core under blast loading. Additionally, the FE numerical model allowed further insights on the nonlinear behaviour of 3D printed crushable cores, specifically the crushing mechanisms observed on their interior.

Finally, Chapter 6 reviewed the design procedure of a sacrificial cladding solution for a given case study, whose crushable core is materialised resorting to the FDM technique. The implementation and validation of the required simplified models was conducted in the referred chapter. The implemented procedure to compute the resistance-deflection curve and the resulting equivalent SDOF model were validated resorting to published experimental results. Next, the design of a sacrificial cladding allowed to increase the blast resistant capabilities of the structural element. Finally, a robustness assessment of the designed solution was performed resorting to a probabilistic approach in which several key parameters were varied according to a given probabilistic distribution.

The research conducted during the present work allowed the author to reach the following conclusions:

- Chapter 2
  - A good agreement was found between the semi-empirical predictions and experimental results reported in the literature for the blast wave parameters;
  - The best practice for the definition of blast wave parameters is the use of the Kingery & Bulmash's semi-empirical predictions, together with the modified Friedlander equation to approximate the positive phase blast wave profile;
  - The effects of blast wave clearing and fluid-structure interaction on the original blast wave profile should be estimated resorting to the method proposed by Hudson and the extended Taylor theory, respectively.
- Chapter 3
  - The research in blast resistant design reported in the last few years, has shown a rapid growth in the use of 3D printing for the manufacturing of sacrificial cladding solutions;
  - A review of the state of the art showed that the developed protective solutions are typically based on thin walled structures and that finite element modelling is a valuable tool to study the energy absorption capabilities of protective systems;

- Most of the reported simulations are performed using homogeneous and isotropic constitutive relations, which represents a major drawback of these numerical models.
- Chapter 4
  - The mechanical behaviour of unidirectional 3D printed FDM samples presented significant anisotropy and compressive/tensile asymmetry;
  - Under compressive loading, when the loading is perpendicular to the manufacturing direction, the maximum stress is 20% higher than the one attained when the loading and manufacturing directions are parallel;
  - Under tensile loading, the maximum resistance was verified when the loading and manufacturing directions are aligned;
  - The maximum stress in 3D printed FDM PLA is inversely proportional to strain rate. However, with the increase of strain, the resulting stress seemed to tend to a constant value, regardless of strain rate;
  - No influence of the manufacturing layer height was found on the energy absorption capacities of the proposed 3D printed crushable core.
- Chapter 5
  - The anisotropic and tension/compression asymmetry of 3D printed PLA was adequately recovered by the MAT\_058 material model;
  - Two limitations were identified for the material model: the inability of the material model to distinguish between compressive and tensile loading when defining the stiffness properties of the composite material and, under high strain rate loading, the elastic properties and the “stress limiting factor” of the material model are strain rate independent;
  - The force peak and plateau stress are directly proportional to the relative density of the 3D printed crushable core, which controls the crushing of the top and bottom layers and the buckling of the interior cell walls.
  - Contrary to what is commonly considered, the front plate initial velocity depends not only on its mass and the applied reflected impulse, but also on the relative density of the crushable core;
  - The simplified model proposed by Hanssen and team was not able to simulate the nonlinear behavior of 3D printed crushable cores for this particular case;
  - A good agreement was attained between the experimental and improved simplified model’s results when it was assumed that the formation of a fully compacted region may not be explicitly considered and that the honeycomb structure contributes as a whole to the mass of the dynamic system.

- Chapter 6
  - The inclusion of the cladding solution increases the blast resistant capabilities of the structural element under impulsive loading regardless of the considered damage level;
  - Under dynamic regime, an enhancement due to the addition of the cladding solution was only verified for the moderate, heavy and hazardous damage levels;
  - The structure’s ability to withstand blast loads, under quasi-static regime, was not enhanced by the sacrificial cladding and the PI curves obtained for the bare RC beam and with the sacrificial cladding overlap;
  - The robustness assessment of the designed solution allowed to verify that, when subjected to an impulsive blast load, the variability of the obtained pressure-impulse diagrams increased as a higher response limit is considered;
  - The result’s variability decreased for all response limits under quasi-static loading, since the influence of the structure’s resistance diminishes;
  - A wider variability was visible for the PI diagrams obtained when the cladding solution was applied to the structural element, due to the lower optimisation of the sacrificial cladding taking into account the probabilistic distribution of its properties;
  - Some regions of the pressure-impulse diagrams obtained with the cladding solution were clearly below the curves computed for the bare structure, specifically at the dynamic and quasi-static responses;
  - Taking into account the probabilistic variability of key parameters is of vital importance when designing sacrificial cladding solutions, since it was shown that the inclusion of a cladding solution, when not properly designed for the structural element it intends to protect, might negatively impact its blast resistant capabilities;
  - The deterministic approach might be against safety. For example, in the reported case study, when comparing the admissible charge weight yielding from deterministic/probabilistic approaches, one verified that the former allows a 40% higher charge weight, which is clearly against safety.

## 7.2 Innovative aspects

The main innovative aspects developed during the present work are summarised as follows:

- The characterisation and consideration of the 3D printed PLA’s anisotropy and compressive/tensile asymmetry for the numerical simulation of additively manufactured protective solutions;

- The modifications proposed to the simplified model defined by Hanssen and team in order to improve its applicability when simulating 3D printed crushable cores;
- The design of sacrificial claddings admitting:
  - the nonlinear behaviour of the structural element;
  - the definition of the blast wave profile using the modified Friedlander’s equation;
  - the effects of the fluid-structure interaction.
- The use of a probabilistic approach to verify the robustness of the designed cladding solution.

### 7.3 Future research

The current work presented the development and study of a high performance protective solution against blast loads, namely a sacrificial cladding solution that resorts to a 3D printed crushable core. Although the development and design of the sacrificial cladding yielded a usable protective solution, further improvements may be attained through additional research.

The effects of fluid-structure interaction on the blast load acting on the target still require experimental validation to verify the accuracy of the extended Taylor theory. Additional research is also required to address the cumulative effect of both blast wave clearing and fluid-structure interaction.

As the influence of strain rate on the 3D printed material behaviour was only studied under compressive loads and with a  $90^\circ$  angle between the loading and manufacturing directions, further studies are required for a better understanding of the anisotropy and asymmetry behaviour under high strain rates.

A full-scale experimental campaign might be of interest to verify the reviewed design procedure. Finally, the design of 3D printed crushable may consider different geometries and materials that out perform the ones considered on the present study, which should be studied under blast loading in order to enhance the predictability of the a baseline for their design procedure.

The development of the present work enabled the implementation of several MATLAB scripts which allow a designer to:

- compute the positive phase parameters according to the Kingery & Bulmash’s semi-empirical predictions for a surface burst;
- simulate a reinforced concrete beam subjected to an arbitrary pressure-time history using a nonlinear equivalent SDOF model (see Section 6.2.2);

- determine the nonlinear response of a sacrificial cladding solution while considering the structural element as rigid (see Section 5.3.2) or as flexible (see Section 6.2.3);
- attain the pressure-impulse diagrams (see Section 6.2.1) of a bare and protected structural element while considering a deterministic approach or establishing an allowed conditional probability;
- design a sacrificial cladding to enhance the blast resistant using the previously referred implementations.

Further development is still required to combine all the implemented modules in a single executable program and to design and implement its graphical user interface.





# Bibliography

- [1] D. W. Abueidda, M. Bakir, R. K. A. Al-Rub, J. S. Bergström, N. A. Sobh, and I. J. “Mechanical properties of 3D printed polymeric cellular materials with triply periodic minimal surface architectures.” In: *Materials & Design* 122 (2017), pp. 255–267. DOI: 10.1016/j.matdes.2017.03.018.
- [2] M. Aleyaasin, J. J. Harrigan, and S. R. Reid. “Air-blast response of cellular material with a face plate: An analytical–numerical approach.” In: *International Journal of Mechanical Sciences* 91 (2015), pp. 64–70. DOI: 10.1016/j.ijmecsci.2014.03.027.
- [3] H. Aoude, F. P. Dagenais, R. P. Burrell, and M. Saatcioglu. “Behavior of ultra-high performance fiber reinforced concrete columns under blast loading.” In: *International Journal of Impact Engineering* 80 (2015), pp. 185–202. DOI: 0.1016/j.ijimpeng.2015.02.006.
- [4] M. F. Ashby, T. Evans, N. A. Fleck, J. W. Hutchinson, H. N. G. Wadley, and L. J. Gibson. *Metal foams: a design guide*. Elsevier, 2000.
- [5] M. Y. H. Bangash and T. Bangash. *Explosion-Resistant Buildings: Design, Analysis, and Case Studies*. Springer-Verlag Berlin Heidelberg, 2006.
- [6] A. T. Barnes, K. Ravi-Chandar, S. Kyriakides, and S. Gaitanaros. “Dynamic crushing of aluminum foams: Part I – Experiments.” In: *International Journal of Solids and Structures* 51.9 (2014), pp. 1631–1645. DOI: 10.1016/j.ijso1str.2013.11.019.
- [7] S. R. G. Bates, I. R. Farrow, and R. S. Trask. “3D printed polyurethane honeycombs for repeated tailored energy absorption.” In: *Materials & Design* 112 (2016), pp. 172–183. DOI: 10.1016/j.matdes.2016.08.062.
- [8] A. Bellini and S. Güçeri. “Mechanical characterization of parts fabricated using fused deposition modeling.” In: *Rapid Prototyping Journal* 9.4 (2003), pp. 252–264. DOI: 10.1108/13552540310489631.
- [9] J. M. Biggs. *Introduction to structural dynamics*. McGraw-Hill, Inc., 1964.
- [10] P. H. Bischoff and S. H. Perry. “Compressive behaviour of concrete at high strain rates.” In: *Materials and structures* 24.6 (1991), pp. 425–450. DOI: 10.1007/BF02472016.

- [11] J. R. Blasko, T. Krauthammer, and S. Astarlioglu. *Pressure–impulse Diagrams of Structural Elements Subjected to Dynamic Loads*. PTC–TR– 002–2007. University Park, PA: Protective Technology Center, 2007.
- [12] D. Bogosian, J. Ferritto, and Y. Shi. “Measuring uncertainty and conservatism in simplified blast models.” In: *30<sup>th</sup> Explosives Safety Seminar*. 2002.
- [13] J. Brennan-Craddock, D. Brackett, R. Wildman, and R. Hague. “The design of impact absorbing structures for additive manufacture.” In: *Journal of Physics: Conference Series* 382 (2012), p. 012042. DOI: 10.1088/1742-6596/382/1/012042.
- [14] H. L. Brode. “Numerical solutions of spherical blast waves.” In: *Journal of Applied Physics* 26.6 (1955), pp. 766–775. DOI: 10.1063/1.1722085.
- [15] P. A. Buchan and J. F. Chen. “Blast resistance of FRP composites and polymer strengthened concrete and masonry structures. A state-of-the-art review.” In: *Composites Part B: Engineering* 38.5-6 (2007), pp. 509–522. DOI: 10.1016/j.compositesb.2006.07.009.
- [16] R. P. Burrell, H. Aoude, and M. Saatcioglu. “Response of SFRC columns under blast loads.” In: *Journal of Structural Engineering* 141.9 (2014), p. 04014209. DOI: 10.1061/(ASCE)ST.1943-541X.0001186.
- [17] *CEB-FIP Model Code 90*. CEB Bulletin No. 213/214. Comité Euro-International du Béton, 1993.
- [18] J. M. Chacón, M. A. Caminero, E. García-Plaza, and P. J. Núñez. “Additive manufacturing of PLA structures using fused deposition modelling: Effect of process parameters on mechanical properties and their optimal selection.” In: *Materials & Design* 124 (2017), pp. 143–157. DOI: 10.1016/j.matdes.2017.03.065.
- [19] L. Chen, J. Zhang, B. Du, H. Zhou, H. Liu, Y. Guo, W. Li, and D. Fang. “Dynamic crushing behavior and energy absorption of graded lattice cylindrical structure under axial impact load.” In: *Thin-Walled Structures* 127 (2018), pp. 333–343. DOI: 10.1016/j.tws.2017.10.048.
- [20] Y. Chen, T. Li, Z. Jia, F. Scarpa, C. Yao, and L. Wang. “3D printed hierarchical honeycombs with shape integrity under large compressive deformations.” In: *Materials & Design* 137 (2018), pp. 226–234. DOI: 10.1016/j.matdes.2017.10.028.
- [21] *China explosions: What we know about what happened in Tianjin*. Aug. 2015. URL: <http://www.bbc.com/news/world-asia-china-33844084> (visited on 12/26/2019).
- [22] C. Cismaşiu, J. R. G. Ferreira, and H. B. Rebelo. “Modelação tridimensional de ondas de choque em LS-DYNA.” In: *Construção Magazine* 86 (2018), pp. 24–28.

- [23] C. Cismaşiu, H. B. Rebelo, V. J. G. Lúcio, M. T. M. S. Gonçalves, G. J. Gomes, and J. P. F. Basto. “Numerical Simulation of Blast Effects on Fibre Grout Strengthened RC Panels.” In: *Key Engineering Materials*. Vol. 755. Trans Tech Publications Ltd. 2017, pp. 18–30. DOI: 10.4028/www.scientific.net/KEM.755.18.
- [24] N. F. E. Command. *Blast Resistant Structures. Design Manual 2.08*. Alexandria, VA, 1986.
- [25] C. Cranz. *Lehrbuch der Ballistik*. Springer, Berlin, 1926.
- [26] D. Darwin, C. W. Dolan, and A. H. Nilson. *Design of concrete structures*. McGraw-Hill Education, 2016.
- [27] C. S. Davis, K. E. Hillgartner, S. H. Han, and J. E. Seppala. “Mechanical strength of welding zones produced by polymer extrusion additive manufacturing.” In: *Additive Manufacturing* 16 (2017), pp. 162–166. DOI: 10.1016/j.addma.2017.06.006.
- [28] D. A. Debeau, C. C. Seepersad, and M. R. Haberman. “Impact behavior of negative stiffness honeycomb materials.” In: *Journal of Materials Research* 33.3 (2018), pp. 290–299. DOI: 10.1557/jmr.2018.7.
- [29] Y. Ding, S. Wang, K. Zhao, Z. Zheng, L. Yang, and J. Yu. “Blast alleviation of cellular sacrificial cladding: A nonlinear plastic shock model.” In: *International Journal of Applied Mechanics* 8.04 (2016), p. 1650057. DOI: 10.1142/S1758825116500575.
- [30] J. R. C. Dizon, A. H. Espera, Q. Chen, and R. C. Advincula. “Mechanical characterization of 3D-printed polymers.” In: *Additive Manufacturing* 20 (2018), pp. 44–67. DOI: 10.1016/j.addma.2017.12.002.
- [31] D. O. Dusenberry. *Handbook for Blast Resistant Design of Buildings*. John Wiley & Sons, 2010.
- [32] B. D. Ellis, B. P. DiPaolo, D. L. McDowell, and M. Zhou. “Experimental investigation and multiscale modeling of ultra-high-performance concrete panels subject to blast loading.” In: *International Journal of Impact Engineering* 69 (2014), pp. 95–103. DOI: 10.1016/j.ijimpeng.2013.12.011.
- [33] I. Elnasri, S. Pattofatto, H. Zhao, H. Tsitsiris, F. Hild, and Y. Girard. “Shock enhancement of cellular structures under impact loading: Part I Experiments.” In: *Journal of the Mechanics and Physics of Solids* 55.12 (2007), pp. 2652–2671. DOI: 10.1016/j.jmps.2007.04.005.
- [34] EN 1990. *Eurocode 0: Basis of Structural Design*. CEN – European Committee for Standardization. Brussels, Belgium, 2004.
- [35] EN 1992-1-1:2004. *Eurocode 2: Design of Concrete Structures - Part 1-1 : General rules and rules for buildings*. CEN – European Committee for Standardization. Brussels, Belgium, 2004.

- [36] R. T. L. Ferreira, I. C. Amatte, T. A. Dutra, and D. Bürger. “Experimental characterization and micrography of 3D printed PLA and PLA reinforced with short carbon fibers.” In: *Composites Part B: Engineering* 124 (2017), pp. 88–100. DOI: 10.1016/j.compositesb.2017.05.013.
- [37] P. D. Flynn. *Elastic response of simple structures to pulse loading*. BRL Memo. Report No. 525. Aberdeen Proving Ground, MD, 1950.
- [38] Francois Nascimbeni/AFP via Getty Images. *FRANCE-ACCIDENT*. 2013.
- [39] H. C. Fu, M. A. Erki, and M. Seckin. “Review of effects of loading rate on concrete in compression.” In: *Journal of Structural Engineering* 117.12 (1991), pp. 3645–3659. DOI: 10.1061/(ASCE)0733-9445(1991)117:12(3645).
- [40] C. J. Gantes and N. G. Pnevmatikos. “Elastic-plastic response spectra for exponential blast loading.” In: *International Journal of Impact Engineering* 30.3 (2004), pp. 323–343. DOI: 10.1016/S0734-743X(03)00077-0.
- [41] L. J. Gibson and M. F. Ashby. *Cellular solids: structure and properties*. Cambridge Solid State Science Series. Cambridge University Press, 1999.
- [42] L. Gong, S. Kyriakides, and W. Y. Jang. “Compressive response of open-cell foams. Part I: Morphology and elastic properties.” In: *International Journal of Solids and Structures* 42.5-6 (2005), pp. 1355–1379. DOI: 10.1016/j.ijsolstr.2004.07.023.
- [43] S. A. Granström. *Loading characteristics of air blasts from detonating charges*. Tech. rep. 100. Royal Institute of Technology Stockholm, Sweden, 1956.
- [44] S. Guessasma, S. Belhabib, H. Nouri, and O. B. Hassana. “Anisotropic damage inferred to 3D printed polymers using fused deposition modelling and subject to severe compression.” In: *European Polymer Journal* 85 (2016), pp. 324–340. DOI: 10.1016/j.eurpolymj.2016.10.030.
- [45] *Guide to dynamic force sensors*. WPL\_30\_0219. PCB Piezotronics, Inc.
- [46] Z. Guo, Z. Xu, C. Chen, B. Zhang, D. E. Lehman, and S. Cao. “Behavior of GFRP retrofitted reinforced concrete slabs subjected to conventional explosive blast.” In: *Materials and Structures* 50.6 (2017), p. 236. DOI: 10.1617/s11527-017-1107-6.
- [47] S. Guruprasad and A. Mukherjee. “Layered sacrificial claddings under blast loading Part I—analytical studies.” In: *International Journal of Impact Engineering* 24.9 (2000), pp. 957–973. DOI: 10.1016/S0734-743X(00)00004-X.
- [48] S. Guruprasad and A. Mukherjee. “Layered sacrificial claddings under blast loading Part II—experimental studies.” In: *International Journal of Impact Engineering* 24.9 (2000), pp. 975–984. DOI: 10.1016/S0734-743X(00)00005-1.
- [49] J. Ha, N. Yi, J. Choi, and J. J. Kim. “Experimental study on hybrid CFRP–PU strengthening effect on RC panels under blast loading.” In: *Composite Structures* 93.8 (2011), pp. 2070–2082. DOI: 10.1016/j.compstruct.2011.02.014.

- [50] J. O. Hallquist. *LS-DYNA Theory Manual*. Livermore, CA, 2006.
- [51] A. G. Hanssen, L. Enstock, and M. Langseth. “Close-range blast loading of aluminium foam panels.” In: *International Journal of Impact Engineering* 27.6 (2002), pp. 593–618. DOI: 10.1016/S0734-743X(01)00155-5.
- [52] J. J. Harrigan, S. R. Reid, P. J. Tan, and T. Y. Reddy. “High rate crushing of wood along the grain.” In: *International Journal of Mechanical Sciences* 47.4-5 (2005), pp. 521–544. DOI: 10.1016/j.ijmecsci.2004.12.013.
- [53] J. J. Harrigan, S. R. Reid, and A. S. Yaghoubi. “The correct analysis of shocks in a cellular material.” In: *International Journal of Impact Engineering* 37.8 (2010), pp. 918–927. DOI: 10.1016/j.ijimpeng.2009.03.011.
- [54] J. A. Harris, R. E. Winter, and G. J. McShane. “Impact response of additively manufactured metallic hybrid lattice materials.” In: *International Journal of Impact Engineering* 104 (2017), pp. 177–191. DOI: 10.1016/j.ijimpeng.2017.02.007.
- [55] Z. Hashin. “Failure criteria for unidirectional fiber composites.” In: *Journal of applied mechanics* 47.2 (1980), pp. 329–334. DOI: 10.1115/1.3153664.
- [56] B. Hopkinson. *British Ordnance Board Minutes, 13565*. 1915.
- [57] C. C. Hudson. *Sound Pulse Approximations to Blast Loading (with comments on transient drag)*. Sandia Corporation Technical Memorandum 191-55-51. Sandia Corporation, MD, 1955.
- [58] D. W. Hyde. *User’s guide for microcomputer programs CONWEP and FUNPRO, Applications of TM 5-855-1: “Fundamentals of Protective Design for Conventional Weapons”*. AD/A-195867. Vicksburg, MS, 1988.
- [59] E. Jacques, A. Lloyd, P. Imbeau, D. Palermo, and J. Quek. “GFRP-retrofitted reinforced concrete columns subjected to simulated blast loading.” In: *Journal of Structural Engineering* 141.11 (2015), p. 04015028. DOI: 10.1061/(ASCE)ST.1943-541X.0001251.
- [60] Joint Committee on Structural Safety. *JCSS Probabilistic Model Code*. 2001.
- [61] N. Kambouchev, L. Noels, and R. Radovitzky. “Nonlinear compressibility effects in fluid-structure interaction and their implications on the air-blast loading of structures.” In: *Journal of Applied Physics* 100.063519 (2006). DOI: 10.1063/1.2349483.
- [62] N. Kambouchev, L. Noels, and R. Radovitzky. “Numerical simulation of the fluid-structure interaction between air blast waves and free-standing plates.” In: *Computers & Structures* 85.11–14 (2007), pp. 923–931. DOI: 10.1016/j.compstruc.2006.11.005.
- [63] D. Karagiozova and M. Alves. “Stress waves in layered cellular materials – Dynamic compaction under axial impact.” In: *International Journal of Mechanical Sciences* 101 (2015), pp. 196–213. DOI: 10.1016/j.ijmecsci.2015.07.024.

- [64] D. Karagiozova, G. S. Langdon, and G. N. Nurick. "Blast attenuation in Cymat foam core sacrificial claddings." In: *International Journal of Mechanical Sciences* 52.5 (2010), pp. 758–776. DOI: 10.1016/j.jmesci.2010.02.002.
- [65] D. Karagiozova, G. S. Langdon, and G. N. Nurick. "Propagation of compaction waves in metal foams exhibiting strain hardening." In: *International Journal of Solids and Structures* 49.19-20 (2012), pp. 2763–2777. DOI: 10.1016/j.jjsolstr.2012.03.012.
- [66] V. Karlos, G. Solomos, and M. Larcher. "Analysis of the blast wave decay coefficient using the Kingery–Bulmash data." In: *International Journal of Protective Structures* 7.3 (2016), pp. 409–429. DOI: 10.1177/2041419616659572.
- [67] C. N. Kingery and G. Bulmash. *Airblast parameters from TNT spherical air burst and hemispherical surface burst*. Tech. rep. ARBRL-TR-02555. Aberdeen Proving Ground, MD: U.S. Army Ballistic Research Laboratory, 1984.
- [68] G. F. Kinney and K. J. Graham. *Explosive Shocks in Air*. 2nd ed. Springer-Verlag Berlin Heidelberg, 1985. DOI: 10.1007/978-3-642-86682-1.
- [69] T. Krauthammer. *Modern Protective Structures*. CRC Press, 2008.
- [70] T. Krauthammer, S. Astarlioglu, J. Blasko, T. B. Soh, and P. H. Ng. "Pressure–impulse diagrams for the behavior assessment of structural components." In: *International Journal of Impact Engineering* 35.8 (2008), pp. 771–783. DOI: 10.1016/j.ijimpeng.2007.12.004.
- [71] M. Kucewicz, P. Baranowski, J. Małachowski, A. Popławski, and P. Płatek. "Modelling, and characterization of 3D printed cellular structures." In: *Materials & Design* 142 (2018), pp. 177–189. DOI: 10.1016/j.matdes.2018.01.028.
- [72] V. E. Kuznetsov, A. N. Solonin, O. D. Urzhumtsev, R. Schilling, and A. G. Tavitov. "Strength of PLA Components Fabricated with Fused Deposition Technology Using a Desktop 3D Printer as a Function of Geometrical Parameters of the Process." In: *Polymers* 10.3 (2018), p. 313. DOI: 10.3390/polym10030313.
- [73] X. Lan, S. Feng, Q. Huang, and T. Zhou. "Blast response of continuous-density graded cellular material based on the 3D Voronoi model." In: *Defence Technology* 14.5 (2018), pp. 433–440. DOI: 10.1016/j.dt.2018.06.003.
- [74] G. S. Langdon, D. Karagiozova, D. Theobald, G. N. Nurick, G. Lu, and R. P. Merret. "Fracture of aluminium foam core sacrificial cladding subjected to air-blast loading." In: *International Journal of Impact Engineering* 37 (2010), pp. 638–651. DOI: 10.1016/j.ijimpeng.2009.07.006.
- [75] D. Lawver, R. Daddazio, G. J. Oh, C. K. B. Lee, A. B. Pifko, and M. Stanley. "Simulating the response of composite reinforced floor slabs subjected to blast loading." In: *ASME 2003 International Mechanical Engineering Congress and Exposition, Washington, DC*. American Society of Mechanical Engineers. 2003, pp. 15–21.

- [76] S. Lee, F. Barthelat, N. Moldovan, H. D. Espinosa, and H. N. G. Wadley. “Deformation rate effects on failure modes of open-cell Al foams and textile cellular materials.” In: *International Journal of Solids and Structures* 43.1 (2006), pp. 53–73. DOI: 10.1016/j.ijsolstr.2005.06.101.
- [77] V. C. Li. “Large volume, high-performance applications of fibers in civil engineering.” In: *Journal of Applied Polymer Science* 83.3 (2002), pp. 660–686. DOI: 10.1002/app.2263.
- [78] Y. Li, O. Algasse, and H. Aoude. “Response of high-strength reinforced concrete beams under shock-tube induced blast loading.” In: *Construction and Building Materials* 189 (2018), pp. 420–437. DOI: 10.1016/j.conbuildmat.2018.09.005.
- [79] Z. Li, W. Chen, and H. Hao. “Blast mitigation performance of cladding using square dome-shape kirigami folded structure as core.” In: *International Journal of Mechanical Sciences* 145 (2018), pp. 83–95. DOI: 10.1016/j.ijmecsci.2018.06.035.
- [80] M. Liang, Z. Li, F. Lu, and X. Li. “Theoretical and numerical investigation of blast responses of continuous-density graded cellular materials.” In: *Composite Structures* 164 (2017). DOI: 10.1016/j.compstruct.2016.12.065.
- [81] L. Linkutė, V. Juocevičius, and E. R. Vaidogas. “A probabilistic design of sacrificial cladding for a blast wall using limited statistical information on blast loading.” In: *Mechanics* 19.1 (2013), pp. 58–66. DOI: 10.5755/j01.mech.19.1.3621.
- [82] S. Liu, Y. Zhou, Q. Zheng, J. Zhou, F. Jin, and H. Fan. “Blast responses of concrete beams reinforced with steel-GFRP composite bars.” In: *Structures*. Vol. 22. Elsevier, 2019, pp. 200–212. DOI: 10.1016/j.istruc.2019.08.010.
- [83] Livermore Software Technology Corporation. *LS-DYNA User Manual: Volumes I & II (Version R10.1)*. Livermore, CA, 2018.
- [84] S. L. Lopatnikov, B. A. Gama, M. J. Haque, C. Krauthauser, J. W. Gillespie Jr, M. Guden, and I. W. Hall. “Dynamics of metal foam deformation during Taylor cylinder-Hopkinson bar impact experiment.” In: *Composite Structures* 61.1-2 (2003), pp. 61–71. DOI: 10.1016/S0263-8223(03)00039-4.
- [85] L. R. Lopes, A. F. Silva, and O. Carneiro. “Multi-material 3D printing: The relevance of materials affinity on the boundary interface performance.” In: *Additive Manufacturing* 23 (2018), pp. 45–52. DOI: 10.1016/j.addma.2018.06.027.
- [86] G. Lu and T. Yu. *Energy absorption of structures and materials*. Woodhead Publishing Series in Metals and Surface Engineering. Woodhead Publishing Ltd, 2003.
- [87] G. W. Ma and Z. Q. Ye. “Analysis of foam claddings for blast alleviation.” In: *International Journal of Impact Engineering* 34.1 (2007), pp. 60–70. DOI: 10.1016/j.ijimpeng.2005.10.005.

- [88] G. W. Ma and Z. Q. Ye. "Energy absorption of double-layer foam cladding for blast alleviation." In: *International Journal of Impact Engineering* 34.2 (2007), pp. 329–347. DOI: 10.1016/j.ijimpeng.2005.07.012.
- [89] A. Maazoun, B. Belkassem, B. Reymen, S. Matthys, J. Vantomme, and D. Lecompte. "Blast response of RC slabs with externally bonded reinforcement: Experimental and analytical verification." In: *Composite Structures* 200 (2018), pp. 246–257. DOI: 10.1016/j.compstruct.2018.05.102.
- [90] J. Magnusson. *Structural Concrete Elements Subjected to Air Blast Loading*. Licentiate Thesis. Trita-BKN. Bulletin 92. KTH Royal Institute of Technology, 2007.
- [91] J. Magnusson and M. Hallgren. *High Performance Concrete Beams Subjected to Shock Waves from Air Blast*. FOA-R-OO-01586-311-SE. Tumba, Sweden: Defence Research Establishment, Weapons and Protection Division, 2000.
- [92] L. J. Malvar and J. E. Crawford. "Dynamic increase factors for concrete." In: *18<sup>th</sup> DoD Explosives Safety Seminar*. 1998.
- [93] L. J. Malvar and J. E. Crawford. "Dynamic increase factors for steel reinforcing bars." In: *18<sup>th</sup> DoD Explosives Safety Seminar*. 1998.
- [94] L. J. Malvar and C. A. Ross. "Review of static and dynamic properties of concrete in tension." In: *ACI Materials Journal* 95.6 (1998), pp. 735–739.
- [95] I. Maskery, A. Hussey, A. Panesar, A. Aremu, C. Tuck, I. Ashcroft, and R. Hague. "An investigation into reinforced and functionally graded lattice structures." In: *Journal of Cellular Plastics* 53.2 (2017), pp. 151–165. DOI: 10.1177/0021955X16639035.
- [96] *MATLAB version 9.3.0 (R2017b)*. The Mathworks, Inc. Natick, MA, 2017.
- [97] A. Matzenmiller, J. Lubliner, and R. L. Taylor. "A constitutive model for anisotropic damage in fiber-composites." In: *Mechanics of materials* 20.2 (1995), pp. 125–152. DOI: 10.1016/0167-6636(94)00053-0.
- [98] S. McKown, Y. Shen, W. K. Brookes, C. J. Sutcliffe, W. J. Cantwell, G. S. Langdon, G. N. Nurick, and M. D. Theobald. "The quasi-static and blast loading response of lattice structures." In: *International Journal of Impact Engineering* 35.8 (2008), pp. 795–810. DOI: 10.1016/j.ijimpeng.2007.10.005.
- [99] R. P. Merrett, G. S. Langdon, and M. D. Theobald. "The blast and impact loading of aluminium foam." In: *Materials & Design* 44 (2013), pp. 311–319. DOI: 10.1016/j.matdes.2012.08.016.
- [100] *Methodology Manual for the Single-Degree-of-Freedom Blast Effects Design Spreadsheets (SBEDS)*. PDC TR-06-01, Rev 1. U.S. Army Corps of Engineers, 2008.



- [101] O. A. Mohamed, S. H. Masood, and J. L. Bhowmik. "Optimization of fused deposition modeling process parameters: a review of current research and future prospects." In: *Advances in Manufacturing* 3.1 (2015), pp. 42–53. DOI: 10.1007/s40436-014-0097-7.
- [102] N. G. Morales, T. J. Fleck, and J. F. Rhoads. "The effect of interlayer cooling on the mechanical properties of components printed via fused deposition." In: *Additive Manufacturing* 24 (2018), pp. 243–248. DOI: 10.1016/j.addma.2018.09.001.
- [103] K. B. Morrill, L. J. Malvar, J. E. Crawford, and J. M. Ferritto. "Blast resistant design and retrofit of reinforced concrete columns and walls." In: *Structures 2004: Building on the Past, Securing the Future*. 2004, pp. 1–8. DOI: 10.1061/40700(2004)154.
- [104] W. E. Morris. *Shock diffraction in the vicinity of a structure*. Tech. rep. WT-786. Naval Ordnance Laboratory, MD, 1959.
- [105] K. M. Mosalam and A. S. Mosallam. "Nonlinear transient analysis of reinforced concrete slabs subjected to blast loading and retrofitted with CFRP composites." In: *Composites Part B: Engineering* 32.8 (2001), pp. 623–636. DOI: 10.1016/S1359-8368(01)00044-0.
- [106] J. P. Murtha. *Blast loading of structures in the regular reflection and low mach-stem regions*. Research Report SC-4239(TR). Sandia Corporation, MD, 1955.
- [107] L. C. Muszynski and M. R. Purcell. "Composite reinforcement to strengthen existing concrete structures against air blast." In: *Journal of Composites for Construction* 7.2 (2003), pp. 93–97. DOI: 10.1061/(ASCE)1090-0268(2003)7:2(93).
- [108] L. C. Muszynski, M. R. Purcell, and R. Sierakowski. "Strengthening concrete structures by using externally applied composite reinforcing material." In: *Proceedings of 7th International Symposium on Interaction of the Effects of Munitions with Structures, Mannheim, Germany*. 1995, pp. 291–298.
- [109] J. Nam, H. Kim, S. Kim, N. Yi, and J. J. Kim. "Numerical evaluation of the retrofit effectiveness for GFRP retrofitted concrete slab subjected to blast pressure." In: *Composite Structures* 92.5 (2010), pp. 1212–1222. DOI: 10.1016/j.compstruct.2009.10.031.
- [110] National Consortium for the Study of Terrorism and Responses to Terrorism (START). *Global Terrorism Database [0617dist]*. 2016. URL: <https://www.start.umd.edu/gtd>.
- [111] C. E. Needham. *Blast Waves*. 2nd ed. Shock Wave and High Pressure Phenomena. Springer, 2018. DOI: 10.1007/978-3-319-65382-2.
- [112] M. D. Netherton and M. G. Stewart. "Blast load variability and accuracy of blast load prediction models." In: *International Journal of Protective Structures* 1.4 (2010), pp. 543–570. DOI: 10.1260/2041-4196.1.4.543.

- [113] M. D. Netherton and M. G. Stewart. "Risk-based blast-load modelling: Techniques, models and benefits." In: *International Journal of Protective Structures* 7.3 (2016), pp. 430–451. DOI: 10.1177/2041419616666455.
- [114] M. D. Netherton, M. G. Stewart, S. J. Buttenshaw, K. Reidy, and B. A. H. Rodgers. *Experimental Data from the University of Newcastle's July 2014 Repeatable Explosive Field Trials*. Tech. rep. Centre for Infrastructure Performance and Reliability, 2016.
- [115] M. D. Netherton, M. G. Stewart, S. Lyons, N. M. Blandford, S. Papp, and L. Pleasance. *Experimental Data from 2012 Repeatable Explosive Field Trials*. Research Report No. 282.07.2014. Centre for Infrastructure Performance and Reliability, 2014.
- [116] P. H. Ng and T. Krauthammer. *Pressure–impulse diagrams for reinforced concrete slabs*. PTC–TR– 007–2004. University Park, PA: Protective Technology Center, 2004.
- [117] P. Olmati, F. Petrini, and K. Gkoumas. "Fragility analysis for the Performance-Based Design of cladding wall panels subjected to blast load." In: *Engineering Structures* 78 (2014), pp. 112–120. DOI: 10.1016/j.engstruct.2014.06.004.
- [118] H. Ousji. "Blast mitigation using crushable core systems: experimental, analytical and numerical study." Doctoral dissertation. Vrije Universiteit Brussel, 2017.
- [119] H. Ousji, B. Belkassem, M. A. Louar, D. Kakogiannis, B. Reymen, L. Pyl, and J. Vantomme. "Parametric Study of an Explosive-Driven Shock Tube as Blast Loading Tool." In: *Experimental Techniques* 40.4 (2016), pp. 1307–1325. DOI: 10.1007/s40799-016-0128-3.
- [120] H. Ousji, B. Belkassem, M. A. Louar, B. Reymen, J. Martino, D. Lecompte, L. Pyl, and J. Vantomme. "Air–blast response of sacrificial cladding using low density foams: Experimental and analytical approach." In: *International Journal of Mechanical Sciences* 128 (2017), pp. 459–474. DOI: 10.1016/j.ijmecsci.2017.05.024.
- [121] H. Ousji, B. Belkassem, M. A. Louar, B. Reymen, L. Pyl, and J. Vantomme. "Experimental Study of the Effectiveness of Sacrificial Cladding Using Polymeric Foams as Crushable Core with a Simply Supported Steel Beam." In: *Advances in Civil Engineering* 2016 (2016). DOI: 10.1155/2016/8301517.
- [122] S. Palanivelu, W. Van Paeppegem, J. Degrieck, B. Reymen, J. Ndambi, J. Vantomme, D. Kakogiannis, J. Wastiels, and D. Van Hemelrijck. "Close–range blast loading on empty recyclable metal beverage cans for use in sacrificial cladding structure." In: *Engineering Structures* 33.6 (2011), pp. 1966–1987. DOI: 10.1016/j.engstruct.2011.02.034.

- [123] F. Parisi. “Blast fragility and performance-based pressure–impulse diagrams of European reinforced concrete columns.” In: *Engineering Structures* 103 (2015), pp. 285–297. DOI: 10.1016/j.engstruct.2015.09.019.
- [124] PCB Piezotronics, Inc. *Model 102B. Installation and Operating Manual*. Depew, NY.
- [125] PCB Piezotronics, Inc. *Model 203B. Installation and Operating Manual*. Depew, NY.
- [126] J.-S. Pei, J. P. Wright, F. Gay-Balmaz, J. L. Beck, and M. D. Todd. “On choosing state variables for piecewise–smooth dynamical system simulations.” In: *Nonlinear Dynamics* 95.2 (2019), pp. 1165–1188. DOI: 10.1007/s11071-018-4622-2.
- [127] W. Peng, Z. Zhang, G. Gogos, and G. Gazonas. “Fluid structure interactions for blast wave mitigation.” In: *Journal of Applied Mechanics* 78.3 (2011), p. 031016. DOI: 10.1115/1.4002758.
- [128] Prusa Research S.R.O. "<https://www.prusa3d.com/>".
- [129] D. D. Radford, V. S. Deshpande, and N. A. Fleck. “The use of metal foam projectiles to simulate shock loading on a structure.” In: *International Journal of Impact Engineering* 31.9 (2005), pp. 1152–1171. DOI: 10.1016/j.ijimpeng.2004.07.012.
- [130] G. Randers-Pehrson and K. Bannister. *Airblast Loading Model for DYNA2D and DYNA3D*. AD/A-322344. Aberdeen Proving Ground, MD, 1997.
- [131] A. G. Razaqpur, A. Tolba, and E. Contestabile. “Blast loading response of reinforced concrete panels reinforced with externally bonded GFRP laminates.” In: *Composites Part B: Engineering* 38.5-6 (2007), pp. 535–546. DOI: 10.1016/j.compositesb.2006.06.016.
- [132] H. B. Rebelo and C. Cismaşiu. “A Comparison between three air blast simulation techniques in LS-DYNA.” In: *11th European LS-DYNA Conference, Salzburg, Austria*. 2017.
- [133] H. B. Rebelo, A. Gregório, P. A. R. Rosa, D. Lecompte, and C. Cismaşiu. “Experimental characterization of 3D printed PLA under uniaxial high strain rate loading.” In: *AuxDefense 2018 – 1st World Conference on Advanced Materials for Defense, Lisbon*. 2018.
- [134] H. B. Rebelo, D. Lecompte, C. Cismaşiu, A. Jonet, B. Belkasssem, and A. Maazoun. “3D printed PLA sacrificial honeycomb cladding blast mitigation.” In: *Proceedings of 18th International Symposium on Interaction of the Effects of Munitions with Structures, Panama City Beach, FL, USA*. 2019.

- [135] H. B. Rebelo, D. Lecompte, C. Cismaşiu, A. Jonet, B. Belkassem, and A. Maa-zoun. “Experimental and numerical investigation on 3D printed PLA sacrificial honeycomb cladding.” In: *International Journal of Impact Engineering* 131 (2019), pp. 162–173. DOI: 10.1016/j.ijimpeng.2019.05.013.
- [136] H. B. Rebelo, F. Amarante dos Santos, C. Cismaşiu, and D. Santos. “Exploratory study on geodesic domes under blast loads.” In: *International Journal of Protective Structures* 10.4 (2019), pp. 439–456. DOI: 10.1177/2041419618820540.
- [137] S. R. Reid and C. Peng. “Dynamic uniaxial crushing of wood.” In: *International Journal of Impact Engineering* 19.5-6 (1997), pp. 531–570. DOI: 10.1016/S0734-743X(97)00016-X.
- [138] *Reims blast and building collapse in France kills three*. Apr. 2013. URL: <https://www.bbc.com/news/world-europe-22328568> (visited on 12/26/2019).
- [139] M. P. M. Rhijnsburger, J. R. van Deursen, and J. C. A. M. van Doormaal. “Development of a toolbox suitable for dynamic response analysis of simplified structures.” In: *30th DoD Explosives Safety Seminar, Atlanta, GA*. 2002.
- [140] S. E. Rigby. “Blast wave clearing effects on finite-sized targets subjected to explosive loads.” Doctoral dissertation. University of Sheffield, 2014.
- [141] S. E. Rigby, A. Tyas, T. Bennett, S. D. Clarke, and S. D. Fay. “The negative phase of the blast load.” In: *International Journal of Protective Structures* 5.1 (2014), pp. 1–19. DOI: 10.1260/2041-4196.5.1.1.
- [142] S. E. Rigby, A. Tyas, S. D. Fay, S. D. Clarke, and J. A. Warren. “Validation of semi-empirical blast pressure predictions for far field explosions-is there inherent variability in blast wave parameters?” In: *Proceedings of the 6<sup>th</sup> International Conference on Protection of Structures against Hazards*. 2014.
- [143] C. A. Ross, L. C. Muszynski, D. M. Jerome, J. W. Tedesco, and R. L. Sierakowski. “RC Beams and Slabs Externally Reinforced with Fiber Reinforced Plastic (FRP) Panels.” In: *Proceedings of the Structural Congress XV — Building to Last, Portland, OR*. 1997, pp. 673–677.
- [144] R. G. Sachs. *The dependence of blast on ambient pressure and temperature*. BRL Report No. 466. Aberdeen Proving Ground, MD, 1944.
- [145] H. Y. Sarvestani, A. H. Akbarzadeh, H. Niknam, and K. Hermenean. “3D printed architected polymeric sandwich panels: Energy absorption and structural performance.” In: *Composite Structures* 200 (2018), pp. 886–909. DOI: 10.1016/j.compstruct.2018.04.002.
- [146] K. Schweizerhof, K. Weimar, T. Munz, and T. Rottner. “Crashworthiness analysis with enhanced composite material models in LS-DYNA—merits and limits.” In: *Proceedings of the 5th International LS-DYNA Users Conference, Southfield, MI*. 1998, pp. 1–17.

- [147] L. E. Schwer, S. W. Key, T. A. Pučik, and L. P. Bindeman. “An assessment of the LS-DYNA hourglass formulations via the 3D patch test.” In: *Proceedings of the 5th European LS-DYNA users conference, Birmingham*. 2005.
- [148] C. J. Shen, G. Lu, and T. X. Yu. “Investigation into the behavior of a graded cellular rod under impact.” In: *International Journal of Impact Engineering* 74 (2014), pp. 92–106. DOI: 10.1016/j.ijimpeng.2014.02.015.
- [149] C. J. Shen, G. Lu, T. X. Yu, and D. Ruan. “Dynamic response of a cellular block with varying cross-section.” In: *International Journal of Impact Engineering* 79 (2015), pp. 53–64. DOI: 10.1016/j.ijimpeng.2014.08.017.
- [150] C. M. A. Silva, P. A. R. Rosa, and P. A. F. Martins. “An innovative electromagnetic compressive split Hopkinson bar.” In: *International Journal of Mechanics and Materials in Design* 5.3 (2009), pp. 281–288. DOI: 10.1007/s10999-009-9101-y.
- [151] C. M. A. Silva, P. A. R. Rosa, and P. A. F. Martins. “Electromagnetic cam driven compression testing equipment.” In: *Experimental mechanics* 52.8 (2012), pp. 1211–1222. DOI: 10.1007/s11340-011-9576-y.
- [152] C. M. A. Silva, P. A. R. Rosa, and P. A. F. Martins. “Innovative testing machines and methodologies for the mechanical characterization of materials.” In: *Experimental Techniques* 40.2 (2016), pp. 569–581. DOI: 10.1007/s40799-016-0058-0.
- [153] D. Sim. *China explosions aftermath: Photos from inside the blast zone show the devastation in Tianjin*. 2015.
- [154] *Single Degree of Freedom Structural Response Limits for Antiterrorism Design*. PDC TR-06–08, Rev 1. U.S. Army Corps of Engineers, 2008.
- [155] R. Smilowitz, C. Arnold, M. Ettouney, M. Hankewycz, W. Blewwet, M. Kaminskas, and E. Letvin. *Reference Manual to Mitigate Potential Terrorist Attacks Against Buildings, FEMA 426/BIPS 06*. 2nd ed. Buildings and Infrastructure Protection Series. Washington, DC: U.S. Dept. of Homeland Security, 2011.
- [156] T. B. Soh and T. Krauthammer. *Load-impulse diagrams of reinforced concrete beams subjected to concentrated transient loading*. PTC-TR-006–2004. University Park, PA: Protective Technology Center, 2004.
- [157] Y. Song, Y. Li, W. Song, K. Yee, K.-Y. Lee, and V. L. Tagarielli. “Measurements of the mechanical response of unidirectional 3D-printed PLA.” In: *Materials & Design* 123 (2017), pp. 154–164. DOI: 10.1016/j.matdes.2017.03.051.
- [158] Structural Engineering Institute. *Blast Protection of Buildings*. ASCE/SEI 59–11. Reston, VA: American Society of Civil Engineers, 2011.
- [159] Y. Sun and Q. M. Li. “Dynamic compressive behaviour of cellular materials: a review of phenomenon, mechanism and modelling.” In: *International Journal of Impact Engineering* 112 (2018), pp. 74–115. DOI: 10.1016/j.ijimpeng.2017.10.006.

- [160] Y. Sun, Q. M. Li, S. A. McDonald, and P. J. Withers. “Determination of the constitutive relation and critical condition for the shock compression of cellular solids.” In: *Mechanics of Materials* 99 (2016), pp. 26–36. DOI: 10.1016/j.mechmat.2016.04.004.
- [161] M. M. Swisdak Jr. *Simplified Kingery airblast calculations*. Naval Surface Warfare Center, Indian Head Division, MD, 1994.
- [162] P. J. Tan, J. J. Harrigan, and S. R. Reid. “Inertia effects in uniaxial dynamic compression of a closed cell aluminium alloy foam.” In: *Materials Science and Technology* 18.5 (2002), pp. 480–488. DOI: 10.1179/026708302225002092.
- [163] P. J. Tan, S. R. Reid, and J. J. Harrigan. “On the dynamic mechanical properties of open-cell metal foams—A re-assessment of the ‘simple-shock theory’.” In: *International Journal of Solids and Structures* 49.19-20 (2012), pp. 2744–2753. DOI: 10.1016/j.ijsolstr.2012.03.026.
- [164] P. J. Tan, S. R. Reid, J. J. Harrigan, Z. Zou, and S. Li. “Dynamic compressive strength properties of aluminium foams. Part I – experimental data and observations.” In: *Journal of the Mechanics and Physics of Solids* 53.10 (2005), pp. 2174–2205. DOI: 10.1016/j.jmps.2005.05.007.
- [165] P. J. Tan, S. R. Reid, J. J. Harrigan, Z. Zou, and S. Li. “Dynamic compressive strength properties of aluminium foams. Part II – “shock” theory and comparison with experimental data and numerical models.” In: *Journal of the Mechanics and Physics of Solids* 53.10 (2005), pp. 2206–2230. DOI: 10.1016/j.jmps.2005.05.003.
- [166] G. I. Taylor. “The formation of a blast wave by a very intense explosion I. Theoretical discussion.” In: *Proceedings of the Royal Society of London. Series A. Mathematical and Physical Sciences*. Vol. 201. 1065. 1950, pp. 159–174.
- [167] G. I. Taylor. “The pressure and impulse of submarine explosion waves on plates.” In: *The scientific papers of G. I. Taylor*. Ed. by G. K. Batchelor. Vol. 3. 1963, pp. 287–303.
- [168] W. J. Taylor. “A method for predicting blast loads during the diffraction phase.” In: *The Shock and Vibration Bulletin* 42.4 (1972), p. 135.
- [169] M. Teich and N. Gebbeken. “The influence of the underpressure phase on the dynamic response of structures subjected to blast loads.” In: *International Journal of Protective Structures* 1.2 (2010), pp. 219–233. DOI: 10.1260/2041-4196.1.2.219.
- [170] M. D. Theobald and G. N. Nurick. “Experimental and numerical analysis of tube-core claddings under blast loads.” In: *International Journal of Impact Engineering* 37.3 (2010), pp. 333–348. DOI: 10.1016/j.ijimpeng.2009.10.003.

- [171] G. Thiagarajan, A. V. Kadambi, S. Robert, and C. F. Johnson. “Experimental and finite element analysis of doubly reinforced concrete slabs subjected to blast loads.” In: *International Journal of Impact Engineering* 75 (2015), pp. 162–173. DOI: 10.1016/j.ijimpeng.2014.07.018.
- [172] U.S. Army Materiel Command Headquarters. *Engineering Design Handbook. Explosions in Air. Part One*. AD/A-003817 (AMC Pamphlet AMCP 706-181). Alexandria, VA, 1974.
- [173] U.S. Department of Defense. *Structures to resist the effects of accidental explosions*. 2008.
- [174] U.S. Department of Defense. *DoD Minimum Antiterrorism Standards for Buildings*. 2018.
- [175] W. Van Paepegem, S. Palanivelu, J. Degrieck, J. Vantomme, B. Reymen, D. Kagogiannis, D. Van Hemelrijck, and J. Wastiels. “Blast performance of a sacrificial cladding with composite tubes for protection of civil engineering structures.” In: *Composites Part B: Engineering* 65 (2014), pp. 131–146. DOI: 10.1016/j.compositesb.2014.02.004.
- [176] L. Wang. *Foundations of Stress Waves*. Elsevier, 2007.
- [177] J. Wei and L. R. Dharani. “Response of laminated architectural glazing subjected to blast loading.” In: *International Journal of Impact Engineering* 32.12 (2006), pp. 2032–2047. DOI: 10.1016/j.ijimpeng.2005.05.012.
- [178] C. Wu, J. Li, and Y. Su. *Development of ultra-high Performance Concrete Against Blasts: From Materials to Structures*. Woodhead Publishing Series in Civil and Structural Engineering. Woodhead Publishing, 2018.
- [179] J. Yang, S. Wang, Y. Ding, Z. Zheng, and J. Yu. “Crashworthiness of graded cellular materials: A design strategy based on a nonlinear plastic shock model.” In: *Materials Science and Engineering: A* 680 (2017), pp. 411–420. DOI: 10.1016/j.msea.2016.11.010.
- [180] Z. Q. Ye and G. W. Ma. “Effects of foam claddings for structure protection against blast loads.” In: *Journal of Engineering Mechanics* 133.1 (2007), pp. 41–47. DOI: 10.1061/(ASCE)0733-9399(2007)133:1(41).
- [181] N. Yi, J. J. Kim, T. Han, Y. Cho, and J. H. Lee. “Blast-resistant characteristics of ultra-high strength concrete and reactive powder concrete.” In: *Construction and Building Materials* 28.1 (2012), pp. 694–707. DOI: 10.1016/j.conbuildmat.2011.09.014.
- [182] Z. L. Yu, P. Xue, and Z. Chen. “Nested tube system applicable to protective structures against blast shock.” In: *International Journal of Impact Engineering* 102 (2017), pp. 129–139. DOI: 10.1016/j.ijimpeng.2016.11.018.

- [183] S. C. K. Yuen, G. Cunliffe, and M. C. du Plessis. “Blast response of cladding sandwich panels with tubular cores.” In: *International Journal of Impact Engineering* 110 (2017), pp. 266–278. DOI: 10.1016/j.ijimpeng.2017.04.016.
- [184] C. Zhang, B. Zhu, D. Li, and L. J. Lee. “Extruded polystyrene foams with bimodal cell morphology.” In: *Polymer* 53.12 (2012), pp. 2435–2442. DOI: 10.1016/j.polymer.2012.04.006.
- [185] Z. Zheng, Y. Liu, J. Yu, and S. R. Reid. “Dynamic crushing of cellular materials: continuum-based wave models for the transitional and shock modes.” In: *International Journal of Impact Engineering* 42 (2012), pp. 66–79.
- [186] Z. Zheng, C. Wang, J. Yu, S. R. Reid, and J. J. Harrigan. “Dynamic stress-strain states for metal foams using a 3D cellular model.” In: *Journal of the Mechanics and Physics of Solids* 72 (2014), pp. 93–114. DOI: 10.1016/j.jmps.2014.07.013.
- [187] Z. Zheng, J. Yu, C. Wang, S. Liao, and Y. Liu. “Dynamic crushing of cellular materials: A unified framework of plastic shock wave models.” In: *International Journal of Impact Engineering* 53 (2013), pp. 29–43. DOI: 10.1016/j.ijimpeng.2012.06.012.
- [188] H. Zhou, Z. Zhao, and G. Ma. “Protection against blast load with cellular materials and structures.” In: *International Journal of Aerospace and Lightweight Structures* 2 (2012), pp. 53–76. DOI: 10.3850/S2010428612000220.
- [189] J. Zhou, Z. Guan, and W. J. Cantwell. “The energy-absorbing behaviour of composite tube-reinforced foams.” In: *Composites Part B: Engineering* 139.15 (2018), pp. 227–237. DOI: 10.1016/j.compositesb.2017.11.066.